Nonlinear Microscopy for Failure Analysis of CMOS Integrated Circuits in the Vectorial Focusing Regime

Marius Rutkauskas

Submitted for the degree of Doctor of Philosophy

Heriot-Watt University

School of Engineering and Physical Sciences

August 2017

The copyright in this thesis is owned by the author. Any quotation from the thesis or use of any of the information contained in it must acknowledge this thesis as the source of the quotation or information.

ABSTRACT

This thesis focuses on the development of techniques for enhancing the spatial resolution and localisation precision in the sub-surface microscopy for failure analysis in semiconductor integrated circuits (ICs). Highest spatial resolutions are obtained by implementing solid immersion lenses (SIL), which provide unsurpassed numerical aperture (NA) for sub-surface microscopy. These high NA conditions mean that scalar diffraction theory is no longer valid and a vectorial focusing description should be applied to accurately describe the focal plane electric field distribution.

Vectorial theory predicts that under high NA conditions a linearly polarised (LP) light focuses to a spot that is extended along the electric field vector, but radially polarised (RP) light is predicted to form a circular spot whose diameter equals the narrower dimension obtained with linear polarisation. By implementing a novel liquid-crystal (LC) radial polarisation converter (RPC) this effect was studied for both two-photon optical-beam-induced current (TOBIC) microscopy and two-photon laser assisted device alteration (2pLADA) techniques, showing a resolution and localisation improvement using the RP beam. By comparing images of the same structural features obtained using linear, circular and radial polarisations imaging and localisation resolutions both approaching 100 nm were demonstrated. The obtained experimental results were in good agreement with modelling and were consistent with theoretically predicted behaviour. Certain artefacts were observed under radial polarisation, which were thought to result from the extended depth of focus and the significant longitudinal field component. In any application these effects must be considered alongside the benefits of the symmetric field distribution in the focal plane.

While SIL sub-surface microscopy offers unmatched spatial resolutions, it is prone to being severely degraded by aberrations arising from inaccurate dimensions of the SIL, imprecise substrate thickness or imperfect contact between SIL and substrate. It is in this context that techniques to identify and even mitigate aberrations in the system are important. A simple approach is demonstrated for revealing the presence of chromatic and spherical aberrations by measuring the two-photon autocorrelation of the pulses at the focal plane inside the sample. In the case of aberration free imaging, it was shown both theoretically and experimentally that the planes of the maximum autocorrelation amplitude and shortest pulse duration always coincide. Therefore, the optics of the imaging system can be first adjusted to obtain the minimum autocorrelation duration and then the wavefront of incident light modified to maximise the autocorrelation intensity, iterating this procedure until the positions of minimum pulse duration and maximum autocorrelation amplitude coincide.

Mama,

Tikiuosi, gali didžiuotis manimi

ACADEMIC REGISTRY
Research Thesis Submission

Name:	MARIUS RUTKAUSKAS		
School:	School of Engineering and Physical Sciences		
Version: *(i.e. First, Resubmission, Final)*	Final	Degree Sought:	Ph.D

Declaration

In accordance with the appropriate regulations I hereby submit my thesis and I declare that:

1) the thesis embodies the results of my own work and has been composed by myself
2) where appropriate, I have made acknowledgement of the work of others and have made reference to work carried out in collaboration with other persons
3) the thesis is the correct version of the thesis for submission and is the same version as any electronic versions submitted*.
4) my thesis for the award referred to, deposited in the Heriot-Watt University Library, should be made available for loan or photocopying and be available via the Institutional Repository, subject to such conditions as the Librarian may require
5) I understand that as a student of the University I am required to abide by the Regulations of the University and to conform to its discipline.
6) I confirm that the thesis has been verified against plagiarism via an approved plagiarism detection application e.g. Turnitin.

* *Please note that it is the responsibility of the candidate to ensure that the correct version of the thesis is submitted.*

Signature of Candidate:		Date:	07 09 2017

Submission

Submitted By *(name in capitals)*:	MARIUS RUTKAUSKAS
Signature of Individual Submitting:	
Date Submitted:	

For Completion in the Student Service Centre (SSC)

Received in the SSC by *(name in capitals)*:			
Chapter 1. *Method of Submission (Handed in to SSC; posted through internal/external mail)*:			
Chapter 2. *E-thesis Submitted (**mandatory for final theses**)*			
Signature:		Date:	

ACKNOWLEDGMENTS

The work behind this thesis is a massive achievement in which a number of people were involved and it would not be possible to without their support. I would like to say thanks to them all.

First and foremost, I would like to express my sincerest gratitude to my academic supervisor Professor Derryck Reid, who guided me through this tough but rewarding journey. I owe you so much for your patience, support and ideas over the years. Your enthusiasm and dedication makes you a brilliant mentor. Thank you for giving me this opportunity.

Many thanks for Dr. Carl Farrell. Your help to get my feet in this project made the first stages a lot easier. Your knowledge, advice and helping hand on the fibre lasers have been exceptionally valuable. Your skill in photonics are as amazing as you are in football pitch.

I would like to thank Oguzhan and Luke, who were the most cheerful labmates of the cursed lab. Our uplifting conversations and sharing of complaints helped me to go through those black days without luck in the lab.

I want to thank all other members of the Ultrafast Optics group Karolis, Richard, Jinghua, Christopher, Zhaowei, Jake, Holly, Toby, Cristtel and Thomas. I am grateful for your help and companionship through this project.

Many thanks to all DSG and Freescale employees, who not only supplied me with the test material and equipment but also made my visits pleasant and welcome.

Special thank for colleagues I have collaborations with. I would like to express my gratitude to Dr. Christophe Dorrer and the University of Rochester for providing radial polarisation converters. I greatly appreciate also the help and theoretical modelling by Dr. Martha Rosete-Aguilar and Dr. Jesús Garduño-Mejía from the Autonomous University of Mexico (UNAM).

I would also like to acknowledge the funding agency. The material in this dissertation is based upon work supported by the the Intelligence Advanced Research Projects Activity (IARPA) via Air Force Research Laboratory (AFRL) Contract No. FA8650-11-C-7104.

And last but not least, I would like to thank my family for your support through the years of this difficult journey. Especially, to my Zsófia for your smile and love. Thank you for reminding me every day that I can do it. Szeretlek nagyon nagyon dilim.

LIST OF PUBLICATIONS BY THE CANDIDATE

Journal Publications

1. **M. Rutkauskas**, D. T. Reid, J. Garduño-Mejía, M. Rosete-Aguilar, Time-domain measurements reveal spatial aberrations in a sub-surface two-photon microscope, Applied Optics 56, 5047-5053 (2017).
2. **M. Rutkauskas**, C. Farrell, C. Dorrer, K. L. Marshall, T. Crawford, T. R. Lundquist, P. Vedagarbha, K. Erington, D. Bodoh and D. T. Reid, Two-photon laser-assisted device alteration in CMOS integrated circuits using linearly, circularly and radially polarised light, Microelectronics reliability **60**, 62–66 (2016).
3. **M. Rutkauskas**, C. Farrell, C. Dorrer, K. L. Marshall, T. R. Lundquist, P. Vedagarbha, and D. T. Reid, High-resolution sub-surface microscopy of CMOS integrated circuits using radially polarised light, Optics Letters **40**, 5502-5505 (2015).

Conference Publications

1. **M. Rutkauskas**, D. T. Reid, J. Garduño-Mejía, M. Rosete-Aguilar, Time-domain measurements reveal spatial aberrations in a sub-surface two-photon microscope, 2015 European Conference on Lasers and Electro-Optics - European Quantum Electronics Conference, Munich, CF-P.3 (25-29 June 2017).
2. **M. Rutkauskas**, D. T. Reid, J. Garduño-Mejía, M. Rosete-Aguilar, Time-domain measurements reveal spatial aberrations in a sub-surface two-photon microscope, CLEO: Science and Innovations 2017, San Jose, ATh4B.5 (14-19 May 2017).
3. **M. Rutkauskas**, C. Farrell, C. Dorrer, K. Marshall, T. Crawford, T. Lundquist, P. Vedagarbha, K. Erington, D. Bodoh, D. T. Reid, Two-Photon Laser-Assisted Device Alteration in CMOS Integrated Circuits Using Linearly, Circularly and Radially Polarised Light, CLEO: Science and Innovations 2015, San Jose, ATu3J.8 (6-10 June 2016).
4. **M. Rutkauskas**, C. Farrell, C. Dorrer, K. L. Marshall, T. Lundquist, P. Vedagarbha, and D. T. Reid, High-Resolution Sub-Surface Microscopy of CMOS Intagrated Circuits Using Radially Polarised Light, 2015 European Conference on Lasers and Electro-Optics - European Quantum Electronics Conference, Munich, CD_11_4 (21–25 June 2015).
5. **M. Rutkauskas**, C. Farrell, C. Dorrer, K. L. Marshall, T. Lundquist, P. Vedagarbha, and D. T. Reid, High-Resolution Sub-Surface Microscopy of CMOS Intagrated Circuits Using Radially Polarised Light, CLEO: Science and Innovations 2015, San Jose, STh1H.7 (10–15 May 2015).

LIST OF ABBREVIATIONS

2pLADA	Two-photon laser assisted device alteration
AFM	Atomic force microscopy
AS	Aperture stop
aSIL	Aplanatic solid immersion lens
ATE	Automatic test equipment
CAD	Computer-aided design
CCD	Charge-coupled device
CL	Collimating lens
CMOS	Complementary metal-oxide-semiconductor
CV	Cylindrical vector
CW	Continuous wave
DOP	Degree of polarisation
DUT	Device under test
DVM	Daley variation mapping
EDFA	Erbium doped fibre amplifier
ESA	Excited state absorption
FA	Failure analysis
FBG	Fibre Bragg grating
FL	Focusing lens
FWHM	Full width half maximum
GDD	Group delay dispersion
GTI	Gires-Tournois interferometer
GVD	Group velocity dispersion
hSIL	Hemispherical solid immersion lens
HWP	Half-wave plate
IC	Integrated circuit
LADA	Laser assisted device alteration
LC	Liquid crystal
LD	Laser diode
LET	Linear energy transfer
LIVA	Light induced voltage alteration
LP	Linear polarisation
LSM	Laser scanning microscope

LVP	Laser voltage probing
MD	Monitor diode
MO	Microscope objective
NA	Numerical aperture
NALM	Nonlinear amplifying loop mirror
NCFPI	Near-confocal Fabry–Perot interferometer
nMOS	N-channel MOSFET
NPR	Nonlinear polarisation rotation
OBIC	Optical beam induced current
OBIRCh	Optical beam induced resistance change
OD	Optical diode
PBS	Polarising beam splitter
PCF	Photonic crystal fibre
PLS	Photoelectric laser stimulation
PM	Polarisation maintaining
pMOS	P-channel MOSFET
PSF	Point spread function
PTD	Propagation time difference
QWP	Quarter-wave plate
RP	Radial polarisation
RPC	Radial polarisation converter
RMS	Root mean square
SA	Saturable absorber
SAM	Self-amplitude modulation
SBR	Saturable Bragg reflector
SEB	Single event burnout
SEE	Single event effect
SEFI	Single event function interrupt
SEHE	Single event hard error
SEI	Seebeck effect imaging
SEL	Single event latchup
SESAM	Semiconductor saturable absorber mirror
SET	Single event transient
SEU	Single event upset
SHG	Second harmonic generation

SIL	Solid immersion lens
SLM	Spatial light modulator
SPA	Single photon absorption
SPE	Spiral phase element
SPM	Self-phase modulation
SPEDF	Stretched pulse erbium doped fibre
SR	Strehl ratio
SRAM	Static random-access memory
SSFS	Self-stimulated frequency shift
STED	Stimulated emission depletion
TIVA	Thermally induced voltage alteration
TOBIC	Two-photon optical beam induced current
TPA	Two-photon absorption
TRAM	Translation microscopy
WDM	Wavelength division multiplier
XIVA	Externally induced voltage alteration
XPM	Cross-phase modulation
YDF	Ytterbium doped fibre

CONTENTS

Chapter 1. Introduction 4

1.1 Motivation 4

1.2 Sub-surface solid-immersion microscopy 5

1.2.1 Introduction to confocal microscopy 6

1.2.2 Solid immersion lenses 8

1.3 Optical absorption in CMOS devices 11

1.3.1 Optical properties of silicon 11

1.3.2 Single-photon absorption 14

1.3.3 Multi-photon absorption 15

1.4 Optical techniques for failure analysis of integrated circuits 17

1.4.1 Laser thermal stimulation techniques 17

1.4.2 Laser photoelectric stimulation techniques 20

1.4.3 Tester based laser stimulation techniques 22

1.4.4 Photon emission microscopy 23

1.5 Thesis outline 24

References 25

Chapter 2. Femtosecond Er:fibre laser for sub-surface imaging at 1550 nm 32

2.1 The Er3+ ion 33

2.2 Introduction to ultrafast fibre laser architectures 35

2.2.1 Active mode-locking 37

2.2.2 Semiconductor saturable absorption 37

2.2.3 Nonlinear amplifying loop mirror 38

2.2.4 Nonlinear polarisation rotation 40

2.3 Pulse shaping effects in ultrafast lasers 41

2.3.1 Dispersion 41

2.3.2 Group delay dispersion compensation 43

2.3.3 Self-phase modulation 46

2.3.4 Optical solitons 47

2.4 Erbium-doped fibre soliton laser 48

2.5 Stretched-pulse erbium-doped fibre laser 49

2.6 Erbium-doped fibre amplifier 51

2.7 Construction 52

2.8 Pulse measurement 55

References 57

Chapter 3. High-resolution sub-surface microscopy of CMOS integrated circuits using radially polarised light ... 61
3.1 Introduction ... 61
3.2 Scalar focusing theory ... 62
3.2.1 Scalar resolution limits ... 62
3.2.2 Scalar beams ... 63
3.2.3 Scalar PSF ... 65
3.3 Vectorial focusing theory ... 66
3.3.1 Cylindrical vector beams ... 66
3.3.2 Focusing properties of CV beams ... 68
3.3.3 Techniques to generate cylindrical vector beams ... 74
3.3.4 Pupil engineering ... 77
3.3.5 Assessing the polarisation purity of cylindrical vector beams ... 80
3.4 Implementation of radially polarised illumination for TOBIC microscopy ... 82
3.4.1 Microscope layout ... 82
3.4.2 Device under test ... 84
3.4.3 Solid immersion lenses ... 86
3.4.4 Liquid-crystal polarisation converters ... 89
3.4.5 Resolution measurement technique ... 91
3.5 Results and discussion ... 92
3.5.1 Evaluation of radial polarisation converter ... 92
3.5.2 Numerical modelling of the point spread function ... 94
3.5.3 TOBIC measurements ... 95
References ... 101

Chapter 4. Two-photon laser-assisted device alteration in CMOS integrated circuits using linearly, circularly and radially polarised light ... 106
4.1 Introduction ... 106
4.2 Radiation effects on silicon circuits ... 107
4.2.1 Ultrashort laser pulse interaction with ICs ... 107
4.2.2 Single event effects ... 109
4.2.3 General SEE testing approaches ... 113
4.2.4 LADA and 2pLADA techniques. ... 115
4.3 Raman-shifted femtosecond Yb:fibre laser for 2pLADA at 1280 nm ... 118
4.3.1 Yb^{3+} optical properties ... 118
4.3.2 Soliton self-frequency shifting ... 119
4.3.3 Raman-shifted femtosecond Yb:fibre laser construction ... 120
4.3.4 Repetition rate stabilisation to an external clock ... 123

4.4 Implementation of 2pLADA ... 124
4.4.1 Description of the device under test ... 124
4.4.2 ATE Tester ... 124
4.4.3 Microscope configuration ... 125
4.5 Results and discussion ... 127
4.5.1 Polarisation-state dependence of 2pLADA spatial resolution ... 127
4.5.2 Time-resolved imaging using 2pLADA ... 130
4.5.3 Observations of single-event upsets ... 131
4.6 Conclusions ... 132
References ... 134

Chapter 5. Spatio-temporal aberrations in sub-surface solid-immersion microscopy ... 140
5.1 Introduction ... 140
5.2 Theory of aberrations ... 142
5.2.1 Seidel aberrations ... 142
5.2.2 Zernike polynomials ... 149
5.2.3 Relationship between Zernike polynomials and third-order aberrations ... 152
5.2.4 Strehl ratio ... 153
5.2.5 Chromatic aberrations ... 153
5.2.6 Aberrations of a simple lens ... 155
5.2.7 Aberrations in solid immersion lens microscopy ... 156
5.3 Experimental investigation of spatio-temporal aberrations ... 157
5.3.1 Pulse measurement at the focus of the SIL microscope ... 157
5.3.2 Observation of focal-dependent spatio-temporal effects ... 160
5.4 Conclusions ... 164
References ... 166

Chapter 6. Conclusions and future developments ... 168
6.1 Technical summary and conclusions ... 168
6.2 Future work ... 170
References ... 175

Chapter 3. Introduction

3.1 Motivation

Failure analysis (FA) is an important tool in semiconductor industry aiming, to analyse failing parts within integrated circuit (IC) devices [1]. Its goal is not only to determine manufacturing flaws but also to offer suitable solutions for the IC design issues. Therefore, the FA is understood to have a direct impact on the IC development. This discipline consists of a wide range of electrical and physical means of testing, which are performed on ICs to measure, analyse and understand the reasons behind the device failures [2, 3]. As FA is a reactive tool of the fast evolving semiconductor industry it typically tries to keep up with manufacturing technology [4]. A constant demand of the state-of-the-art microelectronic equipment dictates the need of its constant development and evolution. Semiconductor industry adheres to the Moore's law and maintains constant scaling towards the 5-nm-technology node (Fig. 1.1) [5, 6]. Scaling is not the only challenge for industry to cope with as ICs tend to develop into more and more complicated and advanced functional designs [7]. The increasing numbers of devices inside a single chip leads to the higher probabilities of failures and defects in the ICs [8]. Therefore, continuous development of novel FA techniques is vital for manufacturers to maintain this exponential progress in IC industry for longer [9, 10, 11].

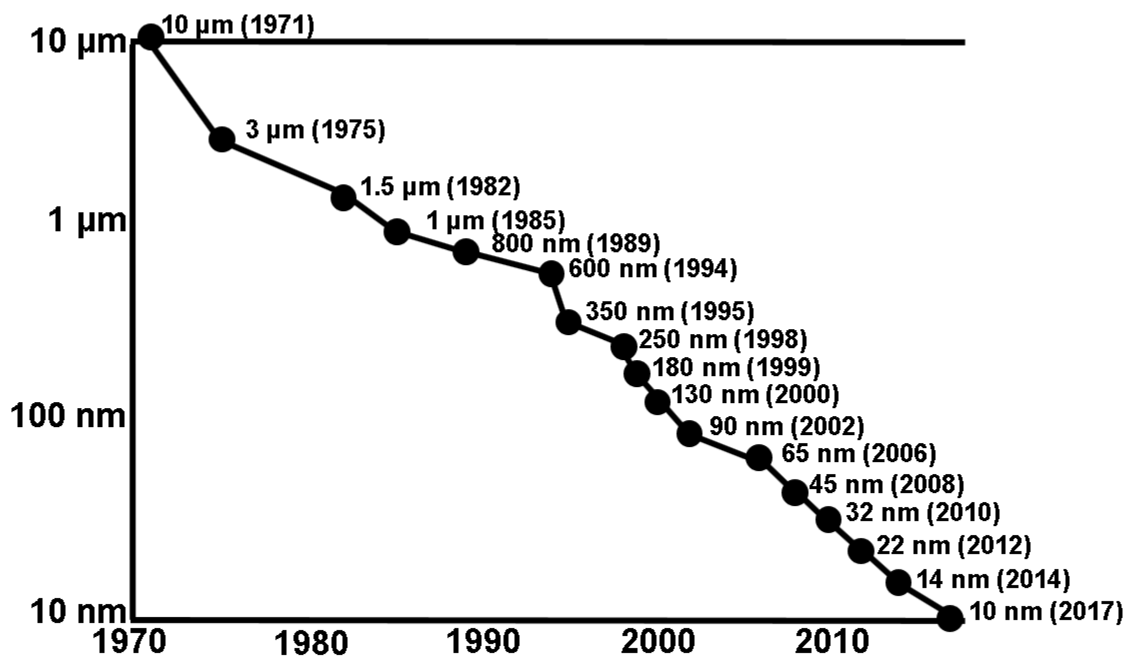

Figure 1.1. The progress of miniaturisation.

Rapidly shrinking features suggest that many FA techniques can no longer provide sufficient localisation resolutions to single out transistors. Other techniques pose limitations on sample preparation to exploit their outstanding imaging resolutions, often leading to the destruction of the testing device [3, 12].

Large number of devices inside the single IC requires increased number of metal interconnect layers, leading to the limitations to probing from the front side [13]. Therefore, imaging from the backside of the device through the thick substrate level typically is the only proper solution for FA [14].

Such requirement can be met by optical microscopy, which is employed for the sub-surface backside imaging of ICs through silicon using infra-red light [15]. However, the resolution of infra-red light optical microscopy is restricted to the diffraction limit, which is approximately equal to a half of wavelength (around 500 nm) of infra-red light, which is more than order of magnitude poorer than what is needed to localise a single transistor of the IC [16].

The invention of solid immersion lens (SIL) made it possible to achieve the highest sub-surface resolutions up to date [17-21]. The SIL is a good solution to enhance the resolution of optical microscopy due to its ability to increase the numerical aperture (NA) considerably up to the value of refractive index of the material [22]. However, this is usually not sufficient to keep up with the miniaturisation of the ICs and therefore additional means of imaging resolution enhancing techniques have to be to developed.

Most recent efforts have developed improvements of localisation resolution by tailoring the laser beam illumination. Phase [23, 24], amplitude [25] and polarisation [26, 27] can be designed to produce a focal spot as sharp as possible. In this thesis, the vectorial focusing conditions of high NA systems were exploited to investigate the impact of the incident beam's polarisation on the imaging and localisation resolutions. Combining the high-NA SIL imaging technique with the nonlinear response of the two-photon absorption makes it possible to achieve sub-100-nm resolutions for non-invasive backside sub-surface microscopy [25].

3.2 Sub-surface solid-immersion microscopy

Since the dawn of optical microscopes in early seventeenth century, optical techniques have been applied in a wide range of applications [28, 29]. For FA of semiconductor ICs optical microscopes can be both applied in front-side and backside probing [30]. The front-side imaging typically employs visible light, which is guided to the device layer via the front of device. Despite short wavelengths making it possible to image with resolutions of 200 nm without any extra effort, strong absorption of visible light in silicon requires polishing of the device and removing highly reflective metal interconnect layers, so rendering the device inoperable. Such preparation of the

ICs is unwanted as it leads to the destruction of the device [14]. Another approach is to exploit the transparency window of silicon, which starts at around 1.1 μm and perform the backside probing using infrared (IR) light [31]. This section now reviews the relevant optical microscopy techniques and its challenges for sub-surface imaging of ICs.

3.2.1 Introduction to confocal microscopy

The basic idea of the confocal microscopy technique is to illuminate the sample using a point light source and to record the response signal, which has passed the pinhole. This idea was suggested by Minsky in 1957 and later it was patented in 1961 [32]. The confocal microscope was invented with the idea to minimise stray light in the measurement [33]. Therefore, it is necessary to perform the lateral scan of the sample to obtain the whole image. As a result, such images are of high quality images over the whole area of the sample, while conventional wide-field microscope is limited to the illuminated area. [34]. Scanning can be initiated by either translating the sample, or translating the laser beam inside the sample [35].

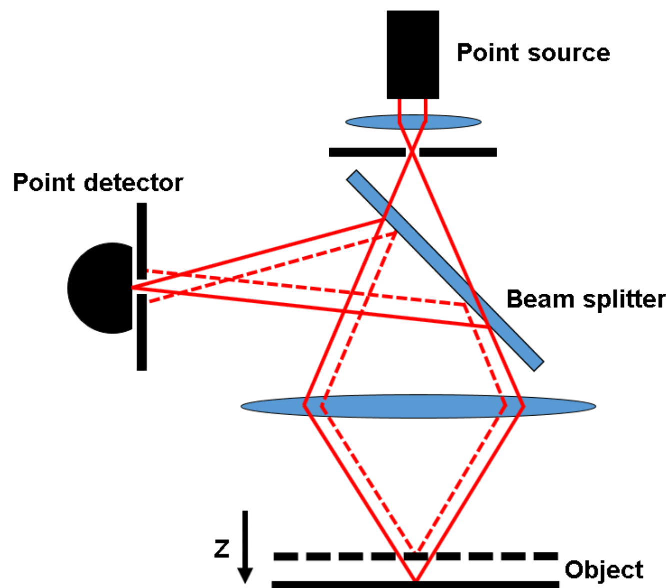

Figure 1.2. The scanning confocal microscope design (adapted from [29]).

Sheppard and Choudhury investigated the scanning confocal microscope theoretically for the first time in 1977 (Fig. 1.2) [36]. Later Sheppard and Wilson demonstrated scanning microscope with a photomultiplier tube and novel scanning stage. They showed that sample can be scanned and a signal obtained with a detector of a finite size. The microscope of such design was able to produce high quality images of ICs [37]. If, on the other hand, both source and detector are point-like, the microscope becomes a confocal microscope.

The quality of an optical microscope is described by its ability to resolve fine details of the sample [38]. Due to the wave nature of light and diffraction, it is impossible to produce a point

image of a point object. Instead it forms a bright spot of light surrounded by concentric diffraction rings, which is called the Airy pattern [39]. Therefore, the resolution of an optical microscope is restricted by the diffraction limit. The Sparrow limit defines the smallest feature that can be resolved with optical system [38]:

$$\text{Resolving power} = k\frac{\lambda}{NA} = k\frac{\lambda}{n\sin\theta}, \qquad (1.1)$$

where λ is the wavelength of the incident light and NA is the numerical aperture of an optical system, n refractive index of the material, θ is the half the angle of the cone of light, and k is the imaging factor (0.47 for the Sparrow limit).

As it is seen from Eq. (1.1), the resolution of the optical system depends on four parameters. Therefore, the following strategies can be exploited to enhance the optical resolving power: decrease the wavelength of the light source, increase refractive index, increase the angular spectrum of the incident light, decrease the k factor [19].

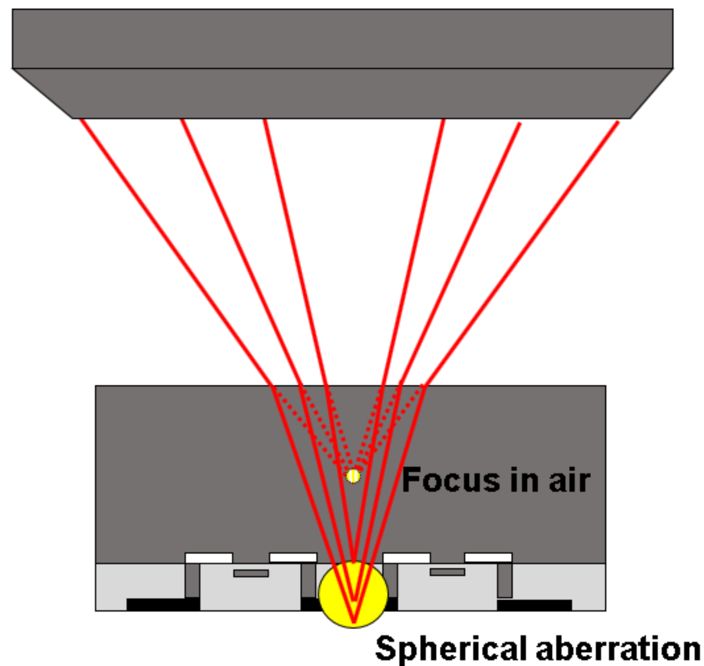

Figure 1.3. Spherical aberration when light is incident through air/silicon interface (adapted from [40]).

Clearly the maximum value of $\sin\theta = 1$. The reduction of wavelength is also limited as shorter wavelengths are absorbed strongly, thus practical wavelengths are restricted to infrared. Only the k factor and refractive index modulation remain as potential promising routes to produce higher spatial resolutions. A few techniques were shown to be able to reduce the k factor: apertures [41, 42], structured illumination [43], polarisation control [26, 44] and laterally interfering beams [45]. A liquid immersion objective lens is the technique appropriate to

increasing the refractive index by replacing the air with oil or water. This allows to obtain a slight improvement in resolution, which is widely used technique in the optical microscope of biological samples [46]. However, for FA there is no such liquid, which is close to refractive index of silicon (3.48). Also as light travels through the air and silicon boundary, spherical aberrations appear, leading to a reduction of the resolution of the optical system (Fig. 1.3) [40, 47].

An elegant solution, which addresses both spherical aberrations and low refractive index problems, is the solid immersion lens (SIL). SILs provide the ability to perform backside IR light imaging and probing of sub-100-nm IC features [48-50].

3.2.2 Solid immersion lenses

It has been always a constant struggle for scientists to deal with improving the spatial resolution. In 1678 Hooke was the first to propose an immersion technique. Only in 1812 Brewster suggested to immerse the objective lens into the liquid medium. The first immersion objective lenses were made around 1840 by Amici [51]. However, this liquid immersion technique is not suitable for semiconductor sub-surface imaging because the refractive index of semiconductors is too high for any liquid to even approach it.

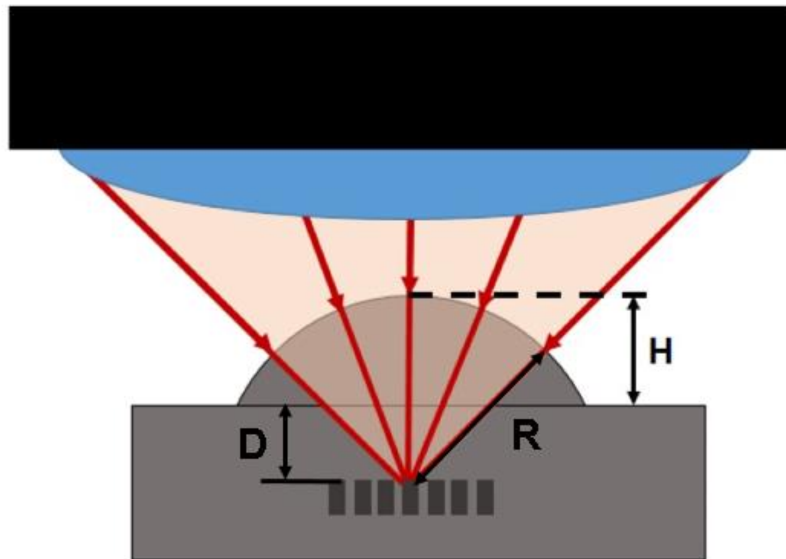

Figure 1.4. The hSIL design for IC sub-surface imaging. H – height of the SIL, D – thickness of silicon substrate, R – radius of the SIL.

At last in 1990 Mansfield and Kino invented the solid immersion microscopy, which was a breakthrough in the semiconductor microscopy [17]. The basic idea of this technique remains the same as in liquid immersion microscopy. However, at the same time solid immersion microscopy enhances the spatial resolution by including the light, rays which are incident at angles higher than the critical angle. There are two types of solid immersion lenses: “central” or hemispherical SILs (hSIL) and “aplanatic” SILs (aSIL) [22].

SILs benefit from the so called aplanatic points, which are the focal points where light can be focused without spherical aberrations. The rays, which are normal to the surface of the sphere, are not refracted at the air-SIL interface. Therefore, all these rays are collected at the centre of the sphere, which is considered the first aplanatic point. The second aplanatic focal position is at the distance $z = (n_1/n_0)R$ from the center of the sphere (R - radius of the sphere, n_0 and n_1 - the refractive indices of the sphere and the air). All the rays, which are refracted at the air-SIL interface, are coincident at this point [22].

hSILs are normally used for imaging structures just beneath the surface. This limitation results from the following Eq. (1.2), which should be fulfilled by the hSIL:

$$H = R - D, \tag{1.2}$$

here H - height of the hSIL, R - radius of the sphere and D - thickness of silicon substrate (Fig. 1.4). Therefore if the hSIL has H equal to R, it can image at the depth D equal to 0. In sub-surface microscopy, a SIL increases the light-gathering power of the objective lens, because it benefits from the first aplanatic point of the sphere (Fig. 1.4). As a result, the hSIL is chromatic aberration free.

The NA can be increased by the hSIL up to the refractive index of the medium surrounding the imaging object. The increase of the NA leads to an improved spatial resolution, which for the hSIL is by a factor n for both the lateral and longitudinal resolutions. This means that the lateral resolution gain when using the hSIL is equal to n. The hSIL also enhances the magnification of the microscope by the same factor of n. However, the best available NA with the hSIL is limited by the NA of the objective lens. To achieve the best values of the spatial resolution would require an objective lens with an NA of 1 [22, 52].

aSILs are used for imaging features which are lying deeper beneath the surface of the device. The aSIL exploits the second aplanatic position (Fig. 1.5). Each aSIL is designed for a certain sub-surface depth as is seen in this equation:

$$H = R\left(1 + \frac{1}{n}\right) - D. \tag{1.3}$$

Also Eq. (1.3) suggests that focal position for the aSIL depends on the wavelength. This also means that aSIL introduces longitudinal chromatic aberration, which is not the case for the hSIL. The aSIL benefits from high magnification even compared with the hSIL. Also it improves the NA by a factor of n^2 up to a maximum value of n. However, it is impossible to reach the maximum possible NA as it requires the rays to be incident at the angle of 90°. As NA describes the spatial resolution, the aSIL can improve it considerably by n^2 [22].

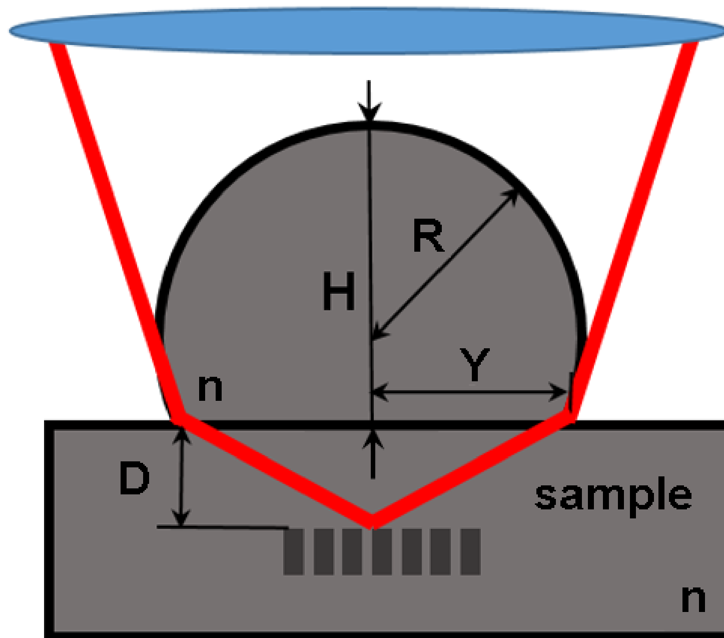

Figure 1.5. The aSIL design for IC sub-surface imaging. H – height of the aSIL, R – radius of the sphere, D – thickness of silicon substrate, n – refractive index, Y – radius of the aSIL base.

The magnification of aSIL is explained as an "optical lever" effect, which has been described by Serrels *et al* [22]. It means that if the beam moves relative to the optical axes, the focal position inside the SIL is translated by a smaller distance. This effect is portrayed in Fig. 1.6. The leveraging effect differs not only for the hSIL and aSIL but also for the transverse and longitudinal directions too (Fig. 1.6).

It was mentioned before that the hSIL has magnification of n and the aSIL of n^2. Therefore, for the hSIL the lateral leveraging factor is $\Delta x/n$, while for the aSIL it is $\Delta x/n^2$, where Δx denotes a lateral displacement of the beam [22].

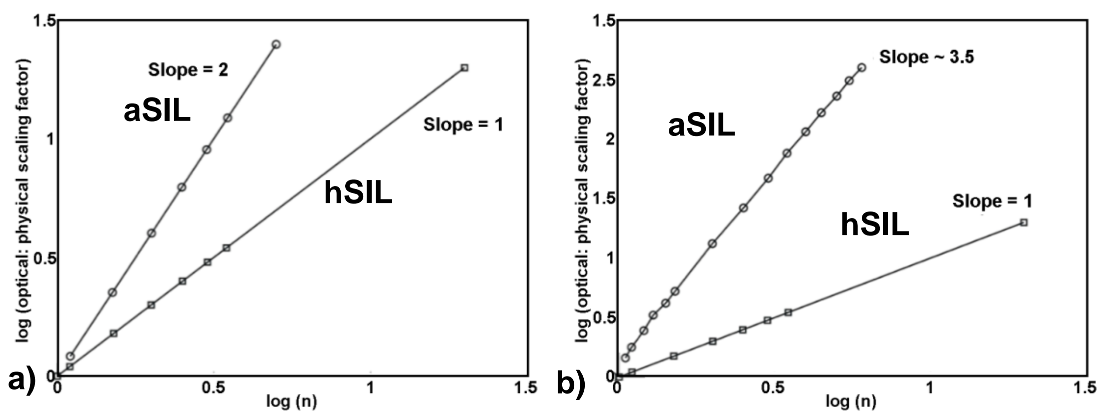

Figure 1.6. (a) Lateral and (b) longitudinal lever effect for both the hSIL and the aSIL designs [22].

3.3 Optical absorption in CMOS devices

Optical FA techniques are based on the ability of the laser beam to locally induce changes to the IC under test. To better understand how the laser beam interacts with the IC first the optical properties of materials comprising devices must be understood. There are many metallic contacts in the IC, which strongly reflect light and are opaque, meaning that fraction of light, which is not reflected, is highly absorbed leading to the photon energy being converted to heat [53] [54]. Polycrystalline semiconductors, which typically form the substrate were found to behave in similar manner [55]. Oxides, which form epitaxy, are typically highly transparent and transmit or reflect light via the Fabry-Perot effect. Finally, semiconductor (transistors) optical properties are determined by the optical absorption coefficient, which is different for pure and doped silicon [15].

3.3.1 Optical properties of silicon

Silicon is the most common material, which is used for the manufacturing of ICs. Therefore, it is essential to understand its optical properties to apply lasers in various FA techniques.

The propagation of the laser beam through silicon is determined by the single, multi-photon and free carrier absorption [56]. There is also a set of nonlinear optical phenomena, including the Kerr effect [57], the Raman effect [58], the Franz-Keldysh effect [62], which influence the propagation of light. This nonlinear behaviour is a cause of physical properties of silicon, such as centrosymmetry and anisotropy.

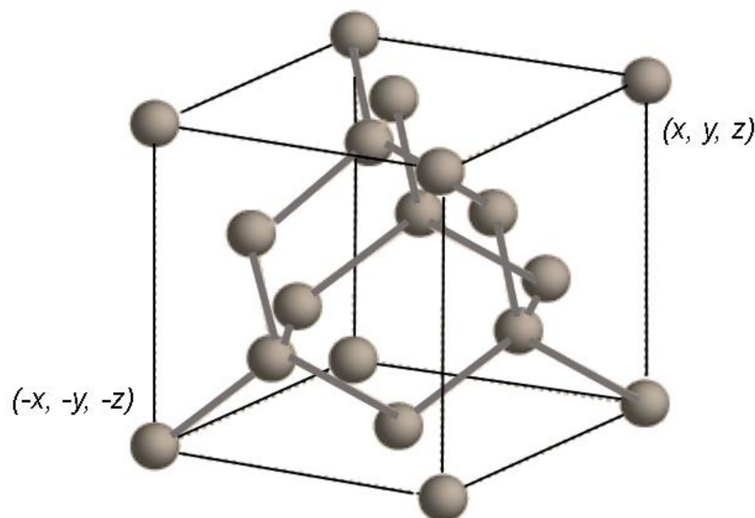

Figure 1.7. Crystal lattice of silicon, which is a centrosymmetric cubic crystal (adapted from [55]).

Centrosymmetric crystals have a lattice where every atom at the (x, y, z) position has an identical atom at the position (-x, -y, -z) (Fig. 1.7). Therefore, this type of symmetry is called inversion symmetry and such a crystal cannot exhibit the second order susceptibility, which is zero [55].

Anisotropy is another property of silicon, which suggests that it has genuine optical characteristics depending on the direction of propagating light [60]. Refractive index typically varies in anisotropic media and depends on both the composition and the crystal structure. An anisotropic crystal whose refractive index is not constant can serve as a polarisation retarder. Silicon exhibits such anisotropic properties as the absorption of light creates an internal electric field, which triggers an electro-optical effect, thus which modifies the optical properties of the medium. Lin *et al* [60] has shown that absorption in silicon differs by 12% between <010> and <011> (Fig. 1.8) propagation direction. Another study demonstrated that anisotropy also affects the carrier mobility within transistors [61].

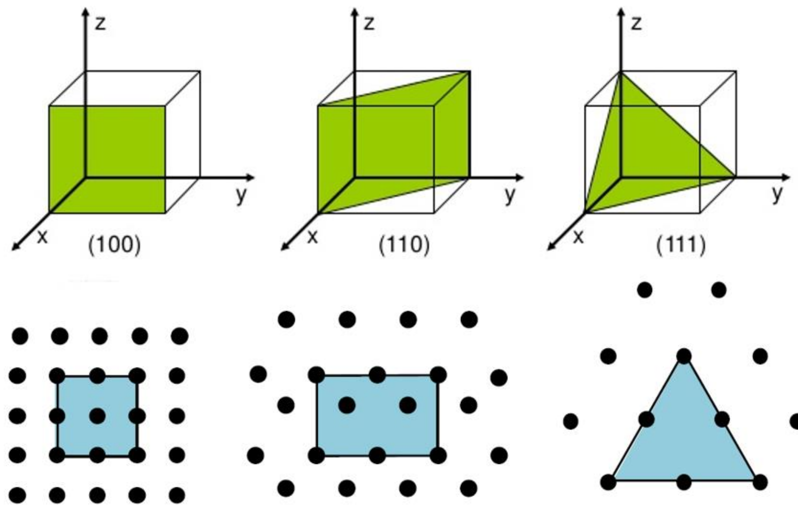

Figure 1.8. Three crystal faces in the silicon cubic lattice structure [60].

For undoped crystalline silicon the absorption happens only via inter-band transitions and therefore depends on the silicon band structure. An incident photon is absorbed only if it is of sufficient energy to move an electron from the valence band to the conduction band. This means that only photons having energy greater or equal to the bandgap energy of silicon bandgap energy can be absorbed, while the lower energy photons pass through the material [62]. Therefore, the crystalline silicon is transparent for wavelengths longer than 1.1 µm and its absorption coefficient for wavelengths $0.8\ \mu m < \lambda < 1.06\ \mu m$ is [63]:

$$a = (85{,}01\lambda^{-1} - 77{,}104)^2. \quad (1.4)$$

Penetration depth, where intensity reaches $1/e$ level, can be written as [63]:

$$d = \frac{1}{a}. \quad (1.5)$$

Also it should be noted that for wavelengths, close to 1064 nm, the transmission of monocrystalline silicon is high, but it decreases rapidly as the wavelength gets smaller. Therefore, near-infrared light is a suitable choice for backside imaging FA analysis.

However, usually silicon is p or n doped to improve the device performance. Therefore, the concentration of impurities also affects the optical absorption coefficient of silicon [64]. The optical transmission curve depicted in Fig. 1.9 shows that the increase of the concentration of impurities in a p-type substrate significantly reduces the optical transmission even at the near-infrared wavelengths [65]. In this case three absorption phenomena limit the transparency of doped silicon: inter-band absorption, absorption by impurities and the absorption by free carriers [66, 67].

Highly doped substrates limit the penetration depth of the laser wave by increasing its absorption coefficient. Silicon still retains relatively high transparency at the wavelengths of 1550 nm, 1340 nm and 1064 nm, which are commonly used in various FA techniques.

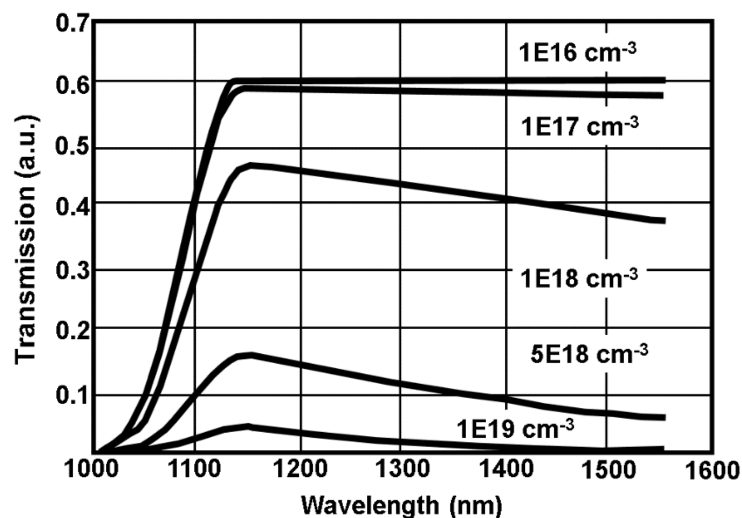

Figure 1.9. P-doped silicon optical transmission over wavelength for different concentrations of impurities (adapted from [64]).

When incident photons hit a surface of silicon there are a few possibilities how events can develop after. First, the photon can be simply reflected. Another outcome is photon absorption via interaction with a silicon crystal lattice if photon does not have sufficient energy for optical absorption. The last event happens if the photon is of sufficient energy to be absorbed via intraband absorption. Therefore, the photon needs energy higher than the bandgap energy of silicon (greater than 1.12 eV or wavelength lower than 1107 nm). In this case the photon energy is transmitted to an electron, which is promoted from the valance band into the conduction band. As, a result, electron-hole pairs are generated creating excess carriers. The penetration depth of light in silicon and the carrier generation rate strongly depends on the absorption coefficient [68, 69].

3.3.2 Single-photon absorption

An optical field interacts with another optical field or even with itself by modifying the properties of the medium [70]. These characteristics of the medium through which an electromagnetic wave propagates are described by the relation between the polarisation of a material system $P(t)$ and the strength of an electric-field $E(t)$. This relation is linear in conventional optics:

$$P(t) = \varepsilon_0 \chi^{(1)} E(t), \tag{1.6}$$

where $\chi^{(1)}$ is the linear susceptibility and ε_0 is the permittivity of the free space.

In linear optics, absorption causes the intensity (I) of the propagating laser beam to decay according to the Beer-Lambert law:

$$\frac{dI(z)}{dz} = -aI(z), \tag{1.7}$$

$$I(z) = I_0 exp(-az), \tag{1.8}$$

where a is the single photon absorption (SPA) coefficient. In this case the energy and momentum conservation laws must be satisfied. Therefore, a photon has to be of the same energy as the difference between the excited and the ground state of molecule or atom. The result of the process is an absorbed photon and an excited molecule. SPA occurs along the whole beam propagation direction, preventing the light from penetrating deeper into the material (Fig. 1.11).

Free carrier absorption occurs when a photon interacts with a free carrier, which consequently moves to upper energy level within the same band. The free carrier density depends on the doping of semiconductor and can be either increased or decreased by controlling the doping concentration. Another cause leading to the high free carrier absorption is the supply voltage, which also injects additional free carriers within the bulk of the silicon. The following equation shows the change in absorption coefficient introduced by the free carrier absorption [71]:

$$\Delta a = \frac{\lambda^2 q^3}{4\pi^2 c^3 \varepsilon_0} \cdot \frac{\Delta N}{nm^2 \mu}, \tag{1.9}$$

where ΔN is the difference of carrier concentration, n is refractive index, q is charge, ε_0 is the permittivity of vaccuum, m is the effective mass of carriers and μ is the carrier mobility. As it is seen from the Eq. (1.9) higher concentrations of free carriers lead to the higher absorption coefficient.

3.3.3 Multi-photon absorption

The theory of two-photon absorption (TPA) was first predicted in 1931 by the Nobel prize laureate Maria Goeppert-Mayer [72]. However, this phenomenon was not confirmed experimentally until the laser was invented in 1961. Kaiser and Garrett focused a red ($\lambda = 694.3$ nm) ruby laser beam into $CaF_2:Eu^{2+}$ crystals and observed a blue fluorescence light, which was generated during the process [73].

As the light intensity reaches high values, nonlinear absorption becomes evident. The TPA occurs when two photons are absorbed by an atom or molecule simultaneously (Fig. 1.10).

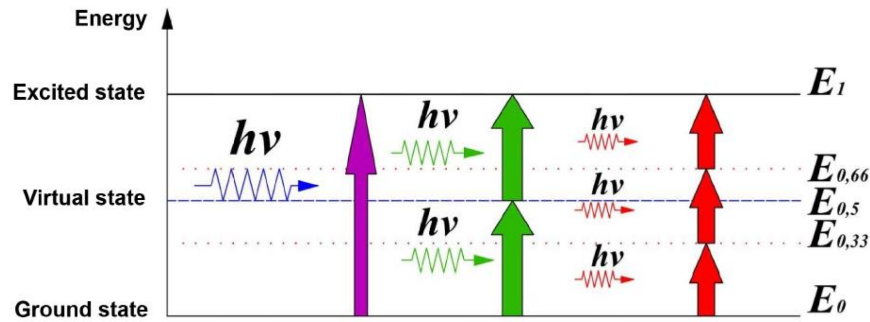

Figure 1.10. The energy level diagram for the one-, two- and three-photon absorption cases.

In linear optics the nonlinear part of the polarisation is neglected while in nonlinear optics it can no longer be ignored. Therefore, the optical response is generalised by expressing the polarisation as a power series:

$$P(t) = \varepsilon_0\left[\chi^{(1)}E(t) + \chi^{(2)}E^2(t) + \chi^{(3)}E^3(t) + \cdots\right] =$$

$$= P^{(1)}(t) + P^{(2)}(t) + P^{(3)}(t) + \cdots. \qquad (1.10)$$

The quantity $\chi^{(2)}$ is the second-order nonlinear optical susceptibility and $\chi^{(3)}$ is the third-order nonlinear optical susceptibility. Therefore,

$$P^{(2)}(t) = \varepsilon_0\chi^{(2)}E^2(t), \qquad (1.11)$$

$$P^{(3)}(t) = \varepsilon_0\chi^{(3)}E^3(t), \qquad (1.12)$$

are known as the second- and third-order nonlinear polarisations, respectively [74].

As it was mentioned in previous sections, second-order nonlinear interactions can be observed only in noncentrosymmetric media, which do not display inversion symmetry. Due to silicon being centrosymmetric the second order nonlinear interaction are not observed. Third-order nonlinear optical interactions can occur for both centrosymmetric and noncentrosymmetric materials [70].

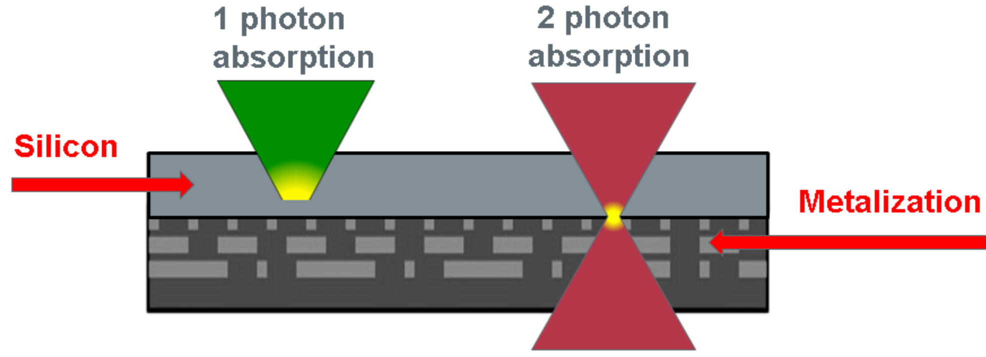

Figure 1.11. Beam propagation through silicon substrate for both SPA and TPA cases.

Due to the third order nonlinearity, TPA happens in a medium with any molecular configuration. The susceptibility that makes the TPA possible is the imaginary part of $\chi^{(3)}$. Consequently, the absorption cross section σ depends linearly on the laser intensity, while for the linear case it is constant:

$$\sigma = \sigma^{(2)} I, \tag{1.13}$$

where $\sigma^{(2)}$ describes strength of the TPA. The absorption due to the nonlinearity is therefore modified such that

$$a = a_0 + \Delta a = a_0 + a_2 I, \tag{1.14}$$

$$\frac{dI(z)}{dz} = -a_0 I(z) - a_2 I^2(z), \tag{1.15}$$

where a_2 is the nonlinear absorption coefficient, which is proportional to the imaginary part of the $\chi^{(3)}$ [75]. Eq. (1.15) shows that absorption is proportional to the square of the incident intensity. Therefore, TPA occurs only at the focal spot and happens through a virtual state (Fig. 1.11). When the photon is absorbed, an electron is excited to the virtual state. However, it can stay there only for a very short time (~10^{-15} s) as Heisenberg's uncertainty principle should be satisfied:

$$\Delta E \cdot \Delta t \approx \hbar. \tag{1.16}$$

TPA occurs only if another photon of the appropriate energy is absorbed before the electron falls down to the ground state. The probability of this phenomenon increases with the light intensity. Therefore, it is possible to tune the laser photon energy below the fundamental electronic band gap of the material, so that the linear absorption vanishes and only the TPA occurs. As a result, a highly localised imaging can be achieved [70, 76-78].

3.4 Optical techniques for failure analysis of integrated circuits

Circuit components in novel IC are as closely packed as never before, therefore such complicated design of the ICs can easily lead to a failing device. To overcome this problem ICs must be probed using suitable techniques to isolate a single failing transistor. It is essential not only to conduct the FA of the device, but also to test the electrical performance of these ICs to improve their design. The decrease of the feature sizes in the ICs requires an increasing performance of the corresponding analytical equipment. The study of defects in ICs strongly depends on their type and origin [1]. Of all localisation techniques available, this thesis is focused on optical probing techniques. Such optical techniques analyse the properties of a test device (the sample), which is under illumination of a laser beam. The incident laser beam can induce a temperature change, a density variation of the charge carriers or the electric field. The main advantage of such optical FA techniques, that analysis of the properties of ICs can be made while they are exercised (i.e. operational). As the response of the IC depends also on the electrical parameters, it allows both fault detection and the analysis of the device operation. In this section some failure analysis techniques are presented while primarily focusing on optical-based techniques.

3.4.1 Laser thermal stimulation techniques

Laser stimulation makes it possible to induce a thermal change into the sample device and therefore change its electrical properties. The main principle of this technique is to detect the resistance variation inside the IC. The thermal laser stimulation exploits the interaction between matter and the laser light when part of the absorbed energy of light is converted into heat. This typically occurs at highly absorbent materials (such as metals) for which the temperature rise is therefore significant. This approach generally employs wavelengths of around 1300 nm, making it possible both to avoid generating photocarriers inside the silicon and to have a local thermal heating of metal regions. The local increase in temperature in the IC leads to the change of resistance and to the generation of electric current [79].

Change of the resistance

The temperature increase may cause a resistance variation of the individual features, which result in an overall sample resistance variation. The rise of temperature affects the number of free carriers involved in the electric current (electrons in the case of metals), while increasing the volume of the material through the thermal expansion phenomenon. Therefore, an increment of temperature leads to a change of the sample's resistance. One can measure the resistance variation and synchronise it to the beam scanning. As a result, the sensitive areas to the laser stimulation can be mapped. Depending on the temperature change ΔT, the change of the resistance ΔR is given by the equation:

$$\Delta R = \frac{\rho_0 L}{S}(\alpha_{TCR} - 2\delta_T)\Delta T, \quad (1.17)$$

where ρ_0 is the resistivity of the material at the reference temperature, α_{TCR} thermal coefficient of resistivity, δ_T the linear thermal expansion coefficient, L is the length and S is the area. For the metal case, the contribution of the thermal expansion part is much lower than that of the resistivity. In addition, the metal tracks are typically coated with oxide, which limits their thermal expansion even more. Therefore, changes in resistance will be strongly related to the change of resistivity and for the most cases the phenomenon of expansion may be ignored. Also, the laser thermal stimulation can contribute only to the positive change of temperature and the change of resistivity depends only on the material. Therefore, a metal which has a positive α_{TCR} leads to an increase of the resistance. The thermal coefficient of resistivity can be negative for some cases, for example semiconductors, causing a negative change of resistance if the temperature increases [79]. If the induced resistance change depends on the expansion of the material considerably, then it is impossible to predict whether the resistance will increase or decrease.

The variation of the resistance of each element affects the electrical properties of the IC, since voltage and current are related to resistance. By scanning the laser beam across the sample and mapping the variations in resistance, it is possible to accurately locate components, which show abnormal thermal sensitivity. These elements may be related to the presence of a defect.

OBIRCh and TIVA techniques

The OBIRCh and TIVA techniques are used to detect the change of the resistance induced by the laser beam. The OBIRCh (Optical Beam Induced Resistance Change) technique detects the change in the current, which is induced as the metal features are heated by the laser. During OBIRCh a constant voltage is applied on the device [80, 81]. Void defects (gaps in metal lines) exhibit a higher temperature rise than the rest of the device increasing the local resistance and thus lowering the current. This technique is typically exploited to reveal the open metal lines. However, the measured currents are low and therefore, a series of trans-impedance amplifiers is required, as the operating point output is affected by temperature and noise of the power supply. This problem can be solved by applying the thermally induced voltage alteration (TIVA) technique. TIVA, which differs from OBIRCh in a way how the sample under test is driven and the how the signal is obtained (Fig. 1.12). TIVA approach is to apply a constant current on the IC and detect voltage modulations introduced by the laser beam, thus highlighting the void areas of the IC [82, 83]. Since ICs typically operate in high impedance mode, a voltage detection can provide a desirable advantage as its change is of a larger extent than that for a current. However, the use of a constant current supply may be incompatible with alternating current devices or

complex ICs such as mixed signal devices. An additional disadvantage of this technique is, that sudden peak voltage change during the thermal stimulation may also lead to the irreversible breakdown of the sample.

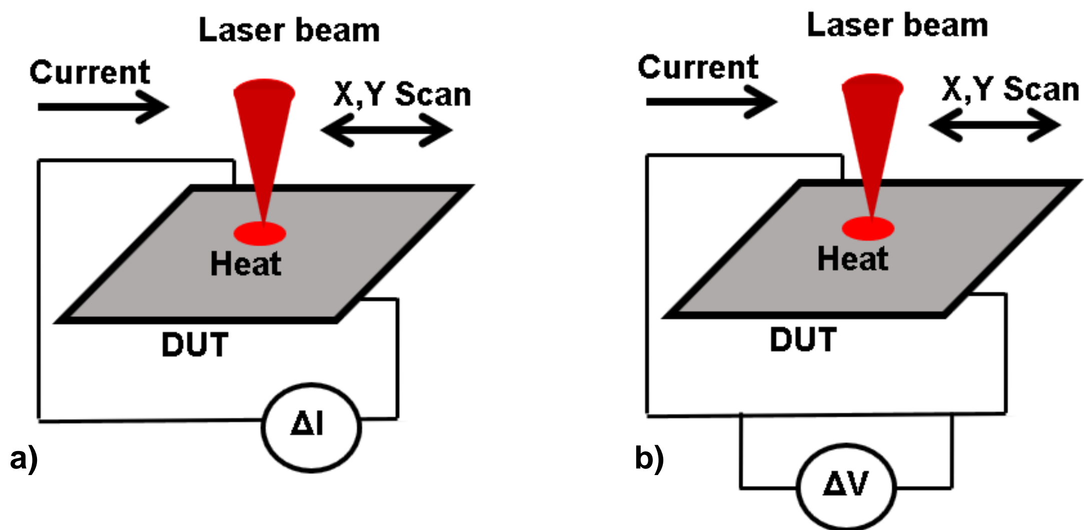

Figure 1.12. The operation principles of (a) OBIRCh and (b) TIVA techniques.

XIVA technique

The externally induced voltage alteration (XIVA) technique offers a way to overcome limitations of OBIRCh and TIVA techniques [84, 85]. This modality implements an inductor within a voltage variation detection scheme to achieve constant voltage bias. This inductor prevents the instantaneous current change as the laser stimulates the DUT. The mapping accuracy can be further enhanced via laser scanning and signal acquisition synchronisation [84]. Also detection sensitivity and noise reduction can be enhanced by implementing a signal amplification with a lock-in amplifier [86].

Seebeck effect imaging technique

The Seebeck Effect Imaging (SEI) technique measures the change of the electrical potential induced by the temperature gradients [82, 87]. This effect is known as the thermoelectric power or the Seebeck effect. The SEI technique is used to localise an open circuit in the test device. If the conductor is electrically intact the potential gradient caused by the heating is compensated by the transistor. However, if the laser beam is incident on a conductor which is isolated from the transistor the electrical potential is changed. In this case, the bias condition of the transistor, which is connected to a stimulated conductor is changed, affecting the transistor's saturation condition and the thermal dissipation. The device must be supplied with a constant current and voltage [87].

3.4.2 Laser photoelectric stimulation techniques

Illuminating the device with photons of sufficient energy for inter-band absorption to occur, generates electron-hole pairs (Fig. 1.13a). These charge carriers then contribute to the photocurrent and therefore this phenomenon is called the photoelectric effect. The silicon bandgap is 1.12 eV, which corresponds to the light of 1107 nm wavelength. Therefore, typically lasers generating 1064 nm wavelength light are employed.

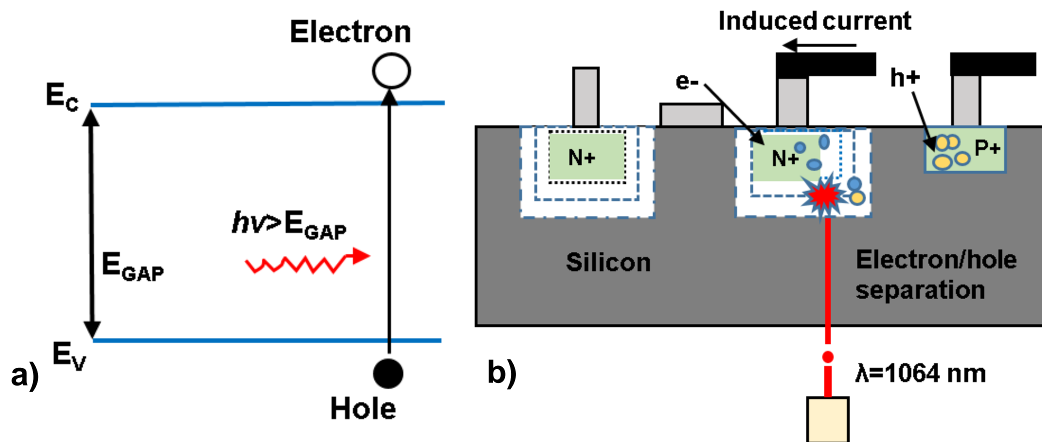

Figure 1.13. (a) Photoelectric effect in semiconductor and (b) current generation in nMOS transistor.

Already excited carriers can still absorb photons leading to free carrier absorption and heating of the device. However, the electron-hole pairs are generated in the entire silicon substrate, while thermal heating via the free carrier absorption is weak and can be neglected since high carrier density regions are confined to a small volume. Thus, this technique is known as Photoelectric Laser Stimulation (PLS), which utilises the laser beam irradiation to locally induce a photocurrent into the active regions of the IC. These excess carriers generated by the laser beam recombine after a characteristic lifetime. However, if carriers appear within or close to the depletion region, they are dissociated by the junction potential (Fig. 1.13b) [88, 89].

LIVA technique

The light induced voltage alteration (LIVA) technique employs a similar detection approach to the TIVA configuration and is based on constant current bias while detecting a voltage variation as a function of carrier stimulation. This technique is effective in imaging defects resulting from junctions connected to open conductors, floating nodes, junction damage and gate oxide ruptures. LIVA has advantage over conventional thermal variation techniques as offers a possibility to investigate IC circuitry by mapping logic states of transistors [90].

OBIC and TOBIC techniques

Optical beam induced imaging (OBIC) was first demonstrated in the 1978 by Wilson and Gannaway [91]. This technique is based on the carrier generation via the photon absorption phenomenon. The light, which has a photon energy higher than the material's bandgap energy, is absorbed, thus generating carriers. In crystalline silicon, even though these carriers are generated they diffuse over time and recombine through non-radiative processes. As a result, no electric current is induced. However, it is different if the carriers are generated in the area of the junction. Here they experience the internal electric field, which leads them to the external circuit, thus generating an optically induced current. This photocurrent can be mapped as a function of the scanned beam position and an image of the circuit can be obtained [92].

OBIC imaging is suitable for the FA of semiconductor devices as it is a non-destructive technique [1, 93]. However, it does not necessarily offer fundamental advantages over the previous imaging techniques. Additionally, OBIC has one major limitation. It is not able to perform a depth-resolved analysis as the SPA happens along the entire propagation path of the beam. Therefore, a nonlinear technique, which is based on the TPA, was suggested as a promising approach to overcome the limitations.

Two-photon OBIC (TOBIC) imaging was first demonstrated by Xu using a 1.3 µm femtosecond optical parametric oscillator [94-96]. It was showed in the previous sections, that in order to achieve TPA in a silicon device, the laser wavelength must be tuned to provide energy lower than the bandgap of the silicon substrate. This enables a laser beam to travel through the material without being absorbed. Therefore, carriers are no longer generated along the beam path. However, the laser beam has to be of a sufficient wavelength that two photons combined would have a higher energy than the energy of the bandgap. As TPA is proportional to the intensity-squared, the high intensities are achieved only in the focal spot, where the TPA happens and generates carriers in a highly localised manner. This localisation makes it possible to acquire a 3D map of absorption sensitivity [97]. Moreover, due to its nonlinear character TOBIC also produces a higher spatial resolution, since the TPA depends on the square of the incident optical intensity. This offers a beneficial reduction of the focal spot radius by a factor of $\sqrt{2}$ [98].

Laser voltage probing

Laser Voltage Probing (LVP) is a backside optical measurement technique of device activity at a specific location on the ICs (Fig. 1.14). LVP measurements are time-domain measurements of the modulation in the operating device. When the transistor is driven with a pulse, it is switching between these states [99]. If the input is fast enough, the time in which the transistor operates in the saturation regime is very short. In the linear operating and the saturation regimes, there are

extra layers called inversion layer and depletion region. These layers are formed because the free carrier densities are changed as a result of the applied voltage [99]. This change in free carrier densities causes a change in the refractive index and in the absorption coefficient. When a laser is focused on one specific position in these regions while the transistor is switching, there is a change in the reflected light because of the change in refractive index and in absorption coefficient. Therefore, when the transistor is driven by a rectangular pulse, a modulation can be observed in the reflected light correlated with the voltage change in the rectangular pulse [99].

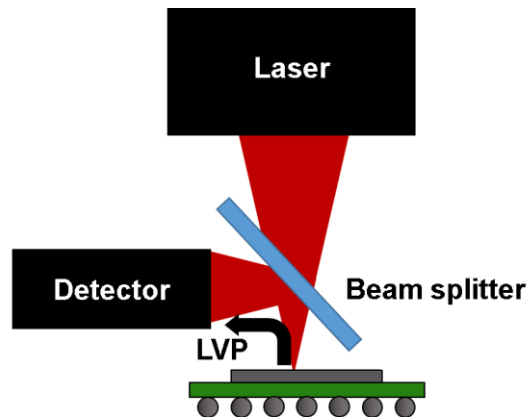

Figure 1.14. LVP technique principle.

3.4.3 Tester based laser stimulation techniques

Static laser stimulation techniques are approaching their limits as ICs get more and more complicated. Therefore, it is highly important to develop new techniques, which could be able to detect failing sites arising from electrical stimulation of defect.

These tester based techniques employ the so called "Shmoo" graphs (Fig. 1.15). A Shmoo graph is a functional representation of the circuit according to two parameters (voltage, frequency, temperature, etc.) for a given test pattern.

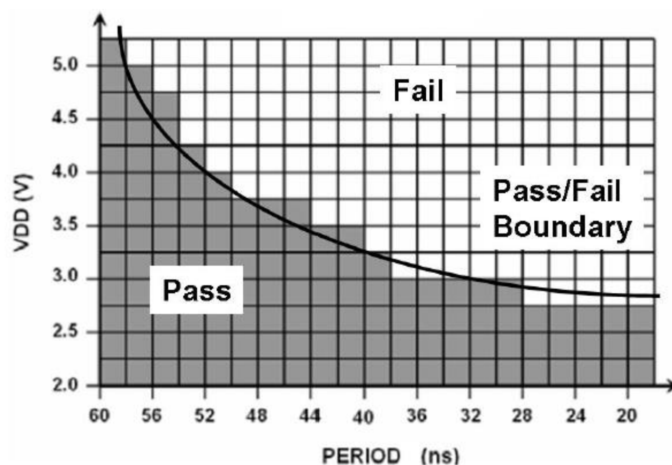

Figure 1.15. Shmoo plot with grey colour representing normal device functionality (adapted from [100]).

The aim of the tester exercising a Shmoo pattern is to create a boundary condition separating the area for which the IC is functional (pass) from the zone for which it fails. This technique is widely used in the microelectronics industries where it employed to study manufacturing processes [100].

Test vectors are applied to the device under test (DUT) and a test program is selected under which the DUT would be close to soft failing condition. Then this failure mode is set to run in a loop while the DUT is irradiated the laser. The tester detects pass-fail or fail-pass transitions and as a results defects leading to these transitions are detected. At each pixel the laser dwells for a specified number of test loops and fail/pass pattern us averaged. Synchronising the laser with the tester and mapping which pixels it was irradiating leads to the image of pass-fail sites.

Laser Assisted Device Alteration (LADA) [101] and Laser Delay Variation Mapping (DVM) [102] techniques extended the development of dynamic laser stimulation modalities beyond the thermal stimulation and the pass/fail state mapping. LADA technique exploits laser stimulation to generate carriers inside the DUT leading to detectable time shifts of transistor switching events. This makes it possible to isolate transistors on the critical signal path. LADA will be introduced in a greater detail in Chapter 4. Also, as my own work described later in this thesis shows, LADA can be extended by using TPA, improving the localisation resolution significantly. DVM directly measures the laser induced time delay within the pass or fail state using a time measurement unit with a resolution in the range of picoseconds.

3.4.4 Photon emission microscopy

Photon emission microscopy is yet another optical FA technique, which is designed to obtain a weak optical signal from a failing IC device. Photons are emitted during the transistor switching events, which are recorded using a CCD camera. The exact location emitting photons can be tracked by overlaying the emission image over the confocal image of the device.

Photon emission in semiconductors can occur due to two different reasons. The first event causing photoemission is a radiative relaxation phenomenon, when carriers having high kinetic energy relax and emit light. Reverse biased junctions of the complementary metal-oxide semiconductor (CMOS) devices are the source of such events, however reverse biased currents are typically very low. Therefore, amplification of currents is necessary to obtain radiation, which is intense enough to be detected. A leakage current can work as a trigger for this amplification. Another principle behind photon emission is the radiative band-band recombination of electrons and holes, which initiates electroluminescence. Recombination involves carriers from conductance and valence bands, meaning that this is an inter-band phenomenon. However, it rarely happens in silicon as it is an indirect semiconductor [103].

3.5 Thesis outline

The primary objective of this thesis is to develop backside optical failure analysis tools to increase the imaging resolutions while using high numerical aperture conditions. To present several approaches for resolution enhancement this thesis was structured in six chapters, with this introduction as the first chapter.

Chapter 2 introduces theory, design and construction of the Er:fibre laser used for two-photon optical beam induced current microscopy.

In Chapter 3 two-photon optical beam induced current microscopy is investigated. After a review of the development of vector diffraction theory, the integral representation of the focal field under high numerical aperture conditions is derived. In addition, implementation of the liquid crystal radial polarisation converter is described and TOBIC imaging results using differently polarised beams are presented.

Chapter 4 explores the two-photon absorption laser assisted device alteration (2pLADA) technique. Detailed experimental implementation of this failure analysis technique under different polarisation conditions is provided and obtained experimental results are discussed.

Chapter 5 studies aberrations under high numerical aperture imaging conditions. Here the relation between pulse broadening and imaging resolution is investigated both theoretically and experimentally. In addition, pulse measurements at the focal plane of a hemispherical solid immersion lens are compared with calculated spatiotemporal dynamics.

Finally, Chapter 6 concludes this thesis with a discussion of the presented results and offers insights into potential improvements.

References

1. B.P. Richards and P.K. Footner, “The role of microscopy in semiconductor failure analysis”, Oxford: Oxford University Press (1992).
2. S. Global, “Sony semiconductor quality and reliability handbook”, Sony Corporation (2011).
3. S. M. Kudva, R. Clark, D. Vallett, D. Ross, T. Hasegawa, G. Gilfeather, M. Thayer, S. Pabbisetty, R. Shreeve, B. Ash, J. Serpiello, K. Huffman, L. Wagner, S. Kazmi, “The SEMATECH failure analysis roadmap”, Proceedings of the International Symposium for Testing and Failure Analysis, 1-5 (1995).
4. D. P. Vallett DP, "Why waste time on roadmaps when we don’t have cars”, Transactions on Device and Materials Reliability **7**, 5-10 (2007).
5. G.E. Moore, “Cramming more components onto integrated circuits”, Electronics Magazine, 114-117 (1965).
6. “International Technology Roadmap for Semiconductors” (2012).
7. E. Cole, “Non-destructive IC defect localization using optical beam-based imaging”, Proceedings of the Custom Integrated Circuits Conference (2008)
8. D. P. Vallett, “IC failure analysis: the importance of test and diagnostics”, IEEE Design and Test of Computers **14**, 76-82 (1997).
9. T. W. Joseph, R.E. Anderson, G. Gilfeather, C. LeClaire, D. Yim, “Semiconductor product analysis challenges based on the 1999 ITRS”, Proceedings of the International Conference on Characterization and Metrology for ULSI Technology, 26-29 (2000).
10. C. Boit, “Can failure analysis keep pace with IC technology development?”, Proceedings of the International Symposium for Physical & Failure Analysis of Integrated Circuits, 9-14 (1999).
11. D. P. Vallet, “Failure analysis requirements for nanoelectronics”, IEEE Transactions on Nanotechnol. **1**, 117-121 (2002).
12. D. L Smith and A. S Alimonda, “A new flip-chip technology for high-density packaging”, Proceedings of the Electronic Components and Technology Conference, 1069-1073 (1996).
13. J. C. H. Phang, D. S. H. Chan, M. Palaniappan, J. M. Chin, B. Davis, M. Bruce, J. Wilcox, G. Gilfeather, C. M. Chua, L. S. Koh, H. Y. Ng, and S. H. Tan, “A review of laser induced techniques for microelectronic failure analysis”, Proceedings of the International Symposium for Physical & Failure Analysis of Integrated Circuits (2004).
14. J. M. Soden and R. E. Anderson, “IC failure analysis - techniques and tools for quality and reliability improvement”, Proceedings of the IEEE **81**, 703-715 (1993).
15. S. E. Aw, H. S. Tan, C. K. Ong, “Optical adsorption measurements of band-gap shrinkage in moderately and heavily doped silicon”, Journal of Physics: Condensed Matter **3**, 8213-8223 (1991).

16. F. H. Koklü, S. B. Ippolito, B. B. Goldberg, and M. S. Ünlü, “Subsurface microscopy of integrated circuits with angular spectrum and polarization control”, Optics Letters **34**, 1261-1263 (2009).
17. S. M. Mans and G. S. Kino, “Solid immersion microscope”, Applied Physics Letters **57**, 2615-2616 (1990).
18. Q. Wu, L. P. Ghislain, and V. B. Elings, “Imaging with solid immersion lenses, spatial resolution, and applications”, Proceedings of the IEEE **88**,1491-1498 (2000).
19. A. N. Vamivakas, R. D. Younger, B. B. Goldberg, A. K. Swan, M. S. Ünlü, E. R. Behringer, and S. B. Ippolito, “A case study for optics: The solid immersion microscope”, American Journal of Physics **76**, 758-768 (2008).
20. S. B. Ippolito, “High spatial resolution subsurface microscopy”, PhD thesis, Boston University (2004).
21. F. H. Koklü, “High numerical aperture subsurface imaging”, PhD thesis, Boston University (2010).
22. K. A. Serrels, E. Ramsay, P. A. Dalgarno, B. D. Gerardot, J. A. O’Connor, R. H. Hadfield, R. J. Warburton and D. T. Reid, “Solid immersion lens applications for nanophotonic devices”, Journal of Nanophotonics **2**, 021854 (2008).
23. Y. Lu, E. Ramsay, C. Stockbridge, A. Yurt, F. Koklü, T. Bifano, M. Ünlü, and B. Goldberg, “Spherical aberration correction in aplanatic solid immersion lens imaging using a MEMS deformable mirror”, Microelectronics Reliability **52**, 2120-2122 (2012).
24. K. A Serrels, K. Erington, D. Bodoh, C. Farrell, N. Leslie, T. R. Lundquist, D. T. Reid, “Two-photon laser-assisted device alteration in silicon integrated-circuits”, Optics Express **21**, 29083-29089 (2013).
25. K. A. Serrels, D. T. Reid, E. Ramsay, “70 nm resolution in subsurface optical imaging of silicon integrated-circuits using pupil-function engineering”, Applied Physics Letters **94,** 073113 (2009).
26. K. A. Serrels, E. Ramsay, R. J. Warburton and D. T. Reid, “Nanoscale optical microscopy in the vectorial focusing regime”, Nature Photonics **2**, 311–314 (2008).
27. A. Yurt, M. D. W. Grogan, S. Ramachandran, B. B. Goldberg, and M. S. Ünlü, “Effect of vector asymmetry of radially polarized beams in solid immersion microscopy”, Optics Express **22**, 7320-7329 (2014).
28. J. Richardson, “Optical microscopy for the materials sciences”, New York: M. Dekker (1971).
29. J. Pawley, “Handbook of biological confocal microscopy”, New York: Springer (2006).
30. C. J. R. Sheppard, “Scanning optical microscopy of semiconductor-materials and devices”, Scanning Microscopy **3**, 15-24 (1989).
31. J. Brown, P. K. Footner, and B. P. Richards, “Failure analysis of plastic encapsulated components - the advantages of IR microscopy”, Journal of Microscopy-Oxford **148**, 179-194 (1987).

32. M. Minsky, “Microscopy apparatus”, US Patent Number 3013467, United States (1961).
33. M. Minsky, “Memoir on inventing the confocal scanning microscope”, Scanning **10**, 128-138 (1988).
34. G. Kino and T. Corle, “Confocal scanning optical microscopy and related imaging systems”, Cambridge: Academic Press (1997).
35. F. Aguilar, E. R. Mendez, “On the limitations of the confocal scanning optical microscope as a profilometer”, Journal of Modern Optics **42**, 1785–1794 (1995).
36. C. J. R. Sheppard and A. Choudhury, “Image formation in scanning microscope”, Optica Acta **24**, 1051-1073 (1977).
37. C. J. R. Sheppard and T. Wilson, “Image formation in scanning microscopes with partially coherent source and detector”, Optica Acta **25**, 315-325 (1978).
38. M. Born and E. Wolf, “Principles of optics, 7th ed.”, Cambridge: Cambridge University Press (2002).
39. C. M. Sparrow, “On spectroscopic resolving power”, The Astrophysical Journal . **44**, 76aAS86 (1916).
40. T. Wilson, “Handbook of biological confocal microscopy, 2nd ed.”, New York: Plenum Press (1995).
41. C. J. R. Sheppar, D. M. Shotto, “Confocal laser scanning microscopy ”, New York: Springer (1997).
42. M. G. L. Gustafsson, S. Lin, P. M. Carlton, C. J. R. Wang, I. N. Golubovskaya, W. Z. Cande, D. A. Agard and J. W. Sedat, “Three-dimensional resolution doubling in wide-field fluorescence microscopy by structured illumination”, Biophysical Journal **94**, 4957-4970 (2008).
43. J. M. Zavislan, “Imaging system using polarization effects to enhance image quality”, United States Patent 6134010 (2000).
44. O. Haeberlé and B. Simon, “Improving the lateral resolution in confocal fluorescence microscopy using laterally interfering excitation beams”, Optics Communications **259,** 400-408 (2005).
45. G. J. Brakenho, P. Blom, and P. Barends, “Confocal scanning light microscopy with high aperture immersion lenses”, Journal of Microscopy- Oxford **117**, 219-232 (1979).
46. P. Torok, P. Varga, Z. Laczik, and G. R. Booker, “Electromagnetic diffraction of light focused through a planar interface between materials of mismatched refractive-indexes - an integral-representation”, Journal of the Optical Society of America A **12**, 325-332 (1995).
47. H. Ling and S. Lee, “Focusing of electromagnetic waves through a dielectric interface”, Journal of the Optical Society of America A **1**, 965–973 (1984).
48. R. Chen, K. Agarwal, C. J. R. Sheppard, J. C. H. Phang, and X. Chen, “Resolution of aplanatic solid immersion lens based microscopy”, Journal of the Optical Society of America A **29**, 1059-1070 (2012).

49. T. Chen, T. Milster, D. Nam, and S. H. Yang, “Experimental investigation of solid immersion lens lithography”, Proceedings of the Society of Photo-Optical Instrumentation Engineers **5754**, 254-261 (2005).
50. D. A. Fletcher, K. B. Crozier, K. W. Guarini, S. C. Minne, G. S. Kino, C. F. Quate, and K. E. Goodson, “Microfabricated silicon solid immersion lens”, Journal of Microelectromechanical Systems **10**, 450-459 (2001).
51. L. N. Magner, “A history of the life sciences, revised and expanded”, New York: Marcel Dekker, Inc. (2002).
52. S. B. Ippolito, B. B. Goldberg and M. S. Ünlü, “Theoretical analysis of numerical aperture increasing lens microscopy”, Journal of Applied Physics **97**, 053105 (2005).
53. D. E. Aspnes and A. A. Studna, “Dielectric functions and optical parameter of Si, Ge, GaP, GaSb, InP, InAs and InSb from 1.5 to 6 eV”, Physical Review B **27**, 985 (1983).
54. H. R. Philipp and E. A. Taft, “Optical constants of silicon in the region 1 to 10 eV”, Physical Review **120**, 37-38 (1960).
55. T. Kamins, “Polycrystalline silicon for integrated circuits and displays, 2nd ed.”, New York: Kluwer Academic Publishers (1998).
56. T. F. Boggess, K. M. Bohnert, K. Mansour, S. C. Moss, I. W. Boyd, and A. L. Smirl, “Simultaneous measurement of the 2-Photon coefficient and free-carrier cross-section above the bandgap of crystalline silicon”, IEEE Journal of Quantum Electronics **22**, 360-368 (1986).
57. B. E. A. Saleh and M. C. Teich, “Fundamentals of photonics”, New York: John Wiley & Sons (1991).
58. C. V. Raman, K. S. Krishnan, “A new type of secondary radiation”, Nature **121**, 501 (1928).
59. C. Xia, H. N. Spector, “Nonlinear Franz–Keldysh effect: two-photon absorption in a semiconducting quantum well”, Journal of the Optical Society of America B **27**, 1571-1575 (2010).
60. J. Zhang, Q. Lin, G. Piredda, R. W. Boyd, G. P. Agrawal, P. M. Fauchet, “Anisotropic nonlinear response of silicon in the near-infrared region”, Applied Physics Letters **91,** 071113 (2007).
61. P. Yanga, W. S. Laua, S. W. Laib, V.L. Lob, S.Y. Siahb, L. Chanb, “Effects of switching from <110> to <100> channel orientation and tensile stress on n-channel and p-channel metal–oxide-semiconductor transistors”, Solid-State Electronics **54**, 461-474 (2010).
62. M. Saritas and H. D. McKell, “Absorption coefficient of Si in the wavelength region between 0.8-1.16 μm”, Journal of Applied Physics **61**, 4923 (1987).
63. M. Saritas and H. D. McKell, “Comparison of minority diffusion length measurements in silicon by the photoconductive decay and surface photovoltage methods”, Journal of Applied Physics **63**, 4561-4567 (1988).

64. J. S. Melinger, S. Buchner, D. Mc Morrow, W. J. Stapor, T. R. Weatherford and A. B. Campbell, “Critical evaluation of the pulsed laser method for single event effects testing and fundamental studies”, IEEE Transactions on Nuclear Science **41**, 2574-2584 (1994).
65. G. N. Koskovich, R. B. Darling and M. Soma, “Effect of first order phonon assisted scattering on near infrared free carrier optical absorption in silicon”, Physical Review B **38**, 1281-1284 (1988).
66. G. N. Koskovich, M. Soma and R. B. Darling, “Near infrared free carrier optical absorption in silicon: Effect of first order phono assisted scattering in a nonparabolic conduction band”, Physical Review B **41**, 2944-2947 (1990).
67. J. M. Essick and R. T. Mather, “Characterization of a bulk semiconductor's via near absorption edge optical transmission experiment”, American journal of Physics **61**, 646-649 (1993).
68. W. Spitzer and H. Y. Fan, “Infrared absorption in n-type silicon”, Physical Review **108**, 268-271 (1957).
69. H. Hara and Y. Nishi, “Free carrier absorption in p-type silicon”, Journal of the Physical Society of Japan **21**, 1222 (1966).
70. R. W. Boyd, “Nonlinear optics, 3rd. ed.”, New York: Academic Press (2006).
71. D. McMorrow, W. T. Lotshaw, J. S. Melinger, S. Buchner, and R.L. Pease, “Subbandgap laser induced single event effects: Carrier generation via two-photon absorption”, IEEE Transactions on Nuclear Science **49**, 3002-3008 (2002).
72. M. Goppert-Mayer, “Über Elementarakte mit zwei Quantensprüngen ”, Annalen der Physik **401**, 273-294 (1931).
73. W. Kaiser and C. G. B. Garrett, “Two-photon excitation in CaF2:Eu2+”, Physics Review Letters **7**, 229-231 (1961).
74. R. L. Sutherland, “Handbook of nonlinear optics, 2nd ed.”, New York: Marcel Dekker, Inc. (2003).
75. F. Gherbremichael, M. G Kuzyk and H. S. Lackritz, “Nonlinear optics and polymer physics”, Progress in Polymer Science **22**, 1147–1201 (1997).
76. H. Misawa and S. Juodkazis,”3D laser microfabrication. principles and applications”, Weinheim: Wiley-VCH (2006).
77. W. Denk and K. Svoboda, “Photon upmanship: why multiphoton imaging is more than a gimmick”, Neuron **18**, 351–357 (1997).
78. D. Lewis, V. Pouget, F. Beaudoin, P. Perdu, H. Lapuyade, P. Fouillat, and A. Touboul, “Backside laser testing of ICs for SET sensitivity evaluation”, IEEE Transactions on Nuclear Science **48**, 2193-2201 (2001).
79. F. Beaudoin, “Localisation de défaut par la face arrière des circuits intégrés”, PhD thesis, University of Bordeaux (2003).

80. K. Nikawa and S. Tozaki, “Novel OBIC observation method for detecting defects in Al stripes under current stressing”, Proceedings of the International Symposium for Testing and Failure Analysis, 310-313 (1993).
81. K. Nikawa and S. Inoue, “New capabilities of OBIRCH method for fault localization and defect detection”, Proceedings of the Asian Test Symposium, 214-219 (1997).
82. E. I. Cole, P. Tangyunyong and D. L. Barton, “Backside localization of open and shorted IC interconnections”, Proceedings of the International Reliability Physics Symposium, 129-136 (1998).
83. D. L. Barton, K. Bernhard-Höfer and E. I. Cole, “Flip-chip and “backside” techniques”, Microelectronics Reliability **39**, 721-730 (1999).
84. M. Palaniappan, J. M. Chin, B. Davis, M. Bruce, J. Wilcox, C. M. Chua, L. S. Koh, H. Y. Ng, S. H. Tan, J. C. H. Phang, G. Gilfeather, “New signal detection methods for thermal beam induced phenomenon”, Proceedings of the International Symposium of Testing & Failure Analysis, 171- 177 (2001).
85. R. A. Falk, “Advanced LIVA-TIVA techniques”, Proceedings of the International Symposium of Testing & Failure Analysis , 59-65 (2001).
86. M. de la Bardonnie, R. Ross, K. Ly, F. Lorut, M. Lamy, C. Wyon, L. F. T. Kwakman, “The effectiveness of OBIRCH based fault isolation for sub-90nm CMOS technologies”, Proceedings of the International Symposium of Testing & Failure Analysis , 49-58 (2005).
87. S. K. Brahma, C. Boit, A. Glowacki, “Seebeck effect detection on biased device without OIBIRCH distortion using FET readout”, Microelectronics Reliability **45**, 1487-1492 (2005).
88. W. van Roosbroeck, “Injected current carrier transport in a semi-infinite semiconductor and the determination of lifetimes and surface recombination velocities”, Journal of Applied Physics **26**, 380-391 (1953).
89. T. Wilson and P. D. Pester, “An analysis of the photoinduced current from a finely focused light beam in planar p-n junctions and Schottky barrier diodes”, IEEE Transactions on Electron Devices **34**, (1987).
90. T. Wilson and E. M. McCabe, “Theory of optical beam induced current images of defects in semiconductors”, Journal of Applied Physics **61**, 191-195 (1987).
91. T. Wilson and J. N. Gannaway, “Examination of grain boundaries in polycrystalline solar cells using a scanning optical microscope”, Electronics Letters **14**, 507–508 (1978).
92. V. J. Cemine, B. Buenaobra, C. M. Blanca, and C. Saloma, “High-contrast microscopy of semiconductor and metal sites in integrated circuits by detection of optical feedback”, Optics Letters **29**, 2479–2481 (2004).
93. C. Werner, D. Reuter, and A. D. Wieck, “Optical beam-induced current in planar two-dimensional n-p-n devices”, Physica E-Low-Dimensional Systems & Nanostructures **32**, 508–511 (2006).

94. C. Xu and W. Denk, "Two-photon optical beam induced current imaging through the backside of integrated circuits", Applied Physics Letters **71**, 2578–2580 (1997).
95. C. Xu and W. Denk, "Comparison of one- and two-photon optical beam-induced current imaging", Journal of Applied Physics **86**, 2226–2231 (1999).
96. C. Xu, L. M. F. Chirovsky, W. S. Hobson, J. Lopata, W. H. Knox, J. E. Cunningham, W. Y. Jan and L. A. D'Asaro, "Two-photon photocurrent imaging of vertical cavity surface emitting lasers", Applied Physics Letters **76**, 1510–1512 (2000).
97. E. Ramsay, K. A. Serrels, M. J. Thomson, A. J. Waddie, M. R. Taghizadeh, R. J. Warburton and D. T. Reid, "Three-dimensional nanoscale subsurface optical imaging of silicon circuits", Applied Physics Letters **90**, 131101 (2007).
98. E. Ramsay, N. Pleynet, D. Xiao, R. J. Warburton and D. T. Reid, "Two-photon optical-beam-induced current solid-immersion imaging of a silicon flip chip with a resolution of 325 nm", Optics Letters **30**, 26–28, (2005).
99. A. Douin, V. Pouget, D. Lewis, P. Fouillat, P. Perdu, "Picosecond timing analysis in integrated circuits with pulsed laser stimulation", Proceedings of the Reliability physics symposium, (2007).
100. K. Baker and J. Van Beers, "Shmoo plotting: the black art of IC testing", Design & Test of Computers **14**, 90-97 (1997).
101. J. A. Rowlette, T. M. Eiles, "Critical timing analysis in microprocessors using near-IR laser assisted device alteration (LADA)", Proceedings of the International Test Conference, 264-273 (2003).
102. K. Sanchez, R. Desplats, F. Beaudoin, P. Perdu, S. Dudit, G. Woods, D. Lewis, "Dynamic laser delay variation mapping (DVM) implementations and applications", Proceedings of the International Symposium of Testing & Failure Analysis, 106-114 (2005).
103. D. K. Schroder, "Semiconductor material and device characterization", John Wiley and Sons, (2006).

Chapter 4. Femtosecond Er:fibre laser for sub-surface imaging at 1550 nm

The experimental work described in this these was based around mode-locked Er:fibre laser, which I refined and then amplified in a separate Er-doped fibre amplifier. Here I introduce the background to the laser design and operating principles.

Optical fibres exhibit many properties that are extremely useful to produce both pulsed [1] and continuous wave (CW) lasers [2]. The optical fibre is a waveguide, where spatial modes can be guided over long distances without high loss [3]. Furthermore, the fibre can serve as a host to rare-earth dopants which can be used as the laser gain [4]. Finally, the fibre has unique properties of nonlinear optical effects that lead to a self-mode-locking operation for the ultrashort pulse generation [5]. These properties make optical fibres the desirable medium for producing high power, high bandwidth ultrashort pulses. In addition, fibre lasers benefit from a compact and robust design, alignment-free operation, efficient heat dissipation and can be low-cost [6]. Therefore, fibre lasers have a high demand over the traditional solid state and gas lasers. Pulsed fibre lasers have a wide variety of possible applications, which depend on the required wavelength and pulse durations, and range from the fundamental science [7, 8] to the medical [9, 10], telecommunications [11, 12] and industrial [13] fields.

The active gain medium of the fibre laser is a fibre waveguide doped with rare-earth ions such as neodymium (Nd^{3+}), praseodymium (Pr^{3+}), ytterbium (Yb^{3+}), erbium (Er^{3+}), thulium (Tm^{3+}) and holmium (Ho^{3+}). The generated wavelength depends on the properties of both the rare-earth ions and the host materials. Fibre lasers cover wavelengths from the ultra-violet to mid-infrared [14-18].

The Er:fibre laser is of particular interest as it provides an emission wavelength of around 1.5 μm. Since this wavelength is located in the telecommunication window, Er-doped fibre lasers have been extensively studied. Also, ultrafast pulses from a mode-locked fibre laser operating at 1.5 μm are interesting for imaging inside silicon ICs. This wavelength propagates inside the silicon with low attenuation and provides nonlinear absorption at the device layer of the chip to generate a photocurrent of a particular area of interest.

Moreover, the large nonlinearity in Er:fibres can be used to create the large wavelength bandwidths required to generate ultrashort optical pulse durations leading to higher peak powers and better confinement of the focal spot, which is crucial to obtain the highest resolution for TOBIC microscopy.

4.1 The Er^{3+} ion

It is essential to know the optical properties of the erbium-doped fibres before introducing the laser design. Erbium-doped glasses display a laser transition at around 1560 nm between the $^4I_{15/2}$ level and the $^4I_{13/2}$ level of the *4f* electron shell [4]. Lower $^4I_{15/2}$ level is a ground state. Therefore, the 1560 nm transition is a part of three-level system between the $^4I_{11/2}$ and the $^4I_{13/2}$ states, while optically pumping with 980 nm. The pump is absorbed in the short-lived $^4I_{11/2}$ state, where excitation rapidly decays via non-radiative phenomenon to the metastable $^4I_{13/2}$ state. Also it can be directly pumped to the $^4I_{13/2}$ state with the 1480 nm optical pump creating two-level system. However, in practice it is more complicated due to the split of levels into sub-manifolds. Sub-levels appear as a result of Stark effect created by the electric field due to the charge distribution in the glass host [19] (Fig. 2.1).

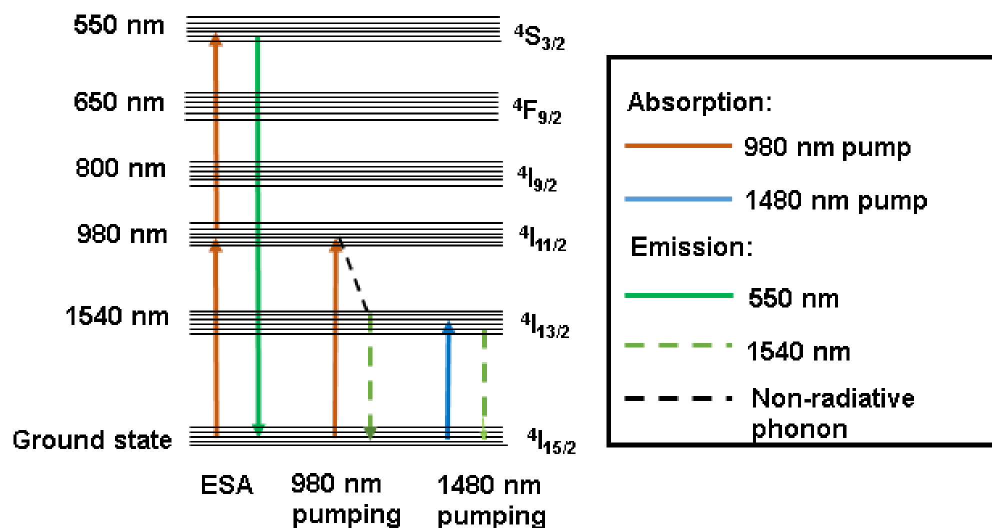

Figure 2.1. On the left, the details of the energy levels of the laser transition. Arrows indicate absorption and emission lines (adapted from [4]).

As the differences between some of the sub-levels are comparable to the thermal energy at room temperature, even some higher sub-levels are populated for both ground and excited states [4]. Populated sub-levels in both the lower and the upper states explain the discrepancies between the absorption and the emission spectra (Fig. 2.2). As a result, erbium-doped glass is a quasi-three-level system [19].

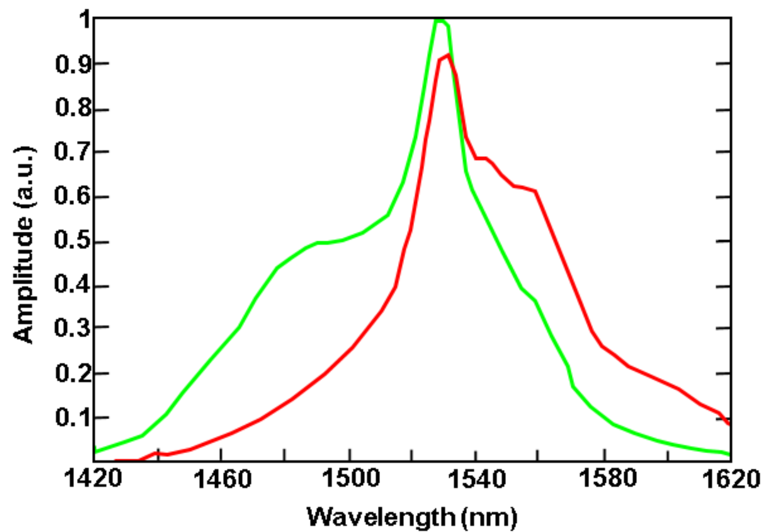

Figure 2.2. Emission and absorption spectra at around 1550 nm wavelength (adapted from [4]).

Stable pumping at 980 nm can be achieved using high power laser diodes leading to intense optical output (Fig. 2.3). Pumping at 1480 nm has it benefits that there are no non-radiative decays so there is no material heating through this process. However, this design suffers from fewer fibre components suitable for the 1480 nm wavelength and also pump sources at this wavelength are not as nearly good as at 980 nm [4].

The 810 nm pump source is not a good choice for erbium-doped as it exhibits strong excited state absorption (ESA) from the upper level of the lasing transition. Also, the quantum defect is quite high. ESA happens when excited ion absorbs phonon [20].

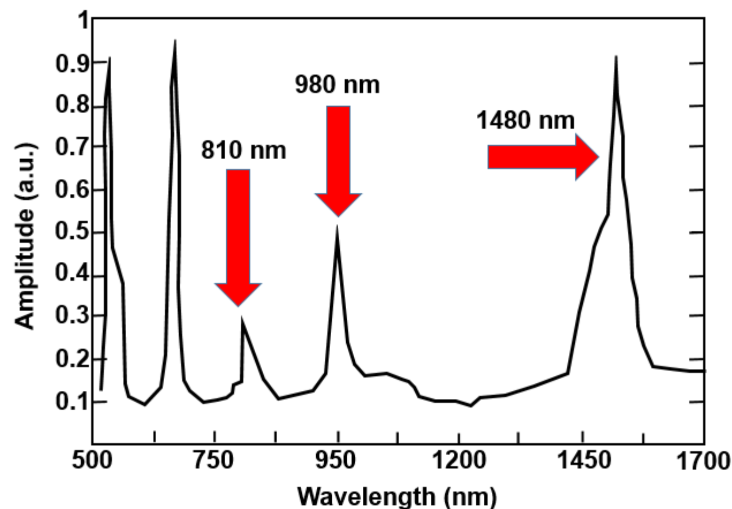

Figure 2.3. Absorption spectrum for an erbium-doped fibre. The three common pumping bands are shown with the arrows. The level involved and the wavelength associated with it are indicated (adapted from [4]).

One way to overcome the pumping issue is to co-dope an Er^{3+} ion with an ytterbium (Yb^{3+}) ion [21, 22]. This approach exploits large absorption cross-section of the Yb^{3+} with an absorption band from 800 to 1100 nm. In this arrangement the Yb^{3+} ion absorbs pump photons more

efficiently than the Er^{3+} ion and transits to the $^2F_{5/2}$ level. In the case of high level doping, energy transfer between ions can occur and the Yb^{3+} ion can pass excitation to the Er^{3+} ion $^4I_{11/2}$ level, which almost instantly decays to the $^4I_{13/2}$ (Fig. 2.4). This co-doping is often employed in the Er:fibre. However, back-transfer from the Er^{3+} ion to the Yb^{3+} ion can sometimes occur as well, thus limiting the conversion efficiency [23].

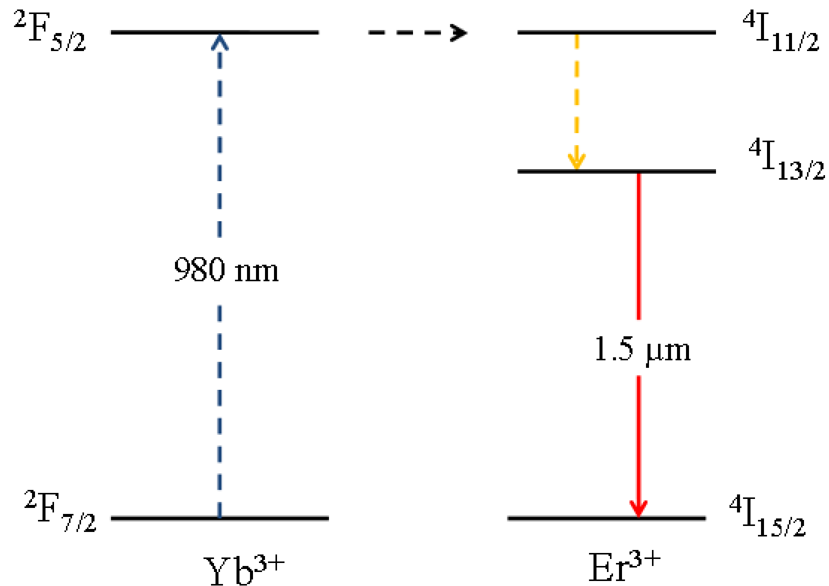

Figure 2.4. Energy transfer between the Er^{3+} and Yb^{3+} ion in a co-doped fibre [88].

4.2 Introduction to ultrafast fibre laser architectures

In order to generate ultrafast optical pulses one has to employ a mode-locking technique. The basic example of the laser is depicted in Fig. 2.5. Here a laser resonator consists of two mirrors covering a gain medium, where M1 is a high reflector and M2 is an output coupler. As the laser is optically pumped the light generated inside the laser cavity bounces back and forth between the mirrors a number of times. Therefore, standing waves are formed inside the cavity, which are called the longitudinal modes [3].

Figure 2.5. Basic configuration of a laser cavity. M1 (high reflector) and M2 (output coupler) mirrors.

In a simple configuration, these longitudinal modes will oscillate independently without any fixed relationship and interfere in such way that a constant intensity will be observed at the output as shown in Fig. 2.6a and is called CW. However, if these modes are fixed in frequency difference and are forced to oscillate with a fixed phase relation then they periodically interfere constructively producing intense output called pulse as shown in Fig. 2.6b, and the laser is said to be mode-locked [3].

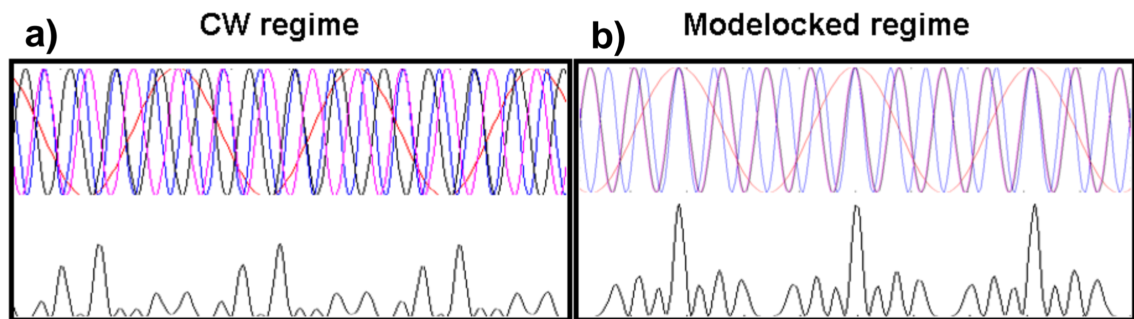

Figure 2.6. (a) Continuous wave operation; the output of the laser is constant. (b) Pulsed operation; the output of the laser will be intense burst and the separation of each peak round trip time of the laser cavity.

Such a standing-wave laser resonator can cause spatial hole burning when standing-wave intensity pattern saturates the gain, which can lead to reduction of the laser efficiency and mode stability. Therefore, more complex ring cavities can be implemented to avoid these limitations (Fig. 2.7). Fibre lasers typically exploit design of such cavities [3].

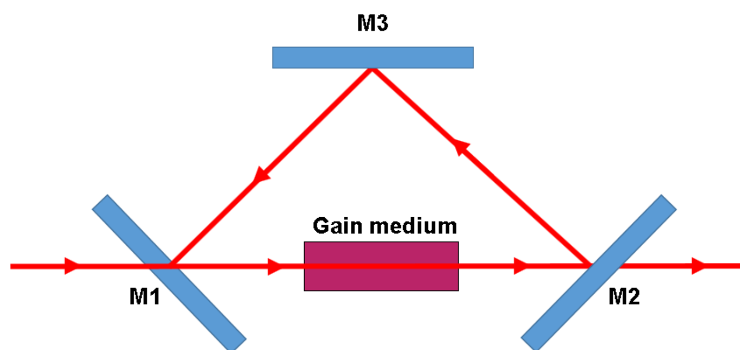

Figure 2.7. Basic configuration of a ring cavity laser. M1, M3 - high reflecting mirrors and M2 - output coupler.

Laser mode-locking can be achieved using both active and passive locking techniques [24]. While applying the passive mode-locking case laser modes are put in phase without active control inside the laser cavity. In fibre lasers the passive mode-locking happens when ultrashort laser pulses are produced via self-amplitude modulation (SAM), which modulates the cavity loss. Passive mode-locking in fibre lasers can be achieved using three different techniques: saturable absorber, nonlinear amplifying loop mirror and nonlinear polarisation rotation [25].

4.2.1 Active mode-locking

Active mode-locking is achieved with insertion of an actively controlled element in the laser cavity. This element modulates either the amplitude or the phase of the light inside the cavity and its frequency should relate to the mode spacing. The modulator creates periodic losses in the laser cavity (Fig. 2.8).

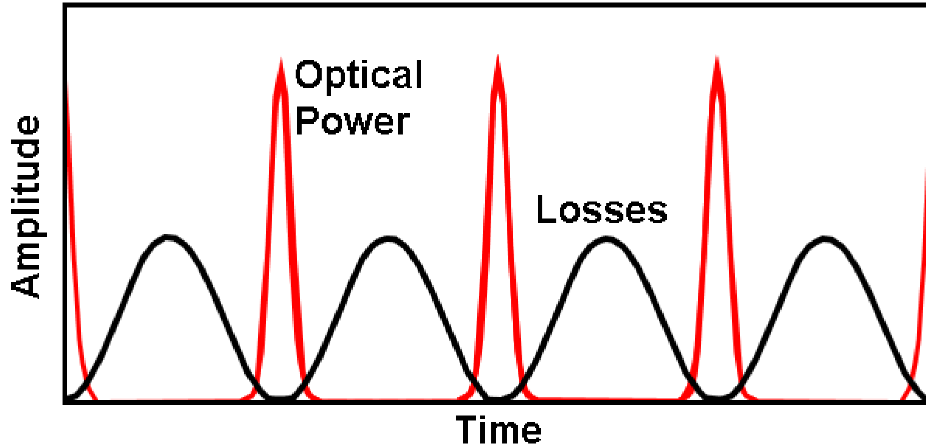

Figure 2.8. Temporal evolution of optical power and losses in an actively mode-locked laser

$$a = a_r + a_m[1 - \cos(\omega_m t)], \tag{2.1}$$

where a_r are the regular cavity losses and a_m is the additional loss created by the modulator with a frequency ω_m.

The laser emits more light when cavity losses are lowest leading to mode-locking after successive round trips [25].

4.2.2 Semiconductor saturable absorption

In passive mode-locking a higher loss at low power is introduced using a nonlinear component so that a shorter pulse with higher peak power experiences a lower loss. One possibility to achieve passive mode-locking is to use a saturable absorber (SA) (Fig. 2.9) [26]. A few types of SA can be used: semiconductor saturable absorber mirror (SESAM), saturable Bragg reflector (SBR), and carbon nanotubes. The SA mode-locking technique offers high repetition frequencies with the limited spectral width and output power. The limit is set by the damage threshold of the SA, which is permanently damaged if the peak intensity of the pulse exceeds it. There are other essential parameters of the SA while designing ultrafast lasers: the recovery time, the modulation depth, the bandwidth, the saturation intensity and the non-saturable losses. The recovery time of the SA determines whether it is a slow (nanosecond) or fast (picosecond) SA [27].

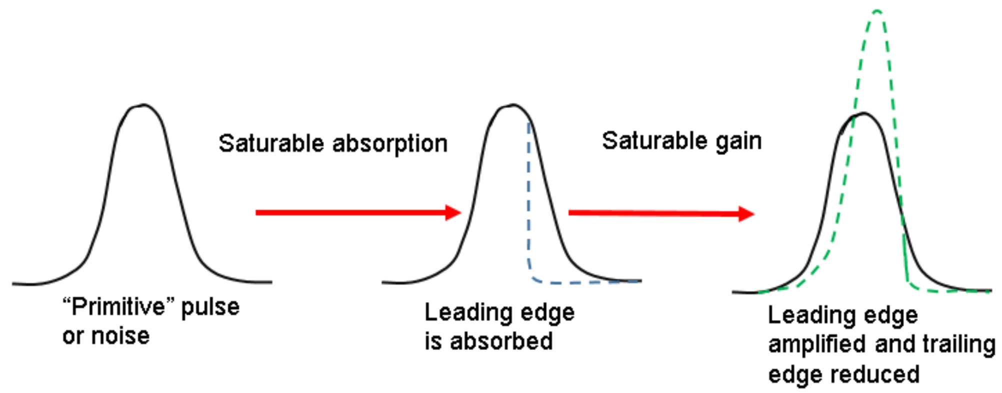

Figure 2.9. Representation of the SA mode-locking technique.

When light hits a slow saturable absorber, pulse's front edge is absorbed forming an excited state, which is transparent to the trailing edge. This is not sufficient to achieve mode-locking therefore, it is important to select a laser medium with a gain relaxation time faster than the cavity round-trip time, but slower than the absorber recovery time. For the fast saturable absorber the recovery time is comparable to the duration of the optical pulse. For this case the pulse intensity also self-modulates the loss in the cavity leading to linear and nonlinear dispersion shaping of the pulse [28].

4.2.3 Nonlinear amplifying loop mirror

It was demonstrated that sub-picosecond pulse durations can be obtained out of the fibre laser while using a nonlinear amplifying loop mirror mode-locking (NALM) technique. The NALM is based on the Kerr effect and can be realised using a figure-of-8 laser configuration (Fig. 2.11). The NALM laser consists of a Sagnac interferometer and a fibre amplifier placed asymmetrically in the loop (Fig. 2.10) [29].

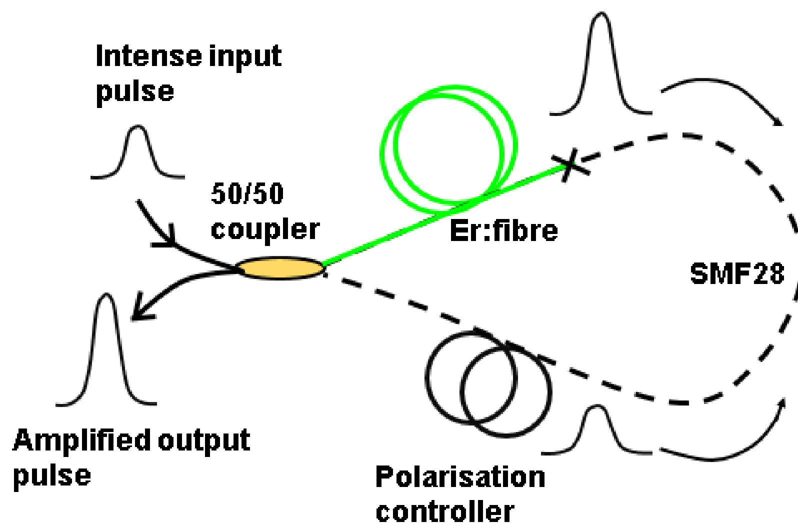

Figure 2.10. The NALM operation principle (adapted from [29]).

The electric field coming out from the left ring is coupled into the loop and split by the 50/50 splitter into two pulses propagating in opposite directions. When the optical power is low, the NALM works in the linear regime and pulses are recombined at the 50/50 splitter. However, high power pulses experience a nonlinear index of refraction. As the gain fibre is placed asymmetrically, the two pulses experience different phase shifts, which can be denoted by:

$$\delta\varphi_1 = \frac{\pi}{\lambda} ngIL, \tag{2.2}$$

$$\delta\varphi_2 = \frac{\pi}{\lambda} nIL, \tag{2.3}$$

where $\delta\varphi_1$and $\delta\varphi_2$ are the nonlinear phase shifts of pulses propagating in the clockwise and counter clockwise direction respectively, λ is a wavelength, n is the nonlinear index of refraction, g is the gain coefficient, I is the signal intensity and L is the loop length. Amplified higher intensity pulses are transmitted out of the laser leading to the mode-locking, which is achieved by carefully adjusting polarisation of the pulse with polarisation controller (explained in next section) [30].

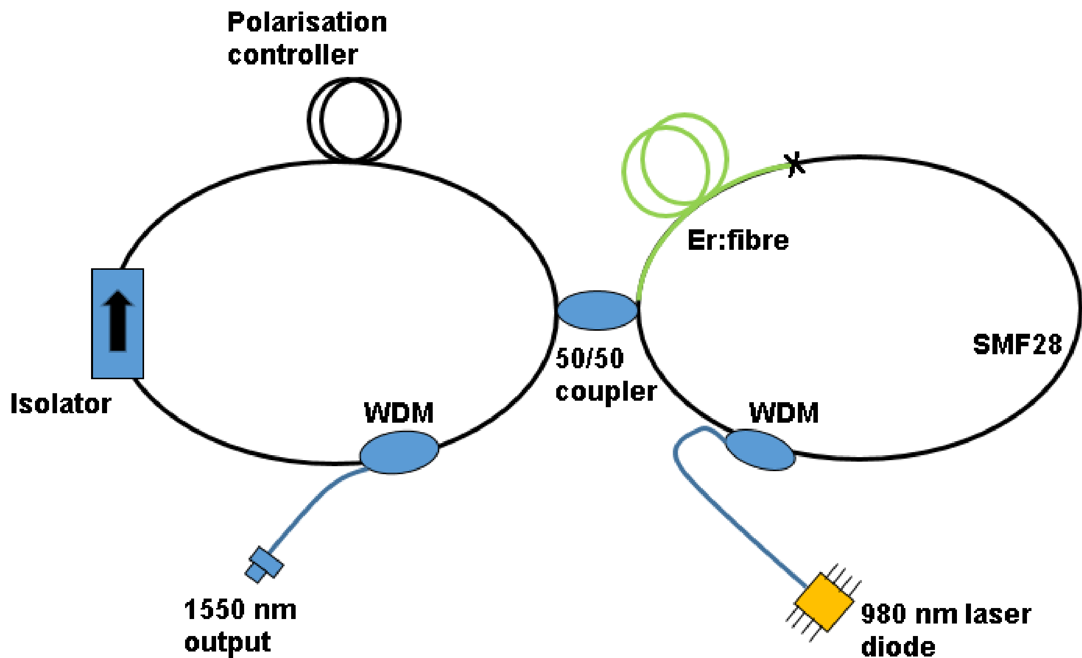

Figure 2.11. Schematic of the figure eight ring laser using a NALM saturable absorber (adapted from [31]).

It has been shown that using the NALM technique pulses of 50 fs can be generated. However, the NALM laser allows to achieve only low repetition rates due to the long cavity (long enough to achieve sufficient amplification) and it has not been demonstrated to self-start [31, 32].

4.2.4 Nonlinear polarisation rotation

Another way to realise a passive mode-locking is the nonlinear polarisation rotation (NPR) technique. The NPR is based on intensity dependent polarisation rotation and was first demonstrated by K. Tamura. [33].

First linearly polarised light is guided through the polariser, which sets the polarisation. Linearly polarised light is converted into elliptical after the quarter-wave plate (QWP) and propagates along a non-polarisation maintaining fibre. If the pulse is of high intensity, the Kerr effect occurs leading to the phase change between the two linear polarisation components of the elliptical polarisation state. This causes a nonlinear rotation of the polarisation state. The created rotation of the polarisation can be controlled with the waveplates to achieve a mode-locking state. The positions of the waveplates are tuned to obtain the maximum transmission through a polariser when the pulse intensity is highest. The polariser blocks low intensity pulses while transmitting the high peak power ones thus acting as the SA [33].

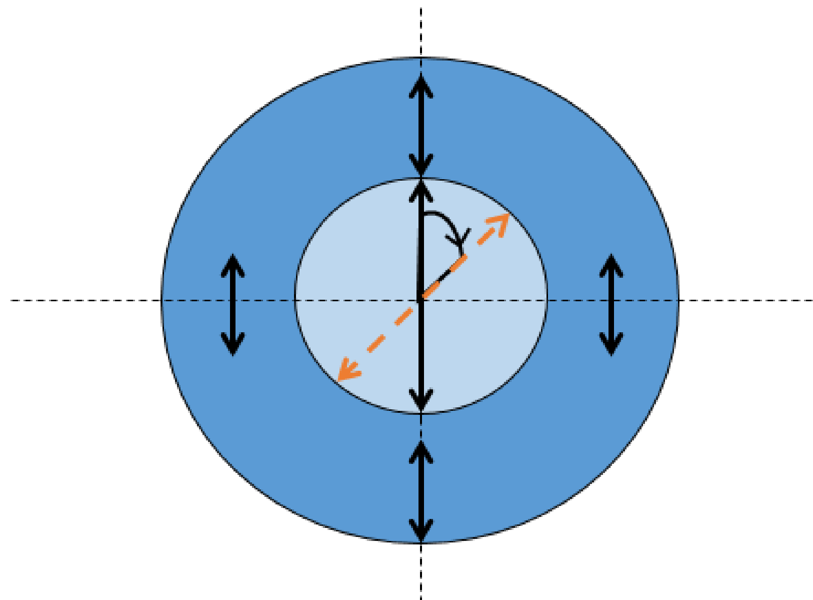

Figure 2.12. The NPR technique representation. The polarisation state in centre of the Gaussian shape pulse is rotated as a result of high peak power leading to the nonlinear Kerr effect, while the lower intensity wings maintain their polarisation (adapted from [33]).

The NPR mode-locking technique is extremely fast as it depends on the Kerr effect. Also a conventional Gaussian shaped pulse profile experiences a polarisation rotation within its peak, while wings remain unaffected (Fig. 2.12). This leads to the further shortening of the pulse and as a result, the shortest pulse durations without practical limit can be achieved.

However, it is difficult to achieve a high repetition rate as a shorter cavity would lead to lower pulse energy, which is not sufficient for the Kerr effect to happen. Also the NPR technique is sensitive to the temperature and fibre curvature changes as it affects polarisation and as a result

waveplate positions. Therefore, the temperature stabilised construction is vital to avoid frequent adjustment of the waveplates.

The described NPR technique was used to obtain mode-locking for the stretched-pulse erbium-doped fibre laser, which is introduced in following sections and was used in TOBIC experiments [34].

4.3 Pulse shaping effects in ultrafast lasers

Ultrashort pulse generation requires to achieve large bandwidths, because the optical pulse duration is directly proportional to the bandwidth [35]. This can be obtained only by the careful management and control of linear and nonlinear effects experienced by the pulse during the propagation through the dielectric media. In order to achieve the proper operation of the fibre laser, suitable pulse propagation conditions must be first accurately modelled and calculated because of the lengths of the fibre material.

4.3.1 Dispersion

Dispersion is one of the main properties of the fibres to be understood before designing a mode-locked fibre laser. The dispersion in the fibre depends not only on the materials, from which it is made, but also waveguide characteristics like the core size and the ratio between refractive indices of core and cladding. The propagation constant in the fibre with a core refractive index of n_1 and a cladding refractive index n_2 can be described by [36]:

$$\beta(\omega) = \frac{n(\omega)\omega}{c}, \tag{2.4}$$

here c is the speed of light, ω is frequency of light and $n(\omega)$ is the effective index of refraction. The propagation constant is limited within the interval of

$$n_1 k \geq \beta \geq n_2 k, \tag{2.5}$$

where $k = \frac{2\pi}{\lambda}$ is the wavenumber of the electromagnetic wave in vacuum. The propagation constant can be normalised and given by [36]:

$$b(\omega) = \frac{\beta^2/k^2 - n_2^2}{n_1^2 - n_2^2}. \tag{2.6}$$

If the most of the power is concentrated in the core and the refractive index difference is small, the propagation constant can be written as:

$$\beta(\omega) = n_2 k[1 + b(\omega)\Delta n], \tag{2.7}$$

where the normalised propagation constant is expressed via normalised frequency [36]:

$$b(\omega) = 1 - \left(\frac{1+\sqrt{2}}{1+\sqrt[4]{4+v(\omega)^4}}\right)^2 . \tag{2.8}$$

One can obtain the effective index of refraction while applying the previous equations:

$$n(\omega) = n_0(\omega)[1 + b(\omega)\Delta n], \tag{2.9}$$

here $n_0(\omega)$ corresponds to the material dispersion and the right term corresponds to the waveguide dispersion.

The material dispersion can be calculated using the Sellmeier equation [36]:

$$n_0(\lambda) = \sqrt{1 + \sum_{i=1}^{m} \frac{A_j \lambda^2}{\lambda^2 - B_j^2}} \approx \sqrt{1 + \frac{A_1\lambda^2}{\lambda^2 - B_1^2} + \frac{A_2\lambda^2}{\lambda^2 - B_2^2} + \frac{A_3\lambda^2}{\lambda^2 - B_3^2}}\ , \tag{2.10}$$

A_j and B_j are the medium's Sellmeier coefficients and wavelength is expressed in μm scale. Using the previous equation both the index of refraction and the group velocity dispersion can be calculated. The group velocity can be written as [36]:

$$v_g = \frac{d\omega}{dk}. \tag{2.11}$$

In vacuum the group velocity is equal to the phase velocity, which in a material is:

$$v_p = c/n\,. \tag{2.12}$$

The group velocity can be expressed via wavelength:

$$v_g = \frac{c}{n\text{-}\lambda\frac{dn}{d\lambda}} = \frac{c}{N_g}, \tag{2.13}$$

where N_g is the group index.

It was mentioned before that the propagation constant depends on the waveguide dispersion as well. The wave, which propagates inside the fibre, experiences different amounts of phase shift than would be the if only material dispersion were present. This waveguide dispersion occurs from the frequency dependent distribution of wave vectors [36].

The group velocity dispersion (GVD) of the cavity determines how the pulse propagates in the fibre laser since each frequency component travels with a different speed. This effect leads to the

broadening of the pulse width and possibly distortion. To calculate the GVD first the propagation constant $\beta(\omega)$ must be expanded as a Taylor series [36]:

$$\beta(\omega) = \beta_0 + \beta_1(\omega - \omega_0) + \frac{1}{2}\beta_2(\omega - \omega_0)^2 + \frac{1}{6}\beta_3(\omega - \omega_0)^3 + \cdots, \tag{2.14}$$

where

$$\beta_1 = \left(\frac{\partial \beta(\omega)}{\partial \omega}\right)_{\omega=\omega_0}, \tag{2.15}$$

$$\beta_2 = \left(\frac{\partial^2 \beta(\omega)}{\partial \omega^2}\right)_{\omega=\omega_0}, \tag{2.16}$$

$$\beta_3 = \left(\frac{\partial^3 \beta(\omega)}{\partial \omega^3}\right)_{\omega=\omega_0}. \tag{2.17}$$

β_2 is the group velocity dispersion or the second order dispersion and ω_0 is the carrier angular frequency. The GVD can be calculated if the net refractive index is known:

$$\beta_2 = \frac{1}{c}\left(2\frac{dn}{d\omega} + \omega\frac{d^2 n}{d\omega^2}\right). \tag{2.18}$$

When a pulse propagates through fibre it is useful to introduce a dispersion length quantity, which is related to the GVD:

$$L_D = \frac{\tau_0^2}{|\beta_2|}, \tag{2.19}$$

here τ_0 is the initial pulse duration. This equation shows that the Gaussian pulse after the distance L_D broadens by a factor of $\sqrt{2}$. It can be seen from the equation that the pulse spreads faster the shorter it is and the higher GVD of the material [36].

4.3.2 Group delay dispersion compensation

GVD over the length of the material produces group delay dispersion (GDD). Excess GDD leads to pulse broadening because each ultrafast optical pulse consists of the wide bandwidth of frequencies, which exhibit different group velocities. Therefore, while designing a fibre laser it is important to ensure that GDD is compensated in order to maintain ultrashort pulse duration during its propagation throughout the optical system.

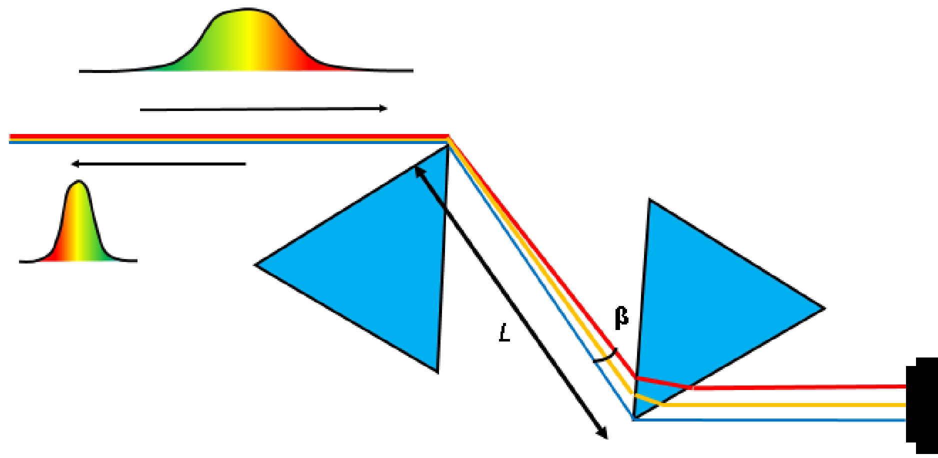

Figure 2.13. The GDD compensation using the prism pair.

A few GDD compensation techniques were demonstrated both theoretically and experimentally. The first conventional approach is to use prisms to introduce a negative GDD. There are two ways in which this GDD compensation technique can be realised: four prisms in a single-pass arrangement and a prism pair in a symmetrical reflection configuration (Fig. 2.13). The prism GDD compensation technique can be implemented intra-cavity where the prisms are inserted near one of the laser cavity mirrors. Prisms introduce the negative GDD into the system to compensate for the positive GDD, which is created by the laser. Negative GDD is established through the geometrical dispersion, because of a wavelength dependent angular response of the prism. To exercise this technique, the prisms need to be aligned to Brewster's angle to ensure the maximum transmission and the minimum Fresnel reflections of the propagating optical beam. Different wavelengths experience different optical paths leading to negative dispersion. The amount of the dispersion introduced can be controlled by tuning the separation l and angular deviation β of the incident rays [37].

Another approach to implement GDD compensation is to use a chirped mirror within the laser cavity (Fig. 2.14). This technique overcomes the complexity of fine beam alignment within the laser system. A chirped mirror is multilayer dielectric stack of periodically alternating layers of different materials. The periodicity of chirped mirror typically increases with a length and provides a control of reflection parameter. This parameter is a function of wavelength and layer period, so that the different wavelengths are reflected at different depths. The longer optical path length cancels out the negative GDD of the pulse. Even though chirped mirrors provide easy insertion within the optical system they need to be carefully designed to provide the correct dispersion compensation as they cannot be tuned [38].

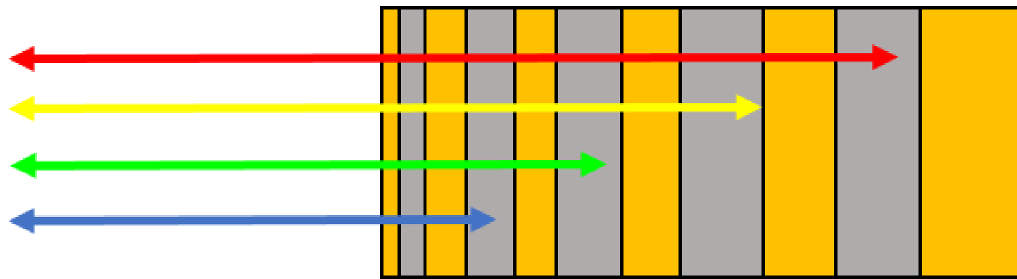

Figure 2.14. The GDD compensation using the chirped mirror.

Chirped mirrors are a free-space solution for GDD compensation. However, a similar configuration can be applied in the optical fibre itself. A fibre Bragg grating (FBG) can be fabricated in a section of the fibre to form a distributed Bragg reflector. This device is designed to reflect a particular range of wavelengths while at the same time transmitting the others. The FBG is manufactured by forming a periodic variation of the refractive index in the fibre core [39].

The next technique to solve GDD compensation is a simple insertion of an additional section of the standard telecommunications silica fibre (SMF28) into the laser system (Fig. 2.15). Silica fibre exhibits negative GDD, which can be used to compensate for the positive GDD if used in the correct length. This technique is typically applied in the erbium-doped fibre laser systems as optical pulses experience positive GDD in Er-doped fibre. This technique was successfully applied in both erbium-doped fibre laser systems and erbium fibre laser amplifiers and also was used to compensate GDD while constructing laser used for TOBIC experiments [40].

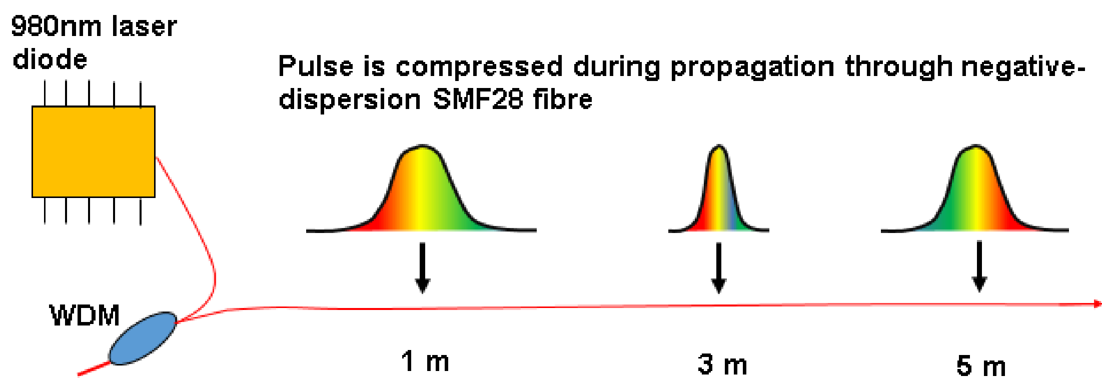

Figure 2.15. The dispersion compensation using the SMF28 fibre cutback.

The magnitude of GDD introduced in the optical system can be designed during initial steps. As GDD depends on the refractive index variation with the wavelength, this property of the optical material can be tailored by increasing or decreasing the doping concentration of the gain fibre. Also it was demonstrated that the refractive index profile can be engineered using photonic crystal fibre (PCF) [41]. PCF is an optical waveguide that exploits a periodic modulation of its refractive

index profile to guide light. There are two possible designs of the PCF: a solid core, which is surrounded by an array of air holes and a hollow core surrounded by an array of air holes (photonic bandgap (PBG) fibre) (Fig. 2.16) [42]. The number of possible PCF designs is countless as it can be designed using materials with different refractive indices as well as applying different patterns and geometries of a periodic modulation. Therefore, there are several designs of PCF, which can be used to obtain a desirable GDD profile. It is even possible to achieve zero GDD across a broad bandwidth of wavelengths eliminating the need for the GDD compensation.

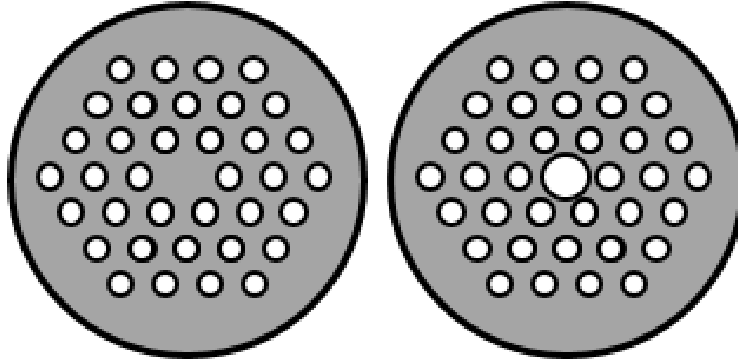

Figure 2.16. Photonic crystal (left) and photonic bandgap (right) fibre designs.

As introduced already, waveguide dispersion occurs as well. It can be compensated while using graded index fibres to match the group velocities and reduce the differences between delay times of the propagating wavevectors.

4.3.3 Self-phase modulation

Self-phase modulation (SPM) is a self-induced phase delay appearing due to the optical Kerr effect, which induces nonlinear refractive index of the medium. Nonlinearity occurs as a high intensity electro-magnetic field forces the anharmonic motion of bound electrons of the dielectric medium. Therefore, the polarisation response P of the dielectric medium can be expressed by the following equation [36]:

$$P = \varepsilon_0\left(\chi^{(1)}E + \chi^{(2)}E^2 + \chi^{(3)}E^3 + \cdots\right), \tag{2.20}$$

where ε_0 is a permittivity in free space and χ is a susceptibility of the material. The first term here denotes the linear polarisation, which is related to the refractive index and the absorption of the material. The second term is the second-order nonlinearity, which is responsible for the nonlinear effects such as second harmonic generation and sum frequency generation. However, optical fibres are made from fused silica, which is a centrosymmetric material, and therefore, $\chi^{(2)} = 0$. As a result, the polarisation of the dielectric material can be described then as [36]:

$$P = \varepsilon_0 \left(\chi^{(1)} + \chi^{(2)} E\right) E. \quad (2.21)$$

$\chi^{(3)}$ is the third-order nonlinearity and is responsible for the third harmonic generation, four-wave mixing and nonlinear refraction. The nonlinear refraction or the optical Kerr effect leads to other nonlinear phenomena in fibres. If a strong electrical field propagates inside such material the total refractive index can be written as:

$$n \approx n_0 + \frac{\chi^{(3)}}{2n_0} E^2 = n_0 + \frac{\chi^{(3)}}{{n_0}^2 c \varepsilon_0} I, \quad (2.22)$$

where n_0 is the linear refractive index, c is the speed of light and I is the intensity of the field. This expression suggests that the refractive index depends on the intensity of the field due to the third-order nonlinearity. The refractive index dependence on the intensity leads to other nonlinear effects such as SPM and cross-phase modulation (XPM). The nonlinear refractive index of the fused silica fibre is approximately 3×10^{-20} $\mathrm{m^2/W}$. This value is smaller than in many other dielectric media, however nonlinear effects are still observed as light is confined in the very narrow core of the fibre [36].

SPM creates a self-induced phase shift by the propagating electric field inside the fibre. This phase shift for an optical pulse can be expressed as:

$$\varphi(t) = \frac{-2\pi n_2 I(t) L}{\lambda}, \quad (2.23)$$

where L is the length of the fibre and λ is the wavelength of the optical beam. This result shows that SPM leads to the spectral broadening of the optical pulses and therefore forms optical solitons along with the negative dispersion of the fibres [36].

Third-order nonlinearity also leads to leads to the Kerr-lensing effect. A Gaussian laser beam experiences larger phase retardation at the more intense centre part of the beam than at its edges. This results in the wavefront curvature and self-focusing [36].

4.3.4 Optical solitons

Optical solitons occur due to combined effects of SPM and linear dispersion. These effects can be tailored to counterbalance each other to obtain a “first order” optical soliton, which maintains its pulse shape intact throughout the full propagation length. As solitons occur due to the combined effect of dispersion and nonlinearity their propagation can be described by [36]:

$$i \frac{\partial A}{\partial z} = \frac{\beta_2}{2} \frac{\partial^2 A}{\partial T^2} - \gamma |A|^2 A, \quad (2.24)$$

where A is the amplitude of the pulse, β_2 is the dispersion parameter and γ describes the SPM. This equation can be normalised via three dimensionless variables,

$$U = \frac{A}{\sqrt{P_P}}, \xi = \frac{z}{L_D}, \tau = \frac{T}{T_0}, \tag{2.25}$$

where P_P is the pulse peak power, T_0 is the pulse duration, and L_D is the dispersion length. Using these parameters optical pulse propagation can be written [36]:

$$i\frac{\partial U}{\partial \xi} = \frac{1}{2}\frac{\partial^2 U}{\partial \tau^2} - N^2|U|^2 U, \tag{2.26}$$

where the parameter N is the soliton number and can be expressed:

$$N^2 = \frac{\gamma P_p T_0^2}{|\beta_2|}. \tag{2.27},$$

Eq. (2.26) can be further normalised with:

$$u = NU = \sqrt{\gamma L_D A}, \tag{2.28}$$

$$i\frac{\partial u}{\partial \xi} + \frac{1}{2}\frac{\partial^2 u}{\partial \tau^2} + |u|^2 u = 0, \tag{2.29}$$

here the first term denotes optical pulse propagation through the medium, the second term describes the dispersion and the third term characterises the SPM. There are multiple solutions to the above equation and they are described by the soliton number N.These solutions depend on the power and duration of the pulse and the dispersion and SPM of the material. The $N = 1$ fundamental soliton propagates through the medium without a change to its envelope, while higher-order solitons experience periodic pulse reshaping over a given length (soliton period) [36].

4.4 Erbium-doped fibre soliton laser

Soliton generation inside a fibre can be exploited to obtain ultrashort laser pulses. As it was discussed before, certain conditions must be fulfilled to reach the soliton generation regime. It is necessary to balance chromatic dispersion with the Kerr effect. As it was suggested in the previous section, one can insert the standard silica fibre (SMF28) to introduce negative group delay dispersion, which compensates the positive dispersion caused by the Kerr effect [43]. If the correct parameters are selected, the fundamental soliton is generated. This soliton can propagate long distances without changing its shape [44]. If the dispersion is not properly balanced, a soliton exhibits periodic broadening and compression in time and frequency domains as it propagates

along the fibre. However, this effect also happens in well compensated systems as nonlinearity and dispersion are not uniformly distributed and typically varies randomly both in space and time, resulting in the Gaussian shaped “breathing” soliton [45].

Sub-picosecond pulses can be generated by the fibre soliton lasers. However, there are a few limitations for the system of this configuration. First, it is typical for these laser systems to operate in a multi pulsing regime. This is a consequence of the soliton energy quantisation, which appears in the laser systems with excessive gain [46]. A soliton has a maximum peak power available and if the pump is higher the excess power leads to the soliton break up into non-periodic multiple pulses. This limitation can be resolved tuning the gain and cavity length. Designing a short laser cavity with the fine tuning of the gain, one can reach a stable soliton regime making it possible to consume all the available gain through the single pulse per round-trip [47].

Another property of soliton lasers is the generation of non-uniform Kelly sidebands. These sidebands appear on the soliton spectrum at around centre peak and are generated due to the soliton filtering. An optical soliton experiences periodic changes in gain and loss as it propagates through the fibre laser and therefore, it is forced to dispense a part of its spectral content. The frequency bandwidth, which is removed, propagates through the system with its phase velocity. At each cavity round trip this dispersed frequency packet experiences destructive interference except at the frequencies which are phase-matched. These phase-matched frequencies form the non-uniform Kelly sidebands via the constructive interference [43].

The distribution of Kelly sidebands around the central peak of the spectral output depends on the pulse width, the dispersion within the cavity and the cavity length. The sidebands are located closer to the central peak, if the pulse duration of the soliton pulse is close to the transform limited [43].

Soliton lasers have a few limitations, which may hinder the best performance of the TOBIC microscope. For example, it can be challenging to obtain enough power and achieve sufficient pulse durations to realise TPA. Therefore, an alternative stretched pulse erbium-doped fibre laser configuration was designed.

4.5 Stretched-pulse erbium-doped fibre laser

The stretched-pulse erbium-doped fibre (SPEDF) laser makes it possible to overcome issues and limitations, which occur in the soliton lasers. The SPEDF laser design contains both high negative and positive dispersion fibre segments within the cavity, which are almost perfectly balanced to result in slightly positive net cavity dispersion. This design provides pulse stretching in the positive segment (erbium-doped fibre) and then compression in the negative segment (standard SMF28 fibre). Therefore, pulses that propagate through the laser cavity have a low peak power

as the pulse widths change by an order of magnitude during one round trip. This leads to the net nonlinear phase shift, which is significantly reduced and thus prevents the saturation. Also the SPM along with the highly positively dispersive erbium fibre provides the possibility to achieve a strong spectral broadening leading to a wide spectral bandwidth and a high energy of the pulse [48].

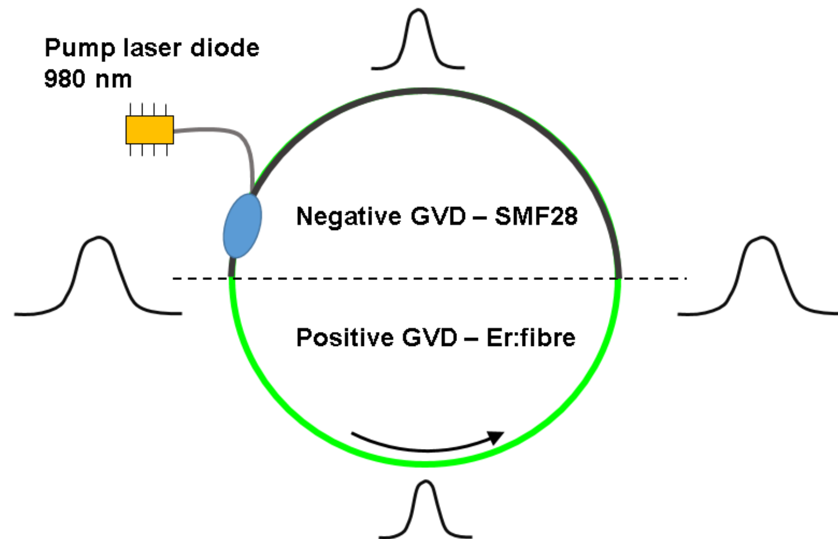

Figure 2.17. The stretched-pulse erbium-doped fibre laser operation principle.

Another advantage of the SPEDF lasers is that the shortest pulse widths are only maintained over a short part of the cavity round-trip. Therefore, the net nonlinear phase shift is limited. Typically, the SPEDF is designed to exploit the negative and positive-dispersion fibre boundary as an output, since it is the low peak power region (Fig. 2.17). As a result, the output pulses are linearly chirped and can be compressed using the standard SMF28 fibre, a prism pair, or the FBG.

The SPEDF laser also benefits from the alternating stretching and compressing of the propagating pulse, which leads to a periodic modulation of wave vector. This suppresses the generation of Kelly sidebands in the output spectrum since the phase-matching condition is more difficult to achieve [48].

The mode-locking and optical pulses in both soliton and stretched-pulse fibre lasers can be described in the time-domain using a steady-state theoretical analysis. This study considers each cavity element's effect on the pulse over every cavity round-trip. The described analysis can be written as the Haus Master Equation [48]. For the SPEDF laser case this analysis uses a chirped Gaussian beam model and accounts for small nonlinear changes per cavity round trip [49]. Theoretical calculations assume the nonlinearity and dispersion variations within the SPEDF laser cavity and treat them as perturbations leading to the predictions of the absence of Kelly sidebands.

$$\left[(g-l)+\left(\frac{g}{\Omega_g^2}+jD\right)\frac{d}{dt^2}+\gamma_0|A_0|^2\left(1-\mu\frac{t^2}{\tau_0^2}\right)-j\delta_0|A_0|^2\left(1-\mu\frac{t^2}{\tau_0^2}\right)\right]a(t)=$$

$$=-j\psi a(t), \quad (2.30)$$

where D is the average dispersion, l is the linear loss per cavity round trip, g is the laser gain, Ω_g is the gain bandwidth, t represents time, A_0 is the peak amplitude of the pulse, γ_0 describes self-amplitude modulation, μ is the curvature of the parabolic time-dependent nonlinear phase shift, δ_0 describes the effects of SPM, τ_0 is the normalised pulse width, and ψ is the net linear phase.

The Master equation of a SPEDF laser has a chirped Gaussian solution,

$$u(t)=A_0\exp\left(-Q\frac{t^2}{2}\right), \quad (2.31)$$

where $u(t)$ denotes the complex amplitude of the oscillating electric field within the cavity and the complex parameter Q is acquired from the balanced Master equation. This Gaussian solution is in agreement with the simplified Kuizenga-Siegman theory [50], which models ultrafast pulse propagation and duration.

4.6 Erbium-doped fibre amplifier

To provide a sufficient peak power for TOBIC imaging experiments after using RP and other components, a fibre amplifier was constructed.

There is a wide variety of applications for the Erbium-doped fibre amplifiers (EDFA) like optical frequency metrology, optical supercontinuum generation and telecommunications industry. Telecommunication industry was the main driving force for EDFA optimisation and characterisation. Fibre amplifiers provide an efficient and entirely optical alternative to amplify an optical signal avoiding the need to convert it to an electrical signal Also the gain bandwidth of EDFA perfectly covers the telecommunications C Band (1530-1565 nm), which can be slightly tuned to be suitable for a small part of the L Band (1565-1625 nm). The EDFA is a critical part in fibre optical communications as the signal has to be transmitted over a long distance, which causes the strong signal attenuation and therefore it needs to be periodically amplified [51].

Many scientific applications, such as nonlinear microscopy require the high peak powers and for those areas the EDFA can be the ideal solution, though sometimes sufficiently complicated to implement. Ultrashort pulses require the management of nonlinear effects within the optical fibre. This needs to be maintained very well in order to obtain ultrafast and good quality pulses and

short pulse durations after the amplification process. The main principle is to decrease the peak intensity within the fibre core. This can be done using a few different techniques: chirped pulse amplification, fibre core-size scaling and nonlinear pulse amplification. The chirped pulse amplification technique is based on pulse stretching before the amplification and compression afterwards. For the fibre core scaling method, the core of the amplifying fibre is manipulated to accommodate an increased number of modes.

In order to obtain nonlinear pulse amplification, an optical pulse is first coupled into an Er-doped fibre. Then this pulse propagates within the fibre amplifier while gain, SPM and dispersion shape it both spectrally and temporally resulting in either a compressed or chirped pulse at the output. The output depends on the sign of the fibre dispersion [51].

If chirped pulses are emitted at the output, they have to be recompressed to obtain a transform limited shape. This typically needs to be addressed in EDFA since Er-doped fibre exhibits the high positive dispersion. Also to ease the post-amplification, the input pulse can be temporally stretched in a length of standard telecommunication negative dispersion fibre (SMF28) before entering the Er:fibre. Control of the length of pre-amplification fibre allows to accurately tune and decrease the peak intensity of the amplified output pulses [51].

Such EDFA configuration when the pulse is amplified using a positive dispersion nonlinear amplification benefits from significantly higher output pulse energies. This is a result of both the spectral broadening via SPM and the temporal stretching within the amplifying fibre [51, 52].

4.7 Construction

The construction of the SPEDF laser is shown in Fig. 2.18. All laser components were standard telecommunication and optomechanical components.

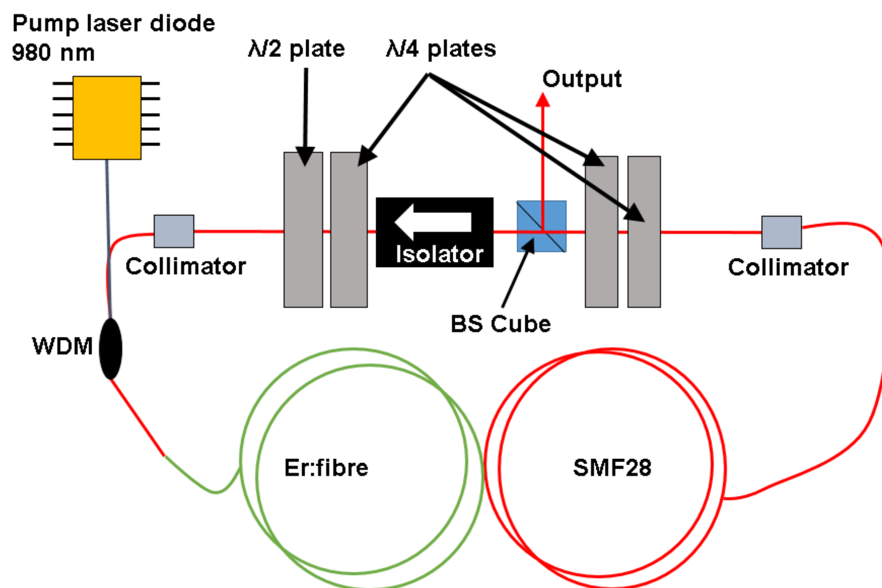

Figure 2.18. The construction of the stretched-pulse erbium-dope fibre laser.

The ring laser was forced into unidirectional operation by employing a polarisation-sensitive optical isolator. After the optical isolator and before the beamsplitter, waveplates were inserted. These waveplates were used for polarisation adjustment to initiate efficient NPR mode-locking operation. They were tuned to produce mode-locked operation and settings were recorded to reacquire similar performance if the laser needed adjustment. A combination of a QWP and a half-wave plate (HWP) at the exit of the isolator was used to create a state of elliptical polarisation before pulse propagation into the fibre. The Kerr effect rotated the polarization ellipse and with another QWP transformed phase modulation into amplitude modulation. The last QWP was used to compensate for any remaining linear birefringence in the fibre.
The cavity had a total length of 304 cm, which comprised 190 cm of standard SMF28 telecommunications fibre, 100 cm of OFS high concentration erbium-doped fibre (negative dispersion, peak absorption at 1530 nm 45-65 dB/m), and 16 cm of free-space. The Er:fibre laser was pumped with a 980 nm laser diode (2000CHP) from 3SPGroup which provided a pump power of 950 mW. The laser was operated in the forward direction and generated 70 mW average output power pulses at a repetition rate of 68 MHz. The obtained optical spectrum is shown in Fig. 2.19.

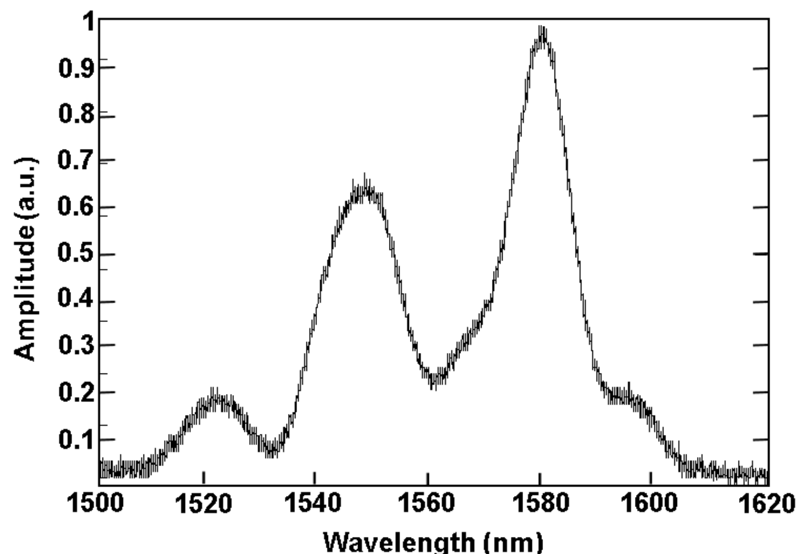

Figure 2.19. The optical spectrum at the Er:fibre laser output.

The design of the EDFA is shown in Fig. 2.20 and was constructed using standard telecommunication component with a help of Dr. Carl Farrell. The amplifier was pumped with 980 nm laser diode LC962U*P(“II-VI”), which generated 750 mW in CW operation, a wavelength division multiplexer (WDM), a 180 cm length of erbium-doped fibre, a SMF28 optical fibre for dispersion compensation (200 cm) and a fibre collimator. The laser diode was attached to the heat sink. A reel of erbium-doped fibre, SMF28 fibre and WDM were placed on the breadboard. The fibre collimator was attached to the holder.

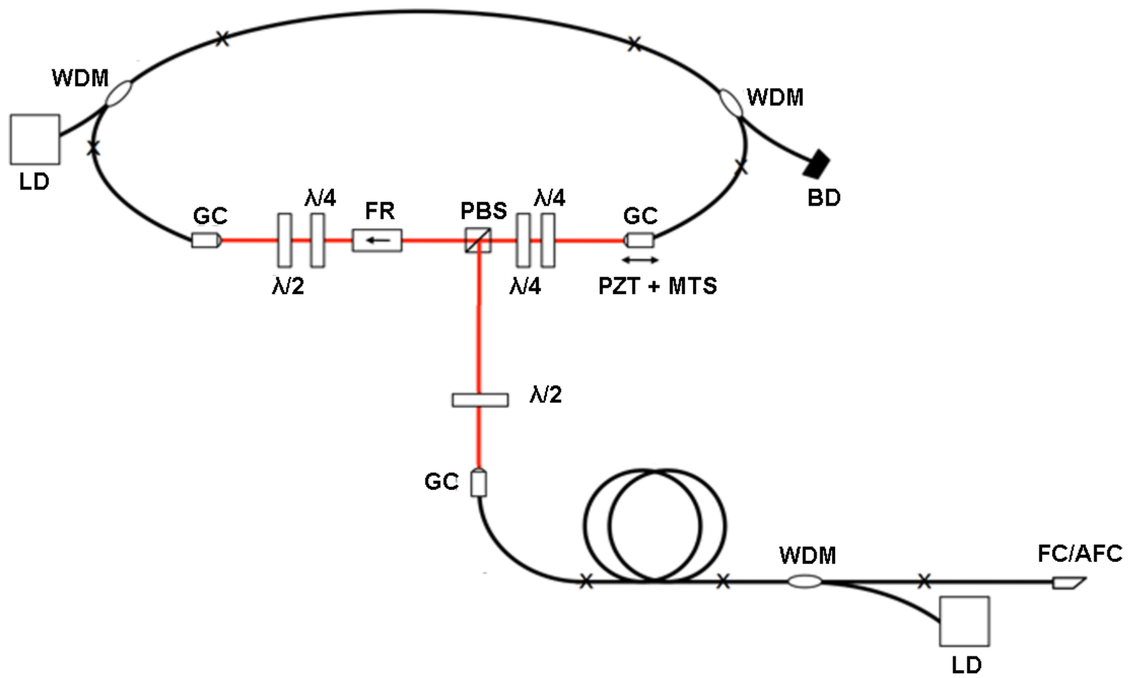

Figure 2.20. Final Er:fibre laser configuration with EDFA. GC: collimator; FR: Faraday rotation isolator; PBS: polarising beam-splitter; WDM: wavelength division multiplexer (980 nm / 1550 nm); LD: fibre-coupled 980-nm laser diode; FC-AFC: angled-fibre connector; BD: beam-dump.

The input laser power from the erbium-doped fibre laser was 70 mW. After nonlinear pulse amplification through the EDFA and after the compression through the cutback of SMF28 fibre, the average power measured at the output of the collimator was 190 mW and the obtained spectrum is shown in Fig. 2.21.

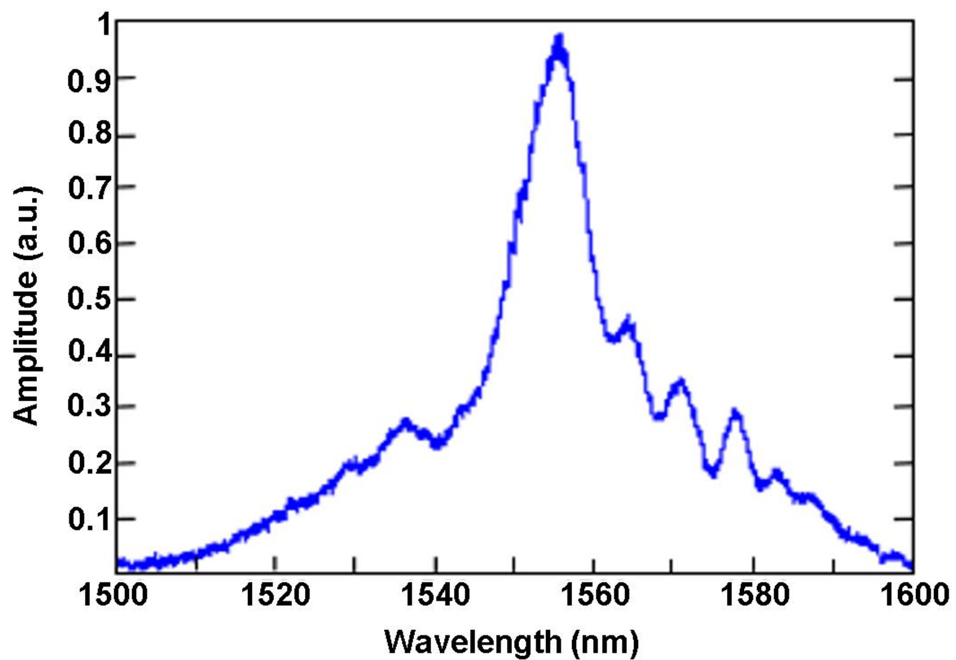

Figure. 2.21. The optical spectrum at the EDFA output.

4.8 Pulse measurement

The optimum performance of the mode-locked laser can be confirmed by measuring the temporal profile of an ultrashort pulse. In order to quantify a short event normally requires the measurement technique to employ a phenomenon, shorter than the event itself. There are various temporal profiling techniques using either an electronic or optical approach. The standard fast photodiodes and streak cameras based on linear techniques have a response rates on the picosecond time scale. Therefore, they can measure the shortest pulse durations of picosecond scale. Various techniques have been developed in order to measure shorter pulses [53]. A simple approach to measure femtosecond pulses is to use nonlinear effects to achieve optical interferometric autocorrelation. This can be done both in an optical crystal or semiconductor diode. Optical interferometric autocorrelation is performed by recording the electric field response of a light pulse against its time-delayed replica. This response function depends on the pulse duration and the separation of the two identical pulses in time. The optical autocorrelation function can be written as [53]:

$$A^{(2)}(\tau) = \int_{-\infty}^{\infty} F(t)F(t-\tau)\mathrm{d}\tau \qquad (2.32)$$

An autocorrelation is typically obtained either by second harmonic generation (SHG) or TPA at the output of the interferometer [54]. This autocorrelation function is always symmetric to time delay and therefore any asymmetry in the pulse is always lost. The pulse duration can be obtained from the autocorrelation trace by dividing the autocorrelation width by a factor depending on the pulse shape (Gaussian 1.414, hyperbolic Secant 1.543) [55].

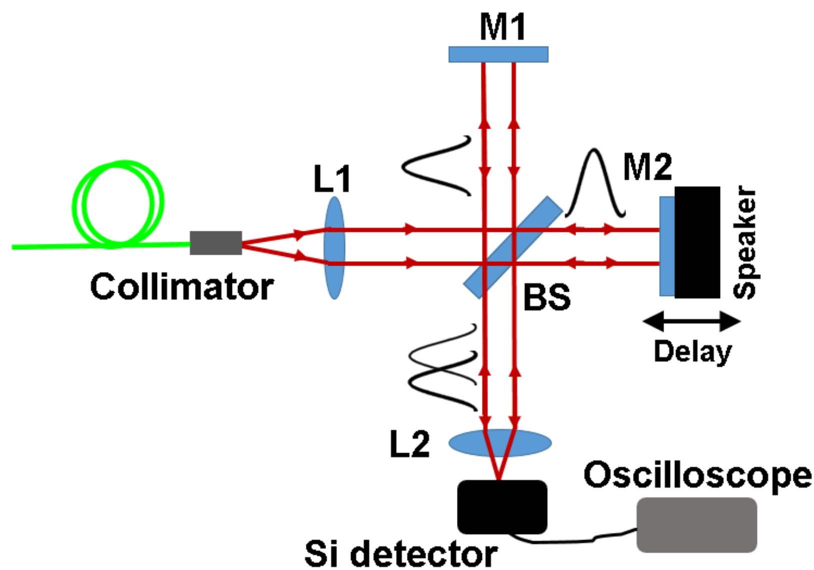

Figure 2.22. Michelson interferometer setup for pulse duration measurements. BS, beam splitter; M1 and M2, mirror. The input beam is split into two pulses by the 50/50 beam splitter. After bouncing back from two mirrors M1 and M2 pulses are recombined again by the 50/50 beam splitter.

A conventional pulse splitting technique is by using a Michelson interferometer (Fig. 2.22). In this approach, the pulse is split in two using a 50/50 beam splitter BS. Pulses are propagated into two different sections of the interferometer. One pulse hits fixed mirror M1 mounted on translation stage and bounces back to the beam splitter. The other one is reflected by the moving mirror M2. Therefore, the first beam has fixed optical path length and the second one has a periodically varying optical path length. Both beams are then recombined again at the beam splitter and focused on the silicon detector. If the system is well aligned the interferometric autocorrelation has a peak to background ratio of 8:1. The interferometric autocorrelation is very sensitive to the pulse shape because of the fourth power of the electric field amplitude. Therefore, vibrations introduced by the delay moving mirror must be reduced [56].

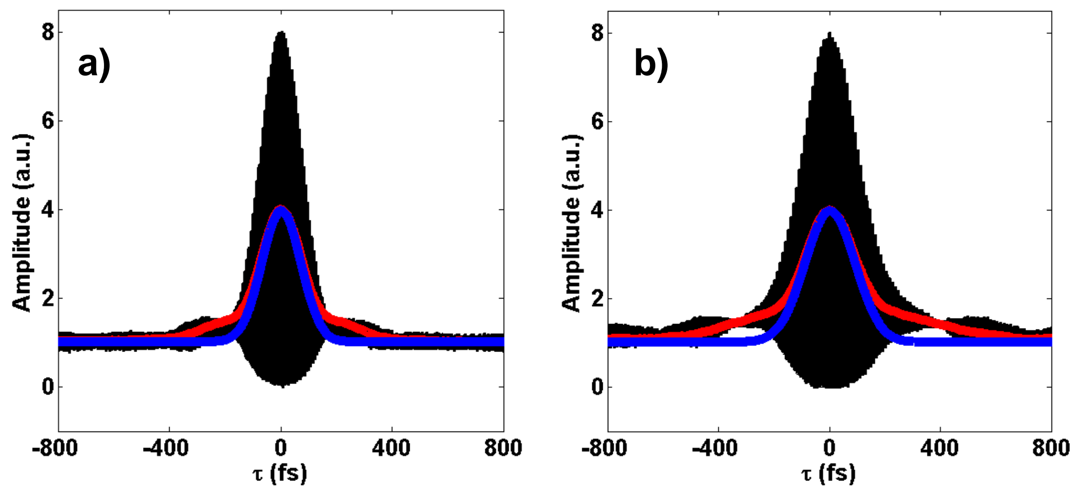

Figure 2.23. (a) Autocorrelation trace of the Er:fibre laser oscillator with pulse duration of 110 fs and (b) autocorrelation trace after EDFA with pulse duration of 140 fs. Pulse durations inferred from a Gaussian envelope (blue) fitted to the intensity autocorrelation trace (red).

The obtained interferometric autocorrelation trace for Er:fibre laser and amplifier are shown in Fig. 2.23. These traces exhibit the proper 8:1 ratio between peak and background with the Gaussian fit on the intensity autocorrelation for pulse duration measurement. The full width half maximum (FWHM) of the pulse duration after the Er:fibre laser was 110 fs and after the EDFA the pulse duration was 140 fs and slightly chirped. This happened because the cutback experiment was done measuring pulse duration at the device layer in the IC; there the pulse duration was 110 fs as it is discussed later in Chapter 5.

References

1. A. Galvanauskas, M. Y. Cheng, K. C. Hou, K.H. Liao, “High peak power pulse amplification in large-core Yb-doped fiber amplifiers”, IEEE Journal of Selected Topics in Quantum Electronics**13**, 559–566 (2007).
2. Y. Jeong, J. K. Sahu, D. N. Payne, and J. Nilsson, “Ytterbium-doped large-core fiber laser with 1.36 kW continuous-wave output power”, Optics Express **12**, 6088–6092 (2004).
3. B. A. E. Saleh and M. C. Teich, “Fundamentals of photonics”, New York: John Willey & Sons, Inc. (1991).
4. M. J. F. Digonnet, “Rare-earth-doped fiber lasers and amplifiers, 2nd ed.”, Boca Raton: CRC Press (2001).
5. K. Tamura, J. Jacobson, E. P. Ippen, H. A. Haus, and J. G. Fujimoto, “Unidirectional ring resonators for self-starting passively mode-locked lasers”, Optics Letters **18**, 220 (1993).
6. M. Chernysheva, C. Mou, R. Arif, M. Al Araimi, M. Rümmeli, S. Turitsyn, and A. Rozhinb, “High power Q-switched thulium doped fibre laser using carbon nanotube polymer composite saturable absorber”, Scientific Reports **6**, 24220 (2016).
7. J. W. Nicholson, A. D. Yablon, P. S. Westbrook, K. S. Feder, and M. F. Yan, “High power, single mode, all-fiber source of femtosecond pulses at 1550 nm and its use in supercontinuum generation”, Optics Express **12**, 3025-3034 (2004).
8. J. M. Dudley, G. Genty and S. Coen, “Supercontinuum generation in photonic crystal fiber”, Reviews of Modern Physics **78**, 1135–1184 (2006).
9. C. Bourolias, E. Prokopakis, E. Sobol, J. Moschandreas, G. A. Velegrakis, and E. Helidonis, “Septal cartilage reshaping with the use of an Erbium doped glass fiber laser. Preliminary results”, Rhinology **46**, 62-65 (2008).
10. C. C. Neubaur and G. Stevens, “Erbium: YAG laser cataract removal: Role of fiber-optic delivery system”, Journal of Cataract and Refractive Surgery **25**, 514-520 (1999).
11. K. Tamura, E. Yoshida, and M. Nakazawa, “Generation of 10GHz pulse trains at 16 wavelengths by spectrally slicing a high power femtosecond source”, Electronics Letters **32**, 1691-1693 (1996).
12. K. Tamura, E. Yoshida, E. Yamada, and M. Nakazawa, “Generation of a 0.5 W average power train of femtosecond pulses at 10 GHz in the 1.55 μm region”, Electronics Letters **32**, 835-836 (1996).
13. S. McCulloch, A. Hassey, P. Harrison, “Fiber laser performance in industrial applications”, Proceedings Society of Photographic Instrumentation Engineers **8603**, 86030C (2013).
14. J. Y. Allain, M. Monerie, and H. Poignant, “High-efficiency CW thulium-sensitized holmium-doped fluoride fiber laser operating at 2.04 μm”, Electronics Letters **27**, 1513-1515 (1991).
15. D. C. Hanna, R. M. Percival, R. G. Smart, and A. C. Tropper, “Efficient and tunable operation of a Tm-doped fiber laser”, Optics Communications **75**, 283-286 (1990).

16. D. C. Hanna, I. M. Jauncey, R. M. Percival, I. R. Perry, R. G. Smart, P. J. Suni, J. E. Townsend, and A. C. Tropper, “Continuous-wave oscillation of a monomode thulium-doped fiber laser”, Electronics Letters **24**, 1222-1223 (1988).
17. D. C. Hanna, R. M. Percival, I. R. Perry, R. G. Smart, P. J. Suni, J. E. Townsend, and A. C. Tropper, “Continuous-wave oscillation of a monomode ytterbium-doped fiber laser”, Electronics Letters **24**, 1111-1113 (1988).
18. Y. Durteste, M. Monerie, J. Y. Allain, and H. Poignant, “Amplification and lasing at 1.3-μm in praseodymium-doped fluorozirconate fibers”, Electronics Letters **27**, 626-628 (1991).
19. E. Desurvire, “Erbium-doped fiber amplifiers: Principles and applications”, New York: John Wiley & Sons (2002).
20. C. R. Giles and E. Desurvire, “Modeling erbium-doped fiber amplifier”, Journal of Lightwave Technology **9**, 271-283 (1991).
21. J. D. Minelly, W. L. Barne, R. I. Laming, P. R. Morkel, J. E. Townsend, S. G. Grubb, and D. N. Payne, “Diode-array pumping of Er3+/Yb3+ co-doped fiber lasers and amplifiers”, IEEE Photonics Technology Letters **5**, 301-303 (1993).
22. G. G. Vienne, J. E. Caplen, L. Dong. J. D. Minelly, J. Nilsson, and D. N Payne, “Fabrication and characterization of Yb3+:Er3+ photosilicate fibers for lasers”, Journal of Lightwave Technology **16**, 1990-2001 (1998).
23. Y. Jeong, D. Lee, J. W. Lee, and K. Oh, “Fiber-optic color synthesizer”, Optics Letters **31**, 2112-2114 (2006).
24. A. E. Siegman, “Lasers”, Sausalito: University Science Books (1986).
25. W.T. Silfvast, “Laser fundamentals. 2nd ed.”, Cambridge: Cambridge University Press (2004).
26. J. Lim, “All-fiber frequency comb employing a single walled carbon nanotube saturable absorber for optical frequency metrology in near infrared”, PhD Thesis, Kansas State University (2011).
27. G. R. Jacobovitzveselka, U. Keller, and M. T. Asom, “Broad-band fast semiconductor saturable absorber”, Optics Letters **17**, 1791-1793 (1992).
28. E. P. Ippen, C. V. Shank, and A. Dienes, “Passive mode-locking of CW dye laser”, Applied Physics Letters **21**, 348 (1972).
29. M. Nakazawa, E. Yoshida, and Y. Kimura, “Low threshold, 290-fs erbium-doped fiber laser with a nonlinear amplifying loop mirror pumped by InGaAsP laser-diodes”, Applied Physics Letters **59**, 2073-2075 (1991).
30. S. Namiki, E. P. Ippen, H. A. Haus, and K. Tamura, “Relaxation oscillation behavior in polarization additive pulse mode-locked fiber ring lasers”, Applied Physics Letters **69**, 3969-3971 (1996).
31. K. Tamura, H. A. Haus, and E. P. Ippen, “Self-starting additive pulse mode-locked erbium fiber ring laser”, Electronics Letters **28**, 2226-2228 (1992).

32. M. L. Dennis and I. N. Duling, "High repetition rate figure eight laser with extracavity feedback", Electronics Letters **28**, 1894-1896 (1992).
33. K. Tamura, C.R. Doerr, L.E. Nelson, H.A. Haus, and E.P. Ippen, "Technique for obtaining high-energy ultrashort pulses from an additive-pulse mode-locked erbium-doped fiber ring laser", Optics Letters **19**, 46-48 (1994).
34. L. E. Nelson, D. J. Jones, K. Tamura, H. A. Haus, and E. P. Ippen, "Ultrashort-pulse fiber ring lasers", Applied Physics B-Lasers and Optics **65**, 277-294 (1997).
35. M. E. Fermann and I. Hartl, "Ultrafast fiber laser technology", IEEE Journal of Selected Topics in Quantum Electronics **15**, 191-206 (2009).
36. G. P. Agrawal, "Nonlinear fiber optics, 4th ed.", New York: Academic Press (2006).
37. R. L. Fork, O. E. Martinez, and J. P. Gordon, "Negative dispersion using pairs of prisms", Optics Letters **9**, 150-152 (1984).
38. R. Szipocs, K. Ferencz, C. Spielmann, and F. Krausz, "Chirped multilayer coatings for broad-band dispersion control in femtosecond lasers", Optics Letters **19**, 201-203 (1994).
39. K. O. Hill, Y. Fujii, D. C. Johnson, and B. S. Kawasaki, "Photosensitivity in optical fiber waveguides - application to reflection filter fabrication", Applied Physics Letters **32**, 647-649 (1978).
40. K. Tamura, E. P. Ippen, H. A. Haus, and L. E. Nelson, "77-fs pulse generation from a stretched-pulse mode-locked all-fiber ring laser", Optics Letters **18**, 1080-1082 (1993).
41. R. F. Cregan, B. J. Mangan, J. C. Knight, T. A. Birks, P. S. Russell, P. J. Roberts, and D. C. Allan, "Single-mode photonic band gap guidance of light in air", Science **285**, 1537-1539 (1999).
42. J. C. Knight, T. A. Birks, P. S. Russell, and D. M. Atkin, "All-silica single-mode optical fiber with photonic crystal cladding", Optics Letters **21**, 1547-1549 (1996).
43. S. M. Kelly, "Characteristics sideband of periodically amplifiers average soliton", Electronics Letters **28**, (1992).
44. M. L. Dennis and I. N. Duling, "Experimentally study of sideband generation in femtosecond fiber laser", IEEE Journal of Quantum Electron **30**, (1994).
45. E. G. Shapiro and S. K. Turitsyn, "Theory of guiding-center breathing soliton propagation in optical communication systems with strong dispersion management", Optics Letters **22**, 1544-1546 (1997).
46. M. E. Fermann, K. Sugden, and I Bennion, "Generation of 10 nJ picosecond pulses from a modelocked fiber laser", Electronics Letters **31**, 194-195 (1995).
47. H. A. Haus, E. P. Ippen, and K. Tamura, "Additive-pulse modelocking in fiber lasers", IEEE Journal of Quantum Electronics **30**, 200-208 (1994).
48. H. A. Haus, K. Tamura, L. E. Nelson, and E. P. Ippen, "Structure-pulse additive pulse mode-locking in fiber ring laser: Theory and experiment", IEEE Journal of Quantum Electrononics **31**, (1995).

49. K. Tamura, E. P. Ippen, and H. A. Haus, "Pulse dynamics in stretched-pulse fiber lasers", Applied Physics Letters **67**, 158-160 (1995).
50. D. J. Kuizenga and A. E. Siegman, "FM and AM mode locking of homogeneous laser - Part 1. Theory", IEEE Journal of Quantum Electronics **6**, 694 (1970).
51. H. J. R. Dutton, "Understanding optical communications", Upper Saddle River: Prentice Hall PTR (1998).
52. E. Hecht, "Optics", San Francisco: Addison Wesley (2002).
53. F. T. S. Yu and X. Yang, "Introduction to optical engineering", Cambridge: Cambridge Academic Press (1997).
54. D. T. Reid, W. Sibbett, J. M. Dudley, L. P. Barry, B. Thomsen, and J. D. Harvey, "Commercial semiconductor devices for two photon absorption autocorrelation of ultrashort pulses", Applied Optics **37**, 8142-8144 (1998).
55. J. C. M. Diels, J. J. Fontaine, I. C. McMichael, and F. Simoni, "Control and measurement of ultrafast pulse shapes (in amplitude and phase) with femtosecond accuracy", Applied Optics **24**, 1270-1282 (1985).
56. P. M. W. French, "The generation of ultrashort laser pulses", Reports on Progress in Physics **58**, 169-262 (1995).

Chapter 5. High-resolution sub-surface microscopy of CMOS integrated circuits using radially polarised light

5.1 Introduction

The ever-diminishing feature sizes in complementary metal-oxide semiconductor (CMOS) ICs [1] demand continuous innovation so that the resolutions provided by optical sub-surface navigation, imaging, probing and fault localisation techniques remain useful. In combination with SIL imaging [2], nonlinear optical techniques including TOBIC microscopy [3-5] and 2pLADA [6, 7] have been shown to provide the best imaging and localisation resolutions to date. This performance can be attributed to the intrinsically high-NA provided by silicon SILs, along with the nonlinear character of the image-bearing signal, which reduces the effective focal spot radius by a factor of $\sqrt{2}$ [8] and eliminates resolution-degrading contributions to the image from carriers generated outside the focal region.

Pupil-function engineering, in which the spatial distribution of the intensity, phase and polarisation of the beam entering the microscope objective are manipulated, has considerable potential for further improving the performance of high-resolution microscopes. Various techniques like annular apertures [9] and polarisation control [10] have been shown to improve the available resolution. Cylindrical vector (CV) beams are particularly promising [11] because they possess unique properties in the vicinity of the focal spot that provide advantages over the conventionally-employed linearly and circularly polarised light [12]. In particular, the rapidly growing number of papers featuring some aspect of radial polarisation, with annual citations growing even faster, proves the high degree of interest in radial polarisation. Beams possessing spatially-varying polarisation properties have been shown to be useful in a wide range of applications including: particle trapping [13], laser machining [14], lithography [15], optical data storage [16] and microscopy [17]. It has been shown both theoretically and experimentally that a radially polarised beam, a type of CV beam, can be focused to a tighter spot in high-NA imaging systems [12], in principle yielding performance better than that from any other polarisation-structured beam.

One of the challenges of practically deploying radial polarisation in an imaging system is the need to generate a radially polarised beam possessing a high degree of mode purity and vector symmetry. There are various ways to generate a high quality radially polarised beam, including phase-tailored fibre [18], direct generation from lasers containing a conical prism [19], polarising grating mirrors [20] and spatial light modulators [21]. In this chapter, I present a research using a novel twisted-nematic liquid-crystal radial polarisation converter (RPC) [22, 23], which has the advantages of low dispersion, static operation, high laser damage threshold and simple insertion

and removal within the imaging system. The experimental work presented in this chapter demonstrates that using radially polarised illumination achieves a sub-surface imaging resolution equivalent to the best resolution achieved with linearly polarised light. The obtained performance is among the highest resolutions achieved to date in sub-surface imaging, surpassed only by nonlinear imaging using annular illumination [9]. Not only do these results show that the radially polarisation is preserved under the high-NA conditions of an aplanatic SIL, but also that radially polarised light provides an optimisation of the system by eliminating the need to adjust the polarisation state of the light for individual feature orientations.

5.2 Scalar focusing theory

5.2.1 Scalar resolution limits

In Chapter 1 it was mentioned that resolving power of an optical system has a direct influence on the focal spot. An optical system creates the image of a point object in the focal plane, which is represented by its point spread function (PSF). Such two adjacent image points can be packed too tightly to be resolved as separate dots if their PSFs overlap too much. This resolving power is one of the main qualities of an imaging system, determining the minimum PSF (Airy pattern) it can obtain in the focal spot, which can be expressed by the following equation [24]:

$$d = 1.22 \frac{\lambda}{2n \cdot \sin\theta}, \tag{3.1}$$

where λ is the wavelength of light, n - the refractive index of the medium and θ – half the angle of the cone of light. Two point objects can be considered to only be resolved if the distance between their centres is at least the radius of the Airy disc, which is called Rayleigh criterion [25]:

$$\text{Resolving Power } = 0.61 \frac{\lambda}{NA}. \tag{3.2}$$

The Rayleigh criterion is typically used to determine the quality of imaging system. However, Sparrow argued that it is still possible to distinguish two point objects if they are closer than Rayleigh's criterion. According to Sparrow, two point sources can be resolved when the second derivative of the total distribution of illuminance in the diffraction image of the two points vanishes on-axis. This is called Sparrow's criterion and is given by the equation [26]:

$$\text{Resolving Power } = 0.47 \frac{\lambda}{NA}. \tag{3.3}$$

Confocal microscopy also provides axial sectioning, with the longitudinal resolution of [27]:

$$\text{Resolving Power (longitudinal)} = 0.44\frac{\lambda}{n\sin^2(\theta/2)}. \qquad (3.4)$$

Eq. (3.1-3.4) indicate that lateral resolution scales linearly with NA, while the longitudinal resolution depends approximately quadratically on the NA [27]. TPA further increases resolution by $\sqrt{2}$. Limits for 1550 nm wavelength nonlinear SIL microscopy is depicted in Fig. 3.1.

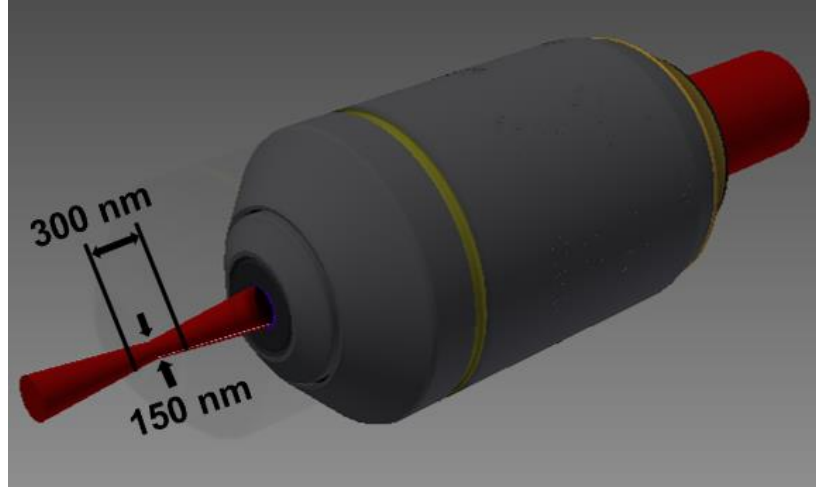

Figure 3.1. Light beam focusing and resolution limits using 1550 nm wavelength light.

The previously introduced resolution limits are determined by the profile of Airy disk, which is a result of the diffraction after a circular aperture. This diffraction is described by the Fresnel-Kirchhoff scalar diffraction theory, which neglects the vectorial nature of light. High-NA imaging conditions introduce new phenomena depending on light polarisation. Here, I first introduce the scalar description before extending this with a discussion of vectorial theory.

5.2.2 Scalar beams

In order to investigate the focusing of vectorial focusing conditions of electromagnetic waves it is first convenient to consider the scalar wave theory [28]. Wave vector equations can be written in the scalar Helmholtz equation form:

$$(\nabla^2 + k^2)E = 0, \qquad (3.5)$$

where E is the magnitude of the scalar electrical field, $k = 2\pi/\lambda$ is the wave number. Solutions of the paraxial Helmholtz equation provides beam modes with spatially homogeneous states of polarisation [29]. The solution in Cartesian coordinates (x, y, z) provides Hermite-Gaussian beams and the solution in cylindrical coordinates (r, φ, z) yields Laguerre-Gaussian beams [30].

This general solution for the electric field of the paraxial beam in Cartesian coordinates can be written as:

$$E(x, y, z, t) = A(x, u, z)\exp[\mathrm{i}(kz\text{-}\omega t)], \tag{3.6}$$

here z is the axial direction of light's propagation, ω is the frequency and t is time. It can be assumed that the envelope's u change is much larger in a scale of length than its wavelength and the second derivative can be neglected [31]. This is called the slowly varying envelope approximation, which in combination with the separation of the variables in *x* and *y* provides with the set of Hermite-Gaussian solutions (Fig. 3.2):

$$A(x, y, z) = E_0 H_m\left(\sqrt{2}\frac{x}{w(z)}\right) H_n\left(\sqrt{2}\frac{y}{w(z)}\right)\frac{w_0}{w(z)} \cdot$$

$$\cdot\ exp[-i\Phi_{mn}(z)]\ exp\left(i\frac{k}{2q(z)}r^2\right), \tag{3.7}$$

where $H_m\left(\sqrt{2}\frac{x}{w(z)}\right)$ is the m-th order Hermite polynomial, w_0 is the beam waist, $w(z)$ is the beam size at a distance z from the beam waist, Φ_{mn} is the Gouy phase shift, z_0 is the Rayleigh range, $q(z)$ is the complex beam parameter and $r = \sqrt{x^2 + y^2}$.

When the parameters are $m = n = 0$, the Gaussian beam solution is obtained [30]:

$$A(r, z) = E_0\frac{w_0}{w(z)}\ exp[-i\Phi_{00}(z)]\ exp\left(i\frac{k}{2q(z)}r^2\right). \tag{3.8}$$

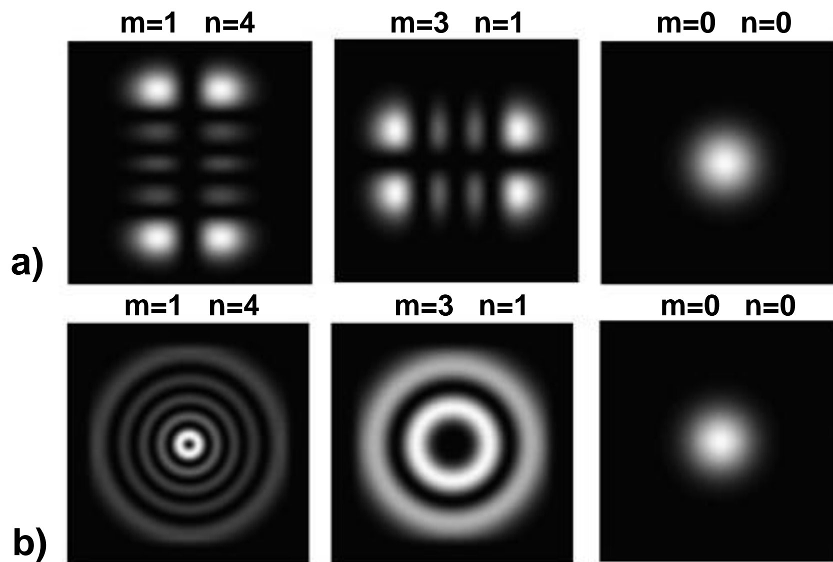

Figure 3.2. Intensity profiles of the (a) Hermite-Gaussian beams and (b) the Laguerre-Gaussian beams, which depend on the parameters m and n (columns). When these parameters $m = n = 0$, the fundamental mode (the Gaussian beam) is obtained (last column) [11].

It can be demonstrated that in cylindrical the Helmholtz equation solution is Laguerre-Gaussian beams (Fig. 3.2) [30]:

$$A(r,z) = E_0 \frac{w_0}{w(z)} exp[-i\Phi(z)]\, exp\left(i\frac{k}{2q(z)}r^2\right)\cdot$$

$$\cdot J_0\left(\frac{\beta r}{1+iz/z_0}\right)\exp\left(-\frac{\beta^2 z/2k}{1+iz/z_0}\right), \quad (3.9)$$

where J_0 is the zeroth-order Bessel function of the first kind, and β is a constant scale parameter.

5.2.3 Scalar PSF

A high-NA imaging system in the scalar diffraction case can be studied using the imaging configuration shown in Fig. 3.3. This case assumes focusing through a lens, which is characterised by an amplitude transmittance $A(r)$ and phase function $\Phi(r)$. It was demonstrated that focusing under scalar approximation can be expressed via an optical field at the observation plane, which provides the PSF of the optical system [24]:

$$E(\eta) = 2\int_0^1 A(r) exp[i\Phi(r)] J_0(\eta r) r dr\,, \quad (3.10)$$

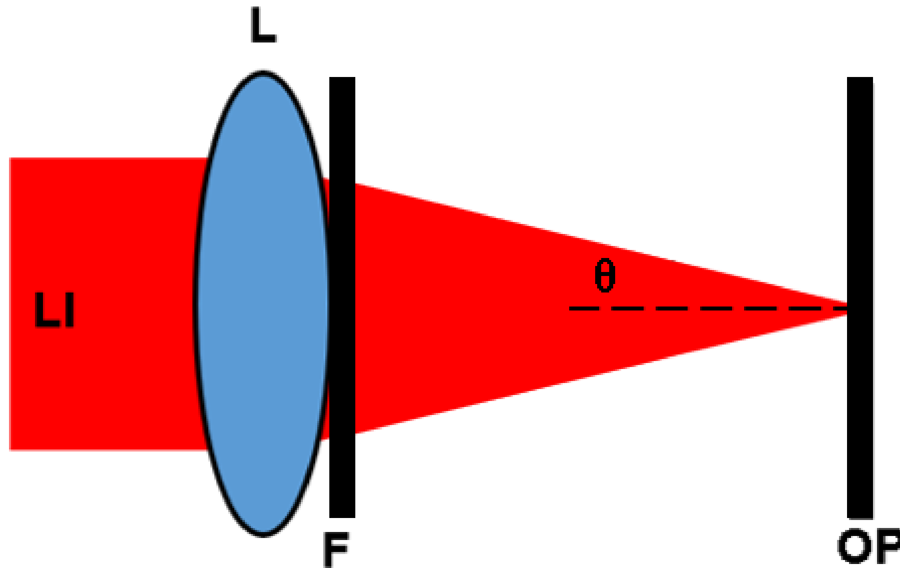

Figure 3.3. Imaging system, where a lens (L) is used to focus laser illumination (LI) on an observation plane (OP) with the cone angle θ and the F is filter to modulate an aperture of the lens.

The dimensionless coordinate η describes the PSF at the observation plane in a way normalised to NA and wavelength [29]:

$$\eta = \frac{\pi D \rho}{\lambda f} = \frac{2\pi \rho NA}{\lambda}, \tag{3.11}$$

where ρ is the radial coordinate at the observation plane, D is the lens diameter, f is the lens focal distance. After normalisation the PSF function is obtained in the following form [32]:

$$E(\eta) = 2\int_0^1 A(r) exp\left[\frac{iu(z)r^2}{2}\right] rdr\,, \tag{3.12}$$

where

$$u(z) = 4kzsin^2\left(\frac{a}{2}\right) = \frac{8\pi}{\lambda} sin^2\left(\frac{a}{2}\right). \tag{3.13}$$

5.3 Vectorial focusing theory

CV beams have recently gained much attention due to their interesting properties and advantages over the conventional linearly and circularly polarised beams. It was shown both theoretically and experimentally, that the radially polarised (RP) beam, a type of the CV beam, can be focused to a tighter spot [12]. This effect is observed due to the strong and localised longitudinal field component, which exists in the focal plane. Here, I present an introduction to the vectorial description of such beams.

5.3.1 Cylindrical vector beams

As it was shown in previous section, the scalar Helmholtz equation is an approximation, which can be applied to explain the propagation of linear monochromatic waves. However, the scalar theory is no longer valid for the light propagating through very small apertures, waveguides and it also ignores polarisation. Therefore, when an optical system benefits from high-NA the scalar Helmholtz equation cannot provide accurate solutions, as polarisation effects become dominant. The light propagation under these conditions requires to be examined as a whole electric field via the vector Helmholtz equation [33]:

$$\nabla \times \nabla \times \vec{E} - k^2 \vec{E} = 0, \tag{3.14}$$

where $k = \omega / c$. Then a circularly symmetric and azimuthally polarised electric field should take the form:

$$\vec{E}(r,z) = U(r,z)exp[i(kz - wt)]\vec{e}_{\phi}, \quad (3.15)$$

where $\vec{e}_{\phi}$ is a unit vector in the azimuth direction. After inserting Eq. (3.15) in to Eq. (3.14) and assuming the paraxial approximation, the scalar equation is obtained:

$$\frac{1}{r}\frac{\partial}{\partial r}\left(r\frac{\partial U}{\partial r}\right) - \frac{U}{r^2} + 2ik\frac{\partial U}{\partial z} = 0. \quad (3.16)$$

This equation for azimuthal symmetry has the solution:

$$U(r,z) = E_0 J_1\left(\frac{\beta r}{1 + i\,z/z_0}\right)u(r,z)Q(z), \quad (3.17)$$

where E_0 is a constant electric field amplitude, β is a constant scale parameter, $u(r,z)$ is elementary Gaussian solution, z_0 is the Rayleigh range and J_1 is the first-order Bessel function of the first kind and

$$Q(z) = exp\left[-\frac{i\beta^2\,z/(2k)}{1 + i\,z/z_0}\right]. \quad (3.18)$$

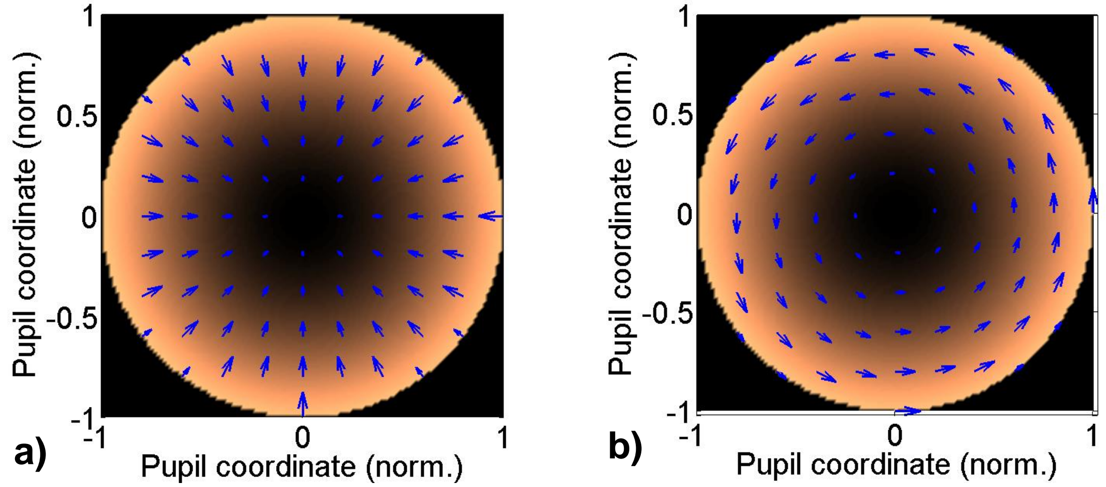

Figure 3.4. Spatial distribution of CV beams: (a) radially polarised mode; (b) azimuthally polarised mode. Arrows indicate the direction of electric field.

This solution corresponds to an azimuthally polarised vector Bessel-Gaussian beam solution. The transverse magnetic field $\vec{H}$ is also the solution of Eq. (3.14):

$$\vec{H}(r,z) = -H_0 J_1\left(\frac{\beta r}{1 + i\,z/z_0}\right)\,\exp\left[-\frac{i\beta^2\,z/(2k)}{1 + i\,z/z_0}\right]\,\exp[i(kz - wt)]\vec{h}_{\phi}\,, \quad (3.19)$$

where H_0 is a constant magnetic field amplitude and $\vec{h}_{\phi}$ is the unit vector aligned azimuthally. This magnetic field solution has the corresponding electric field, which is set in the transverse plane and pointing in the radial direction. These solutions display complete rotational symmetry

about the direction of propagation, while for the linearly polarised Gaussian beam only the magnitude of the field exhibits rotational symmetry. The field illustrated in Fig. 3.4a has its polarisation aligned in the radial direction, which is called the radial polarisation. Similarly, the polarisation pattern shown in Fig. 3.4b is called the azimuthal polarisation. The linear superpositions of these two beams result in the generalised CV beams and they can be decomposed into a superposition of orthogonally polarised Hermite-Gaussian modes, as shown in Fig. 3.5. Due to the transverse field continuity, these CV modes feature the existence of a characteristic null point of the transverse field at the centre of the beam profile [30].

The RP beam under the paraxial conditions can be represented by a combination of two orthogonally polarised Hermite-Gauss modes HG_{01} and HG_{10} [34]:

$$RPB = HG_{10}\vec{n}_z + HG_{10}\vec{n}_y, \tag{3.20}$$

$$APB = -HG_{01}\vec{n}_z + HG_{01}\vec{n}_y, \tag{3.21}$$

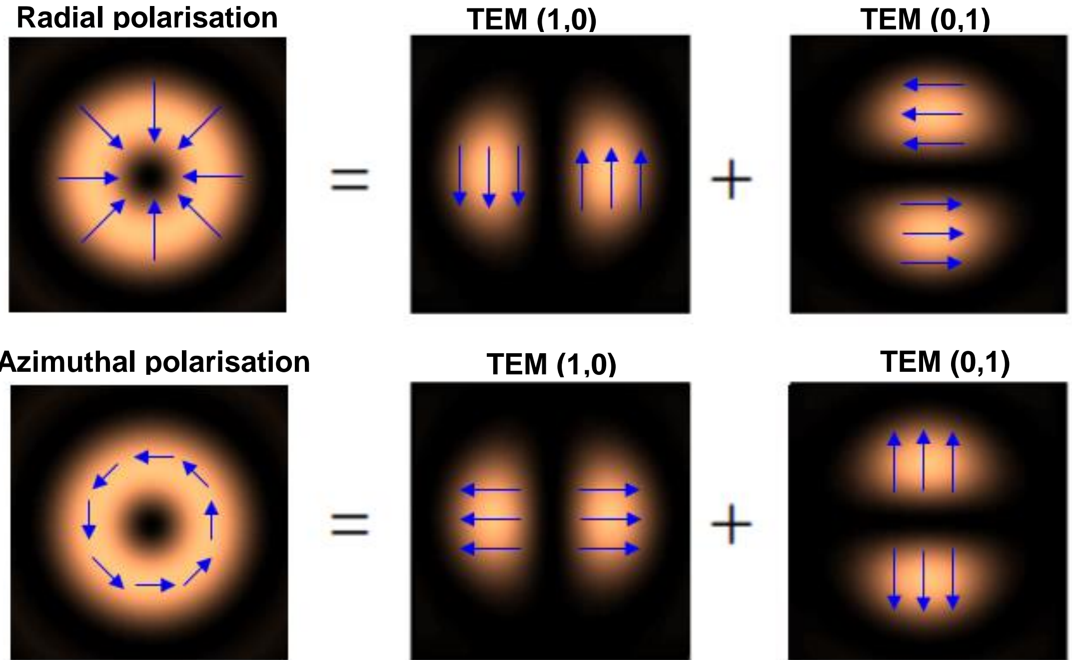

Figure 3.5. CV beams as a superposition of orthogonally polarised (1,0) and (0,1) Hermite-Gaussian modes (adapted from [11]). Top row is radially polarised beam and bottom row is azimuthally polarised beam.

5.3.2 Focusing properties of CV beams

Dipole radiation offers a simple explanation to the tight focusing of the RP beam under high-NA conditions. For this case, a vertically oscillating electric dipole can be assumed to exist at the focal point of the high-NA aplanatic objective lens, which collects and then collimates the dipole's radiation. It is seen from Fig. 3.6 that the polarisation at the lens pupil is perpendicular to the optical axis. Therefore, the reversed system with initial radial polarisation at the pupil plane should recover the vertical dipole radiation in the focal field, thus providing a very tight focus [30].

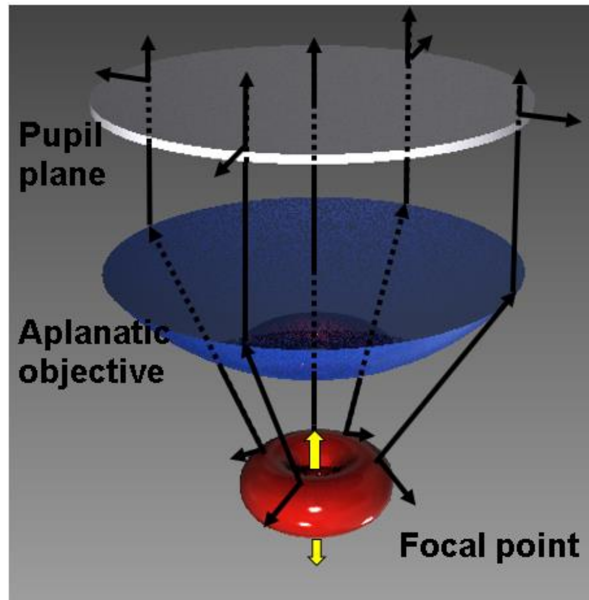

Figure 3.6. Vertically oscillating electric dipole under the high-NA objective lens (adapted from [11]).

The Richards-Wolf vectorial diffraction analysis can be applied to investigate properties and dynamics of the focusing CV beams [24]. The schematic to analyse the introduced problem is depicted in Fig. 3.7. Here the incident CV beam may have any spatial distribution and is assumed to have a planar wavefront at the pupil position. An aplanatic lens produces a spherical wave converging to the focal point [35].

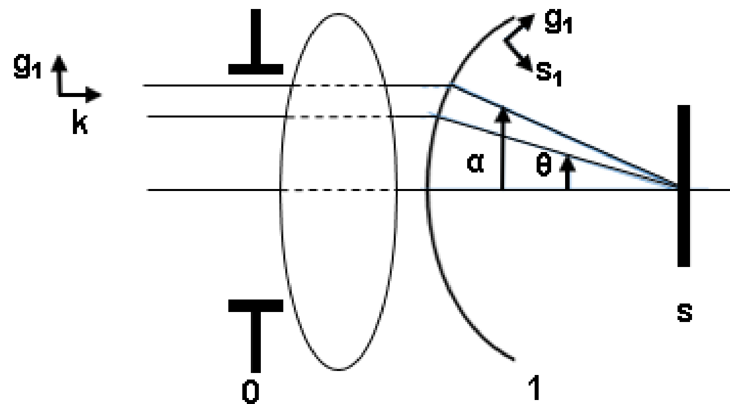

Figure 3.7. Schematic of the high-NA optical system to explain the RP beam focusing properties and dynamics (adapted from [11]).

The initial polarisation is defined in cylindrical coordinates (ρ, φ, z) and directed perpendicularly to the optical axis. Thus, the incident field can be written:

$$\vec{E}(\rho, \phi) = l_0\, P(\rho)\left[\cos\varphi_0\, \vec{e}_\rho + \sin\varphi_0\, \vec{e}_\phi\right], \tag{3.22}$$

l_0 is the peak field amplitude at the pupil plane and $P(\rho)$ is the axially symmetric pupil plane amplitude function, which is normalised to l_0, $\vec{e}_x$ and $\vec{e}_y$ are the unit vectors:

$$\vec{e}(\varrho) = \cos\varphi\, \vec{e}_x + sin\varphi\, \vec{e}_y, \tag{3.23}$$

$$\vec{e}(\phi) = -sin\varphi\, \vec{e}_x + cos\varphi\, \vec{e}_y. \tag{3.24}$$

Amplitude distribution over the pupil is transferred on the spherical wavefront by the ray projection function:

$$\rho/f = g(\theta), \tag{3.25}$$

where f is the focal length of the lens. After refraction the polarisations are altered to:

$$\vec{e}_r = \cos\theta\big(\cos\varphi\, \vec{e}_x + \sin\varphi\, \vec{e}_y\big) + \sin\theta\, \vec{e}_z\,, \tag{3.26}$$

$$\vec{e}_\varphi = -\sin\varphi\, \vec{e}_x + \cos\varphi\, \vec{e}_y\,. \tag{3.27}$$

As stated by Richards-Wolf, the electric field close to the focus is described by the diffraction integral over the vector field on the spherical wavefront with the radius equal to the objective lens focal length:

$$\vec{E}(r,\phi,z) = \frac{-ik}{2\pi}\iint_\Omega \vec{a}(\theta,\varphi)e^{ik(\vec{s}\cdot\vec{r})}d\Omega = \frac{-ik}{2\pi}\int_0^{\theta_{max}} d\theta \int_0^{2\pi} \vec{a}(\theta,\varphi)\, e^{ik(\vec{s}\cdot\vec{r})}\sin\theta \mathrm{d}\varphi, \tag{3.28}$$

here θ_{max} is the angle of the cone of light, k is the wavenumber and the field strength $\vec{a}(\theta,\varphi)$ is

$$\vec{a}(\theta,\varphi) = l_0 f P(\theta)\big[\cos\varphi_0\, \vec{e}_r + \sin\varphi_0\, \vec{e}_\varphi\big]. \tag{3.29}$$

The field has to be transformed from the Cartesian coordinates to cylindrical coordinates and the following equation is obtained:

$$\vec{E}(r,\phi,z) = \frac{-iA}{\pi}\int_0^{\theta_{max}} \mathrm{d}\theta \int_0^{2\pi} P(\theta)\left[\cos\varphi_0\begin{pmatrix}\cos\theta\cos\varphi - \phi\vec{e}_r\\ 0\vec{e}_\phi\\ \sin\theta\vec{e}_z\end{pmatrix} + \sin\varphi_0\begin{pmatrix}\cos\theta\cos\varphi - \phi\vec{e}_r\\ \cos\varphi - \phi\vec{e}_\phi\\ 0\vec{e}_z\end{pmatrix}\right]\exp[ik(z\cos\theta$$

$$+r\sin\theta\cos(\varphi-\phi))]\sin\theta. \tag{3.30}$$

Finally, this expression can be simplified and generalised:

$$\vec{E}(r,\phi,z) = E_r\vec{e}_r + E_z\vec{e}_z + E_\phi\vec{e}_\phi\,, \tag{3.31}$$

here $\vec{e}_r, \vec{e}_z, \vec{e}_\varphi$ are the unit vector along the radial, longitudinal, and azimuthal directions [30].

$$\vec{E}_r(r,\phi,z) = 2A\sin\varphi_0 \int_0^{\theta_{max}} P(\theta)\sin\theta\cos\theta\, J_1(kr\sin\theta)e^{ikz\cos\theta}\mathrm{d}\theta\,, \tag{3.32}$$

$$E_z(r,\phi,z) = i2A\sin\varphi_0 \int_0^{\theta_{max}} P(\theta)\sin^2\theta\, J_0(kr\sin\theta)e^{ikz\cos\theta}\mathrm{d}\theta\,, \tag{3.33}$$

$$E_\varphi(r,\phi,z) = 2A\sin\varphi_0 \int_0^{\theta_{max}} P(\theta)\sin\theta\, J_1(kr\sin\theta)e^{ikz\cos\theta}\mathrm{d}\theta\,. \tag{3.34}$$

Such CV beams benefit from rotational symmetrical intensity profile in the focal spot region (Fig. 3.8).

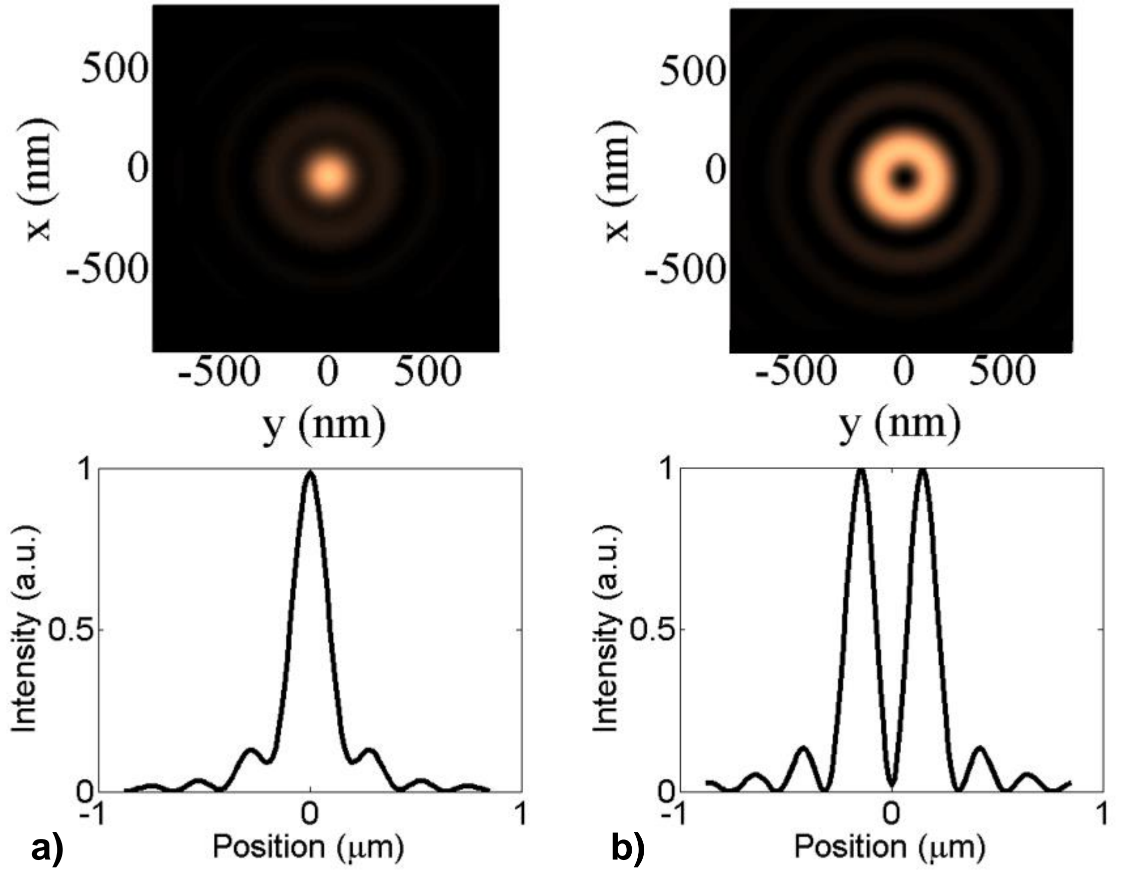

Figure 3.8. Spatial distribution (1D and 2D) of CV beams under high-NA (3.48) focusing conditions: (a) radially polarised mode; (b) azimuthally polarised mode. Radially polarised beam focuses to 190 nm and azimuthally polarised beam focuses to 440 nm focal spot at FWHM level.

Even though the RP beam demonstrates a high resolution under the conditions of certain annular apertures and high NA, it was shown that radially polarised light is not always superior over another polarisations [36, 37]. When a radially polarised beam is focused, the electric field in the focal plane consists of the radial and longitudinal components. The longitudinal component of the RP beam depends on the angle of the cone of light and increases with the NA. Due to constructive interference it has a high intensity and is concentrated within a small spot (Fig. 3.9b). On the contrary, for a linear polarisation the longitudinal component is cancelled at the focal plane on the optical axis. It appears as two lobes, which are oriented symmetrically along the axis (Fig. 3.9a). Therefore, for the lower NA case (<~0.7) when the longitudinal component is dominant, the linearly polarised (LP) beam has the tighter spot size. However, if a high-NA objective lens is used, the RP beam's spot size diminishes (Fig. 3.10) [36].

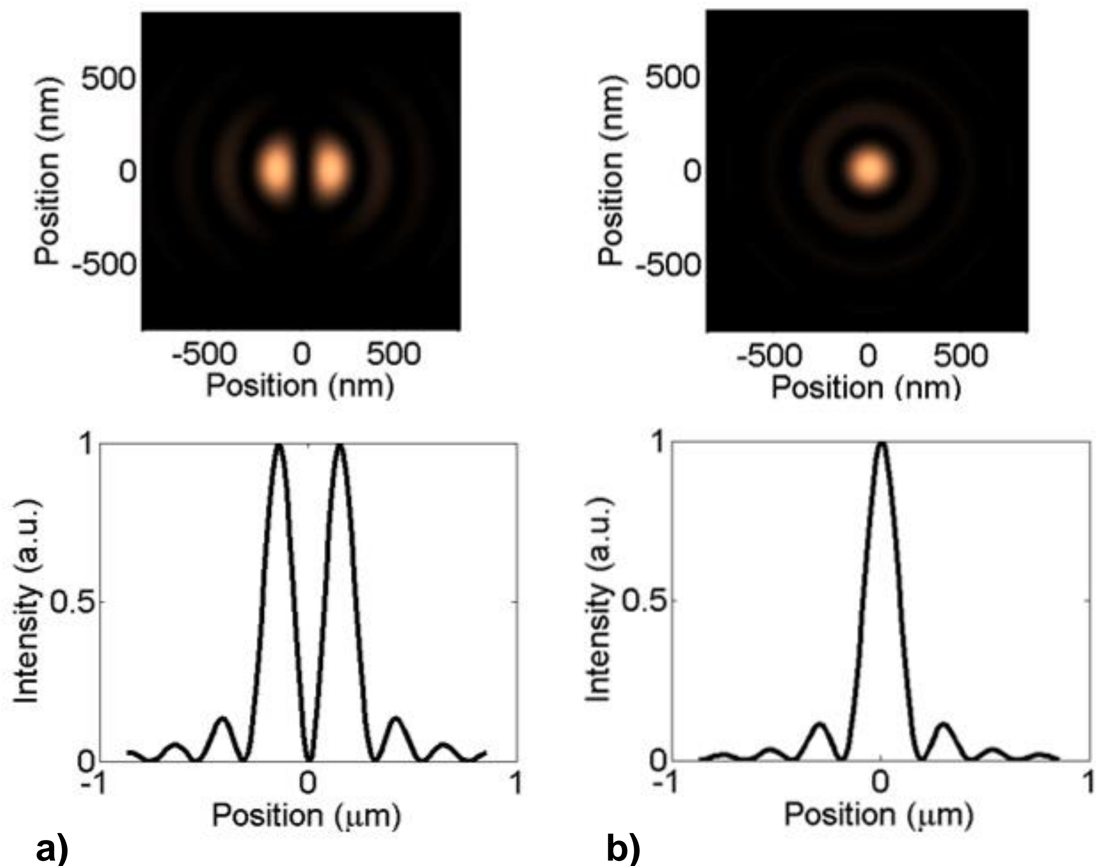

Figure 3.9. Spatial distribution (1D and 2D) of longitudinal component under high-NA (3.48) focusing conditions: (a) linear polarisation; (b) radial polarisation. The longitudinal component of radially polarised beam is concentrated in the middle while linearly polarised beam exhibits distribution of two lobes.

Moreover, Ünlü *et al* have recently shown that RP beams can have certain disadvantages. They investigated the influence of imperfect vector symmetry of RP beam on the spatial resolution. It is assumed that as the RP beam is guided through the microscope setup, it acquires a phase and amplitude term at every optical component. Therefore, the relation between Hermite-Gauss modes, which comprise the RP beam, is changed to:

$$RP_m = HG_{10}\vec{n}_x + ae^{ik\phi}HG_{10}\vec{n}_y, \tag{3.35}$$

here a and ϕ denote the cumulative relative amplitude factor and phase retardance between Hermite-Gauss modes.

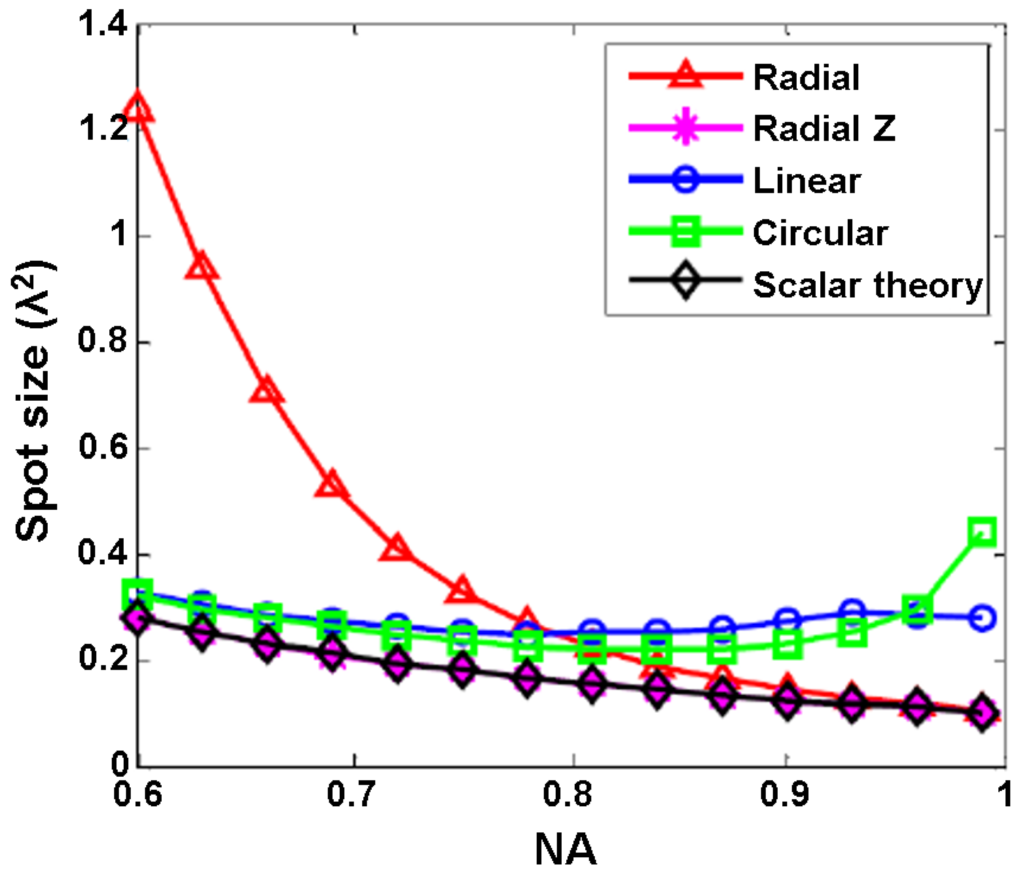

Figure 3.10. The spot size and NA relation for radially (triangles), linearly (circles) and circularly (rectangles) polarised beams. The longitudinal component of the radial polarisation (stars) and results from scalar theory (diamonds) are shown as well [36].

After investigation of the focusing characteristics, it was shown that the phase retardance affects the intensity of the longitudinal component significantly. Therefore, the lower resolution transverse component contributes more to the spot size. Additionally, the shape of both components is altered deforming the focal spot geometry and degrading the spatial resolution significantly. The outcome of the theoretical computation was confirmed by experimental results. It was noticed that Hermite-Gauss modes are retarded by ~0.3λ and as a result the intensity profile

was rotated 90° in comparison to the initial beam. In order to compensate the retardance, a spatial light modulator (SLM) was implemented into the microscope setup. The angle was fully compensated and the resolution significantly improved (Fig. 3.11) [38].

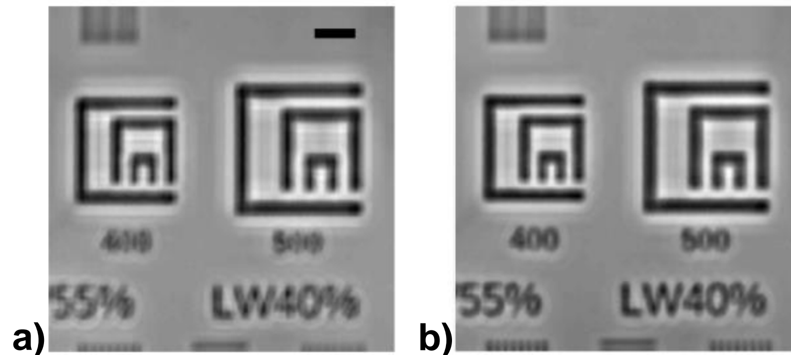

Figure 3.11. Laser scanning microscope image of aluminium structures on the silicon substrate. (a) No compensation applied. The scale bar shows a length of 2 μm. (b) After the phase retardance compensation [38].

5.3.3 Techniques to generate cylindrical vector beams

The peculiar properties of CV beams and their potential applications stimulated a rapid growth of this field. Numerous ways and techniques emerged to generate CV beams. Based on their working mechanisms, these techniques can be classified into active and passive approaches [30]. Typically, active techniques rely on the laser resonators to obtain the CV beams. In this case various intracavity devices are employed to tune the laser in such way, that it would be forced to oscillate in the desired CV modes [39]. Using this approach CV beams emanate directly from the laser output. Usually this approach leads to CV beams with fundamental polarisation mode and practical switching between the modes cannot be achieved. However, active generation can produce both free-space and waveguide mode CV beams. While confined in a metallic waveguide, waveguide mode CV beams benefit from high power [30].

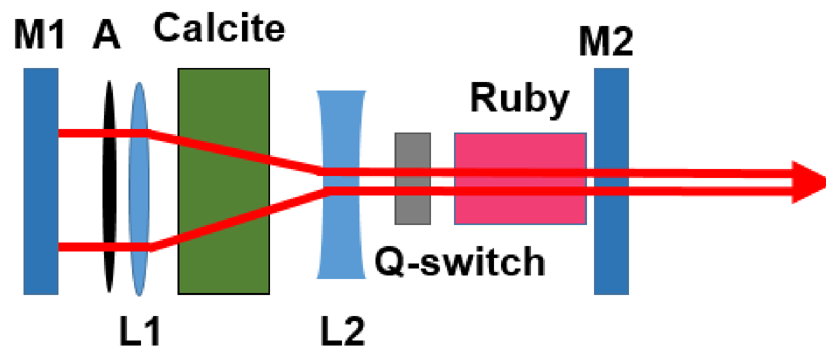

Figure 3.12. Laser-based scheme to generate fundamental mode CV beam using calcite and aperture with stop (adapted from [39]).

Intracavity devices can be axial birefringent components or axial dichroic components to provide a mode discrimination against the fundamental mode. Figure 3.12 shows an example of active CV beam generation, which employs an axial birefringent component [39]. In this setup, fundamental and higher-order modes are differentiated by the circular aperture and the stop. A calcite crystal is placed in a telescope setup with its crystal axis parallel to the optical axis of the cavity. Double refraction leads to the different divergence for ordinary and extraordinary polarisations. Therefore, the selected fundamental mode, either azimuthal or radial is differentiated, while one polarisation is discriminated more because of higher loss. As it is seen this system is capable of generating only a single fundamental mode [39].

Another approach is to create intracavity dichroism instead of birefringence. To generate CV beams in such a way one has to use a conical axicon [40] or Brewster angle reflectors [41, 42]. These techniques use bulk intracavity devices for creating axial birefringence or dichroism. However, recent advances in microfabrication have made it possible to design a fine diffractive phase plate or polarisation selective end mirror devices [43, 44] for CV beam generation. Compact design of the laser cavity makes it possible to optimise for the highest power throughput out of the laser. In addition to those methods CV beams can also be produced with intracavity interferometers while using folded mirrors or prisms designs. For example, by using a Sagnac interferometer setup linearly polarised HG_{01} modes are created by inserting a thin wire within the centre of the cavity. A dove prism aligns orthogonally polarised HG_{10} and HG_{01} modes, which combined create the CV output [45].

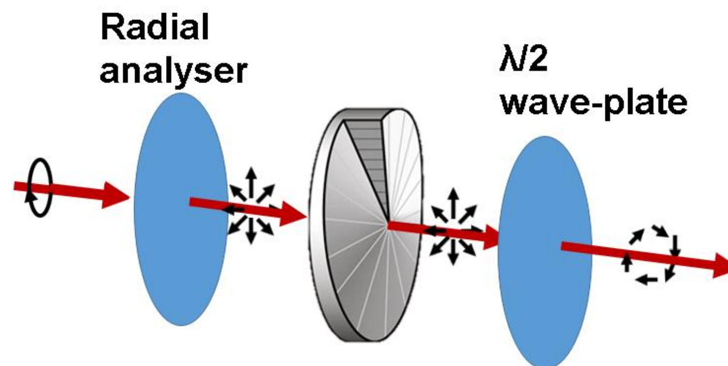

Figure 3.13. Generation of CV beam using radial analyser, SPE and HWP (adapted from [46]).

Also there are passive methods to generate the CV beams in free space. Typically, these methods use devices with spatially variant polarisation properties to convert homogeneous polarisations into CV beams. The same axial birefringence and dichroism techniques can be applied to generate a CV beam outside the laser cavity as well [30]. Simple setups can be arranged with a radial analyser device (Fig. 3.13). In this case, a circularly polarised collimated beam must be used as

the input to the radial analyser. The output from the analyser is either a radially or azimuthally polarised beam with a spiral phase factor on top of it. A spiral phase element (SPE) with the opposite helicity is used to compensate for the phase and obtain the CV beam. A HWP can be inserted to rotate polarisation to the desired pattern [46].

Spatially variant polarisation rotation can also be utilised to easily implement CV beams within the optical system. In this case, linearly polarised light is typically guided through the polarisation tailoring device. The initial linearly polarised beam experiences polarisation rotation for different segments of its profile leading to the generation of a desired spatial polarisation pattern. A twisted nematic liquid crystal (LC) device can be used to obtain radial or azimuthal polarisations. Such a LC polarisation converter was used in the experiments of this thesis and its principle of operation will be explained later [46, 47].

The LC SLM is another very popular and powerful technique to produce CV beams. The SLM offers the flexibility and potential to generate an almost arbitrary complex field distribution. An example to produce CV beams using the SLM is shown in Fig. 3.14 [48]. This setup employs two LC SLMs to generate complicated polarisation patterns of high purity. The first SLM is dedicated to correct the optical system aberrations by applying a phase modulation to the incident laser beam. The integration of the QWP with the second SLM essentially forms the actual polarisation rotator [48]. CV beams are generated and polarisation rotation is obtained by simply modulating the phase at each pixel on the SLM. A proper design of the phase pattern on the second SLM allows the input linear polarisation to be converted into any arbitrary polarisation distribution, including CV beams.

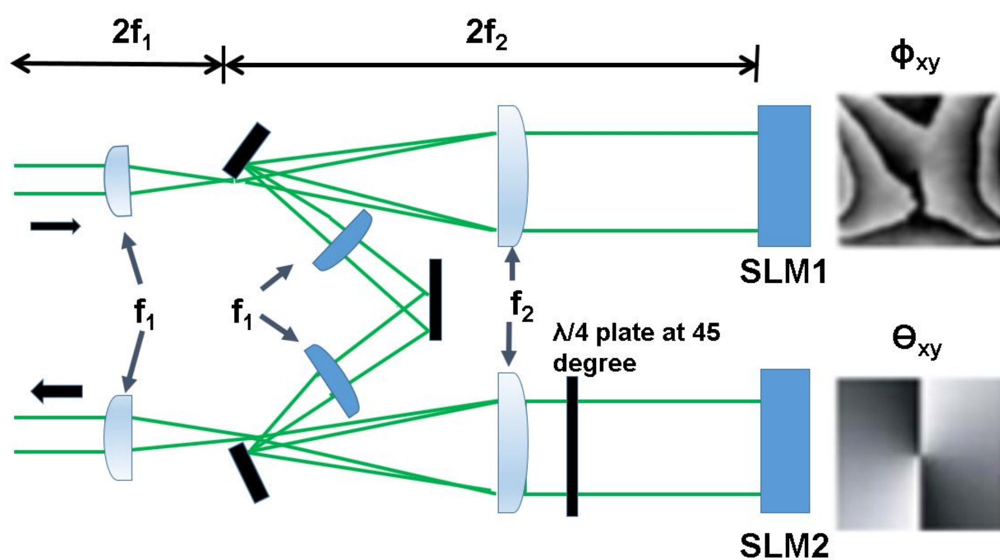

Figure 3.14. A polarisation mode converter setup with two SLMs (adapted from [48]).

Also, CV beams can be produced exploiting interference phenomenon. A Mach–Zehnder interferometer can be combined with a spiral phase plate [49] or a spiral phase created by a LC SLM [50] to generate CV beams and both approaches were able to produce various CV beams. A single path interferometer was also demonstrated to be capable to generate CV beams and other more complex vector beams (Fig. 3.15) [12, 51].

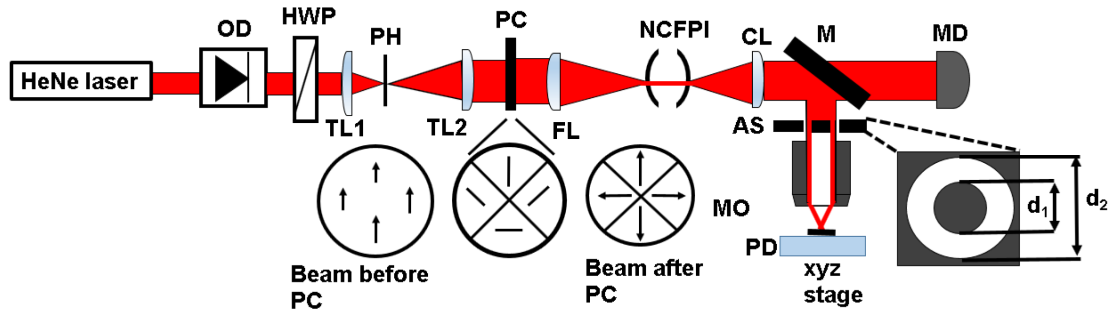

Figure 3.15. Experimental setup that uses a segmented λ/2 plates polarisation converter and a near-confocal Fabry–Perot interferometer (NCFPI) as a mode selector to generate CV beams. OD, optical diode; HWP, half-wave plate; PH, pinhole; TL1, TL2, telescope lenses; PC, polarisation converter; FL, focusing lens; CL, collimating lens; M, four mirrors; MD, monitor diode; AS, aperture stop; MO, microscope objective; PD, photodiode (adapted from [12]).

5.3.4 Pupil engineering

As it was shown in the previous sections, the optical field at focal plane depends on the amplitude and phase of the incident light. Therefore, it offers a possibility to tailor focal spot by manipulating the light before entering the pupil of the microscope objective. Over the years several super-resolution techniques exploiting amplitude engineering have been demonstrated: obscuration [52], annular apertures (Fig. 3.16) [53, 54] and continuous-amplitude filters [55-58]. Phase manipulation techniques are based on the diffractive optical element insertion within the optical system [59, 60]. Also best results can be achieved when both amplitude and phase are manipulated at the same time [61]. Here in this section some of the pupil engineering cases are discussed and the effect on the PSF is presented.

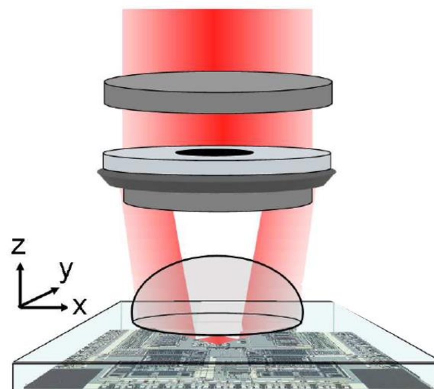

Figure 3.16. Example of pupil engineering in the SIL microscopy [9].

The PSF describes the two-dimensional distribution of light in the focal plane of an imaging system, which can be modified by using an annular aperture instead of a full opening [62]. This generates a Bessel like beam leading to the enhancement of the maximum amplitude of the PSF and the axial elongation of the PSF along the optical axis. These two effects depend on the dimensions of the annular aperture. Theory predicts that an infinitely narrow annular aperture produces a 30% narrower PSF than that of the same radius circular aperture. However, annular apertures generate side-lobes beside the main peak of the PSF, which are equal to 17% of the maximum of the main peak (Fig. 3.17). As a result, the net PSF for annular apertures is a larger PSF. However, for nonlinear microscopy annular apertures are still of interest since TPA, which depends on the square of the intensity of light, suppresses the side-lobes providing a significantly reduced PSF [63, 64].

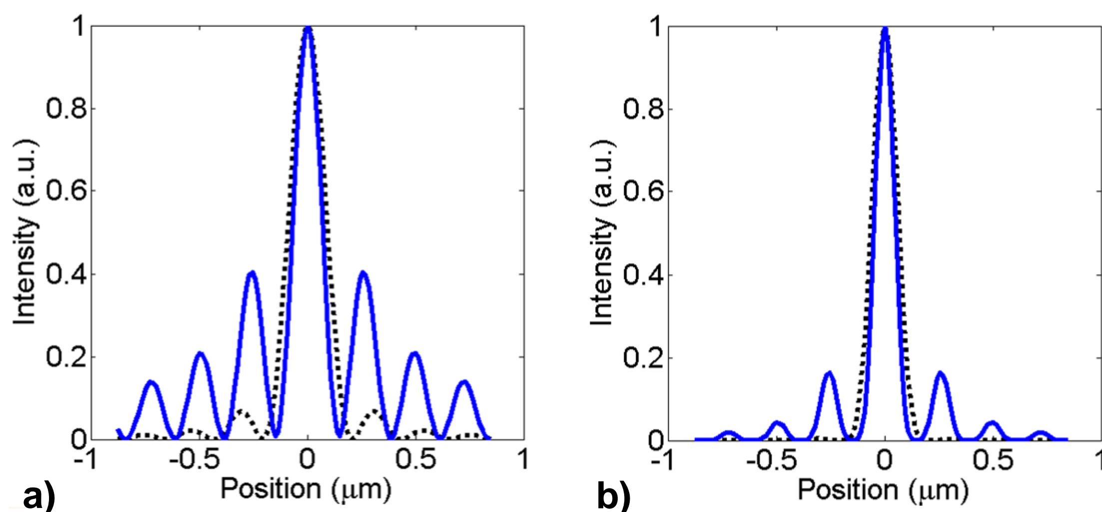

Figure 3.17. Narrowing of the PSF with suppression of the lower spatial frequencies at the expense of the side-lobe formation: (a) single photon case, (b) two-photon response. For conventional microscopy an annular aperture enhances resolution from 190 nm to 140 nm and for nonlinear case from 135 nm to 105 nm. A dashed line represents the intensity profile in the focal spot under high-NA (3.48) conditions without an annular aperture, while a blue solid line depicts the intensity distribution using a 90% annular aperture. Side-lobes have negligible effect for two-photon response.

By combining a SIL and an annular aperture, Serrels *et al* achieved an impressive 70 nm lateral super-resolution equal to 64% of the lateral resolution obtained with a circular aperture [9]. This pupil engineering technique can be further expanded by using it along with radially polarised beams.

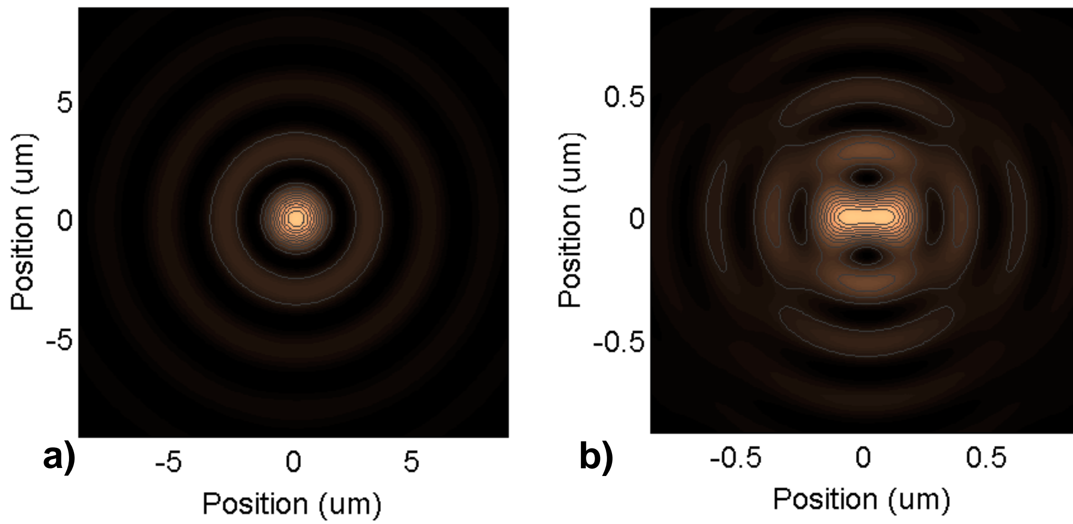

Figure 3.18. Comparison of linearly polarised light focal spots after the insertion of annular aperture for (a) scalar (NA=0.1) and (b) vectorial (NA=1) regimes.

In Fig. 3.18 the comparison between linear polarisation scalar and vectorial focusing cases is presented. For the vectorial focusing case a significant broadening occurs with stronger side-lobes showing a complicated pattern. Interesting effect happens for circularly polarised light. The use of the annular aperture suppresses the side-lobes but at the expense of the PSF broadening (Fig. 3.19).

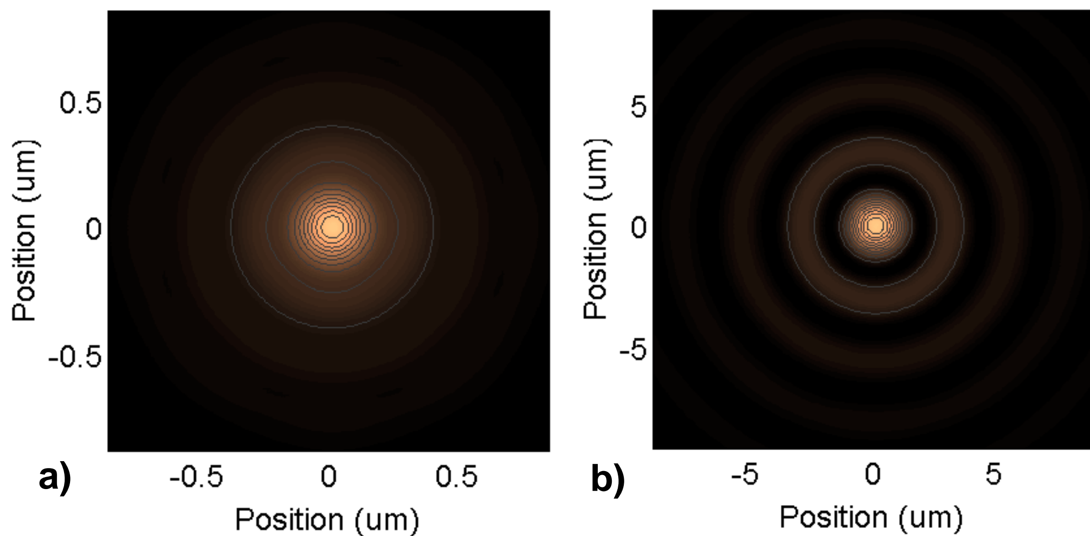

Figure 3.19. Comparison of circularly polarised light focal spots after the insertion of annular aperture for (a) scalar (NA=0.1) and (b) vectorial (NA=1) regimes.

The previously introduced radial polarisation effect can be enhanced with an annular aperture. It blocks the centre part of the beam, which is associated with the transverse component, thus increasing the resolution at the expense of decreasing efficiency. Insertion of the annulus reduces the PSF in exchange for the elongation of the longitudinal field component. Also even though

typically side-lobes are formed, their amplitude is lower compared with other polarisations (Fig. 3.20).

I would like to express gratitude for Prof. Derryck Reid for his help to prepare MATLAB code for the PSF modelling.

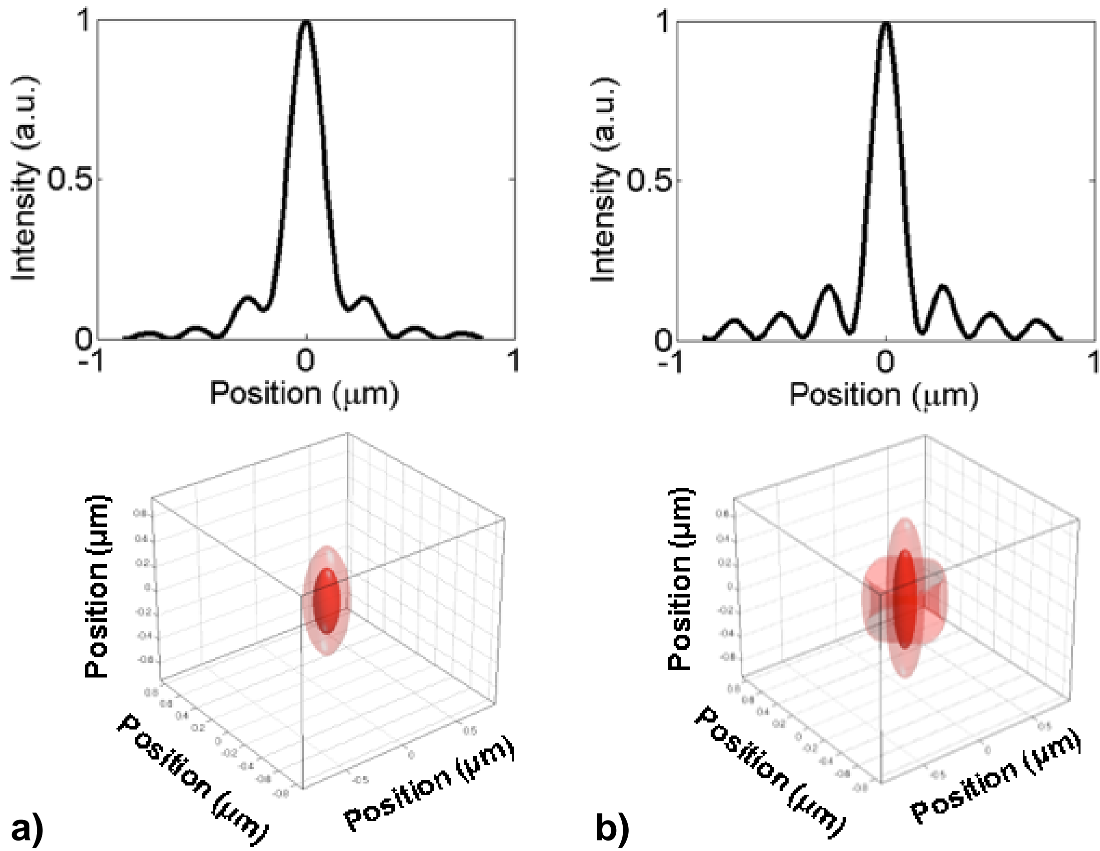

Figure 3.20. Comparison of radially polarised light under high-NA (3.48) focusing condition with (a) no annular aperture and (b) with annular aperture. Top images show 2D modelling of PSF, while bottom images portray 3D modelling results. Both 2D and 3D results indicate PSF narrowing with the expense of the PSF elongation and side-lobes generation. Therefore, annular apertures offer improvement only for 2D TPA imaging, when side-lobes are supressed due to absorption dependence on square of incident light intensity.

5.3.5 Assessing the polarisation purity of cylindrical vector beams

It was pointed earlier that the CV beams do not always have a perfect vector symmetry and modal purity. Therefore, before employing the CV beam in the laser setup it is necessary to assess the degree of polarisation of the generated CV beam. One of the easiest and fastest ways to measure the degree of polarisation is by using Stokes parameters. This set of parameters describe the polarised light [65] and will be further discussed in this section.

The electric vector $\vec{E}$ consists of two components:

$$E_x = a_1 \cos \mu t - \delta_1, \quad (3.36)$$

$$E_y = a_2 \cos \mu t - \delta_2, \quad (3.37)$$

where μ is frequency, t is time, a_1 and a_2 are the amplitudes along the *x* and *y* axes, δ_1 and δ_2 are the phase constants.

One can eliminate the term μt while introducing a phase difference δ to obtain the ellipse equation (Fig. 3.21):

$$\frac{E_x^2}{a_1^2}+\frac{E_y^2}{a_2^2}-\frac{E_xE_y}{a_1a_2}\cos\delta=\sin^2\delta\,. \tag{3.38}$$

If $\delta=m\pi/2$ and $a_1=a_2$, the circle equation is obtained, which means that the light is circularly polarised. If $\delta=m\pi$, then the ellipse is transformed into a straight line, which is the case for the linear polarisation.

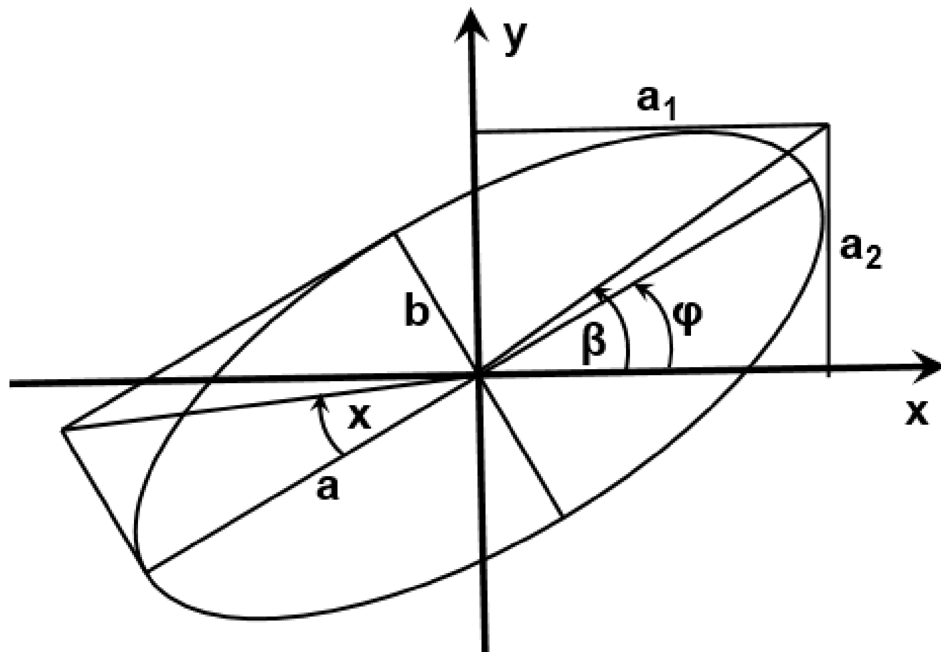

Figure 3.21. Polarisation ellipse, changing parameters lead to different polarisation states. Here is portrayed elliptically polarised light (adapted from [66]).

As it can be seen, any polarisation can be described using amplitudes a_1, a_2 and phases δ_1, δ_2. Therefore, they can provide parameters, which can be used to calculate polarisation. These parameters are called Stokes parameters and can be written as follows:

$$S_0=a_1^2+a_2^2, \tag{3.39}$$

$$S_1=a_1^2-a_2^2, \tag{3.40}$$

$$S_2=2a_1a_2\,cos\,\delta\,, \tag{3.41}$$

$$S_3=2a_1a_2\,sin\,\delta\,, \tag{3.42}$$

S_0 is proportional to the light intensity and is related to other parameters via equation:

$$S_0^2 \geq S_1^2 + S_2^2 + S_3^2. \quad (3.43)$$

If the Stokes parameters are known, then the degree of polarisation can be calculated by applying the following equation:

$$P = \frac{I_{\max} - I_{\min}}{I_{\max} + I_{\min}} = \frac{\sqrt{S_1^2 + S_2^2 + S_3^2}}{S_0}\ , \quad (3.44)$$

where $I_{\max}$ and $I_{\min}$ are the maximum and minimum intensity, respectively, measured behind the rotating analyser [66. 67].

As will be seen later, I have used a direct measurement of the Stokes parameters to assess the quality of preparation of a RP beam for use in TOBIC imaging experiments.

5.4 Implementation of radially polarised illumination for TOBIC microscopy

5.4.1 Microscope layout

To achieve the nonlinear phenomenon of two-photon absorption a laser beam of the high peak power must be employed. The highest peak powers can be achieved with the mode-locked lasers. Furthermore, TOBIC microscopy requires femtosecond laser illumination at a wavelength longer than the band-gap of silicon, which is ~1.05 μm. Therefore, a mode-locked Er:fibre laser was chosen to perform TOBIC microscopy using the experimental scheme illustrated in Fig. 3.22. Operating at 1550 nm, the laser generated 110 fs pulses with a repetition rate of 68 MHz and an average power of 70 mW. The outgoing beam from the laser was expanded and guided through the RPC (manufactured in the University of Rochester) and imaged with a reducing telescope onto the pupil of the microscope objective (Mitutoyo, NA 0.42, ×50) that served as the backing objective for a silicon aplanatic SIL (Doric lenses).

The microscope setup was configured so that the polarisation converting device could be easily implemented in the beam path. This requires expanding the diameter of the beam to cover a reasonable percentage of the LC device to obtain the best conversion to radially polarised light. The beam diameter after L1 was 3 mm, which was confirmed using a knife-edge beam profiling technique. After that the beam was expanded to a diameter of 18 mm by lenses L2 and L3. At this point the LC polarisation converter was added into the beam path before the beam diameter was reduced to 10 mm to slightly overfill the microscope objective. Both telescopes were constructed in a way that the beam profile after the LC device was imaged onto the pupil of the microscope objective (0.42 NA, magnification – ×50, width of entrance pupil – 9 mm, corrected for chromatic aberration from 0.48 μm to 1.8 μm). The beam was steered by gold and silver

mirrors, which offer maximum reflectivity for the 1.55 μm light. After the beam was guided through the objective lens it overfilled the SIL, and propagated into the silicon chip, which was mounted on xyz translation stages (ASI MS-2000). These stages provided a 40 cm range of travel with a resolution of 10 nm. The TOBIC signal was amplified with a low noise current preamplifier (Stanford Research SR570) and detected using a LabjackU6 device with a personal computer.

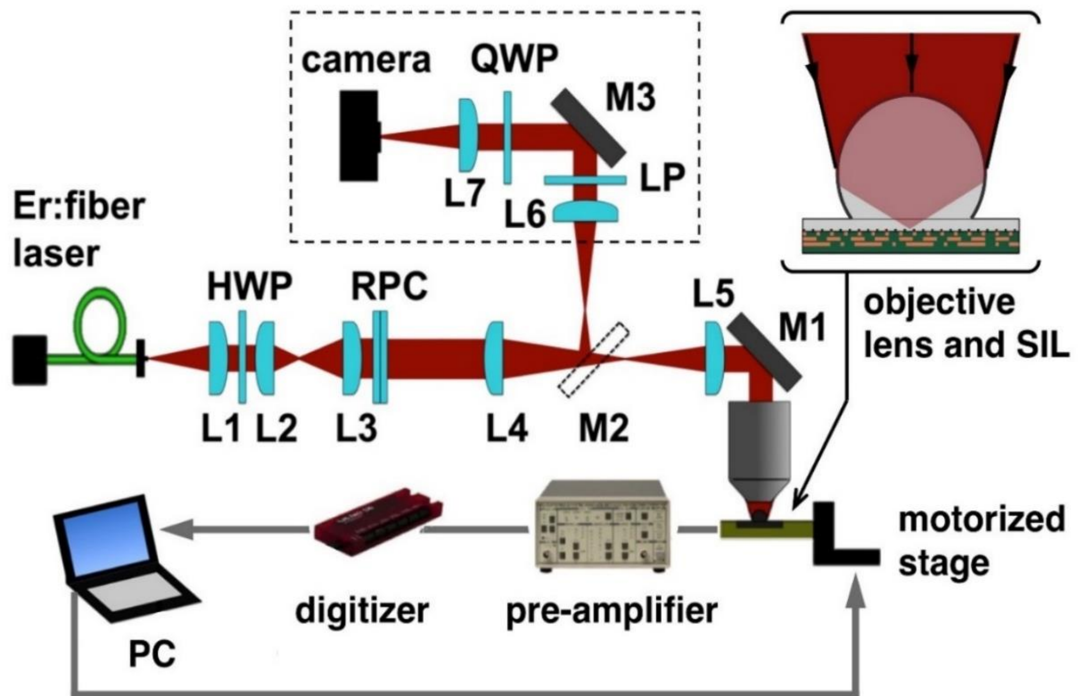

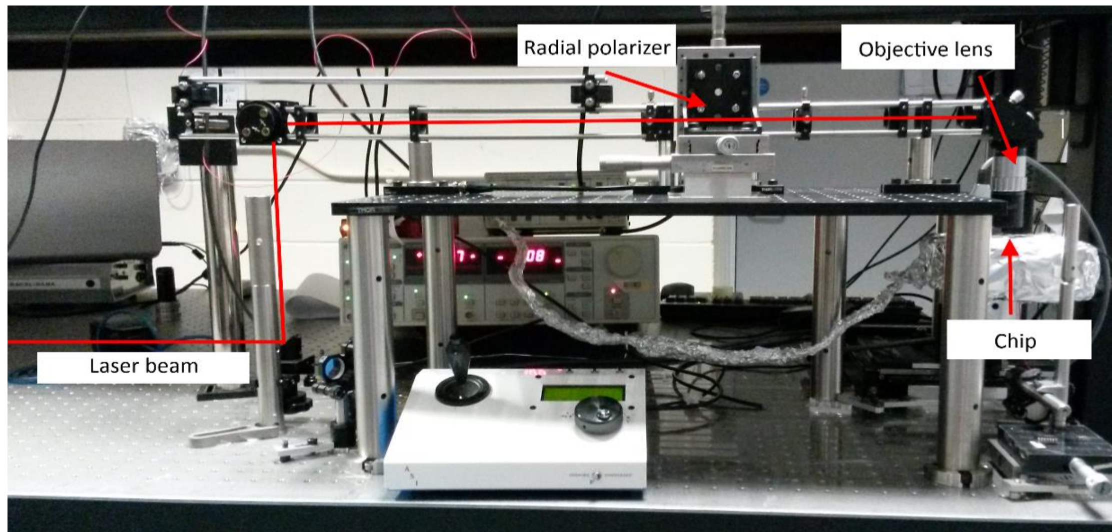

Figure 3.22. TOBIC microscope including RPC. Mirror M2 deflected the beam into the characterisation apparatus (dashed box) but was removed for imaging. A linear polariser (LP) and a quarter-wave plate (QWP) were used to prepare different intensity distributions for the Stokes parameters measurement. Lens L7 imaged the far-field beam profile onto a camera. A half-wave plate (HWP) was used to prepare the correct incident polarisation for the RPC and for imaging experiments with only linearly- polarised light.

5.4.2 Device under test

The sample used for the experiments was a 350-nm-feature-size silicon flip-chip IC. The flip-chip architecture of the device hinders the front-side access to the device layer, which is buried under the five opaque metallisation layers (Fig. 3.23) [68]. Therefore, optical imaging can be performed only through the backside of the device or through the silicon substrate, covering the area of 1 cm^2. To prepare the device for backside imaging it was chemically thinned and polished to a thickness of 85 μm. An optical microscope was used to measure and confirm the specified thickness. Measurement was accomplished by translating the sample through the surface of the substrate to the device layer. This displacement between two planes provided an optical distance, which was inserted in the following equation to calculate the physical thickness of the sample [68]:

$$l = d * n, \tag{3.45}$$

where l is the silicon substrate thickness, d is the displacement of the stage and n is refractive index of silicon.

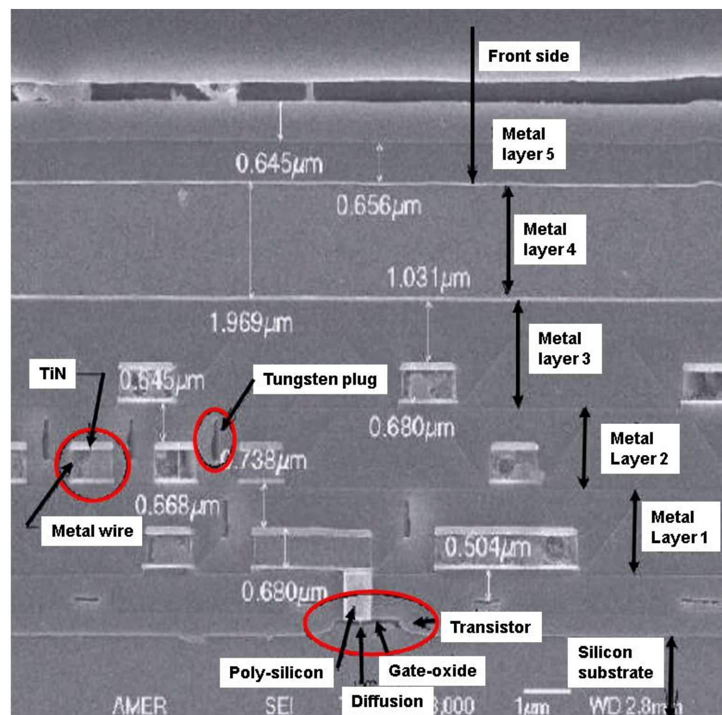

Figure 3.23. Cross-section of the device showing flip-chip architecture and 5 layers of metallisation [8].

The outcome of the measurement was the expected result of 85 μm. It is not enough to have a sample of uniform thickness as the high-resolution SIL measurements require a flat landing zone to establish contact with the substrate [69]. However, the thinning process and the thermal expansion mismatch between different materials inside the device cause a warping, which resembles the principle of a well-known bimetallic strip (Fig. 3.24a) [70]. A warping is the side-effect of sample preparation and is not desirable as a poor surface quality hinders the imaging

resolution [71]. Therefore, a surface mapping interferometer (ZYGO NewView 6300) was used to measure, how badly the IC sample was affected. It was found out that device had a reasonably flat surface with a curvature of only 2 μm, which indicated that the sample was very suitable for SIL microscopy (Fig. 3.24b).

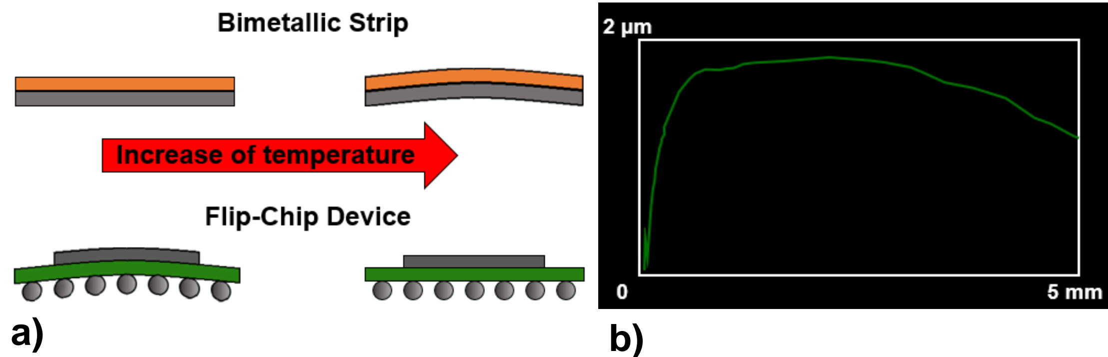

Figure 3.24. Warping of integrated circuits (left), X, Z profile of the silicon substrate of the sample IC device (right), obtained using a Zygo NewView 6300 white-light interferometer.

The device under test contained a standard circuitry (Fig. 3.25a) used in commercial applications and had a photosensitive electrostatic protection device at the input to an inverter chain spanning over 150 um^2 (Fig. 3.25b). Eight n-doped silicon fingers were located in the active region (Fig. 3.25c). The fingers had widths of 4 μm and were separated by gaps of 700 nm. The tips of n-doped structures contained a 3 × 3 matrix of tungsten vias, which were spaced at a pitch of 1.25 μm and had approximate diameters of 1 μm. Surface of the features is uneven and rough.

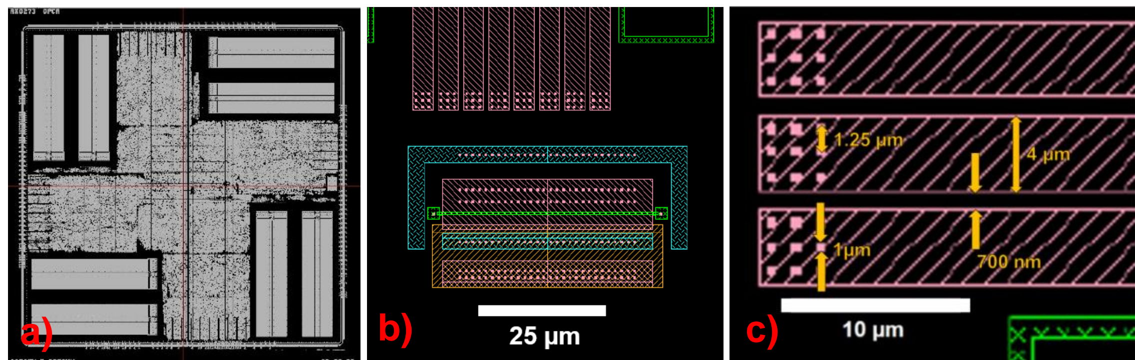

Figure 3.25. (a) Full layout of the device. (b) The floor-plan of the area of interest and (c) n-doped silicon finger structures with tungsten vias on their tips [8].

The laser-beam-generated photocurrent was measured between ground and a pin connected to the active region [72]. The device remained unpowered all the time as the p-n junctions of doped silicon provided an internal electrical field, which is an essential condition for the photocurrent generation via charge carrier separation.

5.4.3 Solid immersion lenses

The SIL is an important component of the TOBIC microscope as its design and its placement decides where the laser beam will be focused inside the IC. Therefore, to achieve the best imaging performance great care must be taken while designing and implementing the aSIL within the optical system.

Equations (1.2 and 1.3) to calculate the exact dimensions of the aSIL were discussed in Chapter 1. They show that the aSIL's design is dictated by the radius of the sphere, refractive index of the material and thickness of IC substrate. All these three parameters must be carefully chosen to suit the imaging system and the IC under test.

In order to work properly the aSIL must be made from a material having the same refractive index as the DUT. Therefore, the aSIL must be made from silicon corresponding to the material of the substrate. The refractive index of silicon at a wavelength of 1.55 μm can be calculated from the appropriate Sellmeier equation [73], which implies a refractive index of 3.48.

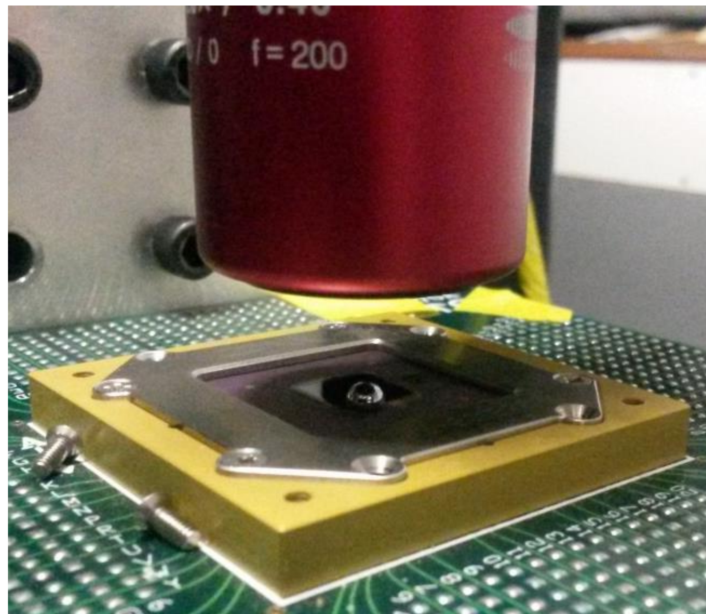

Figure 3.26. A free-standing aSIL under the microscope objective and positioned on the top of the area of interest.

When selecting the radius of the sphere there is a trade-off to fit the aSIL under the microscope objective for the ability to easily move it around. As a consequence of the previous considerations, the radius was chosen to be 2 mm. This design allowed delicate aSIL manipulation with a tweezers while fitting easily between the microscope objective and the DUT. The height of the aSIL was calculated using the Eq. (1.3) and found to be 2.489 mm for 85 μm thickness sample. The height was small enough to conveniently place the lens under the microscope objective, which had a working distance of 13 mm (Fig. 3.26). Also, a half sphere of 2 mm radius can be easily inserted and roughly aligned by hand.

Even a perfectly designed aSIL can produce excessive amount of aberrations if it is not placed in precise area of the IC (Chapter 5). As a result, the faulty placement of the aSIL can lead to a poor quality of the image or for the most severe cases can even prevent from obtaining the image [69]. Therefore, after roughly placing the aSIL by hand it was moved around using vacuum tweezers and a µ-positioning stage. However, the nonlinear nature of the TOBIC signal complicates this task even more. As multi-photon absorption depends on the square of the intensity, the stages must position the DUT at the focal spot of the laser beam, otherwise no signal will be generated. In order to place the aSIL precisely on the top of area of interest, the following procedure was implemented. First, the IC was scanned with the beam of the maximum power to peak up the TOBIC signal without using the aSIL. When an image was acquired, the power level was gradually dropped as the sample was brought to the focus. This z-position of the stage must be changed when introducing the aSIL in the optical path (Fig. 3.27). The change in z-position while imaging with and without aSIL can be accurately calculated.

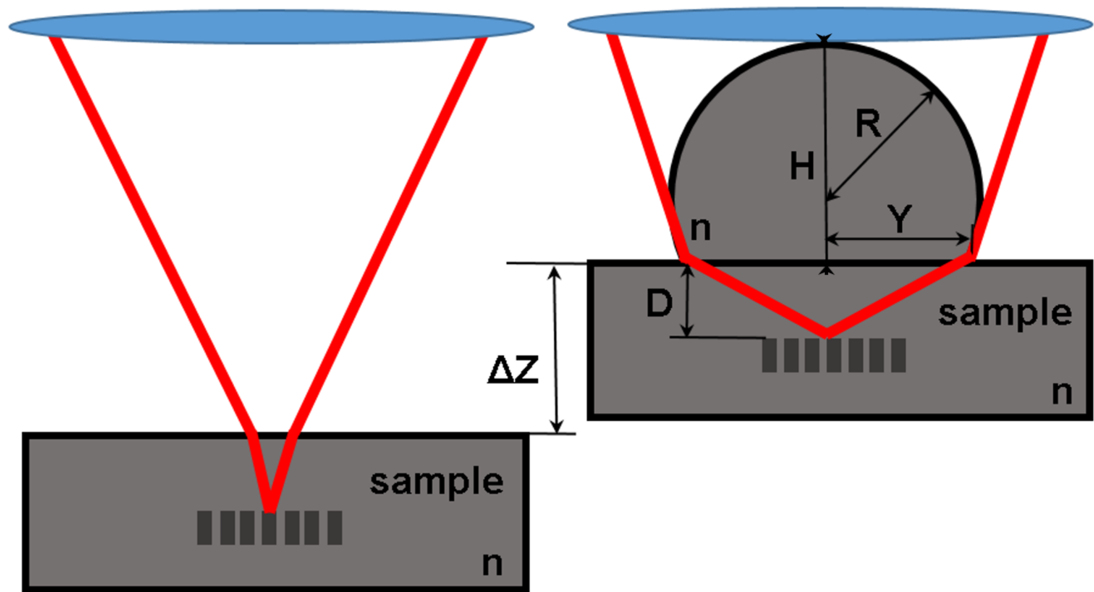

Figure 3.27. Laser beam focusing with and without aSIL.

The laser beam exhibits refraction at the air and silicon interface, while focusing it without the SIL. It not only changes the cone angle of the light but also restricts the maximum available NA. This difference between the cone angles in air and in the silicon can be calculated using Snell's law. Applying the small angle approximation provides the following result for the focal spot distance in air and in silicon:

$$\Delta z_1 \approx 85\mu\text{m}\cdot\left(1-\frac{1}{n}\right) = 60.6\ \mu\text{m}. \quad (3.46)$$

Next one can calculate the distance between focal positions in air and in silicon, when the SIL is used for imaging. The extreme ray angle (α) can be calculate from the right-angled triangle:

$$\sin\alpha = \frac{H-R}{R} = 0.245. \qquad (3.47)$$

After obtaining the angle (α) 14° one can estimate the distance between focal positions with and without SIL:

$$\Delta z = \Delta z_1 + \Delta z_2 = 60.6\ \mu\text{m} + \frac{Y}{\tan\alpha} - 85\ \mu\text{m} = 7.67\ \text{mm}. \qquad (3.48)$$

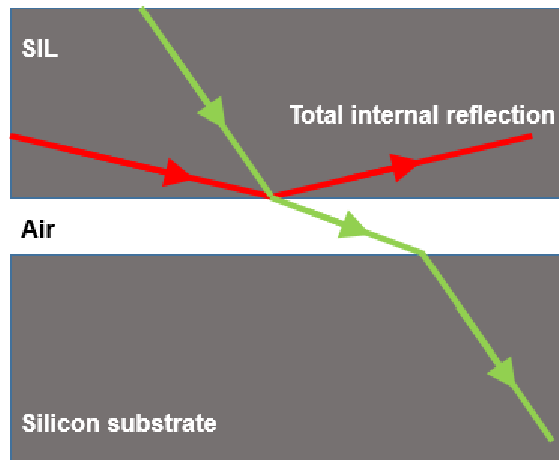

Figure 3.28. Total internal reflection for poor SIL-substrate contact case.

Moving sample by this distance closer to the objective lens ensures that the TOBIC signal is generated after placing the SIL. This angle also provides the maximum NA, which can be exploited from the objective lens while SIL is in use: NA=sinα = 0.24.

Once the sample was in correct z-position the SIL could then be moved in x and y directions to obtain the maximum TOBIC signal level.

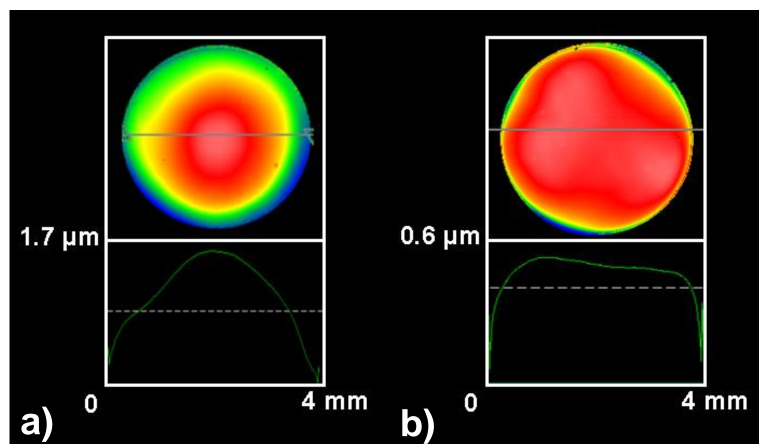

Figure 3.29. (a) Base of the surface of the SIL, which shows bulging of the surface of 1.6 µm, (b) good SIL example.

Another critical quality of the SIL is the roughness and flatness of the base. The maximum contact between the SIL and the IC needs to be established. A poor contact leads to total internal reflection of some rays while passing SIL-air boundary and therefore limiting the resultant NA (Fig. 3.28). Therefore, a surface mapping interferometer (ZYGO NewView 6300) was used to measure the flatness of the SIL's base to ensure that the good optical contact can be established. It was found that SILs degrade over time due to stress on their surface and exhibit severe distortion of their base. Fig. 3.29a shows the degraded SIL, which has curved base, and Fig. 3.29b depicts a good example of another SIL. To ensure the maximum optical contact, the tip of the SIL was pressed onto the IC surface using plastic tweezers.

5.4.4 Liquid-crystal polarisation converters

For the laser beam conversion to the radially polarised beam a LC beam shaper was used. The device was designed to work for 1.55 µm wavelength and was manufactured in the University of Rochester [74]. The LC converter comprised of two glass substrates and the inner surface of each of the substrates was coated with photoalignment material, which dictates the twist angle of the nematic LC. The nematic LC was inserted between the substrates (Fig. 3.32). The photoalignment layers were aligned using a polarised UV source and a mask. LC crystals injected in the device adjust to the orientation of the cells formed by the UV irradiation through the mask. The LC device consists of two substrates and in each of this substrate molecule orientation is different as it is shown in Fig. 3.30. When linearly polarised light is propagating through such LC device light experiences polarisation twist if its polarisation is at right angle to orientation of molecules. Therefor vertically and horizontally polarised light exhibits different polarisation twist by different substrates leading to either azimuthally or radially polarised output (Fig. 3.30). Also, the device thickness must be carefully chosen for the particular wavelength for which device is meant to work. In Fig. 3.30 the actual device is shown [75].

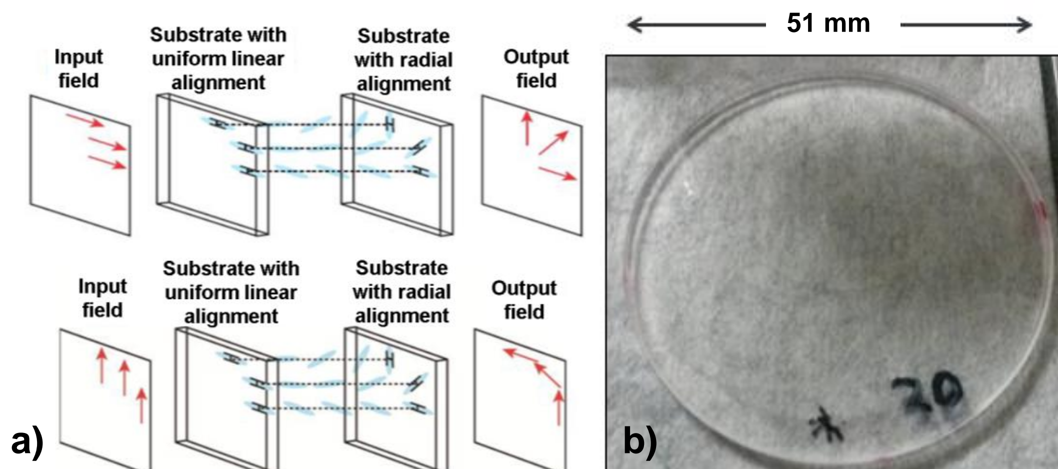

Figure 3.30. (a) A schematic of assemble cell, (b) actual device of 51 mm diameter [75].

The LC devices had a small feature of 300 μm size, where the polarisation was not determined. Due to manufacturing limits, a defect line running along the diameter parallel to the axis appears. This defect is caused by destructive interference of two opposite field contributions of equal amplitude over the same spatial region, as illustrated in Fig. 3.31. The line width is dictated by the fabrication process [75, 76].

Even though the polarisation converters had a disclination line, it was compensated with an appropriate phase step on the outer surface of substrate.

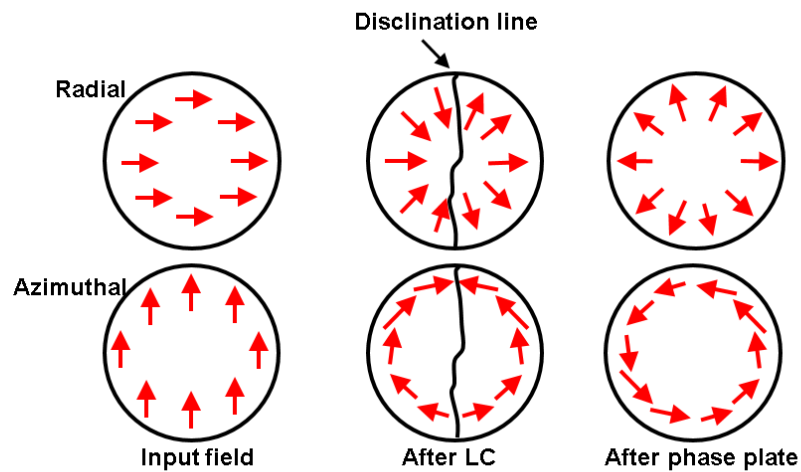

Figure 3.31. Explanation of the polarisation discontinuity (adapted from [75]).

In order to have axially symmetric beams with the desired phase distribution, a phase step is introduced. A phase step is a substrate with built-in step, which creates different optical paths to compensate the phase shift [75]. There are three possible designs of the phase step. The simplest one is a separate external plate (Fig. 3.32a). However, it has a disadvantage that it must be aligned every time the device is used. To overcome this problem, the phase step can be manufactured on the external side of the substrate (Fig. 3.32b). Another approach is to form the internal phase step but in this case only one polarisation can be used and means that the device can provide only either radial or azimuthal polarisation [75]. In the nonlinear TOBIC microscope the RPC with the external integrated phase step was used.

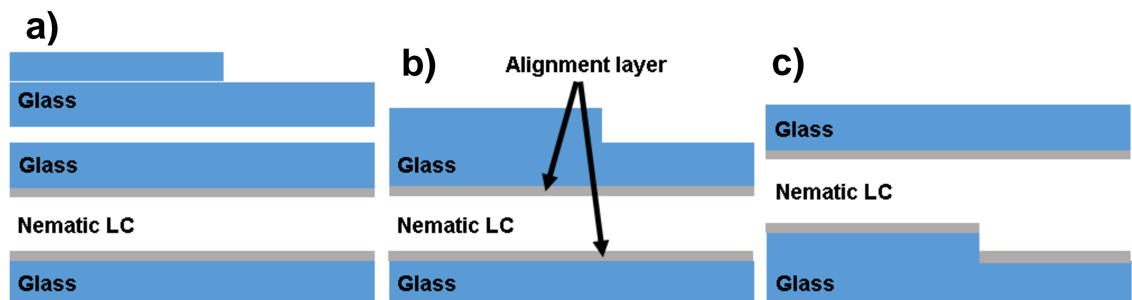

Figure 3.32. Three types of the phase step: (a) external, (b) external integrated, (c) internal (adapted from [75]).

5.4.5 Resolution measurement technique

An edge response of the atomically sharp n-doped finger was used to evaluate the lateral spatial resolution of the nonlinear imaging system. The variation of the TOBIC signal as the beam is scanned across the metal-semiconductor interface enables one to measure the resolution. The photocurrent gives the strongest response when the whole laser beam is focused into the semiconductor finger. However, when the beam is scanned towards the metal region the TOBIC signal gradually diminishes (Fig. 3.33a). Therefore, it is possible to obtain a cross-section of the active area when a line scan across a physical edge of an n-doped finger is performed. This signal response is a combination of the point spread function and the physical edge function. As the physical edge is a step function, the intensity of the signal S can be expressed as a function of the spatial characteristics of the focused Gaussian beam [77]:

$$S(r) = \int_{r=edge}^{r=\infty} I(r)\mathrm{d}r\,, \tag{3.49}$$

where $I(r)$ is intensity of the Gaussian beam. The imaging resolution of the optical system can then be defined from the shape of the curve, which is generated by the response of the TOBIC signal and can be described as the integral of a Gaussian function:

$$f(x) \propto \int_{-\infty}^{+\infty} exp(ax^2)\, dx, \tag{3.50}$$

where $f(x)$ is the curve of the TOBIC signal and x is the lateral position of the beam.

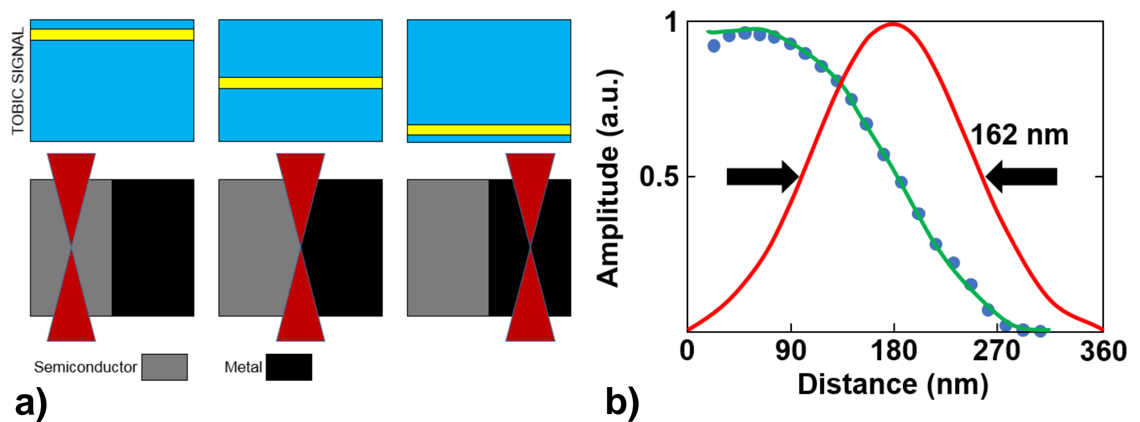

Figure 3.33. (a) TOBIC signal response while scanning laser beam across metal-semiconductor interface, (b) lateral resolution measurement across the edge of the n-doped finger.

Therefore, the numerical integral of Gaussian function can be fitted on the dataset obtained from the TOBIC measurement. A fitting was performed using a multi-dimensional least-squares minimisation algorithm, which simultaneously optimises the width of the point spread function distribution and its centre position. The MATLAB script was written to obtain the Gauss error function after each linescan. The optimised parameters provided the FWHM of the underlying Gaussian function, which is taken as the resolution value as is shown in Fig. 3.33b [68].

5.5 Results and discussion

5.5.1 Evaluation of radial polarisation converter

To investigate the performance of the LC device, a linear polariser and when required, a QWP were placed into the beam path just after the radial polariser in order to calculate a figure-of-merit called the degree of polarisation (DOP). The radial polariser was tested in a transmission setup using laser light from the Er:fibre laser with a centre wavelength of 1.55 μm. This transmission setup included the radial polarisation converter and polarising elements to manipulate and then analyse the radially polarised light in the near and far fields. The experimental setup is shown in Fig. 3.34. The light leaving the Er:fibre laser was linearly polarised and collimated with a beam diameter of 3 mm at lens, L1 using a 300 mm focal length lens. A HWP and a beam expander (L2 and L3) were then employed before the radial polariser to rotate the polarisation state of the beam and to expand the beam diameter from 3 mm to 18 mm. To avoid generating spherical aberration, achromatic lenses were used.

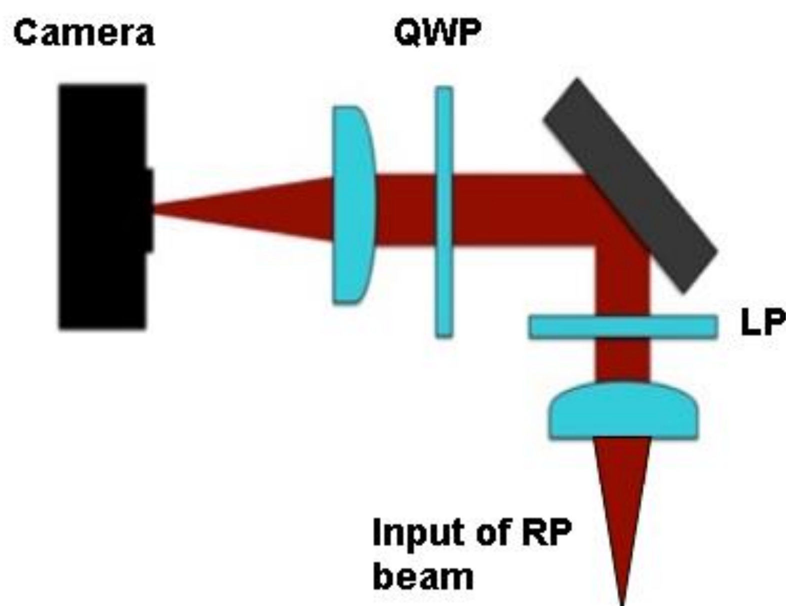

Figure 3.34. Radial polarisation characterisation setup.

The HWP made it possible to dictate the angle of the linear polarisation with respect to the orientation of the radial polarisation converter. Furthermore, the beam was expanded to fill more of the RPC and so obtain higher polarisation purity. After the LC device, the beam was reduced to a diameter of 9 mm using the lenses L4 and L5 and imaged onto an IR Find-A-Scope camera where intensity distribution images were recorded. The DOP is evaluated by calculating a set of values known as Stokes parameters (Eq. 3.44), which are obtained by measuring the light intensity distributions after the linear polariser and after a QWP. Fig. 3.35 shows the recorded intensity distributions that were used to calculate the Stokes parameters and DOP.

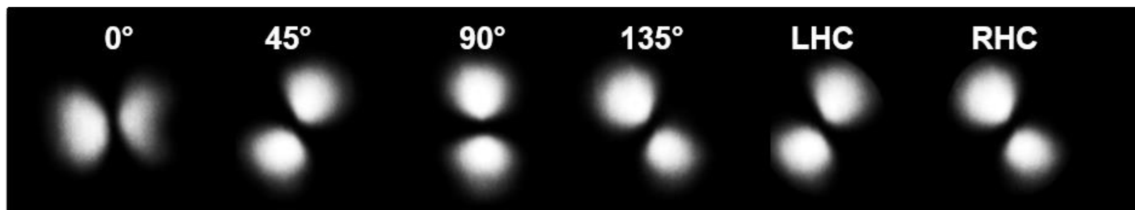

Figure 3.35. Intensity distributions of the polarisation elements of the radially polarised beam.

The recorded fluence distributions were used to calculate the Stokes parameters, which implied a highly radially polarised beam of 94 ± 4% purity with 90% efficiency. Furthermore, Fig. 3.36 shows the near field and far field images of the beam after the radial polariser without any other polarising elements in the path. These intensity distributions are close to what should be expected, albeit there appears to be a disclination line imaged on the near field image. However, the far-field image does show some resemblance to a doughnut shaped intensity distribution, which is what one would expect from radially polarised light imaged in the far field for a low-NA focusing conditions.

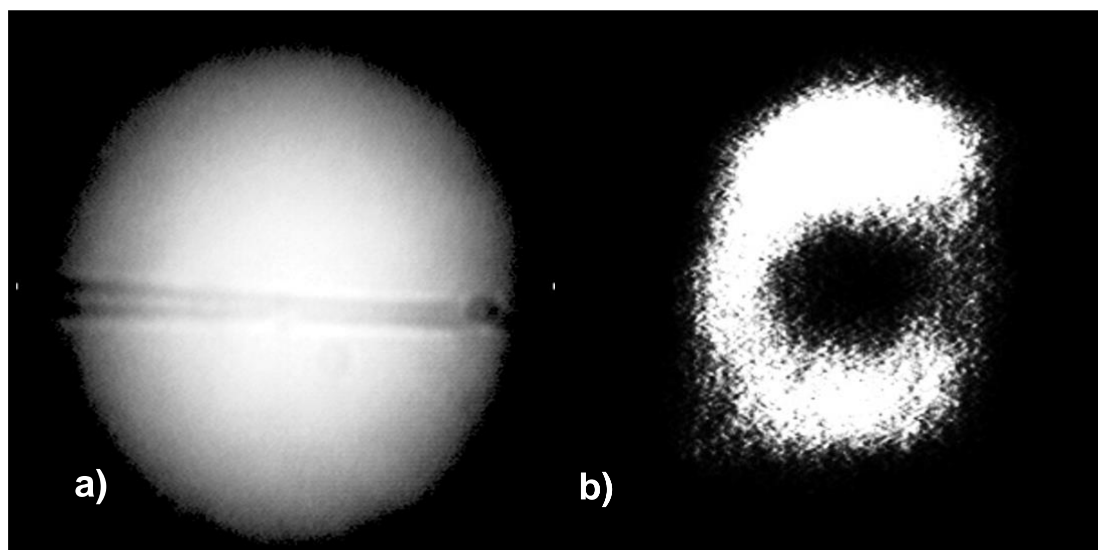

Figure 3.36. (a) Near field and (b) far field intensity distribution of the radially polarised beam.

5.5.2 Numerical modelling of the point spread function

In this section numerical modelling results are presented, while focusing the laser beam under high-NA conditions. The top row of Fig. 3.37 presents the theoretical intensity distributions of the linearly and radially polarised light before (inset) and after (main figure) the objective-SIL combination. The Leutenegger method [78] was employed to calculate these distributions and used experimentally consistent values of wavelength and NA. From these images it is apparent that linear illumination focuses to an approximately elliptical focal spot with its major axis aligned parallel to the electric field vector, whereas for radially and circularly polarised beams the focal spot is symmetrical.

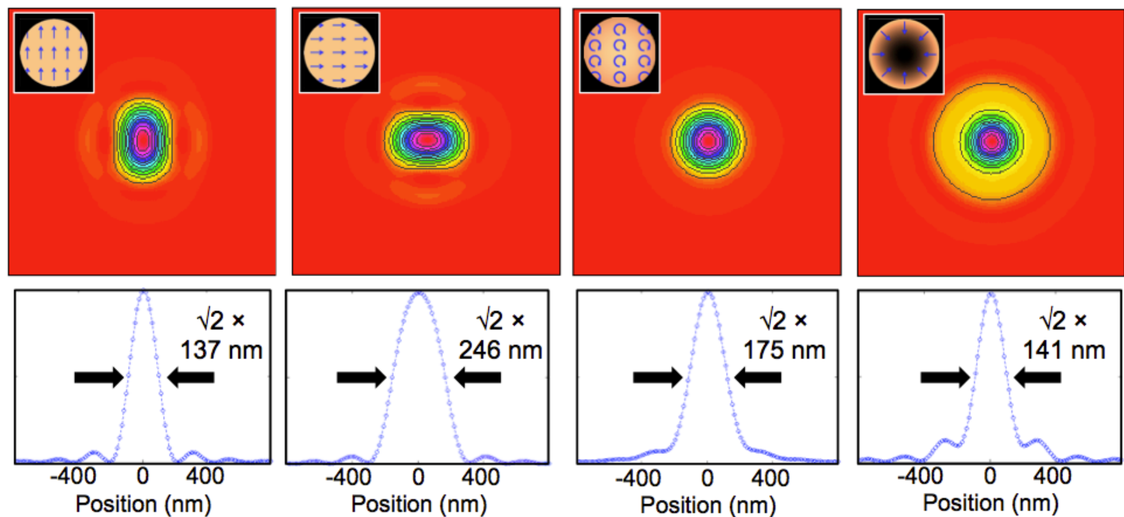

Figure 3.37. Columns, from left to right: linearly polarised light, with electric field parallel then perpendicular to the longer finger edge; circularly polarised light; radially polarised light. Top row: theoretical electric field intensity in the focal plane and (inset) electric field intensity before the pupil; bottom row: corresponding cross-section of the calculated electric field intensity.

Line-cuts through the calculated PSFs are shown in the bottom row, together with full-width at half-maximum diameters. To allow a more meaningful comparison with the experimental two-photon absorption data, the PSF diameters are expressed as √2× the diameter of the squared PSF. The obtained values suggest that the linear polarisation should outperform any other in high-NA imaging. However, it has the major disadvantage that the resolution in the orthogonal direction is degraded severely by 80%. Also the radially polarised beam is only poorer by 3% off but can offer a significant advantage over linear polarisation as the same resolution can be achieved for features of any orientation. Circular polarisation benefits from a symmetrical focal spot but it offers resolution around 25% poorer than radial. However, simple insertion and handling of the QWP can prove to be useful for certain applications. These results are consistent with previously published calculations given by Zhan and correlate well with a theory discussed in the previous chapters [11].

5.5.3 TOBIC measurements

Before the experimental work of TOBIC microscopy, confocal microscopy was demonstrated to compare the same region inside the chip using an aplanatic SIL. Fig. 3.38a shows the confocal image of the area of the chip introduced in Fig. 3.25, while Fig. 3.38b shows the same area but obtained via TOBIC. The TOBIC image appear less noisy since detector via confocal imaging mode detects strongly attenuated signal as the beam should pass the microscope twice. Fig. 3.38a suggests that finger structures have rough and uneven surface.

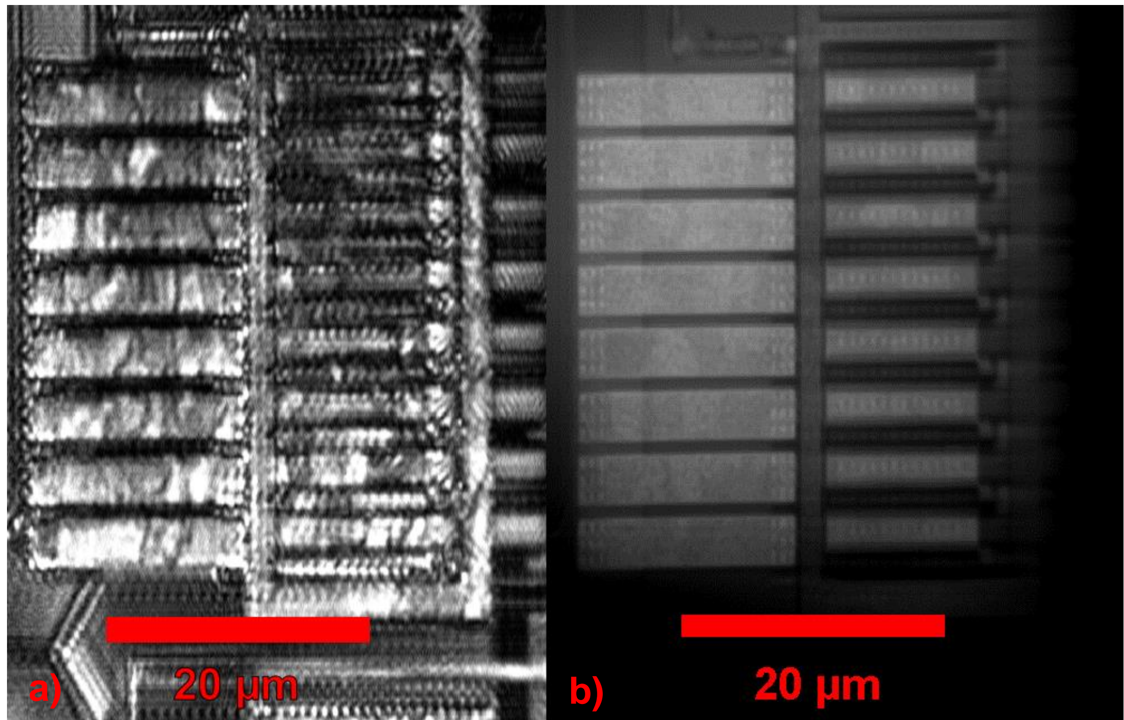

Figure 3.38. (a) Confocal and (b) TOBIC images of the same sensitive area inside the device obtained using aplanatic SIL.

Figure 3.39 shows the 1-D confocal line-scan image along with a least-squares Gauss-error function fit to estimate a resolution value described in Chapter 3.4.5. Error bars in Fig. 3.39b are obtained from signal to noise ratio, which resulted in 12% error. A least-squares Gauss-error fit introduced 12%, which is consistent to the signal to noise error and was estimated from residual values. Therefore, confocal imaging regime provides 220 ± 26 nm resolution (linear polarisation) which agrees very well with Sparrow limit of 223 nm. It is necessary to note here, that resolution obtained with confocal imaging technique is lower as TOBIC microscopy is further enhanced $\sqrt{2}$ times by exploiting TPA.

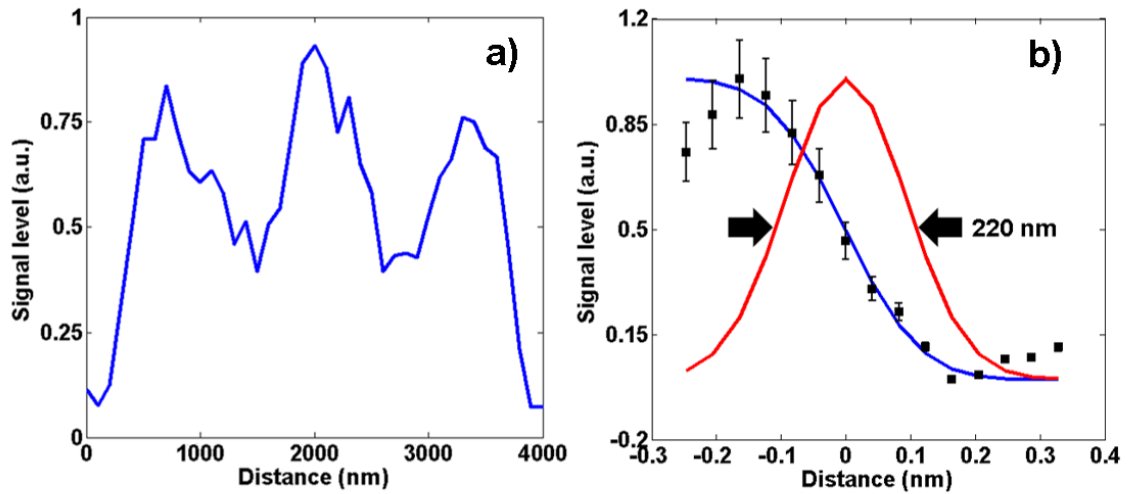

Figure 3.39. (a) Line-cut of the finger structure in the confocal imaging regime with (b) a least-squares Gauss-error fit over edge for resolution estimation (linear polarisation).

Figure 3.40 shows line-cut of silicon finger, acquired via TOBIC technique using linear polarisation. This area was chosen for analysis because the silicon-metal interfaces at the finger edges are sharp, therefore provide a convenient resolution target. Background noise level was used to estimate measurement error of each data point in the line-cut as it is shown in Fig. 3.40. Signal to noise ratio indicated 3.7 % error value.

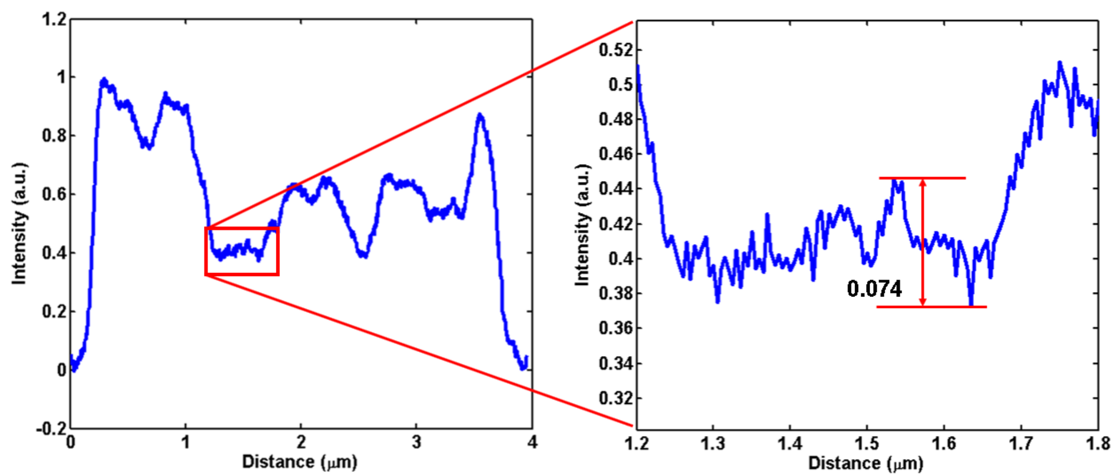

Figure 3.40. Example how error resulting from signal to noise ratio is estimated.

Experimental examples of the imaging quality achieved using linear, circular and radial polarisation are shown in Fig. 3.41, which presents TOBIC images of the n-doped silicon finger structures acquired using optimised linear polarisation (Fig. 3.41a); circular polarisation (Fig. 3.41c) and a radially polarised beam (Fig. 3.41d). Visualisation of the 3×3 matrix of tungsten vias is more distinct using radial and circular polarisations, which both benefit from a symmetrical focal spot. With linear polarisation, the elongation of the focal spot along the direction of the electric field causes the vias pattern to appear more blurred in either the horizontal or vertical direction.

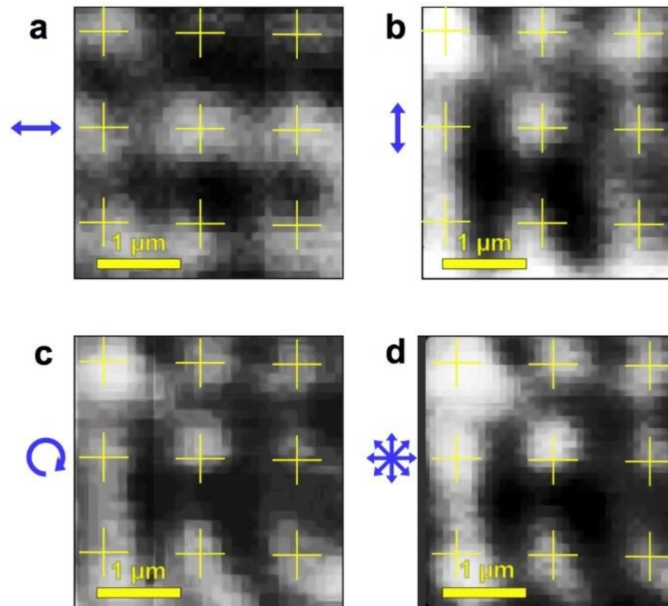

Figure 3.41. TOBIC images acquired for (a) linear parallel; (b) linear orthogonal; (c) circular and (d) radial polarisations of the n-doped silicon finger structures depicted in Fig. 3.25. Yellow crosses indicate the nominal tungsten via positions inferred from the device CAD.

Figure 3.42 shows line-cuts along the direction shown in Chapter 3.5.2, acquired by illuminating the sample with four different states of polarisation: two orthogonal linear polarisations (Fig. 3.42, Columns 1 and 2), circular polarisation (Fig. 3.42, Column 3) and radial polarisation (Fig. 3.42, Column 4). The 1-D line-scan image is shown along with a least-squares Gauss-error function fit, from which a resolution value was obtained as described previously in Chapter 3.4.5. In Fig. 3.42, Column 1 shows the data for the incident linear electric field polarisation lying parallel to the longer dimension of the fingers, while in Column 2 the data were acquired with the orthogonal linear polarisation, in Column 3 the data were obtained with circularly polarised light and in Column 4 using radially polarised light.

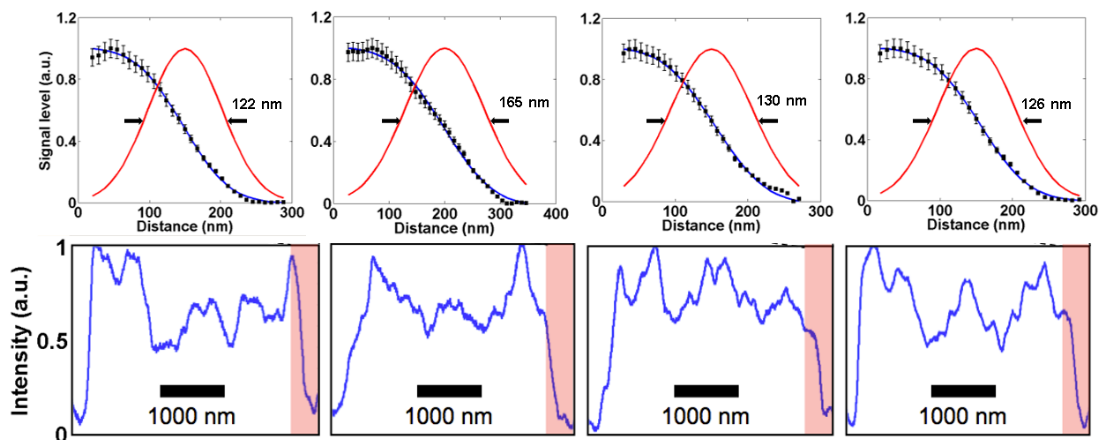

Figure 3.42. Columns, from left to right: linearly polarised light, with electric field parallel then perpendicular to the longer finger edge; circularly polarised light; radially polarised light. Top row: experimental data showing a least-squares Gauss-error fit over a line-cut of n-doped silicon finger edge; bottom row: extended line-cut data showing the region (red shading) used for the Gauss-error analysis.

Fig. 3.43. shows plots of the root-mean square (RMS) fitting error as a function of the FWHM for each polarisation case. The percentage of RMS fitting error is around 2% and is smaller than the error appearing due to signal to noise ratio (3.7%).

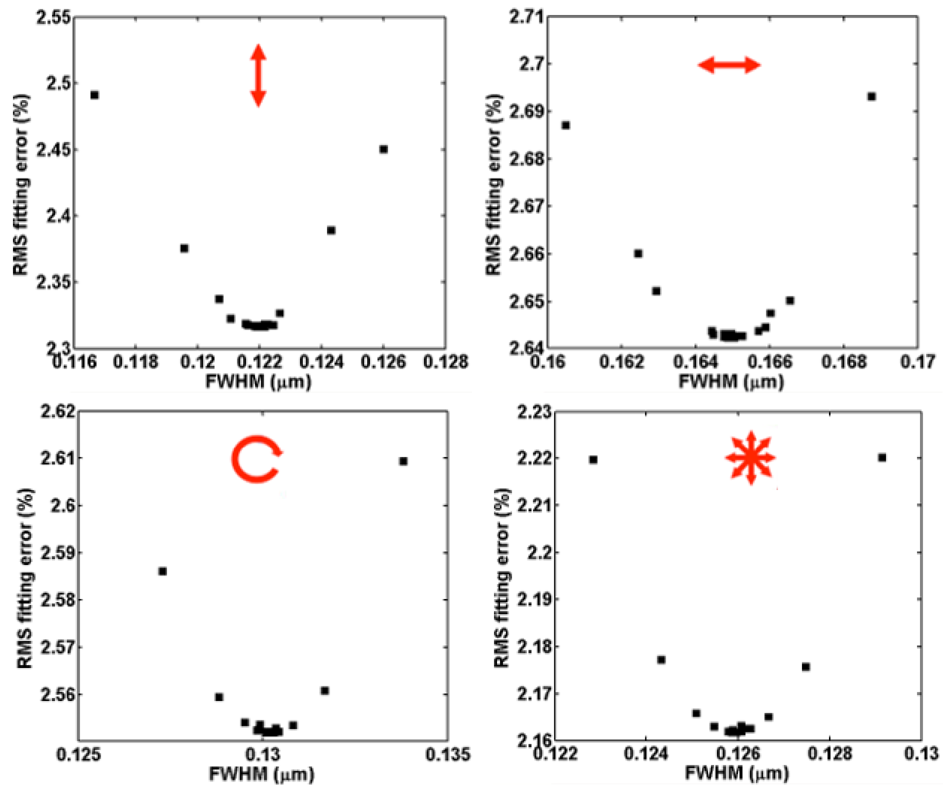

Figure 3.43. Plots of the root-mean square fitting error as a function of the FWHM.

Inspection of the line-cuts in Fig. 3.42 reveals that, when linearly polarised light is used, the gap between the fingers is better resolved when the electric field vector is oriented parallel to the edge of the fingers as compared with an orientation orthogonal to the long finger edges. The elongation of the focal spot along the electric field direction results in a measured resolution of 165 ± 6 nm for the orthogonal case, which is reduced by 25% to 122 ± 5 nm while using parallel polarisation. The achieved result corresponds well with previously reported performance [10]. Imaging using the RPC produced a resolution value of 126 ± 5 nm, which is equal to the optimised linear polarisation case within a small error. This result is significantly better than that achieved with the orthogonal linear polarisation state and could be further improved if the degree of polarisation were increased, as noted by Yurt *et al*, who observed that imperfect vector symmetry of the radially polarised beam can degrade the spatial resolution [38]. Circular polarisation yielded a 130 ± 5 nm spatial resolution, which is reproduces the value of radial and linear polarisations to within an error, however it is not expected to significantly improve by using various techniques like pupil engineering. A comparison between the theoretical and experimental data shows the same relative magnitudes but the experimental values are consistently lower. This difference can be attributed to the local dielectric environment inside the device perturbing the focal-plane field,

and to the fact that the knife-edge type resolution measurement integrates power across the full width of the PSF, rather than performing a true line-cut.

Insertion of the RPC device and waveplates introduce slight change of the incident power used for TOBIC microscopy. The RPC was measured to attenuate laser power by 10%. Therefore, it was necessary to investigate whether power attenuation increase or decrease the performance of the TOBIC microscope. Series of results were recorded with different attenuations, which showed that it can be only slight resolution suppression due to power attenuation (Fig. 3.44).

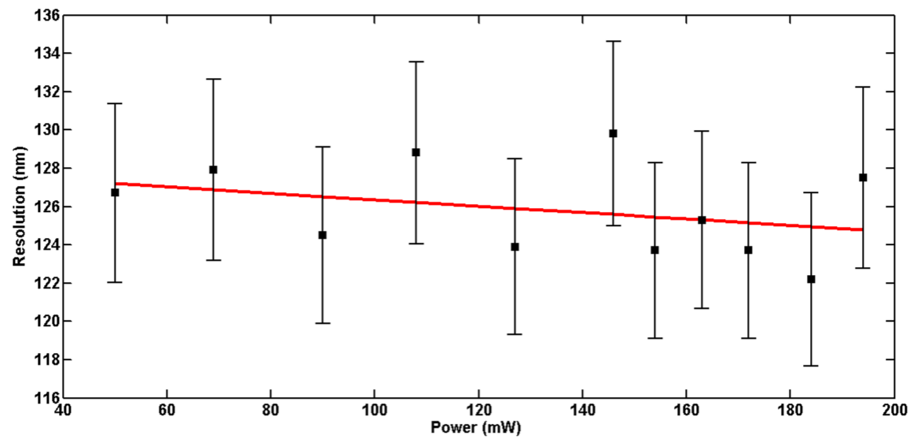

Figure 3.44. Plot showing resolution dependence on the laser power delivered to the sample.

In Fig. 3.45 I present, for the case of illumination using optimised linear polarisation, the variation of the resolution value as the focal position of the device-under-test was adjusted. A smoothly varying monotonic trend is observed, indicating the expected behaviour and providing strong evidence that the high spatial resolutions achieved are genuine and do not result from noise or other image artefacts. Also while changing polarisation state one must make sure that sample is brought back in the focal position and what the measurements are conducted in the focal plane. Therefore, it is critical to repeat the z-scan prior each experiment.

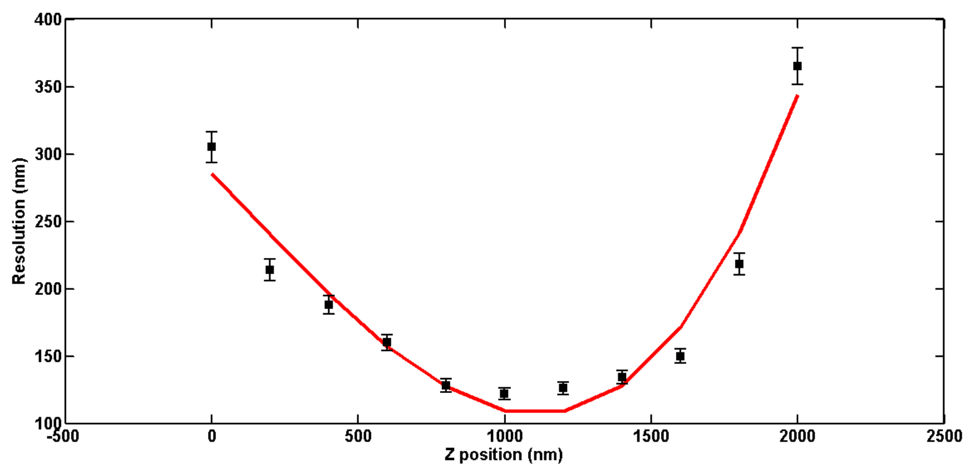

Figure 3.40. Resolution values obtained while changing the laser beam focal position relative to the sample (symbols) and cubic fit to the data (red line).

3.6 Conclusions

In this chapter it was shown that high lateral resolutions can be achieved in sub-surface nonlinear microscopy while using radially polarised beams. It was demonstrated experimentally that using radially polarised illumination achieves a sub-surface imaging resolution equivalent to the best resolution achieved with linearly polarised light. This illumination condition was implemented with a high-throughput RPC device, which eliminated the need to adjust the polarisation state of the light to specifically optimise the resolution for individual feature orientations. The design of the nonlinear microscope presented in this chapter was able to achieve sub-surface imaging resolutions in the region of 100 nm, which are among the best up to date and are surpassed only by nonlinear microscopy complemented with annular illumination [9]. The TOBIC microscope introduced in this chapter could be further enhanced with the insertion of an annular aperture, which is expected to further improve the obtained resolutions. Especially for radial polarisation case, pupil engineering can have a high impact by enhancing the contribution of the longitudinal on-axis electric field component at the focus [12]. Modelling suggests that an improvement of between 10% – 30% should be possible.

References

1. "International technology roadmap for semiconductors" (2013).
2. S. B. Ippolito, B. B. Goldberg, M. S. Ünlü, "High spatial resolution subsurface microscopy", Applied Physics Letters **78**, 4071 (2001).
3. C. Xu and W. Denk, "Two-photon optical beam induced current imaging through the backside of integrated circuits", Applied Physics Letters **71**, 2578–2580 (1997).
4. C. Xu and W. Denk, "Two-photon optical beam induced current imaging through the backside of integrated circuits", Journal of Applied Physics **86**, 2226–2231 (1999).
5. C. Xu, L. M. F. Chirovsky, W. S. Hobson, J. Lopata, W. H. Knox, J. E. Cunningham, W. Y. Jan and L. A. D'Asaro, "Two-photon photocurrent imaging of vertical cavity surface emitting lasers", Applied Physics Letters **76**, 1510–1512 (2000).
6. K. A. Serrels, C. Farrell, T. R. Lundquist, D. T. Reid, and P. Vedagarbha, "Solid-immersion-lens-enhanced nonlinear frequency-variation mapping of a silicon integrated-circuit", Applied Physics Letters **99**, 193103 (2011).
7. K. A. Serrels, K. Erington, D. Bodoh, C. Farrell, N. Leslie, T. R. Lundquist, P. Vedagarbha, and D. T. Reid, "Two-photon laser-assisted device alteration in silicon integrated-circuits", Optics Express **21**, 29083 (2013).
8. E. Ramsay, N. Pleynet, D. Xiao, R. J. Warburton and D. T. Reid, "Two-photon optical-beam-induced current solid-immersion imaging of a silicon flip chip with a resolution of 325 nm", Optics Letters **30**, 26–28 (2005).
9. K. A. Serrels, E. Ramsay and D. T. Reid, "70 nm resolution in subsurface optical imaging of silicon integrated-circuits using pupil-function engineering", Applied Physics Letters **94**, 073113 (2009).
10. K. A. Serrels, E. Ramsay, R. J. Warburton and D. T. Reid, "Nanoscale optical microscopy in the vectorial focusing regime", Nature Photonics **2**, 311 - 314 (2008).
11. Q. Zhan, "Cylindrical vector beams: from mathematical concepts to applications", Advances in Optics and Photonics **1**, 1-57 (2009).
12. R. Dorn, S. Quabis, and G. Leuchs, "Sharper focus for a radially polarized light beam", Physics Review Letters **91**, 233901 (2003).
13. Y. Zhuang, Y. Zhang, B. Ding and T. Suyama, "Trapping Rayleigh particles using highly focused high-order radially polarized beams", Optics Communications **284**, 1734–1739 (2011).
14. A. Kumar, M. C. Gupta, "Laser machining of micro-notches for fatigue life", Optics and Lasers in Engineering **48**, 690–697 (2010).
15. B. Jia, H. Kang, J. Li, M. Gu, "Use of radially polarized beams in three-dimensional photonic crystal fabrication with the two-photon polymerization method", Optics Letters **34**, 1918–1920 (2009).

16. X. Li, Y. Cao, M. Gu, "Superresolution-focal-volume induced 3.0 Tbytes/disk capacity by focusing a radially polarized beam", Optics Letters **36**, 2510–2512 (2011).
17. W. T. Tang, E. Y. S. Yew and C. J. R. Sheppard, "Polarization conversion in confocal microscopy with radially polarized illumination", Optics Letters **34**, 2147– 2149 (2009).
18. S. Ramachandran, P. P. Kristensen and M. F. Yan, "Generation and propagation of radially polarized beams in optical fibers", Optics Letters **16**, 2525 (2009).
19. Y. Kozawa and S. Sato, "Generation of a radially polarized laser beam by use of a conical Brewster prism", Optics Letters **30**, 3063-3065 (2005).
20. M. A. Ahmed, A. Voss, M. M. Vogel and T. Graf, "Radially polarized 3 kW beam from a CO2 laser with an intracavity resonant grating mirror", Optics Letters **32**, 3272-3274 (2007).
21. M. R. Beversluis, L. Novotny and S. J. Stranick, "Programmable vector point-spread function engineering", Optics Express **14**, 2650-2656 (2006).
22. M. Stalder and M. Schadt, "Linearly polarized light with axial symmetry generated by liquid-crystal polarization converters", Optics Letters **21**, 1948–1950 (1996).
23. M. Statt, M. Vargas, J. Oliver, S. Chen, K. Marshall, and C. Dorrer, "Linearly polarized light with axial symmetry generated by liquid-crystal polarization converters", Proceedings of the Conference on Lasers and Electro-Optics, paper JTh2A (2012).
24. M. Born and E. Wolf, "Principles of optics, 7th ed.", Cambridge: Cambridge University Press (2002).
25. E. Hecht, "Optics, 4th ed.", Boston: Addison-Wesley (2002).
26. C. M. Sparrow, On spectroscopic resolving power, The Astrophysics Journal **44**, 76aAS86 (1916).
27. T. Wilson and A. R. Carlini, "Three-dimensional imaging in confocal imaging systems with finite sized detectors", Journal of Microscopy **149**, 51 (1988).
28. D. G. Hall, "Vector-beam solutions of Maxwell's wave equation", Optics Letters **21**, 9-11 (1996).
29. B. A. E. Saleh and M. C. Teich, "Fundamentals of photonics", New York: John Willey & Sons, Inc. (1991).
30. Q. Zhan, "Cylindrical vector beams: from mathematical concepts to applications", Advances in Optics and Photonics.**1**, 1-57 (2009).
31. P. N. Butcher and D. Cotter, "The elements of nonlinear optics", Cambridge: Cambridge University Press (1990).
32. C. J. R. Sheppard and Z. S. Hegedus, "Axial behavior of pupil-plane filters", Journal of the Optical Society of America A-Optics Image Science and Vision **5**, 643-647 (1988).
33. D. G. Hall, "Vector-beam solutions of Maxwell's wave equation", Optics Letters **21**, 9–11 (1996).
34. L. Novotny and B. Hecht, "Principles of nano-optics", Cambridge: Cambridge University Press (2006).

35. K. S. Youngworth and T. G. Brown, "Focusing of high numerical aperture cylindrical vector beams", Optics Express **7**, 77–87 (2000).
36. G. M. Lerman and U. Levy, "Effect of radial polarization and apodization on spot size under tight focusing conditions", Optics Express 16, 4567–4581 (2008).
37. X. Gao, Q. Wang, M. Yun, J. Yu, H. Guo, S. Zjuang, "Conditions for tighter focusing and higher focal depth of radially polarized vector beam", Optica Applicata **42**, 85–101(2012).
38. A. Yurt, M. D. W. Grogan, S. Ramachandran, B. B. Goldberg and M. S. Ünlü, "Effect of vector asymmetry of radially polarized beams in solid immersion microscopy", Optics Express **22**, 7320–7329 (2014).
39. D. Pohl, "Operation of a Ruby laser in the purely transverse electric mode TE_{01}", Applied Physics Letters **20**, 266–267 (1972).
40. J. F. Bisson, J. Li, K. Ueda, and Y. Senatsky, "Radially polarized ring and arc beams of a neodymium laser with an intra-cavity axicon", Optics Express **14**, 3304–3311 (2006).
41. C.-C. Shih, "Radial polarization laser resonator", U.S. patent 5,359,622 (Oct. 25, 1994).
42. Y. Kozawa and S. Sato, "Generation of a radially polarized laser beam by use of a conical Brewster prism", Optics Letters **30**, 3063–3065 (2005).
43. T. Erdogan, O. King, G. W. Wicks, D. G. Hall, E. Anderson, and M. J. Rooks, "Circularly symmetric operation of a concentric-circle-grating, surface-emitting, AlGaAs/GaAs quantum-well semiconductor laser", Applied Physics Letters **60**, 1921–1923 (1992).
44. M. A. Ahmed, A. Voss, M. M. Vogel, and T. Graf, "Multilayer polarizing grating mirror used for the generation of radial polarization inYb:YAG thin-disk lasers", Optics Letters **32**, 3272–3274 (2007).
45. V. G. Niziev, R. S. Chang, and A. V. Nesterov, "Generation of inhomogeneously polarized laser beams by use of a Sagnac interferometer", Applied Optics **45**, 8393–8399 (2006).
46. R. Yamaguchi, T. Nose, and S. Sato, "Liquid crystal polarizers with axially symmetrical properties", The Japanese Journal of Applied Physics Part 1 **28**, 1730–1731 (1989).
47. M. Stalder and M. Schadt, "Linearly polarized light with axial symmetry generated by liquid-crystal polarization converters", Optics Letters **21**, 1948–1950 (1996).
48. M. R. Beversluis, L. Novotny, and S. J. Stranick, "Programmable vector point-spread function engineering", Optics Express **14**, 2650–2656 (2006).
49. S. C. Tidwell, D. H. Ford, and W. D. Kimura, "Generating radially polarized beams interferometrically", Applied Optics **29**, 2234–2239 (1990).
50. B. Jia, X. Gan, and M. Gu, "Direct measurement of a radially polarized focused evanescent field facilitated by a single LCD", Optics Express **13**, 6821–6827 (2005).
51. N. Passilly, R. de Saint Denis, K. A-Ameur, F. Treussart, R. Hierle, and J. F. Roch, "Simple interferometric technique for generation of a radially polarized light beam", Journal of the. Optical Society of America A **22**, 984–991 (2005).

52. C. J. R. Sheppard, “Use of lenses with annular aperture in scanning optical microscopy”, Optik **48**, 329-334 (1977).
53. Z. S. Hegedus, “Annular pupil arrays - application to confocal scanning”, Optica Acta **32**, 815-826 (1985).
54. M. Martinez-Corral, M. T. Caballero, E. H. K. Stelzer, and J. Swoger, “Tailoring the axial shape of the point spread function using the Toraldo concept”, Optics Express **10**, 98-103 (2002).
55. R. Boivin and A. Boivin, “Optimized amplitude filtering for superresolution over a restricted field .1. Achievement of maximum central irradiance under an energy constraint”, Optica Acta **27**, 587-610 (1980).
56. J. S. Liu, A. J. Waddie, and M.R. Taghizadeh, “Phase-only diffractive optical elements with subdiffraction-limited depth of focus”, Journal of Modern Optics **50**, 227-237 (2003).
57. T. R. M. Sales and G. M. Morris, “Diffractive superresolution elements”, Journal of the Optical Society of America A-Optics Image Science and Vision **14**, 1637-1646 (1997).
58. M. R. Wang and X. G. Huang, “Sub-wavelength-resolvable focused non-Gaussian beam shaped with a binary diffractive optical element”, Applied Optics **38**, 2171-2176 (1999).
59. B. J. Davis, W. C. Karl, A. K. Swan, M. S. Ünlü, and B. B. Goldberg, “Capabilities and limitations of pupil-plane filters for superresolution and image enhancement”, Optics Express **12**, 4150-4156 (2004).
60. D. M. de Juana, V. F. Canales, P. J. Valle, and M. P. Cagigal, “Focusing properties of annular binary phase filters”, Optics Communications **229**, 71-77 (2004).
61. T. G. Jabbour and S. M. Kuebler, “Vector diffraction analysis of high numerical aperture focused beams modified by two- and three-zone annular multi-phase plates”, Optics Express **14**, 1033-1043 (2006).
62. T. Wilson and C. Sheppard, “Theory and practice of scanning optical microscopy”, London: Academic Press (1984).
63. S. W. Hell, P. E. Hänninen, A. Kuusisto and M. Schrader, “Annular ouverture two-photon excitation microscopy”, Optics Communications **117**, 20-24 (1995).
64. W. Denk, J. H. Strickler, and W. W. Webb, “Two-photon laser scanning fluorescence microscopy”, Science **248**, 73-76 (1990).
65. G. G. Stokes, “On the composition and resolution of streams of polarized light from different sources”, Transactions of the Cambridge Philosophical Society **9**, 399 (1852).
66. W. Budde, “Photoelectric analysis of polarized light”, Applied Optics **1**, 201–205 (1962).
67. M. Bass, “Handbook of optics, volume II - devices, measurements and properties, 2nd ed.”, New York: McGraw-Hill, Inc. (1995).
68. K. A. Serrels, “Ultra-high-resolution optical imaging for silicon integrated-circuit inspection”, PhD thesis: Heriot-Watt University (2009).

69. M. Baba, T. Sasaki, M. Yoshita, H. Akiyama, “Aberrations and allowances for errors in a hemisphere solid immersion lens for submicron-resolution photoluminescence microscopy”, Journal of Applied Physics **85**, 6923 (1999).
70. Y Li, “Accurate predictions of flip chip BGA warpage”, Proceedings of the IEEE Electronic Components and Technology Conference (2003).
71. J Colvin, “FemtoFarad/TeraOhm endpoint detection for microsurgery of integrated circuit devices”, Proceedings of the International Symposium for Testing and Failure Analysis (2012).
72. E. Ramsay, K. A. Serrels, M. J. Thomson, A. J. Waddie, M. R. Taghizadeh, R. J. Warburton and D. T. Reid, “Three-dimensional nanoscale subsurface optical imaging of silicon circuits”, Applied Physics Letters **90**, 131101 (2007).
73. H. B. Briggs, “Optical effects in bulk silicon and germanium”, Physical Review **77**, 287 (1950).
74. C. Caggiano, “Fabrication and characterization of radial and azimuthal polarization converters with photoaligned liquid crystals”, Laboratory for laser energetics, University of Rochester (2012).
75. C. Dorrer, S. K.-H. Wei, P. Leung, M. Vargas, K. Wegman, J. Boulé, Z. Zhao, K. L. Marshall, and S. H. Chen, “High-damage-threshold static laser beam shaping using optically patterned liquid-crystal devices”, Optics Letters **36**, 4035-4037 (2011).
76. P. Fiala, C. Dorrer, and K. Marshall, “Twisted-nematic liquid crystal polarization rotators for broadband laser applications”, Proceedings of the Conference on Lasers and Optoelectronics, JW2A.68 (2015).
77. S. B. Ippolito, B. B. Goldberg, and M. S. Ünlü, “High spatial resolution subsurface microscopy”, Applied Physics Letters **78**, 4071-4073 (2001).
78. M. Leutenegger, R. Rao, R. A. Leitgeb, and T. Lasser, “Fast focus field calculations”, Optics Express **14**, 11277 (2006).

Chapter 6. Two-photon laser-assisted device alteration in CMOS integrated circuits using linearly, circularly and radially polarised light

6.1 Introduction

The progressive decrease in feature sizes of complementary metal-oxide semiconductor (CMOS) ICs means that diagnostic solutions for spatial fault localisation within these devices must be continuously refined to remain relevant for the prevailing technology node. LADA, which was introduced in Chapter 1.4.3 with other FA techniques, is a well-established imaging/analysis modality used to isolate interaction sites of timing-critical transistors [1]. In its original form, LADA employed a CW laser and therefore provided no detailed temporal information [2, 3], however it was recently shown how this limitation can be overcome by using TPA induced by an infrared femtosecond laser [4]. In this earlier work it was demonstrated how TPA, which generates electron-hole pairs within the active CMOS layer, could be synchronised with the internal clock of the device to allow a race condition to reveal speed-limiting transistor-switching evolution with a timing resolution below 10 ps [3].

In this chapter the role of the polarisation state of the excitation light in 2pLADA performance is discussed. Previously, it was shown that the OBIC lateral resolution is significantly enhanced by TPA due to the effective narrowing of the PSF associated with the nonlinear character of TPA [5]. The resolution achieved in sub-surface CMOS imaging is also considerably enhanced by using a SIL [6] and the highest resolutions can be achieved by combining TPA with SIL imaging [7]. Under the high values of NA associated with SIL microscopy it is known that the polarisation state of the incident light plays a significant role in determining the image resolution [8]. The conventionally employed linearly polarised light forms an approximately elliptical focal spot [9], extended along the electric field vector of the light, implying that RP illumination could be used to reduce the PSF area further, since RP light experiences no equivalent PSF distortion under high-NA focusing [10].

In the following sections the outcomes of 2pLADA imaging using various polarisation states are detailed. Linear, circular and radial polarisations were employed to investigate how 2pLADA imaging resolution depends on the electric field distribution of the incident light. The imaging system employed a liquid-crystal RPC [11, 12] to generate a radially polarised beam with a high degree of mode purity, and in a way which allowed easy insertion and removal of the RPC to facilitate direct comparisons between different polarisation states of the incident light.

6.2 Radiation effects on silicon circuits

This section introduces the photocurrents induced in the elementary devices as well as their influence on transistor switching times. To understand the interaction between the laser generated photocurrents and the semiconductor devices, the physical phenomena behind them are explained. First, this section introduces the laser beam induced photocurrent effect on n-channel MOSFET (nMOS) and p-channel MOSFET (pMOS) transistors.

6.2.1 Ultrashort laser pulse interaction with ICs

Incident light on a device causes two effects to occur: generation of electron-hole pairs and heating of the device. Localised photocurrents within the device are generated by absorbing photons, which are of sufficient energy to span the bandgap of silicon (1.12 eV), and so generate electron-hole pairs. The photo-generated currents affect the timing of a transistor either directly by assisting a load capacitance to charge and discharge or indirectly through the local perturbation of electric potential while altering the transistor's operating point [1]. The localised heating effect is based on affecting the local charge carrier mobility and reducing the net driving strength of the transistor. This leads to a slowdown of the signal transition edges. However, the maximum temperature modulation by the laser is only a few tens of degrees [13], and the delay variation is very weak compared to the propagation through the transistor [14, 15]. As a result, the photoelectric effect is dominant over the weak thermal stimulation, which can usually be neglected [16, 17].

The laser stimulation via SPA generate excess carriers within the active area of the semiconductor. These excess carriers have a characteristic lifetime, after which they recombine via non-radiative processes. However, if excess carriers are generated inside the depletion region they are dissociated by the potential, leading to a localised photocurrent. This photocurrent temporally modifies the switching times of the CMOS inverters [18].

The CMOS inverters are described by their characteristic propagation delay times (time delay between input and output). The propagation delay times determine the signal delay variation during the transistor switching events from low to high (t_{PLH}) and from high to low (t_{PHL}). t_{PLH} and t_{PHL} describe the required time for the signal to reach 50% of the total signal level. The propagation delay formulae for a CMOS inverter are given as:

$$t_{PLH} = 0.52 \frac{C_L V_{DD}}{I_{DSATn}}, \tag{4.1}$$

$$t_{PHL} = 0.52 \frac{C_L V_{DD}}{I_{DSATp}}, \tag{4.2}$$

where C_L is the load capacitance, $V_{DD}$is the supply voltage and I_{DSATn} and I_{DSATp} are the saturation currents for nMOS and pMOS transistors.

The overall propagation delay through the CMOS inverter is the average of the two values:

$$t_{PD} = \frac{t_{PHL} + t_{PLH}}{2}. \quad (4.3)$$

V_{DD} and C_L are not affected by the laser beam, however the charge and discharge time of the load capacitance depends on the generated photocurrent [19].

The induced photocurrent affects the timing properties of device by directly assisting the charging or discharging of a load capacitance (Fig. 4.1). pMOS and nMOS transistors exhibit different characteristics and the locally induced photocurrent can be used to advance or delay the timing of inverters. This approach can be applied to monitor the performance-limiting sections within the critical signal path of IC [20-22].

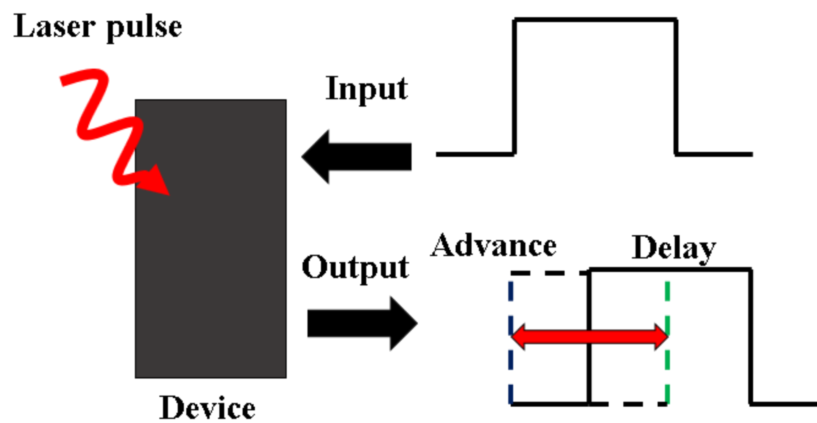

Figure 4.1. Delay variation caused by the laser beam incident on a delay chain [20].

The acquired delay variation at the output depends on the rising and the falling edges, the number of the inverters within the chain and the stimulated device type (nMOS and pMOS). Fig. 4.2 shows the stimulation of a pMOS transistor, which experiences the advance at the rising edge of the output for low to high transition. The laser stimulation generates the additional current within the pMOS transistor and enhances its driving strength. This decreases the charging time of the load capacitance leading to a faster switch of the transistor. The effect on the nMOS transistor is the opposite. When the transistor is going from “off” to “on” state, the additional photocurrent subtracts from the nMOS current and thus slows down the switch on the nMOS device. The same effect alters the charging time of the output load capacitance when the signal is transitioning from the high signal state to the low signal state. Therefore, the discharge time of the load capacitance for the pMOS transistor increases (slowdown of the device) while for the nMOS device the additional photocurrent leads to the faster discharge time (speed up of the device) [1, 22-24].

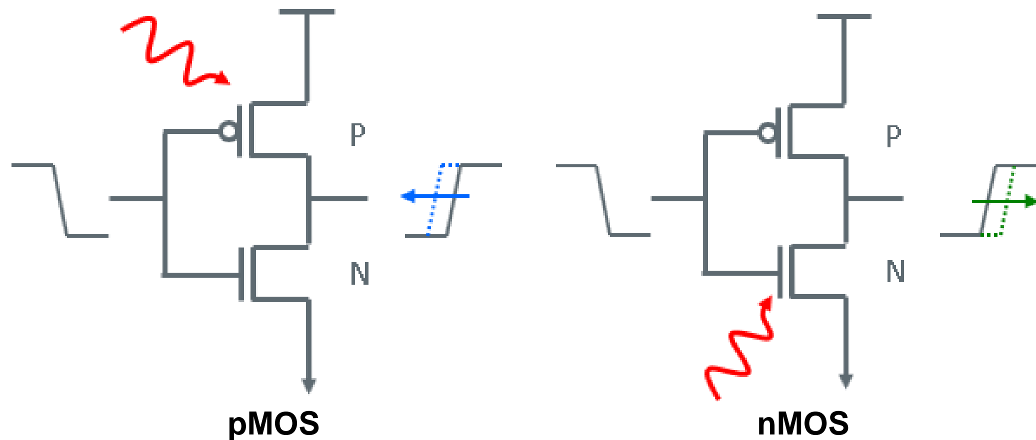

Figure 4.2. The effect of laser impulse on the rising edges of a single inverter output. The blue arrow depicts the rising edge of the pMOS transistor and the green arrow depicts rising edge for the nMOS transistor.

Introducing high current into the device can affect the global response of the sample and alter the response time of even unilluminated sites. To overcome this problem, CW lasers have to be replaced with pulsed lasers, which have high peak powers but low average powers and affect ICs in a highly localised manner [23].

The laser stimulation of ICs can be also applied to inject soft faults into internal nodes of the device. Typically, this soft faults appear in memory elements, such as static random-access memories (SRAMs) or flip-flops. The generated photocurrent increases the signal voltage of the memory element transistor. This voltage alters the logical output of the flip-flop or single event upset (SEU) in the signal value causing an error in the device [25]. Ultra-fast lasers can be employed to drive the soft fault injection technique for the analysis of SEUs. The laser pulse simulates the response of a memory cell as if a heavy ion or cosmic ray is incident into the device, which may cause a corrupt logic signal and lead to the failures of the device [26].

Another application for ultrashort laser pulses is the soft fault injection technique to track down the switching event of the transistor. An ultrashort pulse can be locked to the external trigger provided by the tester to perform a time mapping of the sensitive areas of the device and record the event that is responsible for faulty operation [27]. A more thorough discussion on single-event effects (SEE) is presented in the following section.

6.2.2 Single event effects

Single-event effects are a type of radiation effects caused by the impact of a single energetic particle such as a heavy ion [28, 29]. Energetic particle events occur randomly and can appear in any sensitive node within the device. The incident particle interacts with the silicon lattice and transfers energy to the silicon atom generating electron-hole pairs (Fig. 4.3a). Typically, the heavy

particle leaves a track of electron-hole pairs along its path. These electron-hole pairs can recombine, however the carriers, which do not recombine, can be transported through the silicon by drift and diffusion mechanisms. This generates the transient current, which can disrupt the operation of the device. The reverse-biased junctions are the most sensitive parts of the device, where the electron-hole pairs are the most likely to contribute to the transient current [30].

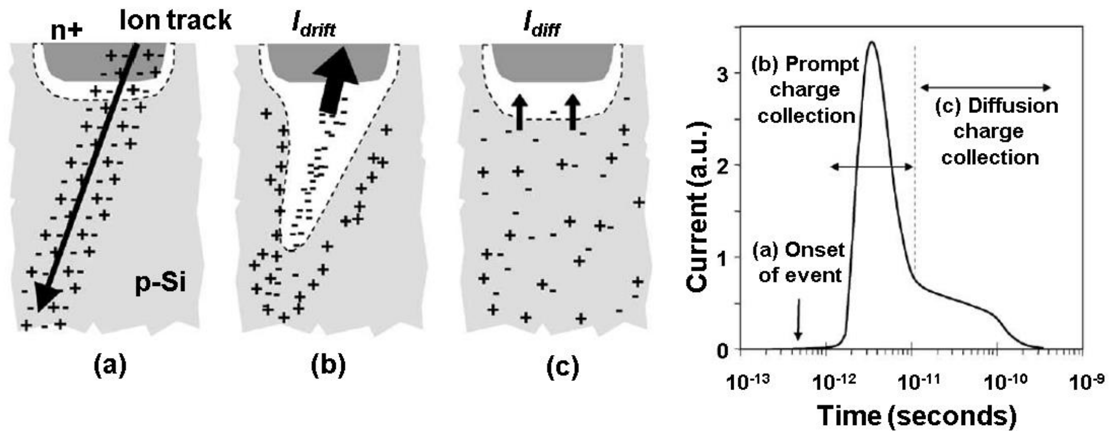

Figure 4.3. Charge generation and collection phases in a reverse-biased junction and the resultant current pulse caused by the passage of a high-energy ion. [30].

If the heavy particle strikes close to the depletion region, electron-hole pairs are rapidly separated by the electric field leading to the high transient current. This form the funnel shaped potential (Fig. 4.3b), which size depends on the doping of the substrate (larger for lower doping) and incoming particle energy. This energy is known as the linear energy transfer (LET), which describes the amount of energy distributed per unit of distance along the particle path [30].
The perturbed potential leads to the enhancement of the drift (charge collection) extending the depletion region deeper in the substrate. This event happens rapidly in the timescale of nanosecond and causes a transient current spike (Fig. 4.3). After that only slow diffusion phenomenon drives the charge collection, which happens over hundreds of nanoseconds until all the excess carriers are collected or recombined (Fig. 4.3c). The high transient current can change the logic state on the sensitive memory elements and cause the system to fail [31-33].

Single event upset

It was introduced in the previous section that the charge collection mechanism in ICs typically appears in reverse-biased junctions due to the presence of the strong electric field in the depletion region. An additional charge can be collected by the diffusion process, which forces carriers outside of the depletion region to return to the junction. A parasitic bipolar transistor introduces another collection mechanism, which is known as the bipolar amplification [34]. These three charge collection mechanisms can contribute to SEEs and lead to the logic upset, significant voltage change, or alteration of stored information causing SEU to occur [35]. SEUs do not only

appear in the space equipment or when the high levels of radiation are present. Cosmic rays also consist of many energetic particles that can generate SEUs in terrestrial equipment.

In CMOS circuits, the "off" transistors struck in the junction area by a heavy ion of high enough LET are prone to lead to SEUs. SEUs are events in which an incident particle can strike a key node within a device resulting in a local ionisation that can cause a change of state [34]. The probability of the SEU to happen depends on factors like the node capacitance, the operating voltage and the speed of the feedback circuit [36]. The node capacitance together with the channel resistance acts as a low pass filter that may reduce the rising slope and magnitude of the induced current pulse. With downscaling of technology and feature sizes, the operational voltage of a device is also decreased. This means that less charge is needed to induce an SEU. Increasing the capacitive load is therefore a known design technique to reduce the sensitivity as the technology nodes gets smaller [37].

Combined, parameters like these define the amount of charge or energy needed to flip the bit of a memory cell. This is also referred to as the critical energy, E_{crit}, or critical charge, Q_{crit}. SEUs can be induced if a charge larger than the critical charge has been collected by the sensitive node [38].

The dominant mechanism of energy loss by a charged particle passing through a material is Coulomb scattering by the atomic electrons of the material, as the nucleus size is very small. Nevertheless, nuclear interactions play an important role prior to the creation of an SEU and will be discussed in this section.

A measure for the energy loss of a particle per unit length is the stopping power. The stopping power can be related to the number of electron-hole pairs produced per unit length along the particle's track. [36]. The stopping power is dependent on the kinetic energy and charge of the particle. Except for very low energies, the higher the charge of the ion the higher is the stopping power. Therefore, the α-particle has a higher stopping power than the proton. After travelling a certain distance in the material, the ion eventually loses all its energy and comes to rest [37].

Highly energetic neutrons and protons can collide even with the nucleus of the target material and induce a nuclear reaction. Compared to the Coulomb interactions nuclear reactions are rare events. However, due to a large number of SRAM cells in modern devices, significant particle fluxes, and the long exposure times, those collisions happen often [37].

Interactions between a proton or neutron and a nucleus can be either elastic or non-elastic. In an elastic interaction the incident and outgoing particles are the same. Due to the small amount of momentum transfer in an elastic collision they are considered to only play a minor role of SEU rates [34]. In a non-elastic interaction additional particles can be created and emitted from the reaction. One or several of the particles may be emitted with the right direction and enough energy

to reach a sensitive transistor. It is typically the recoil ion or an α-particle that possesses enough stopping power to induce an SEU [37].

Single event transient

A single event transient (SET) is a transient pulse in the logic path of an IC. Similar to an SEU, an SET is induced by a charge deposition of a single ionising particle. An SET can be propagated along the logical path where it was created. It may be latched into a register, latch or flip-flop causing their output value to change. Most devices are highly resistant to SETs due to the large capacitive loading of the single path [39]. Compared to SEUs, SETs are therefore considered a negligible problem and are not treated in this thesis.

Single event latchup

Latch-up event (SEL) is typically caused by the parasitic activation of a structure resembling a thyristor composed of two NPN and PNP bipolar transistors. The latch-up can be initiated by a voltage spike, high operating current or a heavy ion. An SEL is often the cause of more severe faults than that of a soft error because a power-reset is required. The SEL can cause a permanent damage to the device by creating a short-circuit if it is not limited on time.

The SEL rate increases significantly with not only higher supply voltage and operating current but also with operating temperature. However, lower voltage and temperature control of the device leads to the poor performance of the IC.

In order, to avoid this undesirable effect there are ways to mitigate SEL, such as the ring guard and the shallow trench isolation. Resistance limits current, however, this makes the design of the device more complicated as the required current limit must be specified. Also, a large resistance will affect the proper performance of a circuit, while a small value may fail to provide protection. The second technique to prevent SEL is using cut-off circuits based on the current comparison.

The failure event causing a latch-up can be visualised using the photon emission technique. Also, the OBIC technique can detect latch-ups by triggering them intentionally with the help of electron-hole pairs generated by the radiation of the laser beam and highlighting the sensitive areas of the device, which may need to be redesigned [40].

Single event function interrupt

Single Event Function Interrupt (SEFI) typically indicates a pseudo-hard error within IC. SEFI temporally alters the device implemented functionality such as a loss of configuration capability, placement in test mode and a lock-up. Usually to recover from SEFI requires a power reset. The SEFI cross section is typically orders of magnitude lower than the SEU cross section [39].

Single event burnout

ICs do not have an intrinsic mechanism to amplify the currents generated by a single event strike, therefore Single Event Burnout (SEB) occurs only under certain conditions. SEU has to create a sufficient charge within the device to initiate avalanche multiplication, which sustains the current flow for minimum time to lead to localised self-heating [41]. This temperature change modifies the current-voltage characteristic of the diode around the strike point, such that the current becomes locally self-sustaining. The self-sustaining current eventually spreads throughout the device due to higher particle mobility in the cooler parts of IC, supporting the ever increasing current until permanent damage through melting or cracking of the device occurs [42].

Single event gate rupture

Single Event Gate Rupture (SEGR) occurs when the energetic particle strikes the drain node in the body area of the epitaxial region, which is at the surface. Two response mechanisms can cause SEGR in the IC: dielectric and epitaxial.

The dielectric SEGR happens when a high positive charge accumulates close to the Si-SiO_2 interface. The charge builds up rapidly on the order of picoseconds time scale and leads to the high electric field, which can cause a breakdown if it exceeds the critical oxide breakdown field. The breakdown caused by SEGR produces permanent damage to the device.

The epitaxial response distorts depletion field in the epitaxial region forming the funnel shape potential, leading to the appearance of the electric field between epitaxial and dielectric layers. If this excess electric field strong enough, the irreversible dielectric breakdown occurs [43 - 45].

Single event hard error

The single event hard error (SEHE) occurs in memory devices, typically SRAMs, where a single bit becomes stuck in a certain state due to permanent or semi-permanent damage caused by ionising radiation. Stuck bits cannot be fixed with a power cycle, however the bit may anneal over time and start to function once more [46].

6.2.3 General SEE testing approaches

As SEEs usually occur in space environments, testing is rather expensive under these conditions. There are three types of high-flux sources for terrestrial IC testing of SEEs: particle accelerators, lasers, and X-ray generators [47, 48].

Particle accelerators

The original sources for terrestrial testing and the closest comparison to actual space environments are particle accelerators. These devices produce energetic ions which can then be used to excite carriers in IC. Most particle accelerators use a broad beam, where particles arrive at random

intervals, across a large region (2 cm^2). A variety of facilities with different ion masses and energies allow for robust characterisation of a wide variety of different environments and effects. Also, there are possibilities to use a smaller region of exposure. Microbeam particle studies have shrunk the window of opportunity to 3.7 mm^2. These devices are able to raster over the region of interest [49]. However, this approach has its limitations to the energy range of particles that can be used in this setup. Particle accelerators are usually an expensive IC testing technique.

Pulsed X-ray technique

Focused X-Ray testing is a relatively recent technique for single event testing, and is still under development [50]. X-Ray irradiation has two main advantages: the carrier generation region can be made to closely match that of a variety of ions and energies, and has the ability to transmit radiation through metal layers. The major issue is that X-Ray irradiation will generate trapped charge in device oxides, which can lead to malfunction of the device [51].

Pulsed laser technique

A main task for the pulsed laser testing technique is to simulate conditions similar to those when a heavy particle strikes the IC. Laser stimulation can generate carriers and create excess charge within the device leading to appearance of SEEs. These later can be used to track down the fundamental mechanisms responsible for their generation. The SEE response is recorded at the different z planes and with varying laser pulse energy. The obtained map of SEEs can be compared with a CAD design of the IC and sensitive transistors can be identified [52]. The use of ultrashort pulse lasers improves the localisation resolution by reducing the diffusion length of the photogenerated carriers.

Many SEEs appear under certain timing conditions, which mostly occur during the transistor's switching events. Therefore, it is highly important to inject carriers at the right time to fully understand the dynamics of the IC. Temporal aspect of ultrashort pulses makes it possible to synchronise the arrival of laser pulses with the tester clock. Such time-resolved carrier injection technique determines a time window when the device is vulnerable to SEEs with the high picosecond resolution accuracy [53, 54].

Also, ultra-short pulses allow to deposit large amounts of energy over very short periods of time leading to the high peak powers. This is very useful for SEE analysis as laser pulses can generate charge densities, which exceed even those generated by the most energetic cosmic rays. Therefore, it is possible to perform very sensitive analysis and simulate permanent failures like SEBs and SELs [55, 56].

For many SEUs to occur, an energetic particle is required to generate excess carriers within two nodes. Therefore, particles must be incident at the angles close to a grazing angle. Laser light can

simulate such conditions by moving the test device out of the focus in order to hit both nodes at the same time. However, such option requires to increase the pulse power to obtain the similar charge densities. [56].

6.2.4 LADA and 2pLADA techniques.

This section introduces the laser-based analytical technique known as LADA, which is qualitatively similar to previously introduced SDL but which differs in both approach and application [1]. Unlike other dynamic analysis techniques, LADA provides the ability to quickly isolate critical signal paths and their limiting elements. LADA can accurately (individual logic gate level) track down the defects, which appear in the device functionality and are not produced during manufacture [57-58].

LADA

The basic concept of LADA technique is introduced in this section. As other dynamic techniques, LADA is based on the functionality test. To implement such test, the circuit is first characterised by obtaining a Shmoo plot, which determines the impact of two parameters on the functionality of the circuit. Most often, these two parameters are the operating frequency of the IC and the supply voltage. For each selected voltage and frequency value, a functional test is carried out and provides the value of the parameters where the circuit is functional (passing) or non-functional (failing). The Shmoo provides the functionality limit of the device. Therefore, IC sample has to be biased close to the IC pass-fail boundary for the obtained fixed voltage and frequency settings. This pass-fail transition, combined with the exact coordinates of the point of impact of the incident laser beam affects the timing of a transistor located within the critical signal path (the longest path between input and output), such that the change in maximum operating frequency can be detected (Fig. 4.4). [1]. It was introduced in the previous sections how laser pulse alters the transistor's timing properties.

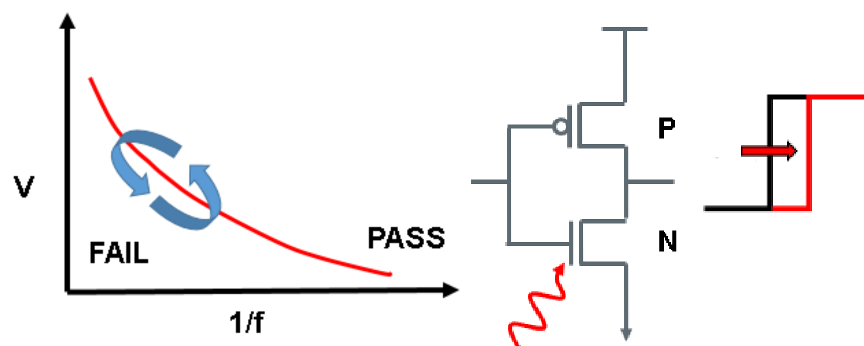

Figure 4.4. The LADA concept: A scanning laser affects a critical-path transistor's characteristics, thereby changing signal timing sufficiently to cause transitions in the device's pass-fail condition.

When the DUT is operated in a pass-fail boundary condition, even small changes in timing within the critical path can lead into a transition from pass to fail or fail to pass states, depending on the DUT's bias and increase or decrease in delay. A CW near-infrared wavelength laser is typically used for LADA and is either raster scanned across the area of interest as the automatic test equipment runs a test pattern or is precisely set at the suspected area of interest. During each test cycle, the passing or failing state of the DUT is resolved and a signal indicating the state of the device is triggered by the tester. This pass-fail trigger is synchronised to the laser spot position in the IC [1].

The amount of timing perturbation is directly related to the laser power introduced in the transistor. Therefore, the laser power can be tuned to reach the threshold of LADA signature appearance. This makes it possible to determine the relative sensitivity of the test device in a highly accurate fashion. Lasers operating at high frequencies are able to be synchronised with tester clocks on a high-resolution timescale of tens of picoseconds or less [1].

It was demonstrated that the pMOS device is more affected than the nMOS transistor. Also, most of the electrons are injected within the n-well junction of the pMOS transistor. These electrons exhibit strong diffusion and thus increase the effective spot radius leading to the inability to isolate the single LADA signatures of the nMOS or pMOS transistors (Fig. 4.5a). This limitation of the LADA technique can be overcome by expanding it to the TPA and introducing 2pLADA [1], which is the subject of the research carried out for this thesis.

2pLADA

Femtosecond near-infrared laser illumination can deliver sufficient levels of optical peak power for the TPA phenomenon to occur. As mentioned before, TPA depends on the square of the irradiation intensity and therefore happens only in the vicinity of the focal spot. As a result, the beam is not absorbed along its path and no carriers are generated. This addresses the problem for the requirement to focus light through a thick substrate while imaging ICs. Moreover, the absorption in a highly localised volume produces a strong signal in the focal spot, while shrinking the PSF at the same time. This can be further enhanced by combining TPA with a pulse-to-DUT synchronisation scheme when the arrival of femtosecond laser pulses could be locked and temporally shifted with relatively to the automatic test equipment (ATE) clock frequency with picosecond precision [59].

As was discussed in the previous section, conventional LADA exhibits a single polarity signature, which is typically biased towards the pMOS transistor due to its favourable light-matter interaction sensitivity [1]. However, 2pLADA can produce highly localised LADA signatures when a pulse arrives at the inverter's switching event. This reveals both individual pMOS and

nMOS transistors and unlike LADA does not exhibit a strong pMOS dominance (Fig. 4.5b). Moreover, 2pLADA achieves higher signal acquisition rates, since the higher peak power of the mode-locked laser pulses makes it possible to perturb and visualise weaker LADA sites more easily without introducing too much average power and damaging the device [59].

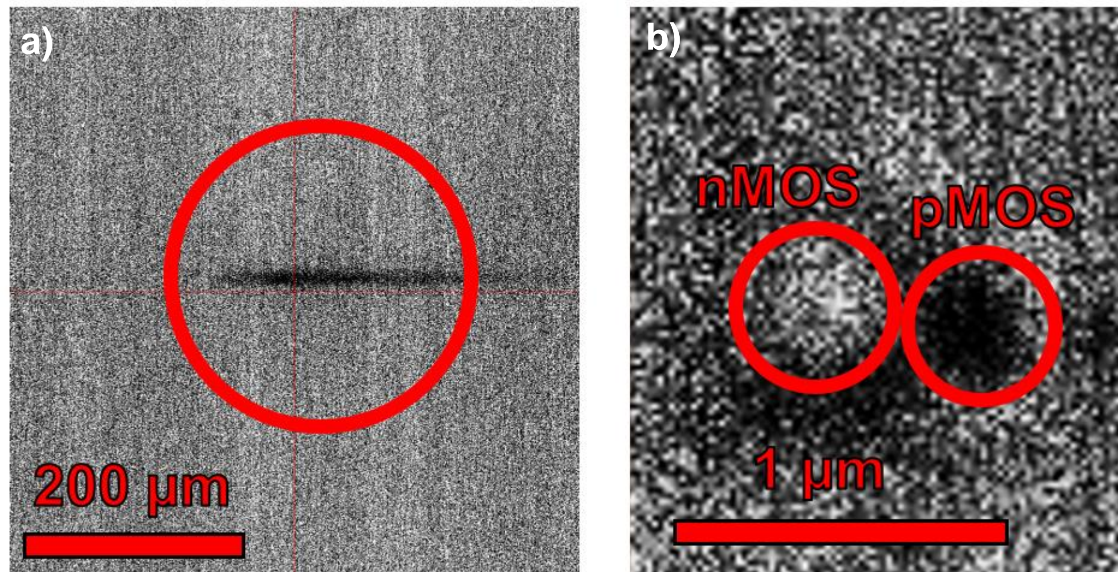

Figure 4.5. (a) LADA and (b) 2pLADA sites, obtained from the DUT by the thesis author in Freescale Semiconductor with the DCG Systems FA tool "Meridian IV". LADA technique exhibits strong pMOS transistor's dominance (black passing signature), which hinders the localisation of nMOS transistor (white failing signature). 2pLADA produces highly localised signatures revealing both pMOS and nMOS transistors.

In addition to the enhanced localisation capabilities provided by 2pLADA, the use of synchronised laser pulses makes it possible to temporally resolve the switching evolution of individual transistors. This was demonstrated by irradiating two neighbouring logical elements in terms of electrical signal propagation. Then the strongest 2pLADA signatures were recorded, which happened to be at the different delay to the test loop trigger. Pulses were shown to arrive at Site A (B) 2.92 ns (3.06 ns) after with a timing accuracy <10 ps. This result was found to have a precise agreement with theoretical modelling results [59].

Another capability of the 2pLADA technique is that the high peak power delivered by the femtosecond laser can also temporarily disturb the prescribed digitisation in the memory cells. This can lead to the generation of the previously described SEUs. These defects can be recorded in the same LADA image, where they produce strong signatures [59].

6.3 Raman-shifted femtosecond Yb:fibre laser for 2pLADA at 1280 nm

In order to implement 2pLADA a suitable laser irradiation source had to be employed. Therefore, in this section a special Raman soliton Yb:fibre femtosecond laser, developed for 2pLADA is introduced. Such an Yb:fibre laser design was chosen as it enabled the generation of ultrashort femtosecond laser pulses at 1280 nm wavelength with a repetition rate of 100 MHz. These parameters were suited very well for the 2pLADA application as the 1280 nm wavelength is a perfect choice because is long enough for TPA in silicon and short enough to enable high localisation resolutions. Femtosecond pulse durations are necessary to obtain high peak powers to initiate TPA and the 100 MHz repetition rate is suitable to lock the laser to the ATE (tester) clock frequency.

6.3.1 Yb^{3+} optical properties

Ytterbium is a rare earth ion, which is an established dopant to provide a laser generation in fibres. The attractiveness of the Yb^{3+} ion as a gain material is because of its simple energy level structure. The Yb^{3+} ion has a ground level $^2F_{7/2}$ with four Stark sub-levels and the metastable excited state $^2F_{5/2}$ with three sub-levels [60-63]. Therefore, there is no ESA at either the pump or lasing wavelength, which is apparent in the Er^{3+} ion as discussed in Chapter (2..1). Yb^{3+} has a large separation between the ground and the excited states preventing nonradiative phonon decay. This allows higher concentration doping even into the high energy phonon silica fibres to reach very efficient lasing. Moreover, the Yb^{3+} absorption and emission spectra are very broad as shown in Fig. 4.6, and also they slightly depend on the glass materials used [64].

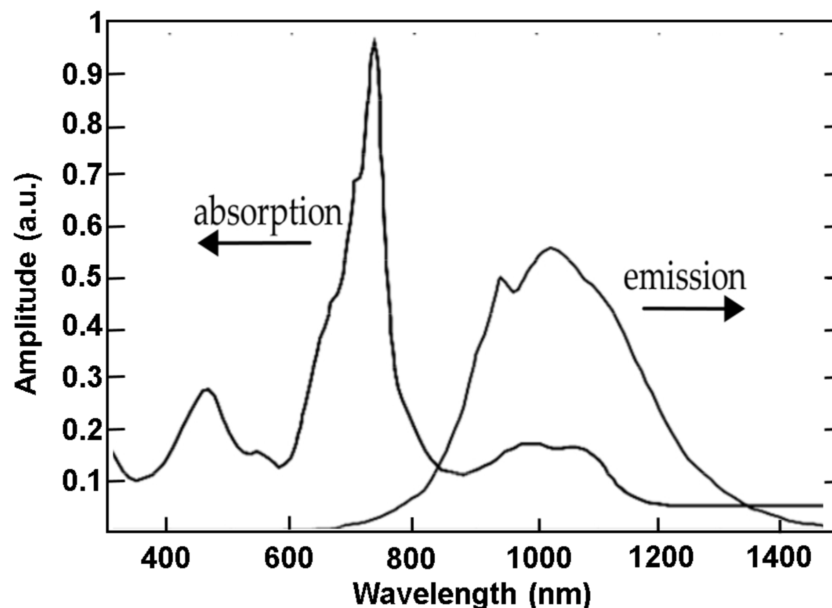

Figure 4.6. Yb^{3+} absorption and emission spectra.

The broad absorption allows a wide choice of high-power pump sources. The absorption spectrum has two peaks at 915 nm and 975 nm, which match the output wavelengths of commercially available laser diodes. Most of these laser diodes have linewidths of a few nanometres, which can be too wide for efficient pumping for other gain media. Even though the pumping with the 975 nm source is more efficient but it requires active cooling as a slight shift in the wavelength can result in a significant change in absorption. This is less critical for a 915 nm pump source [62].

The broad emission spectrum makes it possible to achieve a tunable laser generation and a broadband amplification. The development of fibre gratings also enables a narrow linewidth operation at the desired wavelengths. Finally, the emission and pump wavelengths are close, leading to a low quantum defect and less heat generation within the system [65].

6.3.2 Soliton self-frequency shifting

Solitons have been introduced in Chapter 2 and were shown to possess unique features. Solitons not only preserve their pulse shape as they propagate along the fibre but also can be shifted via the soliton self-frequency shift by changing the input power. This phenomenon can be used to generate new frequencies, which can be useful for optimising the wavelength of the pulsed laser used for FA.

In this section only fundamental solitons are considered since higher-order solitons are not stable and break into several bands, including one or several red-shifted fundamental solitons and blue-shifted nonsolitonic radiation [66].

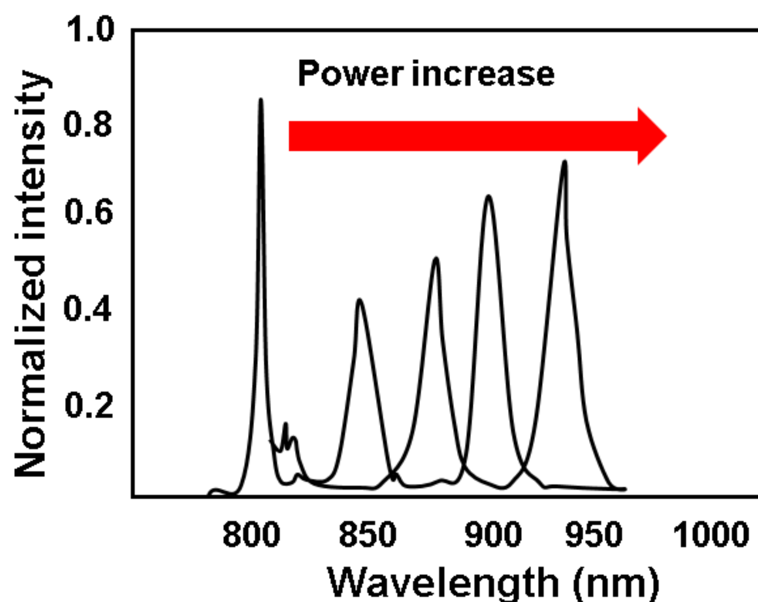

Figure 4.7. Example of increasing soliton redshift with increasing input power (adapted from [67]).

Shift of the main soliton frequency can only appear by frequency-dependent losses or gain in the fibre. If the soliton is of sufficient bandwidth, the Raman scattering amplifies the lower frequency components at the expense of the high frequency components resulting in red-shifting of the soliton. This effect is known as the soliton self-frequency shift (SSFS) and depends on both the peak power of the soliton and its bandwidth. If the soliton spectrum overlaps with the Raman gain spectrum it is possible to derive an equation [67, 68]:

$$\Delta\omega(z) = \frac{-8|\beta_2|T_R}{15T_0^4}z, \tag{4.5}$$

where $\Delta\omega(z)$ is the expected frequency shift over propagation distance z, β_2 is group velocity dispersion, T_R is characteristic Raman response time and T_0 is characteristic soliton time related to its pulse duration $T_{FWHM} = 2\ln(1+\sqrt{2})T_0$. The parameter T_R is related to the Raman response function of the medium $R(t)$, which takes into account the electronic and vibrational Raman response [69]:

$$T_R = \int_{-\infty}^{\infty} tR(t)\,dt\,. \tag{4.6}$$

As it can be seen from Eq. (4.6), the redshift increases linearly over the distance, so the longer the fibre, the higher the final frequency shift at the output (Fig. 4.7). Also the overall redshift has an inverse quartic dependence on soliton pulse duration. Therefore, even a small decrease of the duration and peak power of the pulse translates to an enhanced frequency shift, since the soliton's peak power P_0 is related to the pulse duration T_0 as [70]:

$$P_0 = \frac{|\beta_2|}{\gamma T_0}, \tag{4.7}$$

where γ is a nonlinear coefficient.

SSFS forms the basis of Raman supercontinuum generation when the high power pulse breaks up into several solitons and nonsolitonic radiation. Therefore, a broad spectrum of pulse durations propagates inside the fibre, which leads to a range of total frequency shifts and the net result of the generation of a smooth extended continuous spectrum, or supercontinuum [71].

6.3.3 Raman-shifted femtosecond Yb:fibre laser construction

The Yb:fibre laser employed for the 2pLADA experiments was designed and built by Dr. Carl Farrell. It was shipped to the USA for experiments, which I carried out at Freescale and DCG

Systems. The laser was designed to work in a ring cavity configuration, which is shown in Fig. 4.8.

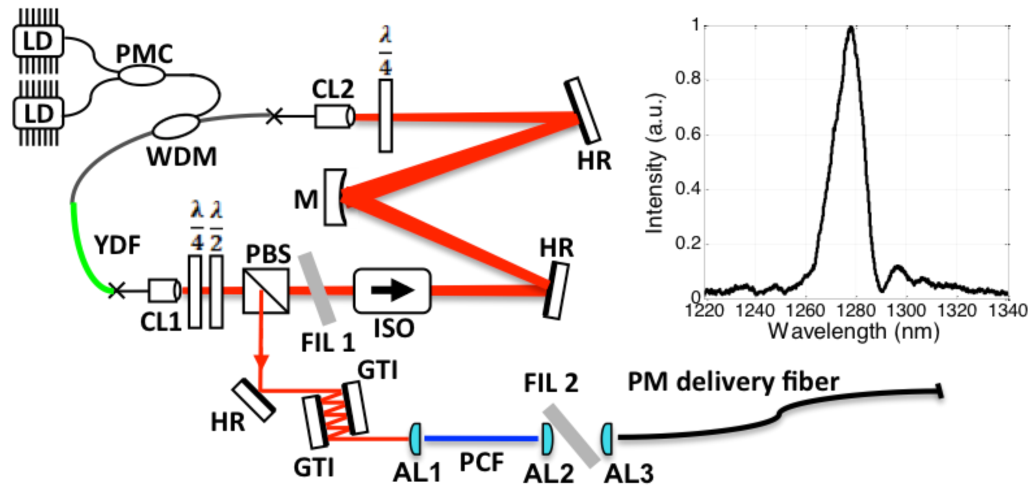

Fig. 4.8. Schematic of the Raman-soliton laser source. WDM, wavelength-division multiplexer; YDF, ytterbium-doped fibre; CL, collimator; λ /2, half-wave plate; λ/4, quarter-wave plate; ISO, isolator; PBS, polarising beam splitter; FIL, interference filter; HR, high reflector; M, curved mirror; LD, laser diode; PMC, polarisation maintaining combiner; GTI, Gires-Tournois interferometer; PCF, photonic crystal fibre; AL1- AL3, aspheric lenses. The laser generated 1280 nm pulses with an average power of 20 mW. Inset: laser spectrum, showing a centre wavelength of 1278 nm and a bandwidth of 13 nm.

The fibre section consisted a 19 cm length of highly doped Yb fibre with a 4.5 cm length collimator spliced onto both ends. Therefore, the total length of the fibre section was 28 cm. The free-space section was designed to be ~190 cm long and contained the components required to achieve mode-locking via NPR [72]. Two QWP and a HWP were used to control the directionality of the polarisation leaving the fibre and the polarising beam-splitting cube worked as an output coupler. A 10 nm bandwidth spectral filter was inserted at an angle to transmit a centre wavelength of 1030 nm. The laser was pumped by two 675 mW and 976 nm diodes, which were polarisation combined into a single fibre using a PM combiner. The pump power was coupled into the Yb fibre with the 78% efficiency through two dichroic mirrors highly transmitting 976 nm and highly reflecting 1030 nm light. The optical isolator was inserted to ensure the unidirectional propagation of light within the ring cavity. Also in the free-space section a curved mirror was placed along with two high reflectors. The curved mirror imaged the mode from the first collimator into the other, yielding an improved coupling efficiency. The suitable curvature of the imaging mirror was chosen using ABCD matrix model and was found to be 500 mm radius of curvature.

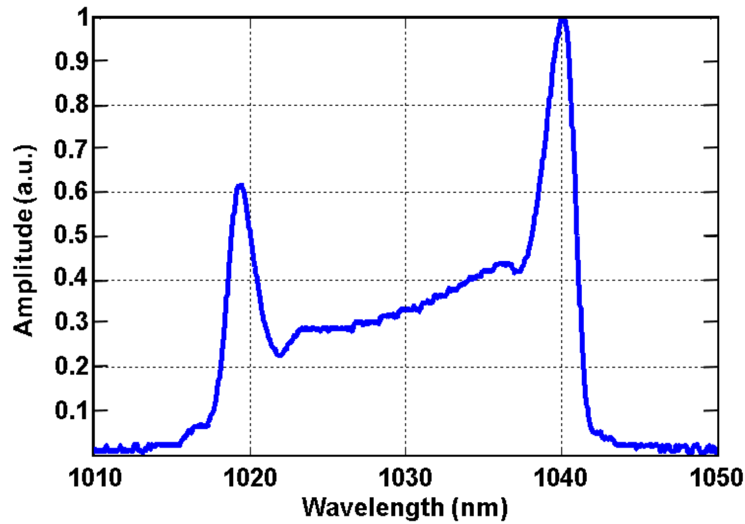

Figure 4.9. The optical spectrum of the mode-locked Yb:fibre laser.

The optimised Yb:fibre laser had an output power of 350 mW at a 100 MHz repetition rate. The measured optical spectrum and interferometric autocorrelation of the laser are shown in Fig. 4.9. As it can be seen, the spectrum cannot be described by common Gaussian or Secant profiles. Therefore, a fitting procedure was performed to estimate the duration and shape of the pulses at the output. For this, the optical spectrum was recalibrated into frequency through the addition of quadratic and cubic spectral phase before conducting a Fourier transformation to obtain the pulse shape. The autocorrelation of this pulse was numerically calculated and matched with the experimental data while changing the quadratic spectral phase. The obtained pulse was found to be of 1.3 ps duration. The pulse was heavily chirped and therefore, Gires-Tournois interferometer (GTI) mirrors were used to compensate GDD and acquire transform limited pulses. By using 10 bounces of the mirrors and one reflection from the steering mirror the pulse was compressed to the value of 160 fs (Fig. 4.10).

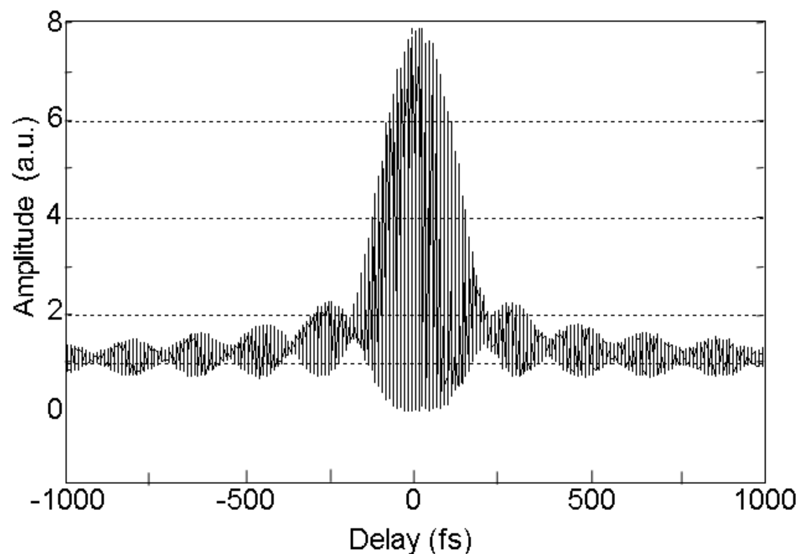

Figure 4.10. Autocorrelation of the 1030 nm pulses after 10 bounces on the GTI mirrors.

Next, these de-chirped pulses were coupled with 75% efficiency into a highly nonlinear PCF. The resulting super-continuum contained chirp-free Raman-soliton pulses at the desired wavelength of 1280 nm, which were then isolated by using a thin-film long-pass filter with a cut-off wavelength of 1200 nm (Fig. 4.11a). Finally, the filtered 1280 nm pulses were coupled into a polarisation-maintaining delivery fibre, after which they were measured to have durations of 200 fs (Fig. 4.11b) and an average power of 20 mW.

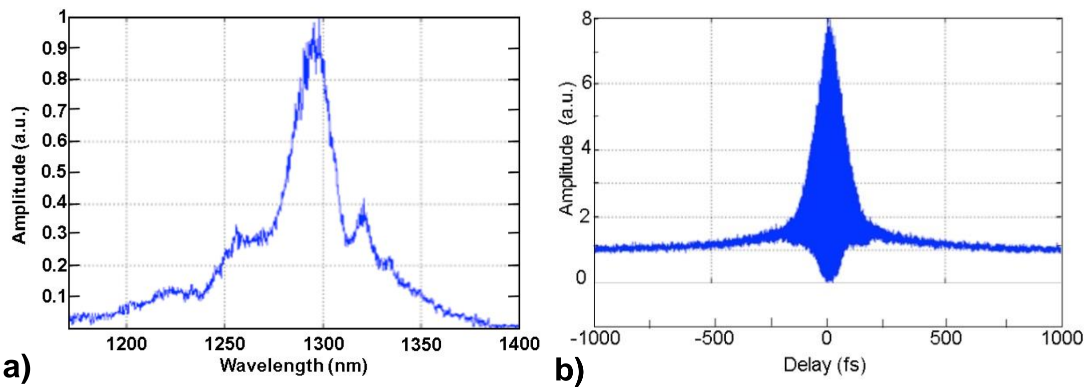

Figure 4.11. (a) The optical spectrum of the SSFS Yb:fibre laser with (b) the corresponding interferometric autocorrelation.

6.3.4 Repetition rate stabilisation to an external clock

The pulse repetition frequency of the Yb:fibre laser was locked to an external 100-MHz clock supplied by the tester. The locking scheme is depicted in Fig. 4.12. A small part of the light after the GTI mirrors was deflected into a fast photodiode. The signal from the fast photodiode was filtered using a < 500-MHz low-pass filter and locked to a tester using mixer (MiniCircuits ZFL-500LN). The resultant beat was passed through a PI controller and through a high-voltage amplifier before reaching the piezo driving the placement of collimator in the cavity.

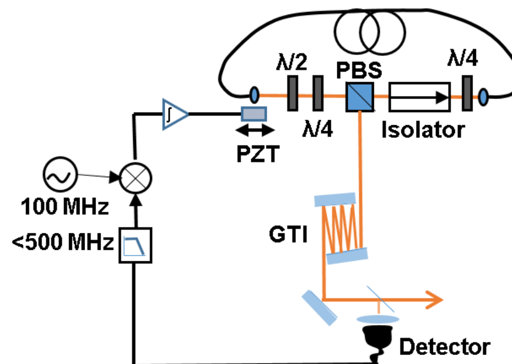

Figure 4.12. The schematic of the repetition rate locking of the Yb:fibre laser.

A 9-µm-travel piezo element was included in the cavity by placing it in the collimator's translation stage, and, due to the stretching of the laser cavity to accommodate the PZT, the resulting Yb:fibre laser now had a pulse repetition frequency of 100 MHz, which could be modified over a range of ~500 Hz.

6.4 Implementation of 2pLADA

6.4.1 Description of the device under test

The device under test was a proprietary 28 nm bulk silicon test device containing production logic blocks. To run a test on the device it was modified to engineer a race condition. The race was created by reducing the time between the rising edges of a capture clock pair. The race was then between the clock pair timing and the propagation time through the connecting data path logic. Using a capture clock pair, it was possible to bias the test close to a 50% fail probability boundary after each successive test loop of 21 μs. The DUT was provided by Freescale Semiconductor.

6.4.2 ATE Tester

An ATE is a system that applies tests to a DUT and makes a pass or fail decision. An ATE can be a simple computer, or a complex equipment containing several sophisticated testing instruments to test complex ICs. An ATE is widely used in electronics manufacturing after production of electronic components and systems. ATEs can also be used to test electrical equipment and automotive electronic modules. They are used for radar and other applications of wireless communication in the military [73].

Figure 4.13. LTX Credence D10 Diamond Series Tester.

Typically, for semiconductor failure analysis ATE architecture consists of a main controller, the synchronisation of signal source and detection devices.

The DUT is physically connected to the ATE through a custom interface adapter. The ATE computer uses modern computer language (such as C, C + +, Java and Smalltalk, or Labview) and additional control statements.

The ATE used in experiments were LTX Credence D10 Diamond Series Tester (Fig. 4.13), provided by the DCG Systems. The Credence D10 operating system provides an easy to use environment and gives a general software platform for test while supporting a variety of industrial standards. This tester exercised the race condition in the chip and monitored its control. Also it performed observation and acquisition of the fail rate of the DUT.

6.4.3 Microscope configuration

The experimental arrangement of the 2pLADA microscope is shown in Fig. 4.14. Femtosecond pulses at 1280 nm were delivered from the laser through a 4-m polarisation maintaining fibre to a collimation module which presented a beam of diameter 4 mm into the telescope system used before the RPC. The collimation module also contained a beam-splitting cube used for the deflection of the returning laser beam to the detector. Lenses L1 and L2 formed a telescope used to increase the diameter of the beam before the RPC device, whose 20 mm aperture made it necessary to use an expanded beam. A second telescope formed by lenses L3 and L4 then reduced the beam to a diameter matching the aperture of the galvanometer mirrors of the laser-scanning microscope (LSM) module. The LSM employed an integrated silicon SIL objective which provided 350× magnification and NA = 2.45. A scalar calculation of the PSF full-width-half-maximum diameter using the Sparrow criterion for the 2pLADA microscope with 1280 nm incident wavelength and NA = 2.45 provides a resolution of 260 nm, however this value takes no account of the resolution improvement due to the effect of nonlinear absorption.

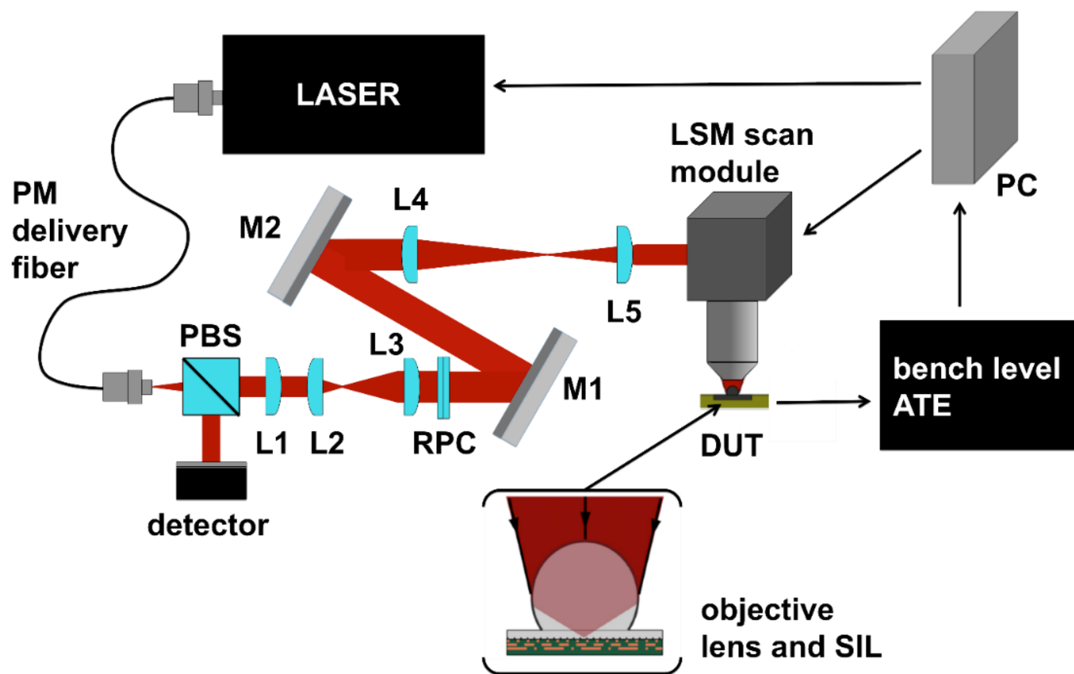

Figure 4.14. 2pLADA microscope layout. The beam to the module is delivered using a polarisation maintaining fibre, where it enters through a PBS. The PBS and its associated detector are used for confocal imaging to navigate to the area of interest in the DUT. After this, the beam is collimated using lens L1 and is expanded using lenses L2 and L3 and guided through the RPC device. Mirrors M1 and M2 are used to fold the layout and to deflect the beam into the reducing telescope (L4-L5), which images it onto the galvanometer mirrors of the LSM scan module. The beam is then guided to the 350× silicon SIL microscope objective (NA = 2.45). A HWP and a QWP were used just before the microscope objective to prepare the incident polarisation for the imaging experiments.

The DUT was a proprietary 28-nm-feature-size bulk silicon test device (V_{DD} = 0.8 V, clock frequency = 50 MHz). The device was engineered to perform a logic operation, which was previously described in [3]. By controlling the supply voltage, the fail rate was set to 50% and typically several hundred 2pLADA images of a region of pMOS and nMOS transistors were recorded using a pixel dwell time of 32 μs and an image size of 512 × 512.

This microscope configuration was implemented in the Freescale Semiconductor. FA lab in Austin, Texas.

RP Module design

The RPC had to be installed in an industrial FA device "Meridian IV" manufactured by the DCG Systems. To successfully achieve this, while respecting the restricted space available for the RPC installation, it was necessary to design a custom module. The final design of the RP module is shown in (Fig. 4.15), the design of the RPC module was a result of the collaborative work with DCG Systems. Many parts of the module were designed and 3D printed at Heriot-Watt University. Achromatic lenses were used in the telescopes to minimise chromatic and spherical aberrations.

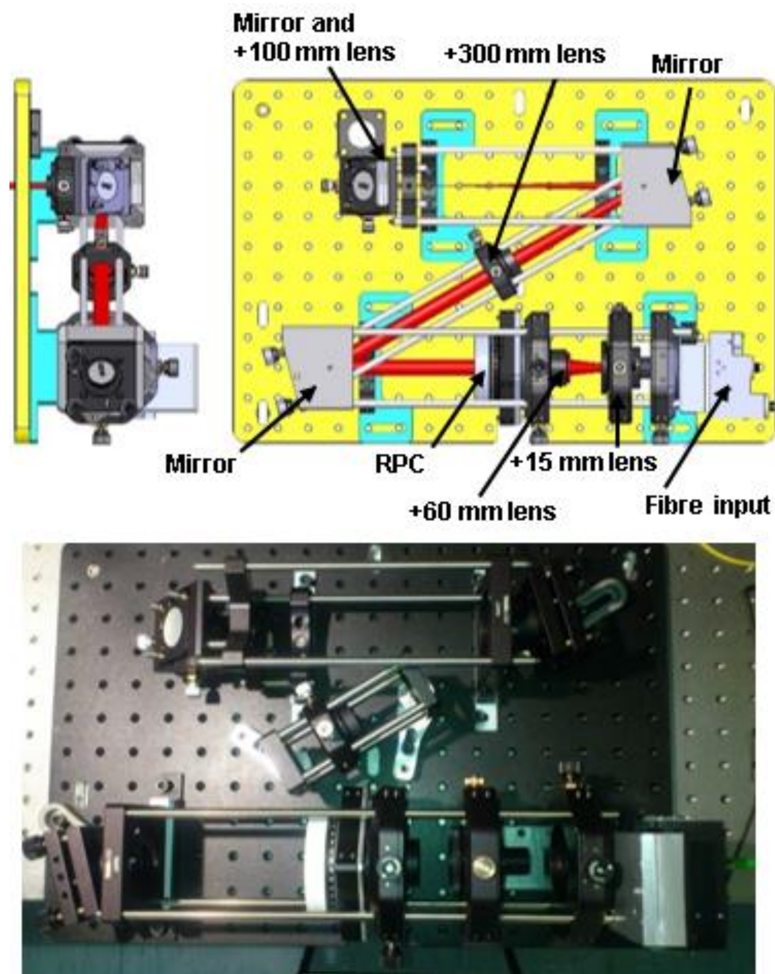

Figure 4.15. RP module design.

6.5 Results and discussion

6.5.1 Polarisation-state dependence of 2pLADA spatial resolution

2pLADA images were obtained using the microscope described previously by averaging 600 frames, with an approximate acquisition time of 300 seconds. Separate images were recorded using parallel linear, orthogonal linear, circular and radial polarisations. In Fig. 4.16 an overview image of a 2pLADA measurement for pMOS and nMOS transistors is depicted, showing the region of interest (red box) used for the quantitative measurements, which are described later.

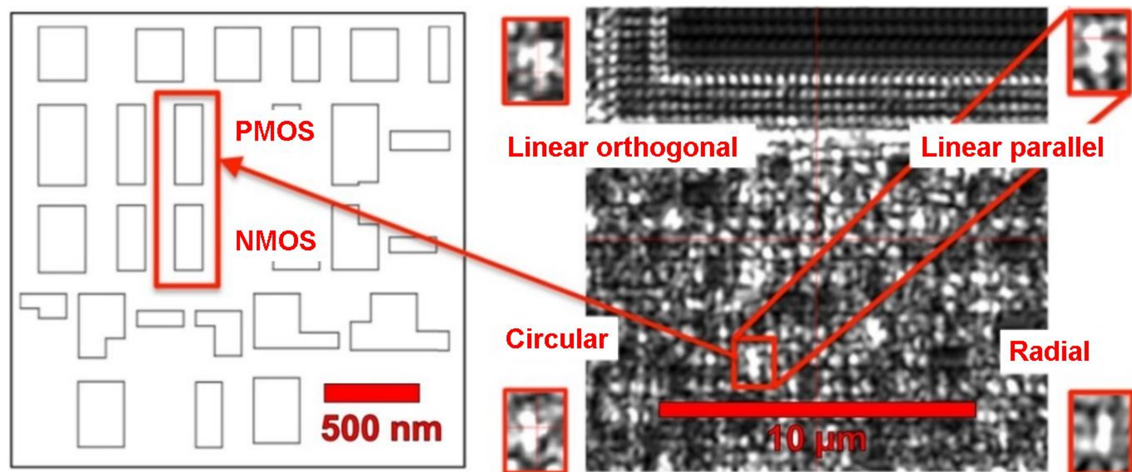

Figure 4.16. Confocal image of the active area of the device. The zoomed-in area (field of view 1.5×1.0 µm) is shown for each of the different polarisation states.

Figure 4.17 shows the 2pLADA images obtained under different incident polarisation conditions for the region of interest indicated in Fig. 4.16. PMOS and nMOS exhibit opposite 2pLADA signature polarities, therefore absolute delay profiles were drawn. To increase accuracy of data analysis a background was subtracted from the data. The images in the top row of Fig. 4.17 include the pMOS and nMOS transistors overlay from the computer-aided design (CAD) image as yellow rectangles, while the bottom row shows corresponding horizontal line-cuts across the centre point of the feature, which allow localisation resolution values to be inferred using a least-squares Gauss error function fit [74]. The CAD overlay indicates a separation between the transistors of 117 nm, which appears to be most clearly resolved when linear polarisation is used with its electric field parallel to the transistor channel. This is an expected result because the point spread function is longer in the direction parallel to the electric field and narrower in the orthogonal direction [8]. Comparable localisation resolution also appears to be possible (Fig. 4.17, bottom row, column 4) when using radially polarised light, which in principle can provide the same PSF width as optimised linear polarisation.

It was compared how closely the 2pLADA signals correlated with the transistor regions defined by the CAD layout by evaluating a normalised overlap integral between the 2pLADA signal and

the area bounded by the left rectangle in the Fig. 4.17 images. The area in the right rectangle was not included in the calculation because in this region the 2pLADA signal was noisier and very sensitive to the relative delay of the laser pulses. It should be noted also that the right rectangle corresponded to the nMOS well, which typically exhibited a weaker and more timing-critical LADA response [3]. The overlap integral was highest for the case of radial polarisation and was normalised to 1.0, giving values for the other cases of 0.82, 0.91 and 0.86. Error for the overlap integral was estimated from signal to noise ratio to be of 13%. Despite the improved correlation between the CAD and the 2pLADA image for radial polarisation, additional artefacts are evident when using RP illumination, for example there is substantial distortion and elongation of the image when compared with linear polarisation case. It is well known that RP illumination exhibits a strong longitudinal component, which can be advantageous by making the focal positioning less critical. The same effect may cause the LADA signal to be generated over an extended depth in the DUT, resulting in a skew in the shape of the 2pLADA image, however the exact cause of the observed distortion is currently unclear. As expected, circular polarisation resolves the gap between the transistors less well than with optimised linear polarisation but with a performance similar to non-optimised linear polarisation [75].

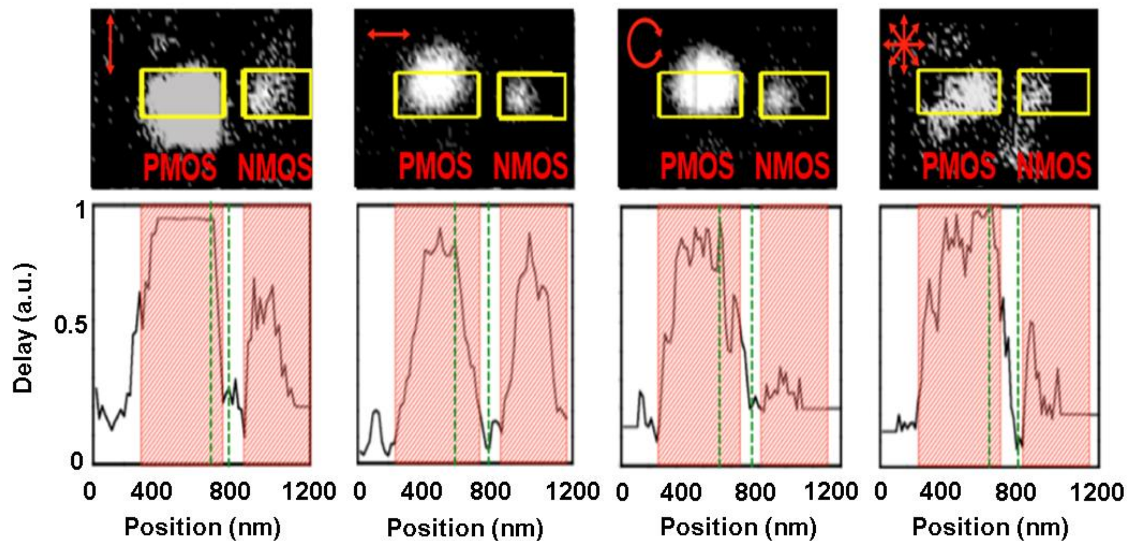

Fig. 4.17. Top row: 2pLADA images of pMOS and nMOS transistors obtained using 600 averages and the linear / circular / radial polarisation states indicated in red. The rectangles show the pMOS and nMOS transistors overlay from the CAD image. Bottom row: corresponding absolute line-cut profiles of the active sites. The red shading depicts the transistor footprints from CAD and the green dashed lines show the region used for the localisation resolution calculation (see text). The overlap integrals between the CAD layout and the 2pLADA images were normalised to the highest overlap value and were (left to right) 0.82±0.11, 0.91±0.12, 0.86±0.11 and 1.0±0.13.

The transition of the 2pLADA signal across the gap between pMOS and nMOS transistors (indicated by the green dashed lines in Fig. 4.17) was used as the basis for making a quantitative estimate of the localisation resolution in each case by fitting a Gaussian error function, as shown in Fig. 4.18. The fitting error resulted in the 10 %, which is lower than that of signal to noise ratio. The line-cuts in the 2pLADA signal (Fig. 4.18) reveal that the gap between the transistors is best resolved for electric field polarisations parallel to the gap, as expected from theory [9] and previous TOBIC experiments [8]. This polarisation leads to a resolution of 99 ± 13 nm, which is decreased by 46% to 144 ± 19 nm when using the orthogonal linear polarisation. Imaging using radially polarised light produced a resolution value of 120 ± 16 nm, the next best resolution value after that obtained using optimised linear polarisation. This poorer RP resolution may be due to the measurement error and due to the purity of the RP state being less than 100%. The measured value was 94% and Yurt *et al* [76] have observed this can be a source of artefacts when using RP illumination. When circular polarisation was used the resolution remained of the same quality 133 ± 17 nm within a small error.

In summary, while the best localisation resolution was obtained using linearly polarised and RP illumination, circular polarisation benefits from a symmetrical focal spot and is free of the artefacts which are apparent when imaging using radial polarisation.

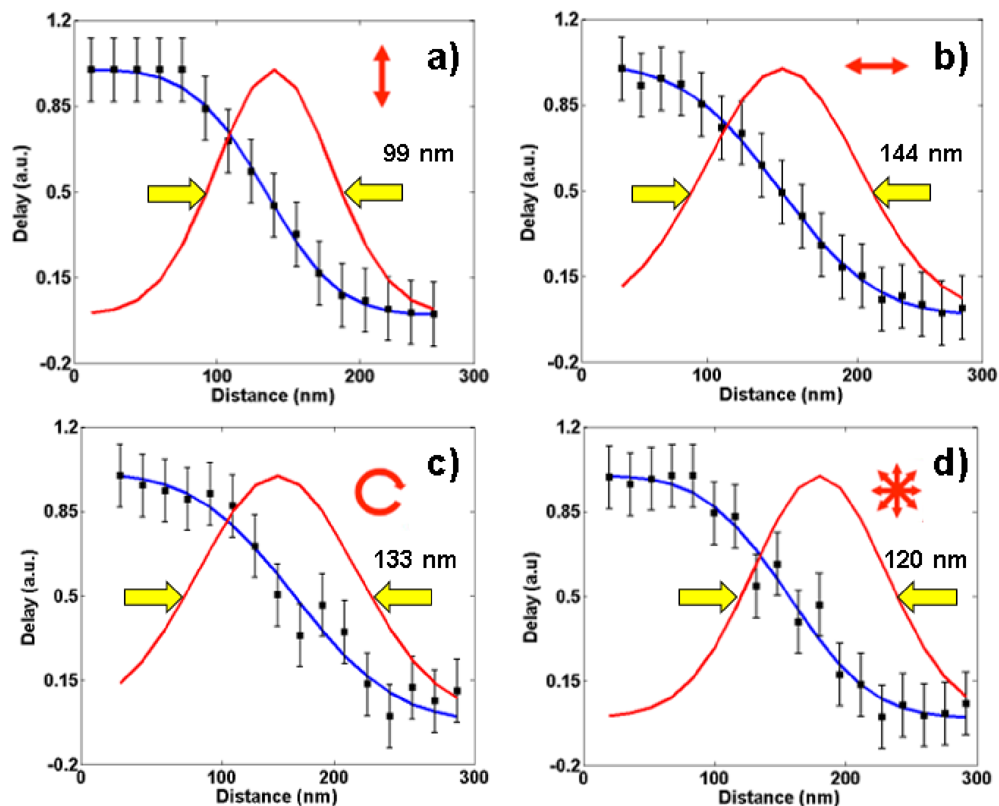

Figure 4.18. Line-cuts of the 2pLADA images of the active area for different polarisation states, recorded between the green dashed lines depicted in Fig.4.17 and fitted with a Gauss error function fit.

The carrier injection responsible for 2pLADA occurs due to two-photon absorption, an effect whose strength depends on the intensity of the laser pulses. Consequently, a strong sensitivity to focal position is expected because of the associated change in the area of the focused beam in the device.

The focal sensitivity was investigated by changing the relative position between the backing objective and the integrated SIL. As Fig. 4.19 illustrates, the 2pLADA localisation resolution displayed a clear minimum over a region of around 3 μm, corresponding to a change in the focal position inside the device of around 250 nm. These data provided a means of ensuring that the focal position had been repositioned consistently in the DUT as these localisation resolution measurements were repeated using different polarisation states. Also the recorded focal dependence of the 2pLADA resolution over the focal position has a similar form to that expected from TPA microscopy. This is an important result, which supports 2pLADA nonlinearity, in contrast to Erington *et al* [77] who reported that the LADA fail rate using 1300 nm CW laser showed a linear relationship while the same 28 nm node DUT was under investigation. This linear behaviour was explained and shown to happen due to heating of the device. Free carrier absorption (FCA) is responsible for this effect, which takes place in the heavily doped source and drain regions [78].

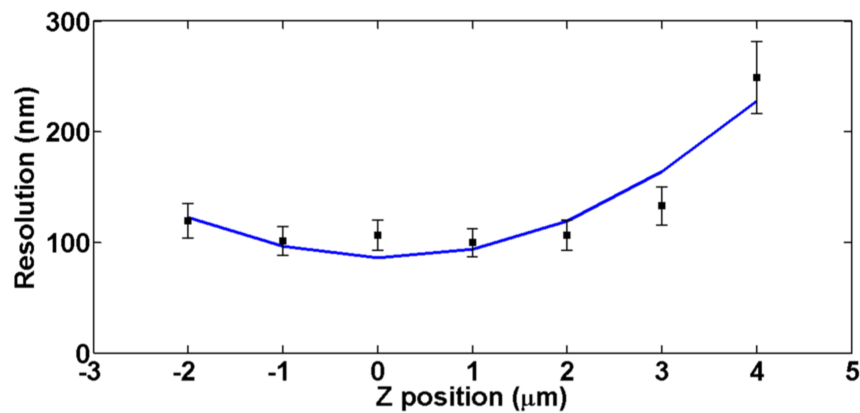

Figure 4.19. Example of the focal influence on the 2pLADA lateral resolution, obtained using parallel linear polarisation.

6.5.2 Time-resolved imaging using 2pLADA

The other novel aspect of 2pLADA is its sensitivity to the relative timing between the laser pulses and the clock signal within the DUT, an important feature which uniquely provides detailed temporal information about the switching of individual transistors. It was therefore essential to synchronise the laser pulse arrival with the transistor switching event occurring at the 2pLADA site. This was investigated by recording a number of 2pLADA images as the delay was adjusted, then extracting corresponding localisation resolution values from these images. As can be seen

from Fig. 4.20, delay adjustments of < 10 ps led to a noticeable degradation of the localisation resolution from its minimum value. This is expected as the best localisation is obtained when an arriving laser pulse affects a transistor, which is turned on by the electrical signal, thus leading to the higher probability to perturb pass/fail rate.

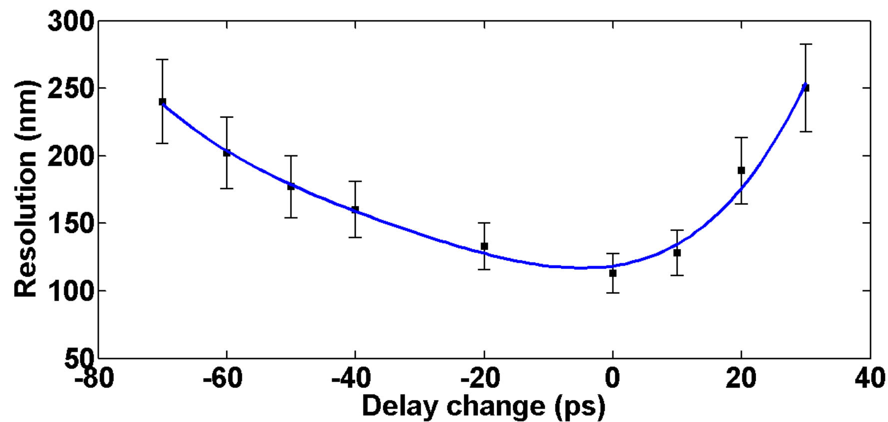

Figure 4.20. Example of the delay dependence of the 2pLADA lateral resolution, obtained using parallel linear polarisation.

6.5.3 Observations of single-event upsets

In this section observations of SEUs induced by TPA are presented. Fig. 4.21 shows SEU signatures using a SIL microscope objective. There is a 2pLADA site, which is surrounded by the cluster of intense white failing sites. It was necessary to determine how the fail rate of the test, pixel dwell time or delay time affected the appearance of the SEUs. However, all tests were negative and were found that these conditions do not have any impact on SEUs. This means that SEUs are not related with a race condition like 2pLADA but instead predefined flip-flops, which obtain the wrong logical value under the illumination of intense laser field.

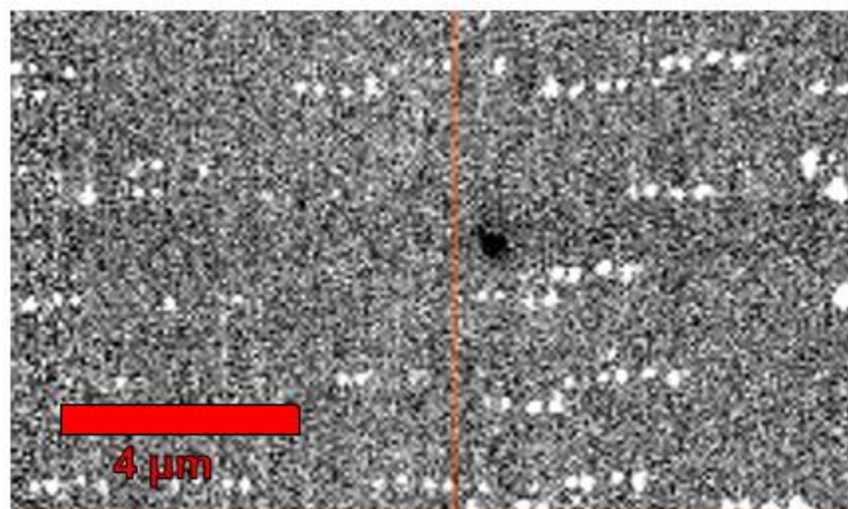

Figure 4.21. 2pLADA site (black passing signature) surrounded by SEUs (failing white dots).

It was noticed during experiment that SEUs unlike 2pLADA sites, changed their width while performing the z-scan. To investigate their behaviour z-scans were done for linear, radial and circular polarisations (Fig. 4.22). It can be seen that when the incident beam arrives at the device layer first there are no SEUs but their intensity grows exponentially. However, as the beam is passing the device layer the intensity of SEUs decrease much slower. This effect may appear due to the defocused beam interaction with the layer of SEUs. As can be seen from Fig. 4.22, when SEUs are affected by the RP beam they change their intensity much more slowly, because of the extended longitudinal component of the RP beam. It is also important that these trends show nonlinear behaviour, which is expected from the TPA.

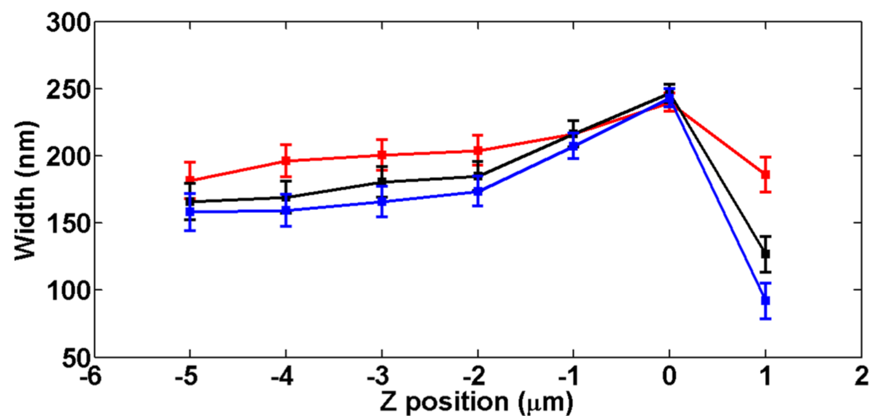

Figure 4.22. SEU intensity (width) against the focal position inside the DUT. Red line depicts the RP beam, blue – circular polarisation and black – linear polarisation.

6.6 Conclusions

The results presented here represent the first detailed assessment of the role of laser polarisation in 2pLADA imaging. Linear polarisation showed a clear advantage for analysing advanced ICs as long as the preferred polarisation direction could be identified, which in fact can easily be established if the polarisation is readily rotatable, e.g. using a HWP. The linear and radial polarisations provided the best lateral localisation resolutions compared to the circular polarisation. In principle, radially polarised light should have the advantage of producing a PSF with circular symmetry, in contrast to the approximately elliptical shape generated in linear polarisation case. However, our results using radial polarisation indicated a distortion of the 2pLADA signature, which appears to be a measurement artefact which is not observed in 2pLADA images recorded with the other polarisation states. This effect may result from the strong longitudinal electric field component of the radially polarised beam interacting with deeper features in the DUT, however more measurements are needed to understand the origin of this behaviour. In less advanced process technologies circular polarisation may be useful due to its symmetric performance and absence of artefacts, even though it provides poorer localisation

resolution. Nevertheless, radial polarisation still promises even better resolution as it is more amenable than other polarisations when incorporating apodization which would then outperform linear polarisation under conditions of NA higher than the value of 2.45 used in this work.

References

1. J. Rowlette and T. Eiles, "Critical timing analysis in microprocessors using near-IR laser assisted device alteration (LADA)", Proceedings of the International Test Conference **1**, 264–273 (2003).
2. K. A. Serrels, C. Farrell, T. R. Lundquist, D. T. Reid, and P. Vedagarbha, "Solid-immersion-lens-enhanced nonlinear frequency-variation mapping of a silicon integrated-circuit", Applied Physics Letters **99**, 193103 (2011).
3. K. A Serrels, K. Erington, D. Bodoh, C. Farrell, N. Leslie, T. R. Lundquist, P. Vedagarbha, and D. T. Reid, "Two-photon laser-assisted device alteration in silicon integrated-circuits", Optics Express **21**, 29083-29089 (2013).
4. K. Erington, D. Bodoh, K. A. Serrels, C. Nemirow, N. Leslie, T. R. Lundquist, P. Vedagarbha, C. Farrell and D. T. Reid, "Measuring propagation delays of critical paths using time-resolved LADA", Proceedings of the IEEE International Reliability Physics Symposium, 3F.4.1-3F.4.5 (2014).
5. C. Xu and W. Denk, "Two-photon optical beam induced current imaging through the backside of integrated circuits", Applied Physics Letters **71**, 2578–2580 (1997).
6. S. B. Ippolito, B. B. Goldberg, M. S. Ünlü, "High spatial resolution subsurface microscopy", Applied Physics Letters **78**, 4071 (2001).
7. A. Serrels, E. Ramsay, P. A. Dalgarno, B. D. Gerardot, J. A. O'Connor, R. H. Hadfield, R. J. Warburton and D. T. Reid, "Solid immersion lens applications for nanophotonic devices", Journal of Nanophotonics **2**, 021854 (2008).
8. K. A. Serrels, E. Ramsay, R. J. Warburton and D. T. Reid, "Nanoscale optical microscopy in the vectorial focusing regime", Nature Photonics **2**, 311-314 (2008).
9. Q. Zhan, "Cylindrical vector beams: from mathematical concepts to applications", Advances in Optics and Photonics **1**, 1-57 (2009).
10. R. Dorn, S. Quabis, and G. Leuchs, "Sharper focus for a radially polarized light beam", Physics Review Letters **91**, 233901 (2003).
11. M. Stalder and M. Schadt, "Linearly polarized light with axial symmetry generated by liquid-crystal polarization converters", Optics Letters **21**, 1948–1950 (1996).
12. M. Statt, M. Vargas, J. Oliver, S. Chen, K. Marshall, and C. Dorrer, "High-damage-threshold components for radially and azimuthally polarized beam generation", Proceedings of the Conference on Lasers and Electro-Optics, JTh2A.56 (2012).
13. E. Cole, P. Tangyunyong, D. Barton. "Backside localisation of open and shorted interconnections", Proceedings of the IEEE International Reliability Physics Symposium, 129-136 (1998).
14. M. Bruce, V. Bruce, D. Eppes, J. Wilcox, E. Cole, P. Tangyunyong, C. Hawkins, "Soft Defect Localisation (SDL) on ICs", Proceedings of the International Symposium for Testing & Failure Analysis, 21-27 (2002).

15. S. Kolachina, B. Taylor, K. Wills, E. Cole. "Application of TIVA in design debug", Proceedings of the International. Symposium for Testing &Failure Analysis, 497-501 (2000).
16. E. I. Cole, J. M. Soden, J. L. Rife, D. L. Barton, and C. L. Henderson, "Novel failure analysis techniques using photon probing with a scanning optical microscope", Proceedings of the International Reliability Physics Symposium, 388-399 (1994).
17. E. I. Cole, P. Tangyunyong, and D. L. Barton, "Backside localisation of open and shorted IC interconnections", Proceedings of the International Reliability Physics Symposium, 129-137 (1998).
18. A. Glowacki, S. K. Brahma, H. Suzuki and C. Boit, "Systematic characterization of integrated circuit standard components as stimulated by scanning laser beam", IEEE Transactions on Device and Materials Reliability **7**, 31-49 (2007).
19. J. M. Rabaey, "Digital integrated circuits: a design perspective", Upper Saddle River: Prentice Hall (1996).
20. S. K. Brahma, C. Boit, A. Glowacki, "Seebeck effect detection on biased devices without OBIRCH distortion using FET readout", Microelectronics Reliability **44**,1487-1492 (2005).
21. R. Minixhofer, "TCAD as an integral part of the semiconductor manufacturing environment", Proceedings of the Simulation of Semiconductor Processes and Devices, 9-16 (2006).
22. K. Sanchez, R. Desplats, F. Beaudoin, P. Perdu, J. P. Roux, G. Woods and D. Lewis, "NIR laser stimulation for dynamic timing analysis", Microelectronics Reliability **45**, 106-114 (2005).
23. T. Kiyan, C. Brillert, C. Boit, "Timing sensitivity analysis of logical nodes in scan design integrated circuits by pulsed diode laser stimulation", Proceedings of the International Symposium for Testing and Failure Analysis, 180-187 (2008).
24. A. Sarafianos, R. Llido, O. Gagliano, V. Serradeil, M. Lisart, V. Goubier, J. M. Dutertre, A. Tria, V. Pouget and D. Lewis, "Building the electrical model of the photoelectric laser stimulation of a PMOS transistor in 90nm technology", Microelectronics Reliability **52**, 2035-2038 (2012).
25. C. H. Kong, E. P. Castro, "Application of LADA for post-silicon test content and diagnostic tool validation", Proceedings of the International Symposium for Testing and Failure Analysis, 431–437 (2006).
26. R. A. Reed, M. A. Carts, P. W. Marshall, S. Buchner, M. LaMacchia, B. Mather, and D. McMorrow, "Single event upset cross section at various data rates", IEEE Transactions on Nuclear Science **43**, 2862–2867 (1996).
27. S. Buchner, "Laser simulation of single-event effects: A state of the art review", Report (1995).
28. R. Koga, S. D. Pinkerton, S. C. Mayer, S. La Lumondiere, S. J. Hansel, K. B. Crawford and W. R. Crain, "Observation of single event upsets in analog microcircuits", IEEE Transactions on Nuclear Science **40**, 1838-1844 (1993).

29. R. Ecoffet, R. S. Duzellier, P. Tastet, C. Aicardi, and M. Labrunee, “Observation of heavy ion induced transients in linear circuits”, Proceedings of the IEEE Radiation Effects Data Workshop Record, 72-77 (1994).
30. R. C. Baumann, “Radiation-induced soft errors in advanced semiconductor technologies”, IEEE Transactions on Nuclear Science **5**, 305-316 (2005).
31. T. Roy, A. F. Witulski, R. D. Schrimpf, M. L. Alles, and L. W. Massengill, “Single-event mechanisms in 90nm triple-well CMOS devices”, IEEE Transactions on Nuclear Science **55**, 2948-2956 (2008).
32. G. Wirth, and C. Fayomi, “The bulk built in current sensor approach for Single Event Transient detection”, Proceedings of the International Symposium on System-on-Chip, 1-4 (2007).
33. J. D. Popp, “Developing radiation hardened complex system on chip ASICs in commercial ultra-deep submicron CMOS processes”, Short Course of the IEEE Nuclear and Space Radiation Effects Conference (2010).
34. J. S. Fu, C. L. Axness, and H. T. Weaver, “Memory SEU simulations using 2D transport calculations”, IEEE Electron Device Lett. **6**, 422–424 (1985).
35. D. Binder, E. C. Smith, and A. B. Holman, “Satellite anomalies from galactic cosmic rays”, IEEE Transactions on Nuclear Science **22**, 2675-2680 (1975).
36. Joseph J. Fabula and Austin Lesea. “The NSEU response of static latch based FPGAs”, Proceedings of the International Military and Aerospace Programmable Logic Devices Conference, C5 (2003).
37. S. Mitra, Z. Ming, S. Waqas, N. Seifert, B. Gill, and K. S. Kim, “Combinational logic soft error correction”, Proceedings of the International Test Conference, 1-9 (2006).
38. K. Roy, S. Kundu, R. Galivanche, V. Narayanan, R. Raina, and P. N. Sanda, “Is the concern for soft-error overblown?”, Proceedings of the International Test Conference, 3 (2005).
39. R. Baumann, “Single-Event effects in advanced CMOS technology”, Short Course of the IEEE Nuclear and Space Radiation Effects Conference (2005).
40. M. C. Cascy, B. L. Bhuva, J. D. Black, L. W. Massengill, O. A. Amusan, A. F. Witulski, “Single event tolerant latch using cascade -voltage switch logic gates”, IEEE Transactions on Nuclear Science **53**, 3386-3391 (2006).
41. G. H. Johnson, J. H. Hohl, R. D. Schrimpf, and K. F. Galloway, “Simulating single-event burnout of channel power MOSFET’s”, IEEE Transactions on Electron Devices **40**, 1001-1008 (1993).
42. G. Busatto, F. Iannuzzo, F. Velardi, and J. Wyss, “Non-destructive tester for single event burnout of power diodes”, Microelectronics Reliability **41**, 1725–1729 (2001).
43. J. R. Brews, M. Allenspach, R. D. Schrimpf, and K. F. Galloway, “A conceptual model of single-event gate rupture in power MOSFETs”, IEEE Transactions on Nuclear Science **40**, 1959-1966 (1993).

44. M. Allenspach, I. Mouret, J. L. Titus, C. F. Wheatley, R. L. Pease, J. R. Brews, R. D. Schrimpf, K. F. Galloway, “Single-event gate-rupture in power MOSFETs: Prediction of breakdown biases and evaluation of oxide thickness dependence”, IEEE Transactions on Nuclear Science **42**, 1922-1927 (1995).
45. C.F. Wheatley, J. L. Titus, and D. I. Burton “Single-event gate rupture in vertical power MOSFETs; An original empirical expression”, IEEE Transactions on Nuclear Science **41**, 2152-2159 (1994).
46. Event Effects Test Method and Guidelines, “Single event effects test method and guidelines”, ESSC Basic Specification No. 25100 (2014).
47. A. J. Tylka, J. H. Adams, P. R. Boberg, B. Brownstein, W. F. Dietrich, E. O. Flueckiger, E. L. Petersen, M. A. Shea, D. F. Smart, and E. C. Smith, “CREME96: a revision of the cosmic ray effects on micro-electronics code”, IEEE Transactions on Nuclear Science **44**, 2150–2160 (1997).
48. J. L. Barth, C. S. Dyer, and E. G. Stassinopoulos, “Space, atmospheric, and terrestrial radiation environments”, IEEE Transactions on Nuclear Science **50**, 466–482 (2003).
49. F. W. Sexton, “Microbeam studies of single-event effects”, IEEE Transactions on Nuclear Science **43**, 687–695 (1996).
50. D. M. Cardoza, S. D. LaLumondiere, M. A. Tockstein, S. C. Witczak, Y. Sin, B. J. Foran, W. T. Lotshaw, and S. C. Moss, “Single event transients induced by picosecond pulsed x-ray absorption in III-V heterojunction transistors”, IEEE Transactions on Nuclear Science **59**, 2729–2738 (2012).
51. D. M. Fleetwood, S. L. Kosier, R. N. Nowlin, R. D. Schrimpf, J. Reber, R. A., M. DeLaus, P. S. Winokur, A. Wei, W. E. Combs, and R. L. Pease, “Physical mechanisms contributing to enhanced bipolar gain degradation at low dose rates”, IEEE Transactions on Nuclear Science **41**, 1871–1883 (1994).
52. V. Pouget, P. Fouillat, D. Lewis, H. Lapuyade, L. Sarger, and F. Roche, “An overview of the applications of the pulsed laser for SEU testing”, Proceedings of the International On-Line Testing Workshop, 52–57 (2000).
53. S. Buchner, M. Baze, D. Brown, D. McMorrow, and J.Melinger, “Comparison of error rates in combinational and sequential logic”, IEEE Transactions on Nuclear Science **44**, 2209–2206 (1997).
54. N. Roche, L. Dusseau, J. Boch, F. Saigne, S. Buchner, J. Warner, D. McMorrow, K. Kruckmeyer, G. Auriel, and B. Azais, “Correlation of dynamic parameter modification and ASET sensitivity in a shunt voltage reference”, IEEE Transactions on Nuclear Science **59**, 2756–2763 (2012).
55. F. Miller, A. Luu, F. Prud’homme, P. Poirot, R. Gaillard, and N. Buard, “Characterization of single event burnout in power MOSFETs using backside laser testing”, IEEE Transactions on Nuclear Science **53**, 3145–3152 (2006).

56. S. Buchner, J. Howard, C. Poivey, D. McMorrow, and R. Pease, "Pulsed-laser testing methodology for single event transients in linear devices", IEEE Transactions on Nuclear Science **51**, 3716–3722 (2004).
57. F. Miller, N. Buard, G. Hubert, S. Alestra, G. Baudrillard, T. Carriere, R. Gaillard, J. M. Palau, F. Saigne, and P. Fouillat, "Laser mapping of SRAM sensitive cells. A way to obtain input parameters for DASIE calculation code", Proceedings of the European Conference on Radiation and its Effects on Components and Systems, E2-1–E2-7 (2005).
58. D. J. Burns, M. T. Pronobis, Ch. A. Eldering, R. J. Hillman, "Reliability/design assessment by internal-node timing -margin analysis using laser photocurrent-injection", IEEE International Reliability Physics Symposium, 76-83 (1984).
59. K. A. Serrels, K. Erington, D. Bodoh, C. Farrell, N. Leslie, T. R. Lundquist, P. Vedagarbha, and D. T. Reid, "Two-photon laser-assisted device alteration in silicon integrated-circuits", Optics Express **21**, 29083-29089 (2013).
60. H. M. Pask, R. J. Carman, D. C. Hanna, A. C. Tropper, C. J. Mackechnie, P. R. Barber, and J. M. Dawes, "Ytterbium-doped silica fiber lasers: Versatile sources for the 1-1.2 μm region", IEEE Journal of Selected Topics in Quantum Electronics **1**, 2-13 (1995).
61. F. Auzel, "On the maximum splitting of the (2F7/2) ground state in Yb3+-doped solid state laser materials", Journal of Luminescence **93**, 129-135 (2001).
62. R. Paschotta, J. Nilsson, A. C. Tropper, and D. C. Hanna, "Ytterbium-doped fiber amplifiers", IEEE Journal of Quantum Electronics **33**, 1049-1056 (1997).
63. R. Selvas, J. K. Sahu, I. B. Fu, J. N. Jang, J. Nilsson, A. B. Grudinin, K. H. Ylä-Jarkko, S. A. Alam, P. W. Turner, and J. Moore, "High-power, low-noise, Yb-doped, cladding-pumped, three-level fiber sources at 980 nm", Optics Letters **28**, 1093-1095 (2003).
64. C. Farrell, "Pulse-pumping of cascaded Raman fibre amplifiers", PhD thesis, University of Southampton (2010).
65. K. O. Hill, Y. Fujii, D. C. Johnson and B. S. Kawasaki, "Photosensitivity in optical fiber waveguides: application to reflection filter fabrication", Applied Physics Letters **32**, 647–656 (1978)
66. P. Beaud, W. Hodel, B. Zysset, H. Weber, "Ultrashort pulse propagation, pulse breakup, and fundamental soliton formation in a single-mode optical fiber", IEEE Journal of Quantum Electronics **23**, 1938–1946 (1987)
67. F. M. Mitschke, L. F. Mollenauer, "Discovery of the soliton self-frequency shift", Optics Letters **11,** 659–661 (1986).
68. J. P. Gordon, "Theory of the soliton self-frequency shift", Optics Letters **11**, 662–664 (1986).
69. A. Bondeson, M. Lisak, and D. Anderson, "Soliton perturbations: A variational principle for the soliton parameters", Physica Scripta **20**, 479 (1979).
70. S. K. Turitsyn, B. G. Bale, M. P. Fedoruk, "Dispersion-managed solitons in fibre systems and lasers", Physics Reports **521**, 135–203 (2012).

71. A. V. Husakou and J. Herrmann, “Supercontinuum generation, four-wave mixing, and fission of higher-order solitons in photonic-crystal fibers”, Journal of the Optical Society of America. B **19**, 2171–2182 (2002).
72. K. Tamura, C. R. Doerr, L. E. Nelson, H. A. Haus, and E. P. Ippen, “Technique for obtaining high-energy ultrashort pulses from an additive-pulse mode-locked erbium-doped fiber ring laser”, Optics Letters **19**, 46-48 (1994).
73. R. P. Tan, “Programming language and tools for automated testing”, PhD Thesis, Polytechnic Institute and State University (2007).
74. S. B. Ippolito, B. B. Goldberg, and M. S. Ünlü, “High spatial resolution subsurface microscopy”, Applied Physics Letters **78**, 4071-4073 (2001).
75. G. M. Lerman and U. Levy, “Effect of radial polarization and apodization on spot size under tight focusing conditions”, Optics Express 16, 4567–4581 (2008).
76. A. Yurt, M. D. W. Grogan, S. Ramachandran, B. B. Goldberg and M. S. Ünlü, “Effect of vector asymmetry of radially polarized beams in solid immersion microscopy”, Optics Express **22**, 7320–7329 (2014).
77. K. Erington, D. Bodoh, K. Dickson, and G. Lange, “The role of free carrier absorption in LADA”, Proceedings of the International Symposium for Testing and Failure Analysis, 73-81 (2014).
78. R. A. Falk, “Near IR absorption in heavily doped silicon – an empirical approach”, ISTFA 2000: Proceedings of the 26th International Symposium for Testing and Failure Analysis, 121-128 (2000).

Chapter 7. Spatio-temporal aberrations in sub-surface solid-immersion microscopy

7.1 Introduction

Many applications require femtosecond pulses to illuminate the sample with the highest possible light intensity. In order to achieve this, tight focusing is necessary while ensuring the pulse remains undistorted in both space and time, so that it has a transform limited time duration and a diffraction limited focused spot size. [1-4] Modern microscope objective lenses are normally well corrected for all spatial aberrations, however in some implementations aberrations arise elsewhere in the imaging system which were not anticipated in the original lens design. [5] In a nonlinear microscope, uncorrected spatial aberrations not only degrade the lateral and axial resolution of the system, but also couple into the time domain to stretch the pulses beyond their minimum transform-limited durations [6]. In particular, two common spatial aberrations significantly affect the pulse durations: chromatic aberration remaps the arrival times at the focal plane of the different colours in the pulse, while spherical aberration leads to another remapping based on the radial position of components of the pulse [7].

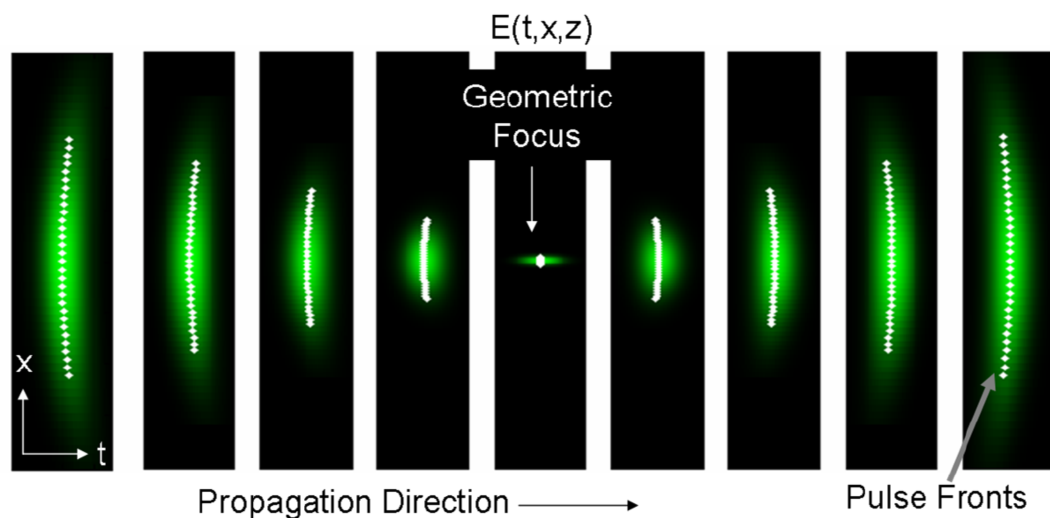

Figure 5.1. Spatio-temporal dynamics of the beam after an ideal lens [8].

The spatiotemporal profile of the beam without aberrations or material dispersion is presented in Fig. 5.1. It shows the beam propagation in the vicinity of the focal spot at different distances from the focus. Here the colour represents the centre frequency of the pulse, which is constant both in space and time because no distortions are present. The white dots show the wavefront dynamics of the propagating beam [8]. When no distortions are present the laser beam is focused at the geometric focus and the spatiotemporal profile is symmetric [9].

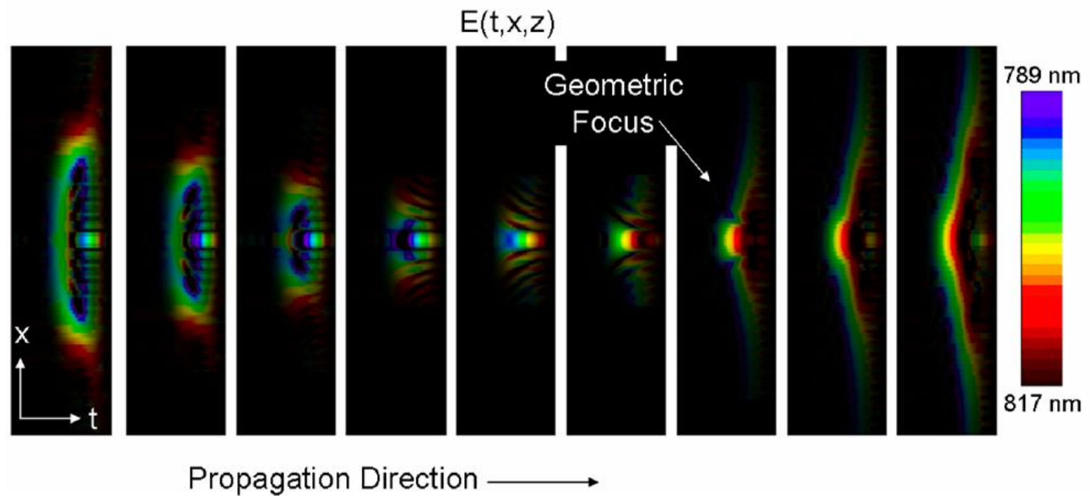

Figure 5.2. The beam focusing with a lens under chromatic aberrations [8].

Figure 5.2 shows a simulation of the focus of a lens with chromatic and spherical aberrations. The figure illustrates that the pulse can exhibit a very complex spatiotemporal shape when common lens aberrations are present. Due to chromatic aberration the pulse's colour splits in x, t and z for a beam propagating along the z-axis, which leads to a narrower local bandwidth [8]. The narrower bandwidth means a longer pulse duration. Also due to the aberrations, the spot size is far from being diffraction limited, as would be needed for most applications. Even in optical systems with perfect dispersion compensation, chromatic aberrations can lead to severe pulse distortion [1].

In this chapter, a technique to identify and to potentially address the problem of aberrations in sub-surface microscopy is presented. As has been previously described, nonlinear microscopy has been applied to sub-surface imaging of CMOS ICs using the TOBIC technique [10-12]. Since optically-based fault localisation normally proceeds by backside imaging through the silicon substrate of the IC and into the device layer of the chip, SIL microscopy is an important technique [13]. However, SIL microscopy in a high refractive index medium like silicon (n = 3.48) requires the dimensions of the SIL to be precisely fabricated for a given substrate thickness (typically around 100 μm), otherwise even for 10 nm discrepancies spherical aberrations will be encountered [14]. The type of SIL used (i.e. central or aplanatic) determines the severity of tolerancing errors in the SIL design or non-uniformity in the substrate thickness [15]. It is commonly observed that the aplanatic design, while generally providing superior resolving power to the central SIL, is substantially (around 10x) more sensitive to fabrication errors than the central SIL [16], meaning that uncorrected aberrations may remain in a system which was otherwise correctly designed. It is in this context that techniques to identify and even mitigate aberrations in the system are important.

7.2 Theory of aberrations

In this section an overview of aberration theory will be given. Presenting first the geometrically derived Seidel Aberrations and then moving to the Zernike Polynomials.

7.2.1 Seidel aberrations

The wavefront of the beam propagating through a real lens can have a complex form, since there are generally errors introduced in the lens design, manufacturing or assembly processes. Each point of the object has a quasi-spherical wavefront converging from the exit pupil (x, y) toward the paraxial image point (x_0, y_0) (Fig. 5.3). Therefore, the wavefront can be expanded as a power series [16]:

$$W(x,y,x_0) \cong W(x^2+y^2\,, xx_0\,, x_0^2) = a_1(x^2+y^2) + \\ +a_2xx_0 + a_3x_0^2 + b_1(x^2+y^2)^2 + \\ +b_2xx_0(x^2+y^2) + b_3x^2x_0^2 + b_4x_0^2(x^2+y^2) + b_5xx_0^3 + b_6x_0^4\,. \qquad (5.1)$$

The first term of Eq. (5.1) represents defocus, a longitudinal shift of the centre, while the second term is a transverse shift - tilt. The third term leads to a phase shift, which is constant across the exit pupil. This term does not affect the wavefront and therefore, does not affect the image. For monochromatic light, these three terms typically have coefficients equal to zero. However, they are non-zero for broadband light and cause the chromatic aberrations, which are explained in Section 5.2.5 [17-18].

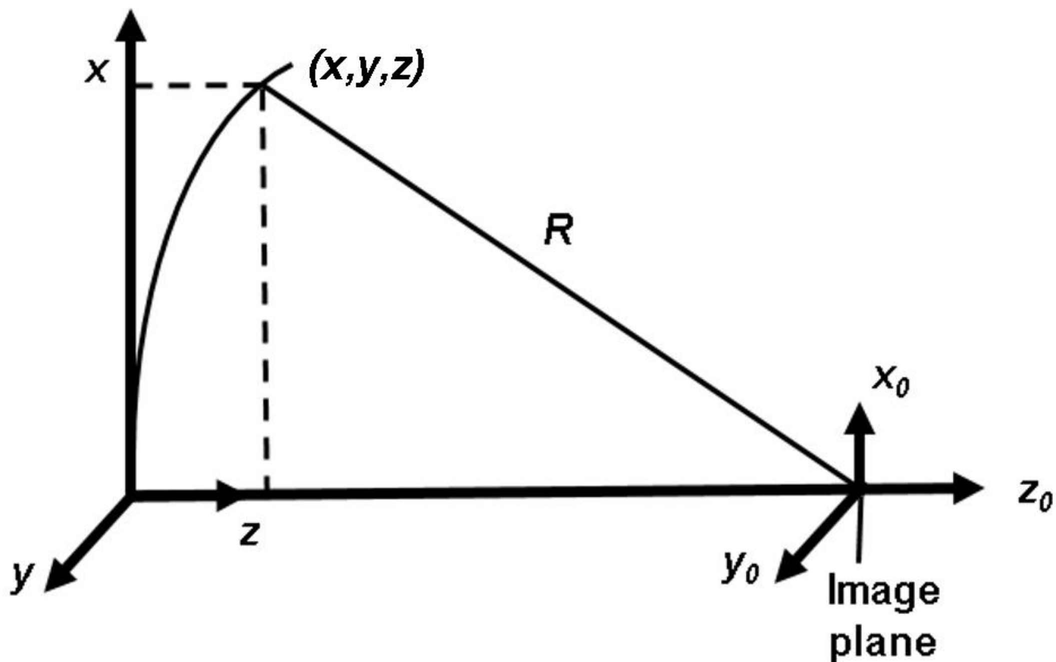

Figure 5.3. Coordinate frame for a wavefront converging from the exit pupil coordinates toward the image plane (adapted from [16]).

The last six terms with coefficients b_n are of fourth degree when describing wavefront aberrations, and are of third degree when describing transverse ray aberrations. Therefore, they are known as third-order aberrations. Also, there exist higher order terms of fifth- and seventh-order aberrations. The third-order aberrations are known as Seidel aberrations, called after the variables used by Seidel in his earlier work [19].

The Seidel aberrations are expressed in polar coordinates $y = \rho \sin\theta$ and $x = \rho\cos\theta$ in the pupil plane. The radial coordinate ρ is typically normalised to be equal to 1 at the pupil plane. The coordinate x_0 is also normalised to 1 at the maximum field position. Therefore, using polar coordinates, the wavefront can be written as follows:

$$W(x_0,\rho,\theta) \cong \sum_{j,m,n} W_{klm} x_0^k \rho^l \cos^m\theta =$$
$$W_{200}x_0^2 + W_{111}x_0\,\rho\cos\theta + W_{020}\rho^2 + W_{040}\,\rho^4 + W_{131}x_0\,\rho^3\cos\theta +$$
$$+W_{222}x_0^2\,\rho^2\cos^2\theta + W_{220}x_0^2\,\rho^2 + W_{311}x_0^3\,\rho\cos\theta, \qquad (5.2)$$

with $k = 2j + m, l = 2n + m.$

This can be expressed using Seidel coefficients [16]:

$$W(x_0,\rho,\theta) = \frac{1}{8}S_1\rho^4 + \frac{1}{2}S_3x_0^2\,\rho^2\,cos^2\theta + \frac{1}{4}(S_3 + S_3)x_0^2\,\rho^2 + \frac{1}{2}S_5x_0^3\,\rho\,cos\,\theta. \quad (5.3)$$

Spherical aberration

Spherical aberration can be defined as the change of the focal point with a change of aperture. The field variable x_0 does not occur in the spherical aberration description meaning that spherical aberration is constant over the field. The rays from an axial object cross the axis in front of or behind the focus if the angle is high enough. The point at which the rays propagate through the edge of the aperture intersect the axis is called the marginal focus (Fig. 5.4). While the point at which the rays propagate through the region near the centre of the aperture (paraxial rays) cross the axis is called the paraxial focus [19].

The aberration components for transverse ray aberration for the spherical aberration case are:

$$\varepsilon_x = -\frac{4RW_{040}}{h}x(x^2 + y^2), \qquad (5.4)$$

$$\varepsilon_y = -\frac{4RW_{040}}{h}y(x^2 + y^2), \qquad (5.5)$$

where h is the pupil radius and R is the radius of curvature of the spherical wavefront. As the aberration is symmetrical about the optical axis, the transverse aberration due to third-order spherical aberration can be written as [16]:

$$\varepsilon_x = \varepsilon_y = -\frac{4RW_{040}}{h}\rho^3. \tag{5.6}$$

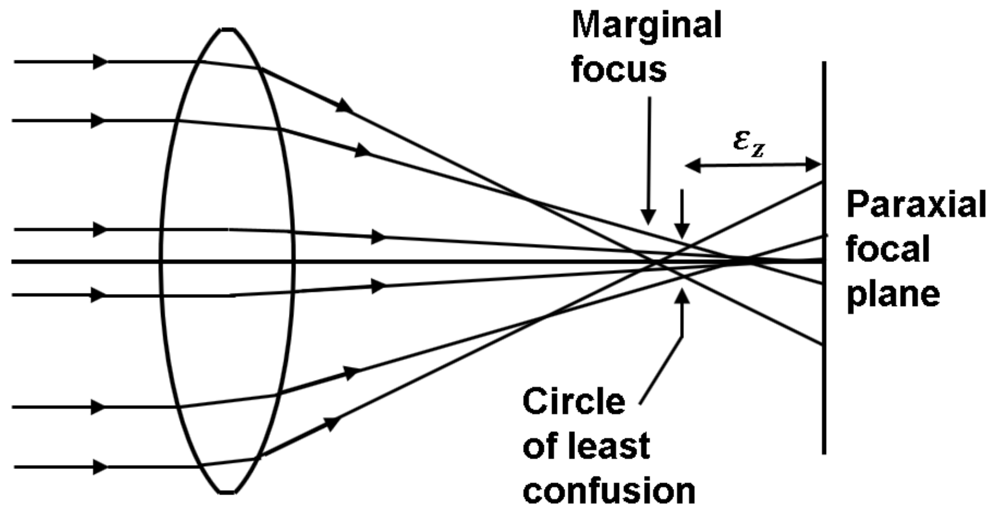

Figure 5.4. A simple converging lens with spherical aberration. The rays further from the axis are brought to a focus nearer the lens (adapted from [16]).

Since the focal point is shifted it results in a PSF, which is elongated in the axial direction. Therefore, as the observation plane is shifted by distance ε_z the wavefront aberration can be expressed as follows [16]:

$$\Delta W = W_{040}\rho^4 + \frac{\varepsilon_z h^2}{2R^2}\rho^2, \tag{5.7}$$

where ε_z is positive if the shift is away from lens ($+z$ direction). The effect of the focal shift on the size of the image equivalent to adding a linear term for the transverse aberration [15]:

$$\varepsilon_x = \varepsilon_y = -\frac{4RW_{040}}{h}\rho^3 - \frac{\varepsilon_z h}{R}\rho. \tag{5.8}$$

Since the image plane is shifted, there is a position for which the elongation is a minimum, which is called the circle of least confusion. The circle of confusion is a patch of the focused light caused by imperfect focusing conditions. Fig. 5.4 shows that this corresponds to the position where the ray from the pupil crosses the caustic [19]. The circle of least confusion is positioned three-quarters of the distance from the paraxial focus to the marginal focus, and therefore, it has the radius of one-quarter the radius of the image at the paraxial focus RW_{040}/h and as a result the wavefront aberration is [16]:

$$\Delta W = W_{040}(\rho^4 - 1.5\rho^2). \tag{5.9}$$

The PSF of a circular aperture was introduced in Chapter 3 with the Eq. (3.12). For the spherical aberration case it can be modulated by [16]:

$$\vartheta(\rho) = \exp\left[i\frac{2\pi}{\lambda}W_{040}\rho^4\right], \tag{5.10}$$

with defocus it becomes

$$\vartheta(\rho) = \exp\left[i\frac{2\pi}{\lambda}(W_{040}\rho^4 + W_{020}\rho^2)\right]. \tag{5.11}$$

Figures 5.5 and 5.6 compare diffraction patters with and without spherical aberration.

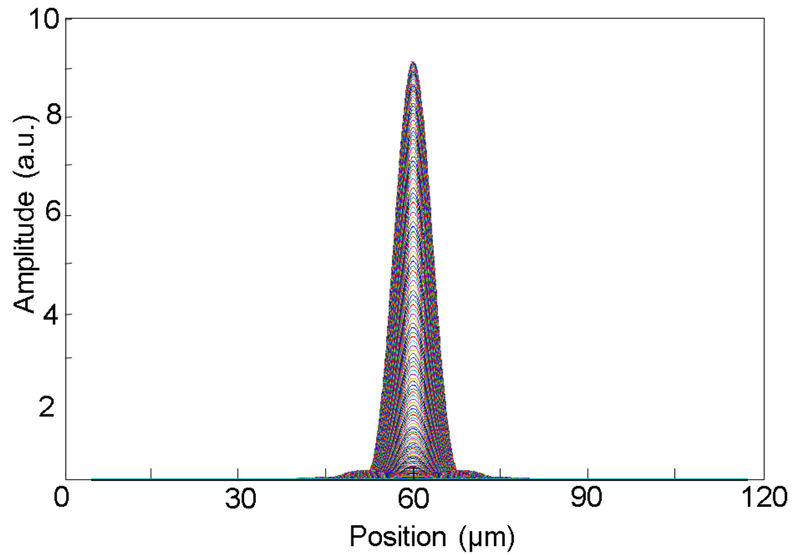

Figure 5.5. Diffraction pattern of a circular pupil with no spherical aberration present.

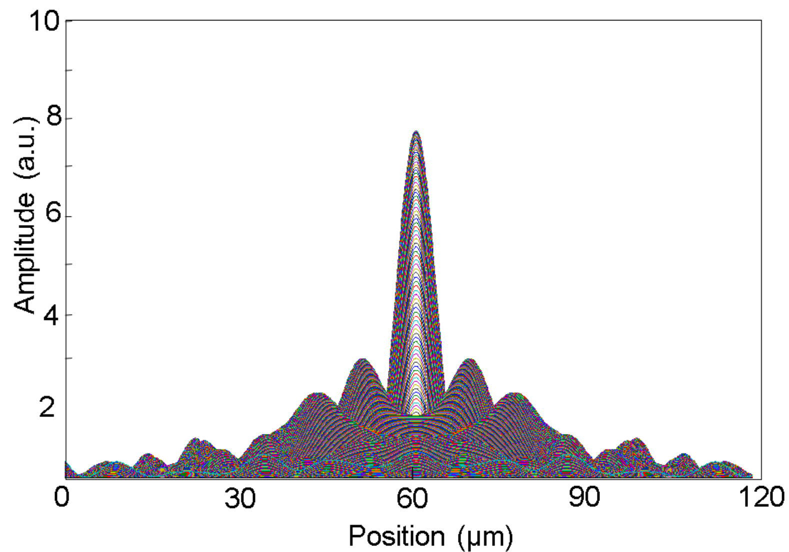

Figure 5.6. Diffraction pattern of a circular pupil with spherical aberration.

Coma

Coma is defined as the variation in the image magnification along the aperture. This aberration creates comet like images when the rays passing through the centre of a lens are imaged at a different height than those passing through the edges. [19]. Coma typically occurs only for a beam, which is not on the optical axis and aberration increases with angle and distance from the optical axis. The transverse aberration components for this case are [16]:

$$\varepsilon_y = -\frac{2RW_{131}}{h} x_0 xy = -\frac{RW_{131}}{h} x_0 \rho^2 \sin 2\theta \,, \tag{5.12}$$

$$\varepsilon_x = -\frac{RW_{131}}{h} x_0 (3x^2 + y^2) = -\frac{RW_{131}}{h} x_0 \rho^2 (2 + \cos 2\theta). \tag{5.13}$$

Coma cannot be fixed by shifting the focal position. However, it can be shifted in the lateral direction to decreases the coma effect on the wavefront.

Sometimes coma aberration may appear for a beam, which is propagating on axis, which can be a result of the optical system misalignment with tilted and decentred components [16].

Fig. 5.7 shows how the position at which rays appear on a coma patch depends on the location at which the ray propagates through the lens [19].

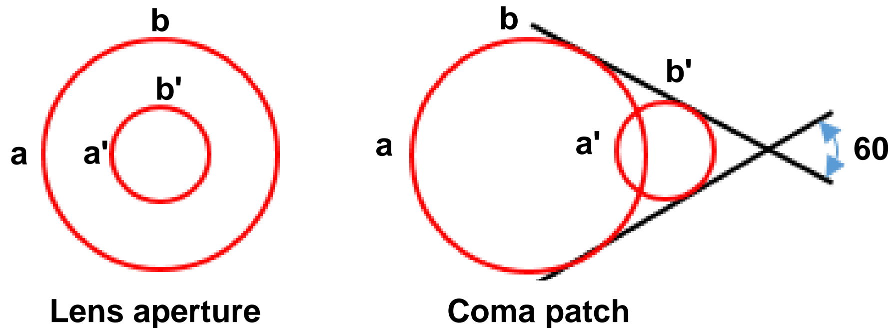

Figure 5.7. The relationship between the position of a ray in the lens aperture and its position in the coma patch. The diameters of the circles in the image are proportional to the square of the diameters in the aperture (adapted from [16]).

Astigmatism

In order to describe astigmatism, it is useful to introduce the descriptions of tangential and sagittal rays. A plane containing the optical axis is known as the tangential plane. Therefore, rays that lie in this plane are called tangential rays. The tangential ray passing through the centre of the entrance pupil is called the principal ray (Fig. 5.8). The sagittal plane contains the principal ray and is perpendicular to the tangential plane. Rays that do not lie in either the tangential or sagittal planes are called skew rays [19].

In the case of astigmatism, wavefront aberration does not occur in the sagittal plane, however in the tangential plane the wavefront experiences the additional curvature since the aberration depends quadratically on x. The curvature in the x section increases with the square of the field angle. Astigmatism appears when during the fabrication of the lens its optical surface is made slightly cylindrical, instead of perfectly spherical. As a result, the wavefront propagating through the surface has a different radius of curvature in two perpendicular directions [16].

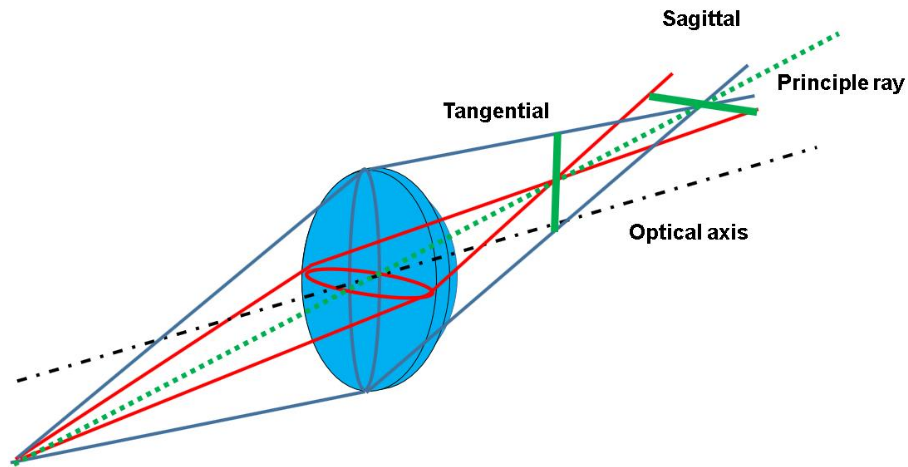

Figure 5.8. Visualisation of astigmatism, depicting the tangential and sagittal foci (adapted from [16]).

For astigmatism, the components of transverse aberration are

$$\varepsilon_y = 0, \tag{5.14}$$

$$\varepsilon_x = -\frac{2RW_{222}}{h} x_0^2 x = -\frac{2RW_{222}}{h} x_0^2 \rho \cos\theta \,. \tag{5.15}$$

Therefore, the image is stretched to $4RW_{222}x_0^2/h$ at the meridional plane. This aberration can be mitigated by a focal shift, which improves the image. Along with a wavefront aberration the transverse aberration becomes [16]:

$$\Delta W = W_{222}x_0^2 x^2 + \frac{\varepsilon_z h^2}{(2R^2)(x^2 + y^2)}. \tag{5.16}$$

The focal shift can be designed to be

$$\frac{\varepsilon_z}{R} = \frac{2RW_{222}x_0^2}{h^2}. \tag{5.17}$$

For this case a stretched image is formed at the sagittal plane, which leads to the result that all rays pass through two orthogonal lines (Fig. 5.8). The vertical line (the sagittal astigmatic focal line)

is the focus for rays from the y section and the horizontal line (tangential focal line) is the focus for rays from the x section.
The best image is generally observed at the half distance between the astigmatic foci. At this focal position the smallest PSF is formed and therefore it is called the circle of least confusion [19].

Field curvature

The fourth Seidel aberration depends on a pupil diameter as a focal shift does, however it depends on the square of the field magnitude. If there are no other aberrations, true images are formed on a curved image surface, called the Petzval surface with a curvature of $4R^2(W_{220}/h^2)$ (Fig. 5.9). This gives the aberration the name of "field curvature". Astigmatism and field curvature always appear together since they both depend on the squared magnitude of the field [16, 19].
If astigmatism does not occur, the sagittal and tangential image surfaces coincide and are formed on the Petzval surface. However, when astigmatism is present, the tangential image surface is three times further from Petzval surface as the sagittal image surface is, and both are on the same side of the Petzval surface (Fig. 5.9) [16].

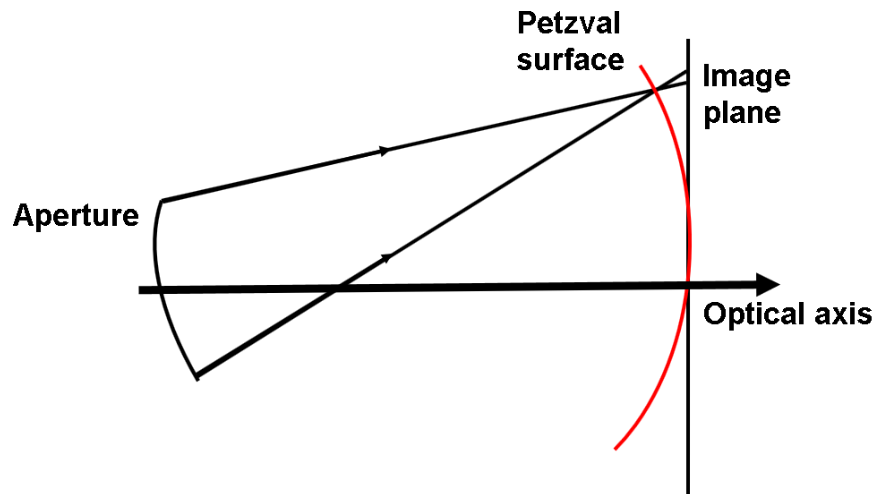

Figure 5.9. Field curvature (adapted from [16]).

Distortion

The last Seidel aberration is distortion, which shifts the image's position by a distance [16]:

$$\varepsilon_x = -\frac{RW_{311}}{h}x_0^3. \tag{5.18}$$

Cube of the image coordinate leads to the distortion of the image. This leads to the effect that the image of any straight line is curved with the increase of curvature depending on the radial distance. The effect can be visualised with a square placed symmetrically with respect to the

optical axis and by shifting each point radially an amount proportional to the cube of its distance from the centre (Fig. 5.10) [16].

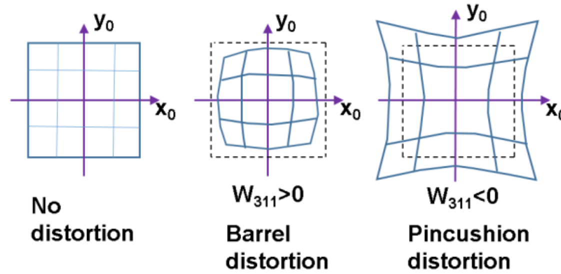

Figure 5.10. Distortion aberration (adapted from [16]).

7.2.2 Zernike polynomials

It is usually convenient to express wavefront data in polynomial form. Zernike polynomials are often used for this approach since they contain terms, which have the similar form to the observed aberrations [16]. However, Zernike polynomials are not always the best polynomials used for fitting data. For example, these polynomials have little value when taking into account air turbulence. As a result, in the experimental results additional terms must be added to Zernike polynomials to accurately represent alignment errors [20, 21].

Zernike polynomials are of high interest for a few reasons. First, they are one of an infinite number of complete sets of polynomials in two real variables, ρ and θ' that are orthogonal in a continuous trend over the interior of a unit circle [16].

Next Zernike polynomials have three properties that distinguish them from other sets of orthogonal polynomials. First, they have rotational symmetry, which leads to a polynomial product of the form

$$R(\rho)G(\theta'), \tag{5.19}$$

where $G(\theta')$ is a set of trigonometric functions repeating every 2π radians:

$$G(\theta') = e^{\pm im\theta'}, \tag{5.20}$$

where m is any positive integer or zero.

Also it fulfils the requirement that even when the coordinate system is rotated by an angle α the polynomial always keep the same form [16]:

$$G(\theta' + \alpha) = G(\theta')G(\alpha). \tag{5.21}$$

The second characteristic of Zernike polynomials is that the function must be a polynomial in ρ of degree n and contain the power of no less than m.

The third property is that $R(\rho)$ depends on m and is even if m is even or odd if m is odd.
The radial polynomials can be obtained from Jacobi polynomials $R_n^m(\rho)$. Thus having properties of [16]:

$$\int_0^1 R_n^m(\rho) R_{n'}^m(\rho) \rho d\rho = \frac{1}{2(n+1)} \delta_{nn'}, \tag{5.22}$$

$$R_n^m(1) = 1. \tag{5.23}$$

The radial polynomial can be expressed via:

$$R_{2n-m}^m(\rho) = Q_n^m(\rho)\rho^m, \tag{5.24}$$

$Q_n^m(\rho)$ can be written generally as

$$Q_n^m(\rho) = \sum_{s=0}^{n-m} (-1)^s \frac{(2n-m-s)!}{s!\,(n-s)!\,(n-m-s)!} \rho^{2(n-m-s)}. \tag{5.25}$$

Typically, the radial polynomials are combined with sines and cosines, which give the final Zernike polynomial series for the wavefront [16]:

$$W = \overline{\Delta W} + \sum_{n=1}^{\infty} \left[A_n Q_n^0(\rho) + \sum_{m=1}^{n} Q_n^m(\rho)\rho^m (B_{nm} \cos m\theta' + C_{nm} \sin m\theta') \right], \tag{5.26}$$

where $\overline{\Delta W}$ is the mean wavefront, and A_n, B_{nm}, and C_{nm} are individual polynomial coefficients, n is the radial order and m is the meridional frequency.
For a symmetrical optical system, the wave aberrations are symmetrical around tangential plane and as a result only even functions of θ' are allowed [16].
The first 9 Zernike shapes are shown in Fig. 5.11. The root-mean-square (RMS) wavefront aberration indicates the quality of the optical system. The value of the Zernike coefficient is the RMS wavefront of that aberration type. According to the Marechal criterion, a diffraction-limited imaging system requires a RMS wavefront error less than $\lambda/14$ [22]. The Marechal criterion states that an optical system is considered to be well corrected for aberrations if the normalised intensity at focus is greater than or equal to 0.8, which relates to an RMS wavefront error [16]. As a result, for the case of imaging through silicon, the system residual RMS error should be less than 110 nm using 1550 nm illumination.

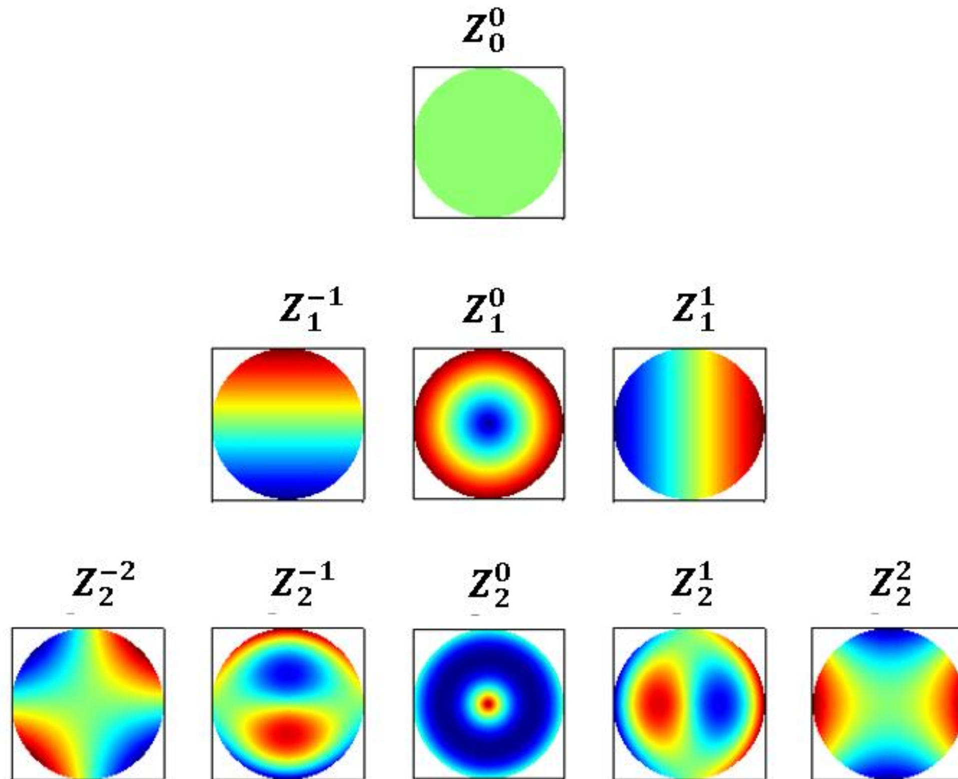

Figure 5.11. First 9 Zernike shapes on a unit circle, arranged vertically by radial order and horizontally by meridional degree. Colours represent normalised deflection of the shape with blue [16].

n	M	No.	Polynomial	Aberration
0	0	1	1	Piston
1	-1	2	Psinθ	Tip
1	1	2	Pcosθ	Tilt
2	-24	√6	p^2sin20	Astigmatism, axis ±45°
2	0	3	$2p^2$-1	Defocus
2	2	√6	p^2cos20	Astigmatism, axis 0° and 90°
3	-3	2√2	p^3sin30	Trefoil
3	-1	2√2	($3p^3$-2p) sin20	Vertical coma
3	1	2√2	($3p^3$-2p) cos20	Horizontal coma
3	3	2√2	p^3cos30	Trefoil
4	-4	√10	p^4sin40	Quadrafoil
4	-2	√10	($4p^3$-$3p^2$) sin20	2nd order astigmatism
4	0	√5	$6p^4$-$6p^2$+1	3rd order spherical
4	2	√10	($4p^4$-$3p^2$) cos20	2nd order astigmatism
4	4	√10	p^4cos40	Quadrafoil

Table 5.1. Zernike radial polynomials [16].

7.2.3 Relationship between Zernike polynomials and third-order aberrations

First-order wavefront properties and third-order wavefront aberration coefficients can bem obtained from the first nine Zernike polynomials coefficients [16]:

$$\begin{gathered}W(\rho,\theta') = Z_0 + Z_1\rho\cos\theta' + Z_2\rho\sin\theta' + Z_3(2\rho^2-1) + \\ +Z_4\rho^2\cos 2\theta' + Z_5\rho^2\sin 2\theta' + Z_6(3\rho^2-2)\rho\cos\theta' + \\ +Z_7(3\rho^2-2)\rho\sin\theta' + Z_8(6\rho^4-6\rho^2+1).\end{gathered} \tag{5.27}$$

The aberrations and properties corresponding to these Zernike terms are shown in Table 1. The wavefront can be expanded via the field-independent wavefront aberration coefficients [16]:

$$W(\rho,\theta) = W_{11}\rho\cos\theta + W_{20}\rho^2 + W_{40}\rho^4 + W_{31}\rho^3\cos\theta + W_{22}\rho^2\cos^2\theta\,. \tag{5.28}$$

These terms do not depend on the field, therefore, they are not exact Seidel aberrations. Interferometer for the wavefront measurement can only produce data of a single field point. This makes field curvature to appear as focus, and distortion to appear as tilt [19]. Therefore, a number of field points must be measured to determine the Seidel aberrations. The first- and third-order field-independent wavefront aberration terms are acquired from Zernike polynomials [16]:

$$\begin{aligned}
W(\rho,\theta') &= Z_0 - Z_3 + Z_8 && \text{Piston}\\
&+\rho\sqrt{(Z_1-2Z_6)^2+(Z_2-2Z_7)^2} && \\
&\times\cos\left[\theta' - \tan^{-1}\left(\frac{Z_2-2Z_7}{Z_1-2Z_6}\right)\right] + && \text{Tilt}\\
&+\rho^2\left(2Z_3 - 6Z_8 \pm \sqrt{Z_4^2+Z_5^2}\right) \pm && \text{Focus}\\
&\pm 2\rho^2\sqrt{Z_4^2+Z_5^2}\cos^2\left[\theta' - \frac{1}{2}\tan^{-1}\left(\frac{Z_5}{Z_4}\right)\right] && \text{Astigmatism}\\
&+2\rho^3\sqrt{Z_6^2+Z_7^2}\cos^2\left[\theta' - \tan^{-1}\left(\frac{Z_7}{Z_6}\right)\right] && \text{Coma}\\
&+6\rho^4 Z_8\,. && \text{Spherical}
\end{aligned} \tag{5.29}$$

7.2.4 Strehl ratio

The maximum intensity for the case without the presence of aberration is formed at the lens focal point, which is called the diffraction focus. For small aberrations the diffraction focus can be obtained by modifying the wavefront with proper amount of tilt and defocus to acquire the minimum wavefront change [22].

The ratio of the intensity at the focal point in the presence of aberrations, divided by the intensity for no present aberration, is called the Strehl ratio (SR), which is given by [16]:

$$SR = \frac{1}{\pi^2}\left|\int_0^{2\pi}\int_0^1 e^{i2\pi\Delta W(\rho,\theta)}\rho d\rho d\theta\right|^2, \tag{5.30}$$

where ΔW in units of waves is the wavefront aberration relative to the reference sphere for diffraction focus. The Eq. (5.30) may be expanded in series [16]:

$$SR = \frac{1}{\pi^2}\left|\int_0^{2\pi}\int_0^1 \left[1 + i2\pi\Delta W + \frac{1}{2}(i2\pi\Delta W)^2 + \cdots\right]\rho d\rho d\theta\right|^2. \tag{5.31}$$

If the aberrations are very small, the third-order and higher-order powers of terms $2\pi\Delta W$ can be neglected. This simplifies SR expression to the form of [16]:

$$SR \approx 1 - (2\pi\sigma)^2, \tag{5.32}$$

$$\sigma = \overline{\Delta W^2} - (\overline{\Delta W})^2, \tag{5.33}$$

where σ is in units of wavelenghts. Therefore, when the aberrations are small, the SR is smaller than the ideal value by an amount proportional to the wavefront deformation.

Eq. (532) is suitable for SRs as low as about 0.5. A more accurate approximation for most types of aberration is [16]:.

$$SR \approx e^{-(2\pi\sigma)^2} \approx 1 - (2\pi\sigma)^2 + \frac{(2\pi\sigma)^4}{2!} + \cdots, \tag{5.34}$$

which is suitable for SRs as small as 0.1.

7.2.5 Chromatic aberrations

As stated before, the index of refraction depends on the wavelength of light, so focusing properties of optical systems and elements also a function on a wavelength. Chromatic aberration occurs for two cases: 1. paraxial image-forming property variation with wavelength and 2. aberration dependence on wavelength [16].

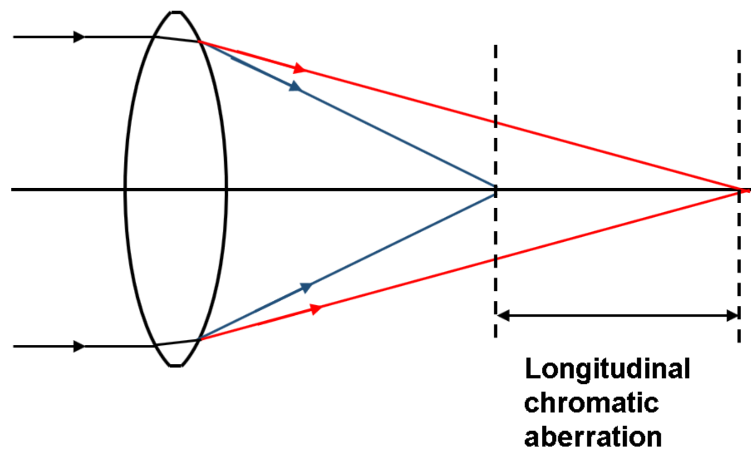

Figure 5.12. Longitudinal chromatic aberration (adapted from [16]).

Typically, the first type of chromatic aberration significantly affects the system and is dominant over the second type chromatic aberration. The Gaussian optics properties of any optical system depend only on the position of principal planes and focal planes. Chromatic aberrations appear when the location of any of the planes is wavelength-dependent [19].

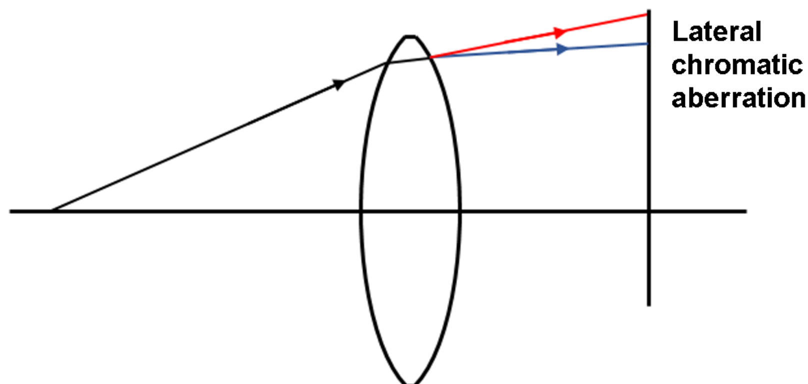

Figure 5.13. Lateral chromatic aberration (adapted from [16]).

Longitudinal chromatic aberration is the change of focal point with wavelength. The refractive index is higher for shorter wavelengths than it is for long wavelengths. Therefore, shorter wavelengths experience stronger refraction at each surface of a lens (Fig. 5.12) [19]. As a result, shorter wavelength rays are focused closer to the lens than the longer wavelength rays. This distance along the optical axis between the produced focal points is known as the axial or longitudinal chromatic aberration. As a result, the focal point has a yellowish dot (formed by the orange, yellow, and green rays) and a purplish halo (formed by the red and blue rays). Therefore, if the screen is moved toward the lens, the central dot turns to blue; if it is moved away, the central dot changes to red.

Also, an optical system can produce images of varying dimensions depending on wavelength or form a rainbow for the off-axis image. The difference in the dimensions depending on colour is known as lateral chromatic aberration (Fig. 5.13) [16].

7.2.6 Aberrations of a simple lens

In many optical systems the main cause of the aberrations is a simple thin lens. The third-order aberrations for a thin lens can be calculated using the previously introduced equations [19]. Therefore, the third-order spherical aberration introduced by a thin lens can be written as: [16]:

$$W_{sph} = \frac{h^4 \Phi^3}{32 n_0}\left\{\left(\frac{n}{n-1}\right)^2 + \frac{(n+2)}{n(n-1)^2} + \left[B + \frac{2(n^2-1)}{n+2}C\right]^2 - \frac{n}{n+2}C^2\right\}, \quad (5.35)$$

where h is diameter of the pupil, n_0 is refractive index of surrounding environment, n is refractive index of lens, Φ is power, C_1 and C_2 are curvatures of lens surfaces, B is the shape factor $B = (C_1 + C_2)/(C_1 - C_2)$, C is the conjugate variable $C = (U_1 + U_2')/(U_1 - U_2')$, and U_1 and U'_2 are defined in Fig. 5.14 [16].

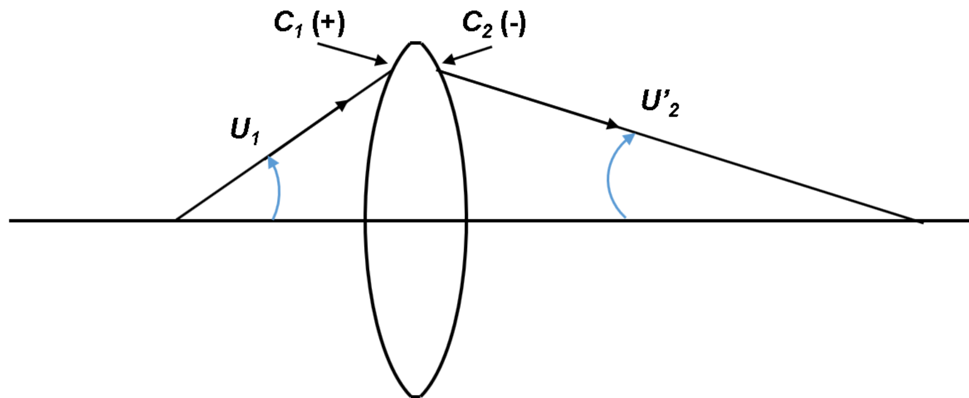

Figure 5.14. Angles for incident and refracted ray for the thin lens case (adapted from [16]).

The shape factor B is zero for a lens, which has both surfaces of the same curvature (equi-convex). It also is 1 for a plano-convex lens, when the rays are incident on the convex surface, and is equal to -1 when the rays are incident on the plano-surface. For equal conjugates, the conjugate variable C is zero. If the object is at the focus $C = 1$, and if the object is at infinity $C = -1$ [16].

If the medium surrounding the lens is air ($n = 1$), and the lens is made from glass ($n = 1.5$) and $C = \pm 1$ the minimum spherical aberration [16]:

$$W_{sph_{min}} = 0.264\, h\, NA^3. \quad (5.36)$$

The minimum coma for a thin lens in air is

$$W_{coma} = \frac{h\,NA^2\overline{U}}{4}\left(\frac{1}{n+2}\right). \tag{5.37}$$

The expression for a thin lens astigmatism in air can be written as

$$W_{astig} = \frac{1}{2}(h\,NA\,\overline{U}^2). \tag{5.38}$$

7.2.7 Aberrations in solid immersion lens microscopy

For SIL microscopy there are several sources for possible aberrations: substrate thickness error, SIL fabrication error, off-axis aberration from beam scanning and index mismatch from different materials [23]. Due to the high NA, any mismatch between the SIL imaging depth and the sample thickness generates significant spherical aberration. In the case of a hSIL (central SIL), the tolerance to mismatch is relatively high, whereas for the aplanatic configuration the tolerance to mismatch is relatively low. The SIL tolerance to thickness mismatch is depicted in Fig. 5.15 for both types of SIL configuration by comparing the SRs.

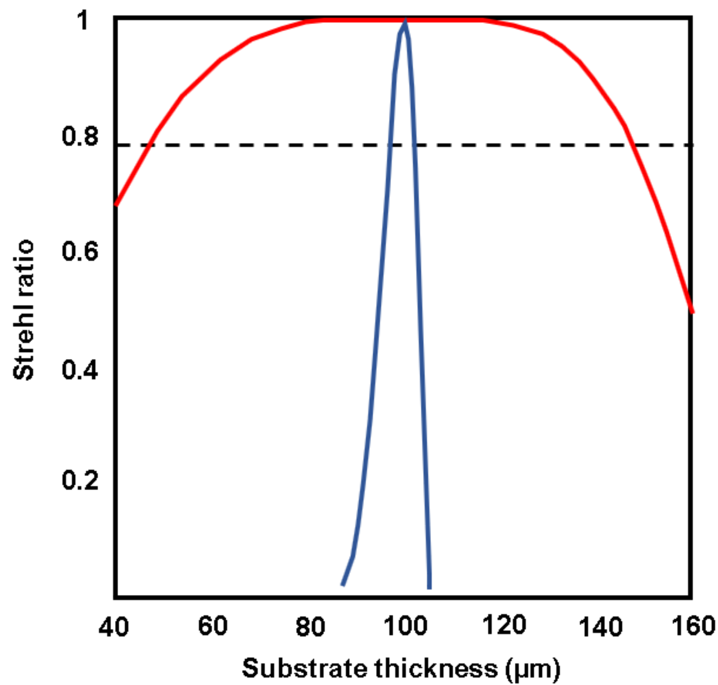

Figure 5.15. Comparison of SRs between hSIL (red) and aSIL (blue) to sample thickness error tolerance (adapted from [15]).

As it was mentioned before a SR of 0.8 or higher is considered to be of a well aligned and compensated optical system [22]. If the SILs are designed to work at the 100 μm depth sample with similar, the hSIL can tolerate up to 50 μm of sample thickness error, while the aSIL's (aplanatic SIL) tolerance to thickness mismatch is only about 5 μm. Due to both SIL and sample thickness tolerance in fabrication and polishing, it is difficult to obtain a perfect thickness match

to locate the object in the aplanatic plane. A thickness mismatched sample mainly introduces spherical aberration that lowers the peak intensity and adds side-lobes to the focal spot, consequently reducing the measured signal intensity and imaging quality [24, 25]. As can be seen from Fig. 5.15 for the aSIL the tolerance of thickness mismatch is better when the substrate is too thin than when it is too thick. Therefore, it is a good strategy, when preparing the sample, to keep polishing down the substrate if there is any doubt that substrate is of the correct thickness.

7.3 Experimental investigation of spatio-temporal aberrations

In sub-surface TOBIC microscopy the spatial aberrations described in Section 5.2 also affect the pulse duration and peak power, both parameters which can be revealed by using the photocurrent induced in the integrated circuit to measure the autocorrelation profile of the pulses. In this section it is shown that in a nonlinear microscopy system the effects of chromatic and spherical aberrations are revealed by a difference in the focal positions corresponding to the shortest pulse duration and the minimum lateral resolution. Interpreting experimental results from a high-numerical-aperture two-photon microscope using spatio temporal model it that the two-photon autocorrelation of the pulses at the focal plane can be used to minimise both the chromatic and spherical aberrations of the system. Based on these results, a possible optimisation strategy is proposed whereby the objective lens is first adjusted for minimum autocorrelation duration, then the wavefront before the objective is modified to maximise the autocorrelation intensity.

7.3.1 Pulse measurement at the focus of the SIL microscope

Illuminated with near-infrared femtosecond pulses, the microscope uses the TOBIC effect to produce images, which are maps of the photocurrent generated by the device as the location of the focal spot is raster scanned across the chip. The experimental set-up is illustrated in Fig. 5.16. A mode-locked Er:fibre operating at 1550 nm wavelength was employed to perform the TOBIC microscopy. The laser generated 140 fs pulses with a repetition rate of 68 MHz and an average power of 200 mW.

The TOBIC signal depends quadratically on incident peak intensity [10], so the CMOS device itself provides a nonlinear response, which is suitable for pulse-duration estimation by recording $g_2(\tau)$, the interferometric second-order autocorrelation profile [26]. By inferring the autocorrelation width at the focal plane it is possible to compensate and manipulate the pulse chirp before entering the pupil of the focusing optics. This offers a way of reducing the durations of the laser pulses while providing aberration free imaging at the focal plane and maximizing the two-photon signal. As shown later with measurements of the lateral imaging resolution, the autocorrelation durations recorded at out-of-focus planes provide a metric which can be used to find optimal focusing by conducting a sequence of rapid autocorrelation measurements.

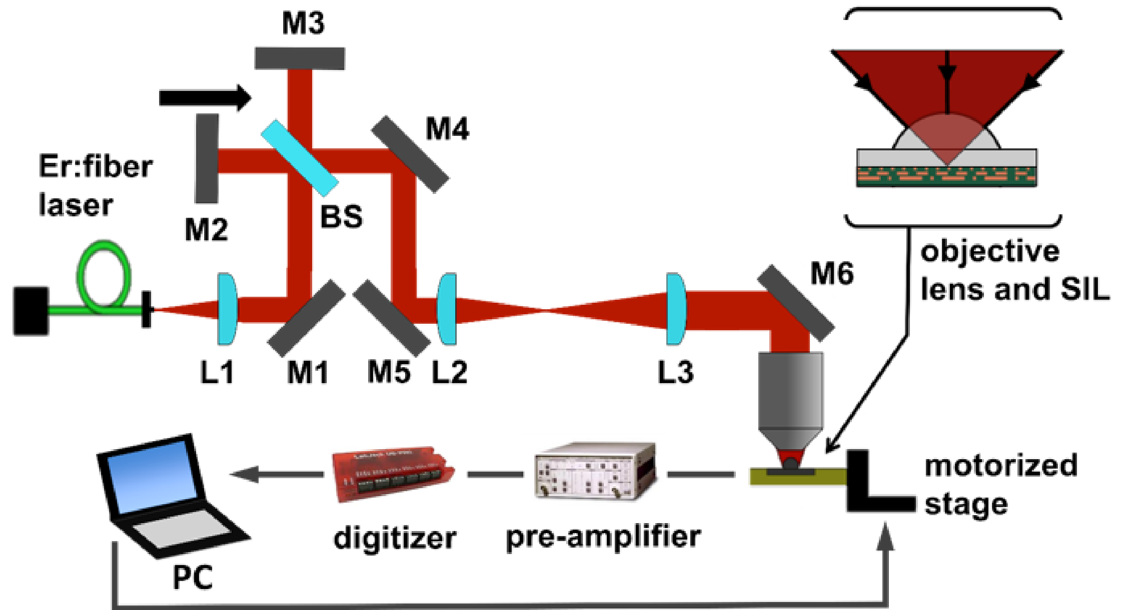

Figure 5.16. TOBIC microscope. Mirror M1 deflected the beam into the Michelson interferometer.

The beam from the Er:fibre laser was collimated by lens L1 before entering a Michelson interferometer in which the pulses were split into two time-delayed replicas which could later be recombined in the device to yield the interferometric autocorrelation function. At the output of the interferometer the beam was expanded to a diameter of 9.8 mm using a telescope (lenses L2 and L3) to overfill the 8.4-mm-diameter of the microscope objective (NA 0.42, 20x). An adjustable aperture was inserted immediately before the objective lens to allow spherical aberration to be diagnosed by performing finite-aperture experiments, in which the NA of the imaging system was moderately reduced. To conduct the resolution measurements without interference effects, the moving mirror M2 was blocked.

The nonlinear TOBIC microscope incorporated a silicon hSIL, which takes advantage of the first aplanatic point of the sphere [13]. The diameter of the hSIL was chosen to be 4 mm and it was cut to a height of 1.73 mm. The design and the basic working principle of the hSIL have been described before in Chapters 1 and 2. The inclusion of the silicon SIL in the imaging system enhanced the NA of the microscope by a multiple of the refractive index of silicon (3.48) to NA 1.46.

The device used for the experiments was a 350-nm-feature-size CMOS IC., which was introduced in the Chapter 3. The laser-generated photocurrent was measured between ground and a pin connected to the active region [27]. The device remained unpowered at all times. The sample was mounted on a computer controlled motorised 3-axis translation stage (ASI MS-2000), which had a (16½ x 23 x 9) cm travel range with a minimum physical step of 10 nm.

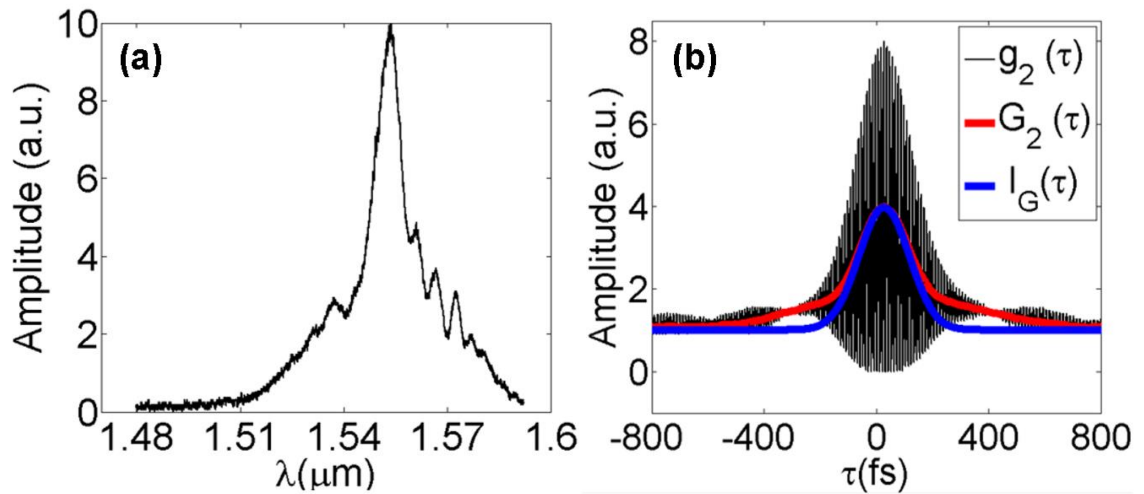

Fig. 5.17. Characterisation of the of the Er:fibre laser showing (a) the optical spectrum and (b) the autocorrelation profile at the output. The FWHM pulse duration was 140 fs, inferred from a Gaussian envelope (blue) fitted to the intensity autocorrelation trace (red).

Before conducting pulse duration measurements using the device itself, the laser operation was characterised by measuring its spectral distribution (Fig. 5.17a) and the autocorrelation at the laser output (Fig. 5.17b). The two-photon autocorrelation was recorded using a silicon photodiode and the spectrum was measured with a real-time laser spectrum analyser. The two-photon autocorrelator was extensively discussed in the Chapter 2. The laser was optimised to have the shortest pulse durations (corresponding to near-transform-limited pulses) at the device layer inside the silicon chip. Therefore, it can be seen in Fig. 5.17b that the pulses measured directly after the laser output had a noticeable (and negative) chirp.

An edge response at the silicon-metal transition of one of the finger structures was used to evaluate the lateral spatial resolution of the nonlinear imaging system. The resolution measurement and error estimation technique is presented in Chapter 3. The FWHM of the underlying Gaussian function gives the resolution limit of the system. Example data are shown in Fig. 5.19a indicating a 345 ± 17 nm spatial resolution.

Resolution measurements were performed as the device was moved through the focal plane of the microscope. Two datasets were recorded, one with an unrestricted pupil (Fig. 5.18b, "open aperture") and a second with the aperture before the pupil reduced to a diameter of 2 mm (Fig. 5.18b, "closed aperture"). The zero position corresponds to where the PSF FWHM was smallest (a value of 345 ± 17 nm), and values of $z > 0$ indicate moving the sample further from the objective lens. The presence of spherical aberration causes the PSF FWHM minimum to shift when the aperture is closed, and this is observed in the data in Fig. 5.18b. The data also show the expected broadening of the PSF FWHM due to the decrease in NA when the aperture is closed. In the following section this spatial behaviour is correlated with time-domain measurements based on two-photon autocorrelation.

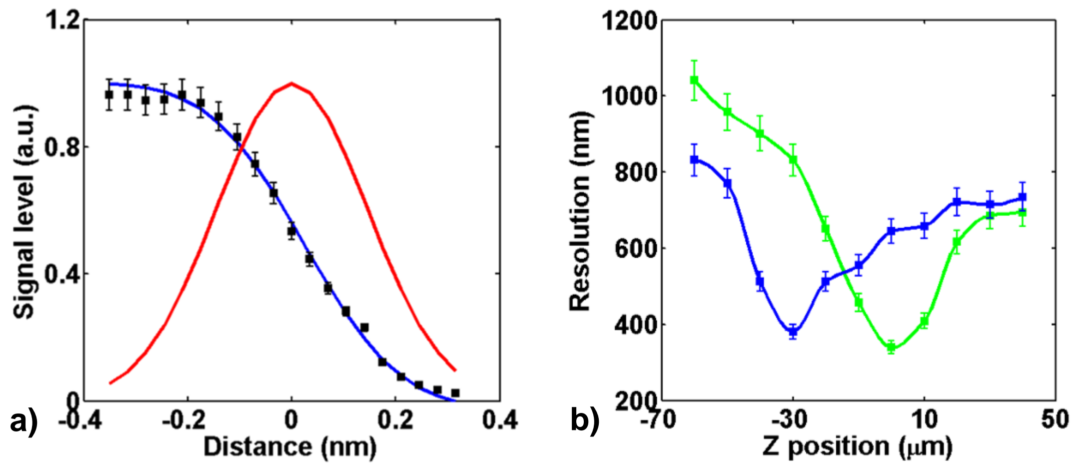

Figure 5.18. (a) Data showing a least-squares Gauss-error fit over a line-cut of n-doped silicon finger edge, (b) resolution values obtained while changing the laser beam focal position relative to the sample (blue line closed aperture, green line open aperture).

7.3.2 Observation of focal-dependent spatio-temporal effects

In a two-photon microscope the autocorrelation signal contains two distinct pieces of information. As already introduced, the pulse duration estimated from the autocorrelation width provides insights into the chromatic and spatial aberrations, but the autocorrelation intensity at zero delay is also correlated with the peak intensity at the focus, which is sensitive to both spatial and temporal distortions. This analysis is based on two parameters: 1. the pulse duration estimated from the TPA fringe-averaged autocorrelation, $G_2(\tau) = < g_2(\tau) >$; and 2. the maximum amplitude of $G_2(\tau)$. The aim of the analysis is to understand how the minimum pulse duration and the maximum autocorrelation signal amplitude vary as a function of the defocusing. For the data fitting the MATLAB Curve Fitting Toolbox™ was applied in two steps: firstly, by fitting a Gaussian envelope to $G_2(\tau)$, it provided an estimate of the pulse duration at every defocusing position; and secondly, by using a polynomial fit to the ensemble of pulse duration measurements, it was used to reveal the dependence of pulse duration on defocus, including appropriate confidence bounds. The minimum pulse duration and the maximum of the $G_2(\tau)$ autocorrelation amplitude were extracted from the fitting results as a function of the defocusing. In order to estimate the intensity autocorrelation, $G_2(\tau)$, from the fringe resolved interferometric autocorrelation traces, $g_2(\tau)$, a filtering process based on a Fourier Transform methods was applied. $g_2(\tau)$ was Fourier transformed and then a low-pass filter was applied to extract the fringe-averaged function, $G_2(\tau)$. The $G_2(\tau)$ shown in red colour in Figure 5.19, was fitted with a Gaussian function, $I_G(\tau)$, applying the MATLAB Curve Fitting Toolbox™, shown in blue. The FWHM pulse durations were estimated assuming Gaussian pulse intensity profiles a deconvolution factor of $\sqrt{2}$.

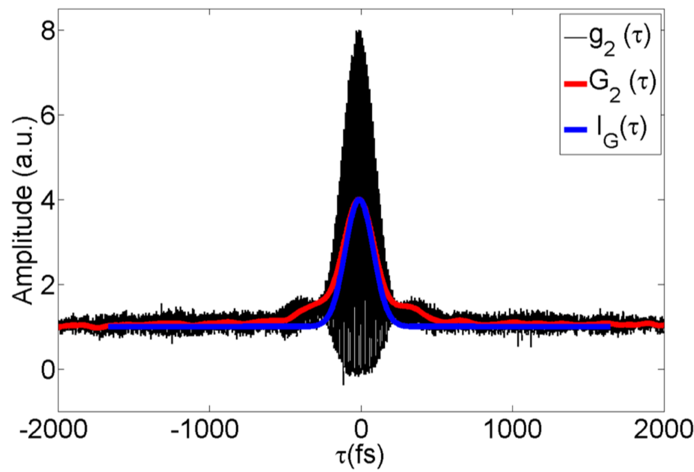

Figure 5.19. Interferometric autocorrelation ($g_2(\tau)$, black) measured at the focus of the microscope, shown with the fringe-averaged autocorrelation ($G_2(\tau)$, red) and corresponding Gaussian fit ($I_G(\tau)$, blue).

The autocorrelation amplitude was defined as the peak value of $g_2(\tau)$ with respect to the base line (Fig. 5.19.). The same filtering and fitting criteria were applied to measure the pulse duration and the autocorrelation amplitude as a function of focal position, generating corresponding datasets describing the variations of pulse duration and autocorrelation amplitude with defocus.

A near-infrared (Plan APO Mitutoyo 20X) long working distance microscope objective was used in all the experiments to focus the pulsed beam. This objective had a wavelength correction from the visible to near-infrared (1800 nm) and was corrected for an infinite conjugate, i.e. a plane wavefront incident on the objective.

The behaviour of three distinct optical systems was analysed as the device was scanned through the focal plane. The first system comprised the 20x microscope objective (MO) and the central SIL (hSIL) described before, and employed an adjustable aperture ("closed aperture") located in front of the objective lens. The next was identical except has no aperture, and the third was simply the microscope objective with no SIL and no aperture.

Objective lens and SIL with a closed aperture

The results are presented in Fig. 5.20. These calculations and fits were performed collaboratively by Dr. M. Rosete-Aguilar and Dr. J. Garduño-Mejía. The relative focal position for z=0 was located at the maximum of the Gaussian fitting of the autocorrelation amplitude. Polynomial fitting to the pulse durations shown in Fig. 5.20a. indicates that the minimum duration is located at z = 90 μm. The solid black circles indicate the experimental data, obtained with the procedures described previously and the black line is a second-order polynomial fit using a least squares fit. The blue dashed lines indicate the prediction bounds of the lower and upper values of the associated interval, defined by the uncertainty around the predicted fit. The level of certainty for the calculations is 90%. The data points outside the prediction bounds (red stars) were excluded from the fitting process, for instance the point at around z = -90 μm in Fig. 5.20a.

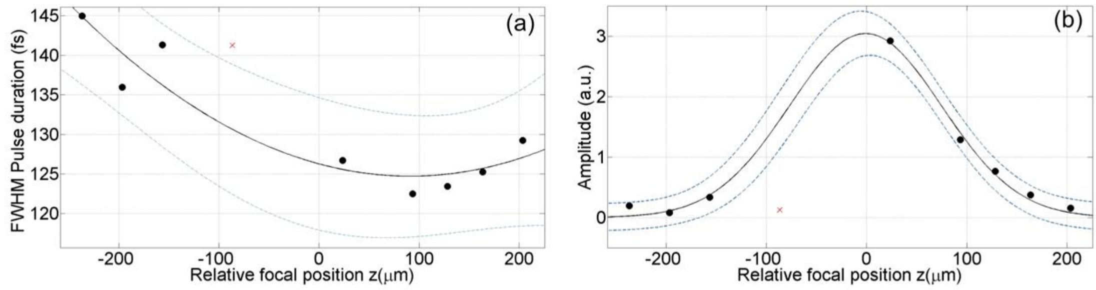

Figure 5.21. Effects of defocusing for a system comprising an objective lens, SIL and a closed aperture. (a) Pulse-duration dependence on defocus, where the solid black circles are experimental data and the black line is a second-order polynomial fit. The interval delineated by the blue dashed lines indicates the prediction bounds with a level of certainty of 90%. (b) Autocorrelation amplitude dependence on defocus, where the solid black circles are experimental data and the black line is a Gaussian fit. The blue dashed lines indicate the 90% certainty bounds as in (a).

In Fig. 5.21b, the experimentally measured autocorrelation amplitude is plotted as a function of defocus, together with a least-squares Gaussian fit to the data. It can be seen that the points fit well to the Gaussian, where the maximum amplitude is located at z = 0 µm.

From these results, the position for the maximum autocorrelation signal amplitude is at z = 0 µm, whereas the shortest pulse duration is at z = 90 µm, a difference of 90 µm. This result indicates a problem with either spherical aberration or propagation time difference (PTD) or both [6], where PTD describes the temporal broadening of the pulse introduced by chromatic aberration.

Objective lens and SIL with no aperture

Treating the data in the same way as described in the previous section, a second-order polynomial fit (Fig. 5.22a.) revealed that the position for the shortest pulse duration with aperture removed was at z = 105 µm. As before, the relative focal position for z = 0 µm was also defined at the maximum of the Gaussian fitting of the autocorrelation amplitude (Fig. 5.22b.). Again, this result indicates a problem with either spherical aberration or chromatic aberration, or both.

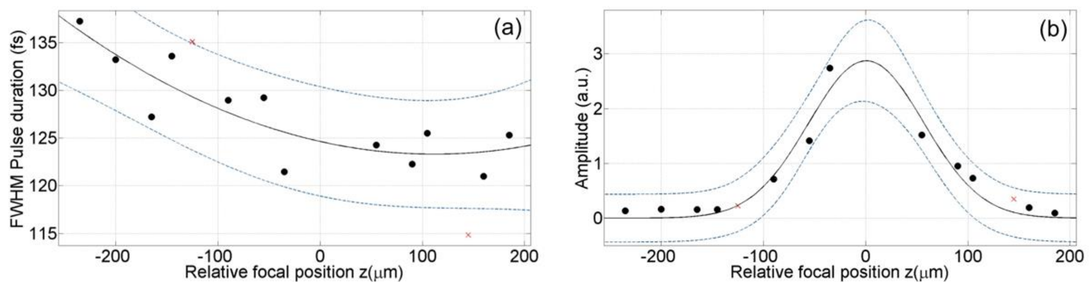

Figure 5.22. Effects of defocusing for a system comprising an objective lens, SIL but no aperture. (a) Pulse-duration dependence on defocus, and (b) autocorrelation amplitude dependence on defocus. For definitions of symbols and lines see Fig. 5.21.

Objective lens with no SIL or aperture

The analysis was repeated for a final time using data obtained with only the objective lens and with no SIL or aperture. In Fig. 5.23a, the pulse duration is plotted as a function of relative focal position z (μm). In Fig. 5.23b the experimentally measured autocorrelation amplitude is plotted as a function of relative focal position z (μm), together with a least-squares Gaussian fit to the data..

A second-order polynomial fit reveals that pulse duration does not change with z whereas the Gaussian fit to the autocorrelation amplitude shows the maximum amplitude located at z = 0 μm. Previously published modelling results from García-Martínez *et al* [6] showed that the maximum autocorrelation signal amplitude is located at the position where spherical aberration is the smallest, which in turn gives the position for the best spatial resolution. In other words, by locating the maximum autocorrelation signal amplitude, the best spatial resolution position will be located. The same authors also showed that the positions corresponding to the minimum pulse duration and the maximum autocorrelation amplitude always coincide for an aberration-free lens, whereas a difference in positions indicates the presence of aberrations or group velocity dispersion, GVD. With these theoretical results in mind, the difference in the positions of minimum pulse duration and maximum autocorrelation signal amplitude with a closed aperture (Fig. 5.21) and without an aperture (Fig. 5.22) indicate that chromatic aberration, spherical aberration or GVD are present. Assuming that the microscope objective is an optical system highly corrected for spherical aberration and chromatic aberration, the aberrations must therefore arise from either the SIL or from an aberrated incident wavefront on the objective lens or both.

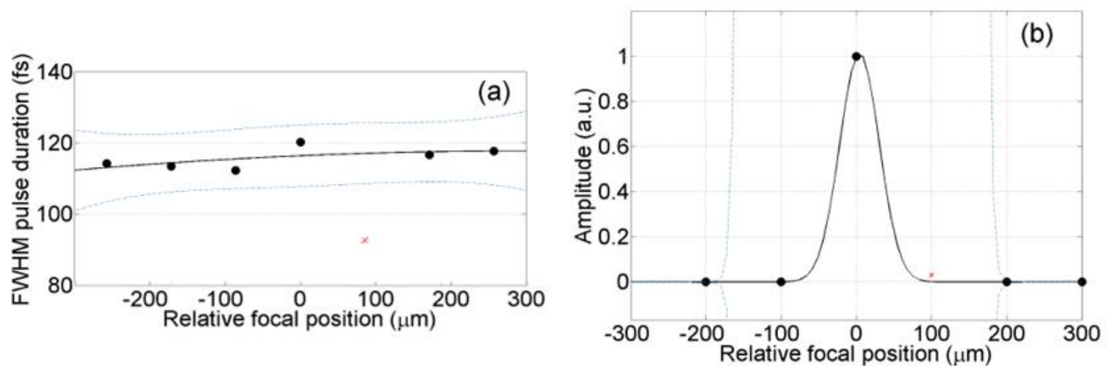

Fig. 5.23. Effects of defocusing for a system comprising an objective lens with no SIL lens or aperture. (a) Pulse-duration dependence on defocus, and (b) autocorrelation amplitude dependence on defocus. For definitions of symbols and lines see Fig. 5.21.

The modelling in reference [6] uses two approximations: 1. the scalar diffraction theory and, 2. the bandwidth of the pulse, $\Delta\omega$, is smaller than the angular frequency of the carrier, ω_0 i.e., $\Delta\omega/\omega_0 \ll 1$. The numerical aperture for the systems presented in Fig. 5.21, Fig. 5.22 and Fig. 5.23 are 0.35, 1.46 and 0.42 respectively. Only the systems with NA of 0.35 and 0.42 are

well described by the scalar diffraction theory, whereas the system with NA of 1.46 is not. The second approximation is satisfied in all cases, since the ratio between the bandwidth and the angular frequency of the carrier of the pulses is $\Delta\omega/\omega_0 = 0.019$, assuming 120 fs at 1.55 μm pulses modulated by a Gaussian envelope. The experimental results presented in Fig. 5.23a for the objective lens with no SIL lens show that the pulse duration does not change with z. Previous experiments reported in the literature [20,21], with lenses that satisfy both approximations, show that large monochromatic aberrations and defocus do not change pulse duration, so the experimental results presented in Fig. 5.23a agree with previous experimental results. These results are not sufficient to conclude if the incident wavefront on the objective lens is well corrected or not. On the other hand, the experiment with the objective lens and SIL lens with a closed aperture also satisfies both approximations, and the experimental results presented in Fig. 5.21a show a change in pulse duration along z direction, therefore deduction that the SIL lens induces the change in pulse duration along z direction can be made.

It is apparent that SIL lens introduces spherical aberration, chromatic aberration and variation of group velocity dispersion across the aperture of the lens. On the other hand, a poorly corrected incident wavefront on the objective lens will produce an aberrated wavefront incident on the SIL lens, which in turn will increase even more the aberration introduced by the not quite hemispherical condition. In the experiment the GVD introduced by thickness material is compensated but a variation of GVD across the aperture may remain.

Although the SIL lens is introducing spherical, chromatic aberration and a variation of GVD, however, large aberrations in the incident wavefront on the objective lens can be potentially introduced by the singlet lenses in a beam expanding telescope prior to the objective lens.

7.4 Conclusions

These results are the first example of applying the theoretical insight from [6] in a nonlinear microscope. The approach offers a potentially simple means of detecting and potentially minimising whole-system aberrations by iteratively optimising the objective lens position and the illumination wavefront until the minimum difference has been found between the positions of minimum pulse duration and maximum autocorrelation signal. The inclusion of a motorised stage to actuate the objective position, together with a liquid-crystal spatial light modulator (SLM) to control the wavefront before the objective lens would form the basis for this approach. Autocorrelation data recorded in only a few seconds would be sufficient to construct amplitude and pulse duration scans similar to those in Fig. 5.22. The difference in the positions of minimum duration and maximum intensity would provide a metric on which an optimisation strategy could be based. A simple hill-climbing approach in which the SLM was used to apply defocus or

another low-order aberration could be investigated. Stochastic optimisation methods such as simulated annealing or genetic algorithms would offer a more general solution [30], in which the SLM would be used to randomly perturb the wavefront and gradually drive the error towards smaller values. In this way the optical system before the microscope could be adjusted to minimise its contribution to the aberrations of the whole system, leaving only the intrinsic aberrations of the sample and objective-SIL lens combination.

References

1. U. Fuchs, U. D. Zeitner, and A. Tuennermann, "Ultra-short pulse propagation in complex optical systems", Optics Express **13**, 3852-3861 (2005).
2. M. Kempe, U. Stamm, B. Wilhelmi, and W. Rudolph, "Spatial and temporal transformation of femtosecond laser pulses by lenses and lens systems", Journal of the Optical Society of America B **9**, 1158-1165 (1992).
3. M. Kempe and W. Rudolph, "Impact of chromatic and spherical aberration on the focusing of ultrashort light pulses by lenses", Optics Letters **18**, 137-139 (1993).
4. Z. Bor, "Distortion of femtosecond laser pulses in lenses", Optics Letters **14**, 119-121 (1989).
5. J. B. Pawley, "Handbook of biological confocal microscopy, 3rd ed.", New York: Springer (2006).
6. L. García-Martínez, M. Rosete-Aguilar, and J. Garduño-Mejía, "Gauss-Legendre quadrature method used to evaluate the spatio-temporal intensity of ultrashort pulses in the focal region of lenses", Applied Optics **51**, 306–315 (2012).
7. B. Sun, P. S. Salter and M. J. Booth, "Effects of aberrations in spatiotemporal focusing of ultrashort laser pulses", Journal of the Optical Society of America **31,** 4 (2014)
8. P. Bowlan, "Measuring the spatiotemporal electric field of ultrashort pulses with high spatial and spectral resolution", PhD thesis: Georgia Institute of Technology (2009).
9. D. Oron and Y. Silberberg, "Spatiotemporal coherent control using shaped, temporally focused pulses", Optics Express **13**, 9903-9908 (2005).
10. C. Xu and W. Denk, "Two-photon optical beam induced current imaging through the backside of integrated circuits", Applied Physics Letters **71**, 2578–2580 (1997).
11. C. Xu and W. Denk, "Two-photon optical beam induced current imaging through the backside of integrated circuits", Journal of Applied Physics **86**, 2226–2231 (1999).
12. C. Xu, L. M. F. Chirovsky, W. S. Hobson, J. Lopata, W. H. Knox, J. E. Cunningham, W. Y. Jan and L. A. D'Asaro, "Two-photon photocurrent imaging of vertical cavity surface emitting lasers, Applied Physics Letters **76**, 1510–1512 (2000).
13. K. A. Serrels, E. Ramsay, P. A. Dalgarno, B. D. Gerardot, J. A. O'Connor, R. H. Hadfield, R. J. Warburton and D. T. Reid, "Solid immersion lens applications for nanophotonic devices", Journal of Nanophotonics **2**, 021854 (2008).
14. M. Baba, T. Sasaki, M. Yoshita, H. Akiyama, "Aberrations and allowances for errors in a hemisphere solid immersion lens for submicron-resolution photoluminescence microscopy", Journal of Applied Physics **85**, 6923 (1999).
15. Y. Lu, T. Bifano, S. Ünlü, B. Goldberg, "Aberration compensation in aplanatic solid immersion lens microscopy", Optics Express **21**, 28189-97 (2013).
16. J. C. Wyant and K. Creath, "Applied optics and engineering, Vol. 9", New York: Elsevier (1983).

17. W. T Welford, “Aberrations of the symmetrical optical system”, London: Academic Press (1974).
18. W. T. Welford, “Aberrations of optical systems”, Bristol: Adam Hilger (1986).
19. W. J. Smith, “Modern optical engineering, 4th ed.”, New York: McGraw-Hill (2008).
20. G. Conforti, “Zernike aberration coefficients from Seidel and higher-order power-series coefficients”, Optics Letters **8**, 407-408 (1983).
21. R. K. Tyson, “Conversion of Zernike aberration coefficients to Seidel and higher-order power-series aberration coefficients”, Optics Letters **7**, 262-264 (1982).
22. M. D. Perrin, A. Sivaramakrishnan, R. B. Makidon, B. R. Oppenheimer, and J. R. Graham, “The structure of high Strehl ratio point-spread functions”, Astrophysical Journal **596**, 702-712 (2003).
23. S. B. Ippolito, B. B. Goldberg, and M. S. Ünlü, “Theoretical analysis of numerical aperture increasing lens microscopy”, Journal of Applied Physics **97**, 053105 (2005).
24. E. J. Botcherby, R. Juskaitis, M. J. Booth, and T. Wilson, “Aberration-free optical refocusing in high numerical aperture microscopy”, Optics Letters **32**, 2007-2009 (2007).
25. M. J. Booth, “Adaptive optics in microscopy”, Philosophical Transactions, Series A. Mathematical, Physical, and Engineering Sciences **365**, 2829-2843 (2007).
26. J. C. M. Diels, J. J. Fontaine, I. C. McMichael, and F. Simoni, “Control and measurement of ultrafast pulse shapes (in amplitude and phase) with femtosecond accuracy”, Applied Optics **24**, 1270-1282 (1985).
27. E. Ramsay, N. Pleynet, D. Xiao, R. J. Warburton and D. T. Reid, “Two-photon optical-beam-induced current solid-immersion imaging of a silicon flip chip with a resolution of 325 nm”, Optics Letters **30**, 26-28 (2005).
28. M. González-Galicia, J. Garduño-Mejía, M. Rosete-Aguilar, N.C. Bruce and R. Ortega-Martínez, “Effects of primary spherical aberration, coma, astigmatism, and field curvature on the focusing of ultrashort pulses: Gaussian illumination and experiment,” Journal of the Optical Society of America A **28**, 1990-1994, (2011).
29. M. Rosete-Aguilar, J. Garduño-Mejía, and N. C. Bruce, “Focusing ultrashort laser pulses with achromatic doublets,” SPIE Newsroom 10.1117/2.1201504.005926 (2015).
30. O. Katz, E. Small, Y. Bromberg and Y. Silberberg, "Focusing and compression of ultrashort pulses through scattering media," Nature Photonics **5**, 372-377 (2011).

Chapter 8. Conclusions and future developments

This chapter concludes the thesis by summarising all the experimental work and results presented in the previous chapters. Here a discussion is provided to explain the novelty, significance and context of achieved results in the field of the IC failure analysis. Also directions and guidelines for the future work to enhance and further extend our results on nonlinear sub-surface microscopy are given.

8.1 Technical summary and conclusions

Chapter 2 introduced the Er:Fibre laser, which was used as an illumination source. This laser was chosen as it suits the TOBIC application very well. The Er:Fibre laser generates a wavelength of 1550 nm, which fits in the silicon transparency window, while at the same time enables TPA as two photons combined have the energy higher than the silicon bandgap. Also the Er:Fibre laser generates pulses of 110 fs, which are short enough to produce a high peak power in the vicinity of the focal spot, which is necessary for the TPA to occur. The simple and inexpensive design of the Er:Fibre laser as well as its reliability and straightforward operation provided a practical laser system with which to implement the nonlinear microscope.

In Chapter 3 nonlinear TOBIC microscope is described, which was constructed for IC imaging. The main goal in this work was to explore the possibility to further improving the lateral resolution of the SIL enhanced TOBIC microscope. Building upon the previous findings of the significant polarisation influence on the focal spot shape and size [1], theoretical calculations were performed for illumination under the high NA conditions for various polarisation cases. The expected findings suggested that a RP beam had the potential to improve the imaging localisation resolution. Therefore, a LC RPC was introduced in the nonlinear microscope to test the modelling results experimentally. It was found that using the RP beam under high NA imaging conditions it was possible to produce as small a focal spot as with LP light. It was possible to achieve this result only with a high degree of polarisation purity of the RP beam, which was measured using Stokes parameters to be 94%.

The obtained imaging resolutions correlated well with other theoretical calculations and experimental results [2]. While radial polarisation makes it possible to achieve a comparable lateral resolution to that level of linearly polarised illumination, it has the major advantage providing this resolution in all directions. This leads to an improvement of the nonlinear microscope system by way of eliminating the need to adjust polarisation for single feature orientations.

The achieved resolutions were in the 100 nm range, which are surpassed only by nonlinear microscopy complemented with annular illumination [3]. Modelling results of such a system, were presented in Chapter 3 and predicted even further resolution improvement for the RP beam using an annular aperture. As the RP beam consists of radial and longitudinal components, pupil engineering makes it possible to suppress the lower resolution provided by the radial component [4]. Therefore, later in this chapter further enhancement of the nonlinear TOBIC microscope using annular aperture along with the RP beam was proposed.

Chapter 4 expanded the study of the benefits of certain polarisation states from imaging to localisation of errors. Here, the influence of the polarisation was explored for the first time in the context of the timing-resolved 2pLADA failure analysis technique. To obtain higher localisation resolutions it was decided to construct a laser, which would generate a shorter wavelength than 1550 nm. As a result, a Raman soliton laser generating 1280 nm wavelength and 140 fs was constructed. To implement the RPC in the 2pLADA tool, a custom-designed RP module was installed in the industrial failure analysis system (Meridian IV).

Experiments once again proved that the quality of the spatial localisation depends on the polarisation state. Also it was found that the spatial localisation of the 2pLADA site depended on the temporal overlap between the optical pulses (laser) and electrical (ATE) pulses. Again, as in TOBIC microscopy, linear polarisation showed a clear advantage as long as the preferred polarisation direction could be identified. The RP beam provided the best localisation resolution benefiting from its symmetrical focal spot, however it led to a distortion of the 2pLADA signature, which was attributed to the strong longitudinal electric field component.

Measurements at different focal depths (z-scans) revealed the nonlinear nature of the 2pLADA signal using the pulsed Raman soliton laser, which is not the case for the CW laser, where free carrier absorption (FCA) dominates [5]. However, further investigation is necessary to evaluate the FCA influence on 2pLADA signature. Therefore, multiphoton microscopy was proposed to be a good tool to overcome the drawbacks of possible FCA.

Chapter 5 examined spatio-temporal aberrations arising in the sub-surface nonlinear microscope and presented experimental validations for the previous theoretical calculations [6], which ultimately offered a straightforward optimisation strategy for the imaging system. By comparison with theory it was shown that the simple measurement of the pulse autocorrelation at the test device provided information about both spherical and chromatic aberrations inside the microscope, correlating with the position of the optimum spatial resolution. These can be diminished by optimising the objective lens position and the wavefront of the incident beam so that the maximum amplitude of the autocorrelation signal and shortest pulse duration would

coincide at the same focal position. Also there are other means to mitigate aberrations and some of the promising techniques for the sub-surface imaging are suggested later in this chapter.

8.2 Future work

The project's goal to achieve the highest possible localisation resolution for failure analysis is a constant struggle with the ever shrinking feature sizes of the ICs. Therefore, it is essential to offer a few techniques, which could make it possible to push the presented research further and greatly improve the localisation resolutions to keep pace with the semiconductor industry's demanding requirements.

Annular apertures

The performance of pupil-plane amplitude filters in nonlinear sub-surface microscopy has been successfully demonstrated before and a reduction from 100 nm to 70 nm using an obscuration disc was achieved [3]. A similar approach can be introduced in the current microscope design, easily improving the imaging resolution. In Chapter 2 the effects of radial polarisation along with annular apertures were theoretically modelled suggesting further improvements of the resolution. Therefore, annular apertures are an attractive and simple technique to further improve the fault localisation resolution. This effect can be enhanced by introducing phase masks with SLMs as well. This approach has been proposed and shown experimentally, though not yet in the defect injection failure analysis techniques [7, 8].

Radially polarised higher-order Laguerre-Gaussian beam

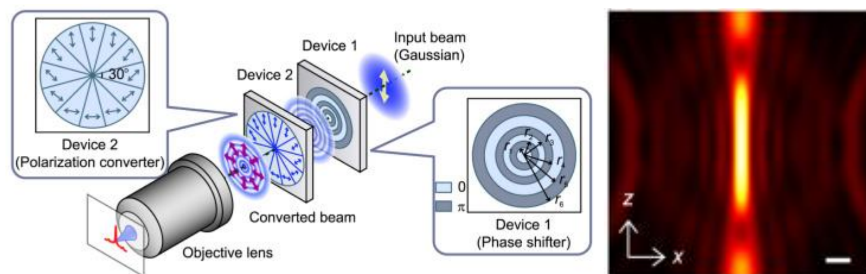

Fig. 6.1. Microscopy using RP higher-order Laguerre-Gaussian beam [12].

It has recently been demonstrated that a RP higher-order Laguerre-Gaussian beam can be focused to a tight focal spot, which is laterally smaller and longitudinally longer [9]. This needle shaped beam compared with a linearly polarised beam or circularly polarised beam can be focused to a tighter spot [10]. It was presented before in Chapter 3 and 4 that the liquid crystal polarisation converter can be used to convert a linearly polarised beam into an RP beam. By inserting the SLM and applying a six-ringed mask to it, a higher-order RP beam is obtained [11], which can yield super-resolution performance (Fig. 6.1) [12].

Subtraction microscopy

There is another approach in which CV beams can be used to produce high-resolution imaging. The so-called subtraction imaging using radially and azimuthally polarised beams was demonstrated by [13]. This technique exploits the fact that the focal spot created by the radially polarised beam consists of longitudinal and radial electric field components. As it was demonstrated in Chapter 2, the longitudinal component produces a sharp and high-resolution lateral spot, while the radial component forms a doughnut-shaped pattern. This pattern is very similar to that created by the focused azimuthally polarised beam. Therefore, if the azimuthal pattern is subtracted from the radial pattern, the remainder is a high-resolution pattern formed by the longitudinal component (Fig. 6.2). This effectively leads to the improvement of the spatial resolution [13]. This is a simple technique to implement as the image processing is quite easy and the AP beam can be generated by rotating the linear polarisation of the incident light to the RPC by 90°, which can be performed with a simple rotation of the HWP by 45°.

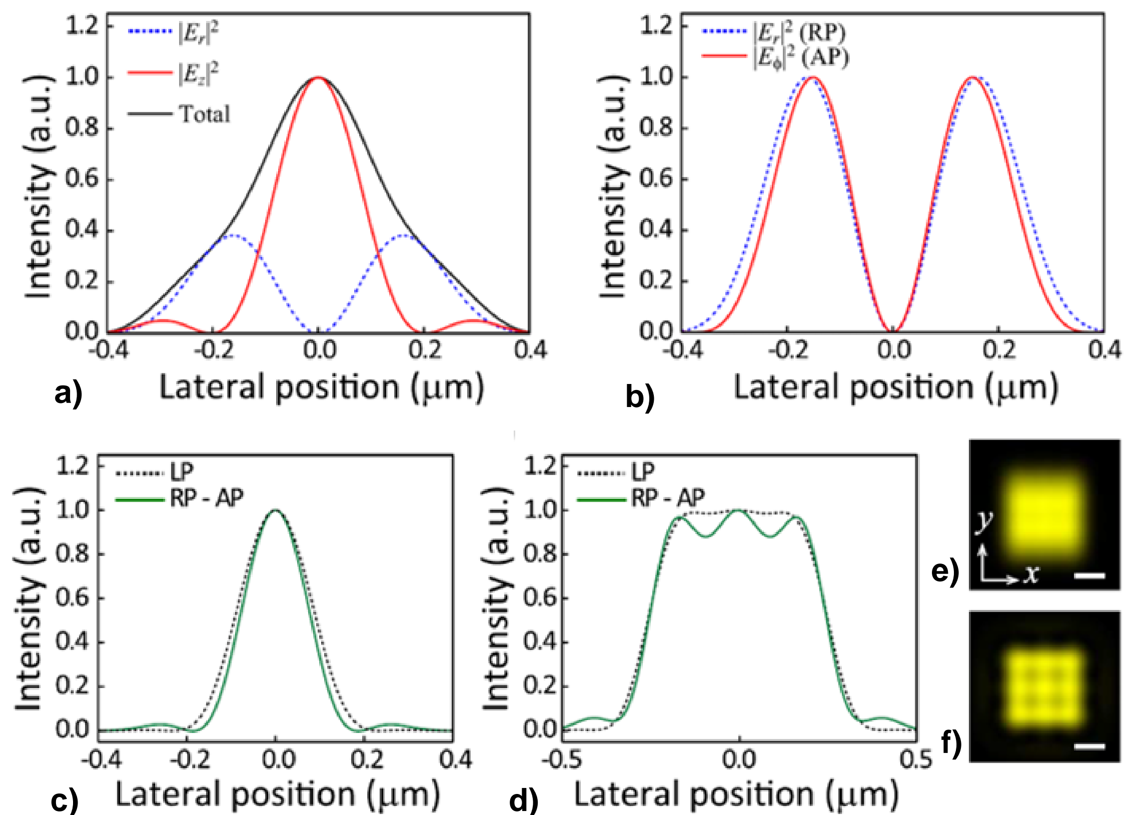

Figure 6.2. (a) Intensity profiles of the RP beam at the focal plane and (b) Intensity profiles radial component of the RP beam and azimuthal component of the AP beam. (c) Comparison between the PSF of the LP beam and the PSF of the subtraction imaging. (d) Intensity profiles of simulated images shown in (e) and (f); (e) the confocal image using LP and (f) using subtraction imaging [13].

Aberration mitigation

Another possible enhancement of nonlinear microscope using SLM can be done with aberration mitigation. As it was predicted in Chapter 4, the optical system before the microscope objective could be adjusted to minimise its contribution to the aberrations of the whole system. This can be done with the help of an SLM. The SLM simply would have to generate a phase and amplitude pattern to obtain shortest pulse duration and maximum autocorrelation signal amplitude at the same longitudinal z position. This would automatically give the highest aberration free point spread function of the system.

Yet another approach for aberration suppression would be to employ wavefront detector and feedback it using the SLM or the deformable mirror as it was previously done by Y. Lu et. al. [14]. Another promising technique for aberration mitigation is based on orthogonal mode decomposition, regardless of the distribution of the optical aberrations. This approach can be used to restore the optimal focal spot in live. This technique can be understood as an interplay between energy conservation and constructive interference effects. The optimal focal sport leads to the increase in the energy density at the selected point. This method is able to compensate all time-invariant aberrations, from weak aberrations to scattering from highly turbid media (Fig. 6.3). This optimisation technique was previously demonstrated for the optical micromanipulation, which is highly sensitive to aberrations [15].

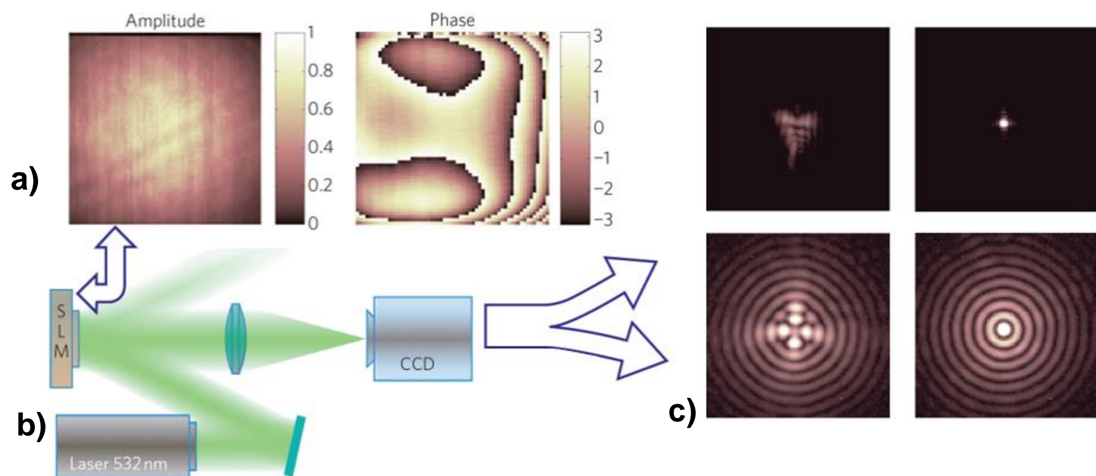

Figure 6.3. Demonstration of the optimisation method. (a) Amplitude and phase of the modes. (b) Optical setup basic principle. (c) Focal spot before and after applying the phase correction [15].

Multiphoton absorption microscopy

K. Erington et. al. [5] showed that free carrier absorption plays important role in LADA signature generation. It was demonstrated that a 1300 nm CW laser shows linear LADA behaviour, which is unrelated to TPA. This effect is caused by free carrier absorption in highly doped regions, while heating the sample at the same time. Free carrier absorption can reduce the benefits obtained using the 2pLADA technique, therefore it is essential to investigate further what effect it has on the pulsed lasers. Also it would be beneficial to use multiphoton absorption, which would have a lower probability for the free carrier absorption. The recent advancements in mid-infrared OPO reaching wavelengths of 12 µm (Fig. 6.4), with pulse durations of femtosecond scale and powers of tens of milliwatts, using orientation-patterned gallium phosphide (OP-GaP) gain material [16] can be of particular interest to explore multiphoton absorption dynamics of silicon, maybe with the potential to increase localisation resolutions in 2pLADA technique. As up to now the nonlinear properties of silicon were investigated only up to the wavelength of 6 µm [17]. However, the resolution would degrade to around 500 nm.

Also as suggested in [17], TPA in silicon at the wavelength around 2.1 µm occurs at the highest rate with the lowest free carrier absorption. Therefore, this wavelength could be of particular interested for sub-surface microscopy of ICs while still imaging in the TPA regime. However, the trade-off in resolution would be 210 nm instead of 160 nm.

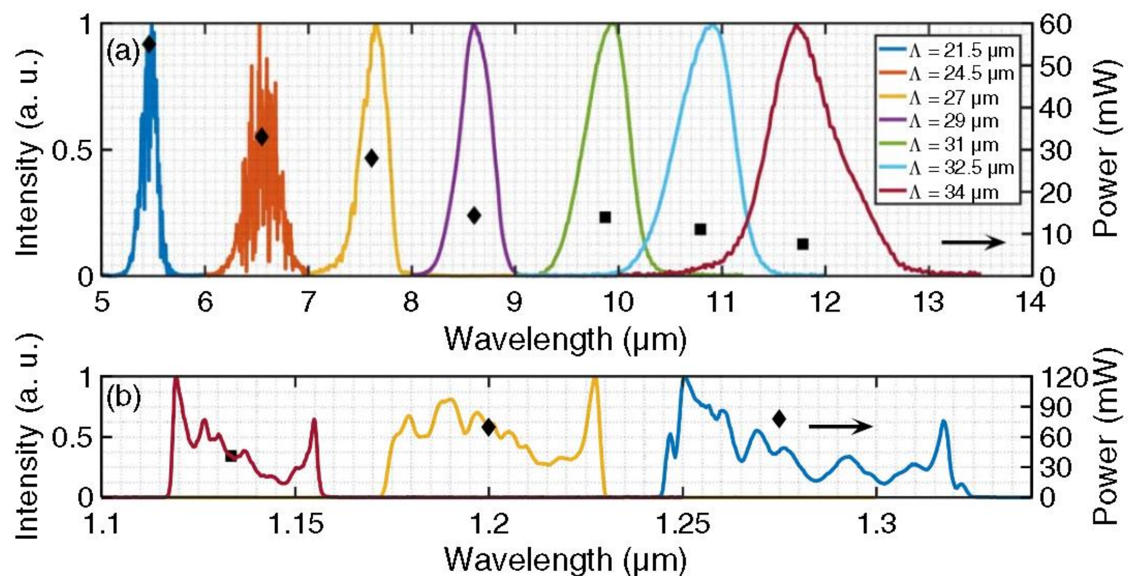

Figure 6.4. Idler (top) and signal (bottom) spectra obtained using OP-GaP gain media [16].

Translation microscopy (TRAM)

The last technique, which could greatly increase the sub-surface resolution is the so-called translation microscopy (TRAM) technique. While super-resolution microscopy techniques like stimulated emission depletion technique (STED) and atomic force microscopy (AFM) are hardly implemented in the sub-surface microscopy, the novel TRAM technique offers simple approach to achieve super-resolutions. In TRAM, the super-resolution is achieved applying signal processing techniques to a set of diffraction-limited low-resolution images obtained by translating the sample in the XY plane (Fig. 6.5). One of the advantages of this modality that the sample can be shifted in multiple directions without the need of exact step sizes. Therefore, the TRAM technique can be easily applied in the current nonlinear microscope, which is already equipped both with sample scanning stages and galvanometer mirror scanner. As a result, TRAM can be performed by moving the sample with the stages and then obtaining an image rapidly by employing the beam scanner.

It was recently shown that TRAM can achieve up to a 7-fold increase in lateral resolution in a cellular environment. In a sub-surface imaging context this would mean, that sub-100-nm resolutions for IC imaging without using the SIL or of the range of 10 nm with the SIL could be achieved [18].

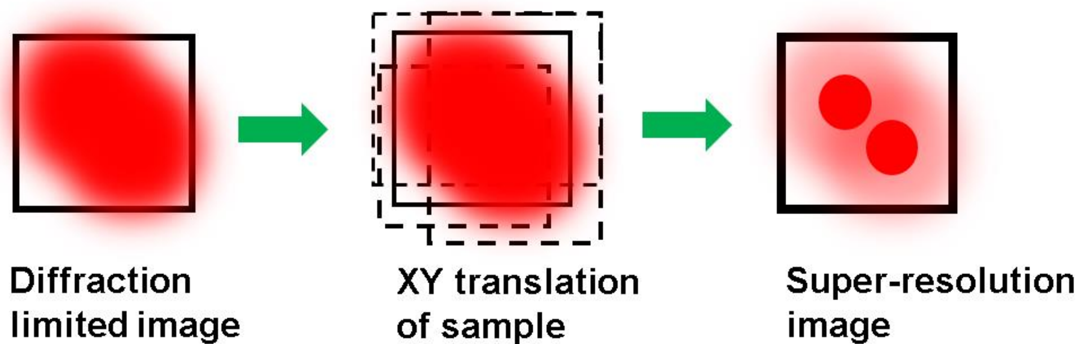

Figure 6.5. Schematic illustration of translation microscopy (TRAM). This technique is based on obtaining multiple shifted images. This data then used to compute and resolve the super-resolution image.

References

1. K. A. Serrels, E. Ramsay, R. J. Warburton and D. T. Reid, "Nanoscale optical microscopy in the vectorial focusing regime", Nature Photonics **2**, 311 - 314 (2008).
2. Q. Zhan, "Cylindrical vector beams: from mathematical concepts to applications", Advances in Optics and Photonics **1**, 1-57 (2009).
3. K. A. Serrels, E. Ramsay and D. T. Reid, "70 nm resolution in subsurface optical imaging of silicon integrated-circuits using pupil-function engineering", Applied Physics Letters **94**, 073113 (2009).
4. R. Dorn, S. Quabis, and G. Leuchs, "Sharper focus for a radially polarized light beam", Physics Review Letters **91**, 233901 (2003).
5. K. Erington, D. Bodoh, K. Dickson, G. Lange, "The role of free carrier absorption in LADA", ASM International **9**, 73-81 (2014).
6. L. García-Martínez, M. Rosete-Aguilar, and J. Garduño-Mejía, "Gauss-Legendre quadrature method used to evaluate the spatio-temporal intensity of ultrashort pulses in the focal region of lenses", Applied Optics **51**, 306–315 (2012).
7. S. F. Pereira and A. S. van de Nes, "Superresolution by means of polarisation, phase and amplitude pupil masks", Optics Communications **234**, 119-124 (2004).
8. H.X. Luo and C.H. Zhou, "Comparison of superresolution effects with annular phase and amplitude filters", Applied Optics **43**, 6242-6247 (2004).
9. Y. Kozawa, S. Sato, "Sharper focal spot formed by higher-order radially polarised laser beams", Journal of the Optical Society of America A **24**, 1793-1798 (2007).
10. H. Wang, L. Shi, B. Lukyanchuk, C. Sheppard, T. C. Chong, "Creation of a needle of longitudinally polarised light in vacuum using binary optics", Nature Photonics **2**, 501-505 (2008).
11. Y. Kozawa, T. Hibi, A. Sato, H. Horanai, M. Kurihara, N. Hashimoto, H. Yokoyama, T. Nemoto, S. Sato, "Lateral resolution enhancement of laser scanning microscopy by a higher-order radially polarised mode beam", Optics Express **19**, 15947-15954 (2011).
12. H. Dehez, A. April, M. Piché, "Needles of longitudinally polarised light: guidelines for minimum spot size and tunable axial extent", Optics Express **20**,14891-14905 (2012).
13. S. Segawa, Y. Kozawa, and S. Sato, "Demonstration of subtraction imaging in confocal microscopy with vector beams", Optics Letters **39**, 4529-4532 (2014).
14. Y. Lu, T. Bifano, S. Ünlü, and B. Goldberg, "Aberration compensation in aplanatic solid immersion lens microscopy", Optics Express **21**, 28189-28197 (2013).
15. T. Čižmár, M. Mazilu and K. Dholakia, "In situ wavefront correction and its application to micromanipulation", Nature Photonics **4**, 388 - 394 (2010).
16. L. Maidment, P. Schunemann, and D. Reid, "Molecular fingerprint-region spectroscopy from 5 to 12 μm using an orientation-patterned gallium phosphide optical parametric oscillator", Optics Letters **41**, 4261-4264 (2016).

17. T. Wang, N. Venkatram, J. Gosciniak, Y. Cui, G. Qian, W. Ji, and D. Tan, “Multi-photon absorption and third-order nonlinearity in silicon at mid-infrared wavelengths”, Optics Express **21**, 32192-32198 (2013).
18. Z. Qiu, R. S. Wilson, Y. W. Liu, A. R. Dun, R. S. Saleeb, D. S. Liu, C. Rickman, M. Frame, R. R. Duncan, W. P. Lu, “Translation Microscopy (TRAM) for super-resolution imaging”, Scientific Reports **6**, 19993 (2016).